Univerzita Karlova v Praze
Přírodovědecká fakulta

Studijní program: Aplikovaná geologie

Mgr. Tomáš Svitek

Laboratórne štúdium 3D elastickej anizotropie hornín
Laboratory study of 3D elastic anisotropy of rocks

Dizertačná práca

školiteľ: Ing. Tomáš Lokajíček, CSc.

konzultant: RNDr. Václav Vavryčuk, DrSc.

Praha, 2015

Prehlásenie:

Prehlasujem, že som záverečnú prácu spracoval samostatne a že som uviedol všetky použité informačné zdroje a literatúru. Táto práca ani jej podstatná časť nebola predložená k získaniu iného alebo rovnakého akademického titulu.

V Prahe, 19.01.2015

Podpis

Poďakovanie

Na tomto mieste by som rád poďakoval najmä Ing. Tomášovi Lokajíčkovi, CSc. za jeho odbornú pomoc a vedenie počas celého štúdia. Za mnoho hodín konzultácií a objasňovania teórie anizotropie ďakujem RNDr. Václavovi Vavryčukovi, DrSc. Ďalej ďakujem Matějovi Petružálkovi za jeho často podnetné pripomienky a kolegiálny prístup. Za pomoc pri realizácii laboratórnych experimentov ďakujem technickému personálu laboratória Fyzikálnych vlastností hornín, GLÚ, AVČR, v.v.i., Vlastimilovi Fillerovi, Julii Erdingerovej, Vlastimilovi Nemejovskému, Zdeňkovi Erdingerovi a Miroslavovi Grussmanovi.

Na záver by som rád poďakoval svojim rodičom za ich vytrvalú podporu počas celého vysokoškolského štúdia, manželke Lucinke za jej trpezlivosť a vieru a Lilli za inšpiráciu a motiváciu.

Práca vznikla s podporou výskumných projektov RVO 67985831, Kontakt II LH13102, P104/12/0915, P210/12/1491 a 13-13967S. Ďakujem!

Obsah

Zoznam obrázkov

Zoznam príloh

Zoznam použitých skratiek a veličín

P	prvá vlna (z anglického ‘primary‘)
S	druhá vlna (z anglického ‘secondary‘)
S1	rýchla S vlna
S2	pomalá S vlna
RMS	druhá odmocnina súčtu štvorcov (z anglického ‘root mean square‘)
LPO	prednostná orientácia mriežky (z anglického ‘lattice preferred orientation‘)
SPO	prednostná orientácia tvaru minerálnych zŕn (z anglického ‘shape preferred orientation‘)
TOF	doba letu (z anglického ‘time of flight‘)
RTG	röntgenové žiarenie
ASR	alkalicko-silikátová reakcia (z anglického ‘alcali-silicate reaction‘)
SWS	štepenie strižných vĺn (z anglického ‘shear-wave splitting‘)
STA	priemer krátkeho okna (z anglického ‘short-term average‘)
LTA	priemer dlhého okna (z anglického ‘long-term average‘)
T_P	pozdĺžne polarizovaný vysielač
T_{Sh}	horizontálne polarizovaný vysielač
T_{Sv}	vertikálne polarizovaný vysielač
R_P	pozdĺžne polarizovaný prijímač
R_{Sh}	horizontálne polarizovaný prijímač
R_{Sv}	vertikálne polarizovaný prijímač
HOS	štatistické momenty vyšších rádov (z anglického ‘high-order statistics‘)
c	fázová rýchlosť
$\mathbf{c}$	vektor fázovej rýchlosti
v	grupová rýchlosť
$\mathbf{v}$	vektor grupovej rýchlosti
p	pomalosť
$\mathbf{p}$	vektor pomalosti
Γ_{ij}	Christoffelov tenzor

δ_{ij}	Kroneckerovo delta
n	vektor fázovej normály
N	vektor smeru lúča
g	polarizačný vektor
a_{ijkl}	hustotne normalizovaný elastický tenzor
a^{0}_{ijkl}	hustotne normalizovaný elastický tenzor referenčného prostredia
Δa_{ijkl}	odchýlky hustotne normalizovaného elastického tenzoru
e_{mean}	priemerné odchýlky teoretických a predikovaných rýchlostí
e_{max}	maximálne odchýlky teoretických a predikovaných rýchlostí

Abstrakt

V predkladanej práci je hodnotený význam merania rýchlosti akustických S vĺn na stanovenie elastickej anizotropie hornín. S vlny sú v porovnaní s P vlnami citlivejšie na anizotropiu prostredia, ktorým sa šíria. Na základe ich štepenia je možné stanoviť silu anizotropie a orientáciu štruktúr, ktoré sú za anizotropné chovanie materiálu zodpovedné. S vlny sú tak nutné k popisu anizotropného chovania materiálu a k stanoveniu kompletného tenzoru elastických parametrov. Aby bolo možné S vlny registrovať bolo však nutné existujúcu meraciu aparatúru vyvinutú pre meranie rýchlostí P vĺn významne inovovať. Vykonané inovácie poskytli meranie P vĺn v pozdĺžnom smere a S vĺn v dvoch navzájom kolmých priečnych smeroch. Kalibračné merania na homogénnych izotropných materiáloch potvrdili stálosť a opakovateľnosť registrovaných údajov. Nové usporiadanie ultrazvukového merania na guľových vzorkách za pôsobenia všesmerného hydrostatického tlaku a možnosť registrovať vlnové obrazy S vĺn umožnilo určovať anizotropiu hornín s kvalitatívne lepšou presnosťou než oproti doterajšiemu spôsobu spracovania. Meranie S vĺn si vyžiadalo úpravu spracovateľského softwaru a vývoj nových algoritmov interpretácie nameraných dát. K overeniu funkčnosti navrhnutých spracovateľských postupov boli realizované syntetické testy vyhodnocujúce variabilitu, vplyv nepresnosti a typ vstupných premenných pre výpočet tenzoru elastických parametrov. Testy potvrdili, že meranie rýchlostí S vĺn vedie k významnému zlepšeniu presnosti meranej anizotropie. Ukázalo sa, že meranie rýchlosti P a S1 vĺn nie je úplne postačujúce. Najlepšie výsledky sú dosiahnuté pri výpočte s prispením rýchlostí P, S1 aj S2 vĺn. Aplikácia výpočtu na reálne dáta potvrdila výsledky syntetického testu. Práca tak dokumentuje nutnosť znalosti rýchlostí S1 a S2 vĺn v dostatočnom množstve nezávislých smerov pre hodnoverné stanovenie anizotropie skúmaného materiálu.

Abstract

The presented work evaluates the significance of measuring acoustic S-wave velocities for determination of elastic anisotropy of rocks. The S waves are more sensitive to anisotropic properties of a medium than the P waves. Analyzing the S-wave splitting, it is possible to determine strength of anisotropy as well as the orientation of structures responsible for the anisotropic behavior of the medium. The S waves are necessary for determining the complete tensor of elastic parameters. In order to record the S waves, the measuring head of the present apparatus has been significantly adapted. Implemented innovations provided measurements of the P waves together with two orthogonally polarized S waves. The calibration performed on homogeneous isotropic materials proved that the recorded data are accurate and of high quality. The ultrasonic measurements on spherical samples under confining pressure and recording of the S waveforms significantly improved the accuracy of the retrieved elastic parameters compared to the measurements in standard use. The analysis of the S-wave records also required modifications of the processing software and a development of new algorithms. The proposed methods were tested on synthetic data. The tests evaluated the robustness of the inversion for anisotropy as a function of the number of measurements, their accuracy and type of waves recorded. The tests revealed that measuring the P-wave velocities is not sufficient for calculating the complete tensor of elastic parameters. When using measurements of the P- and S1-wave velocities, the accuracy is usually improved. However, the best accuracy is achieved if measurements of the P-, S1- and S2-wave velocities are inverted. The results of the synthetic tests were confirmed by the application of the proposed inversion methods to real data. This application documented the necessity for knowledge of the S1- and S2-wave velocities measured in a sufficient number of independent directions in order to determine anisotropy reliably.

1. Úvod

1.1 Téma a ciele práce

Predkladaná dizertačná práca sa zaoberá štúdiom elastickej anizotropie hornín pomocou metódy ultrazvukového prežarovania v režime hydrostatického zaťažovania. Dôraz je kladený na vplyv meraných rýchlostí S vĺn (spoločne v kombinácii s P vlnami) na určovanie elastických vlastností materiálu, ktorým sa vlnenie šíri. Práca je založená na meraní a spracovaní unikátnych laboratórnych dát a na vývoji nových postupov a metód ich interpretácie.

Väčšina zaťažovacích experimentov je štandardne robených na horninových vzorkách tvaru valca, hranolu či kocky (Al-Sahawneh, 2013; Kwasniewski et al., 2012; Stanchits et al., 2006). Experimenty vyhodnocované v tejto práci sú vykonané na vzorkách tvaru gule. Napriek tomu, že testovanie guľových vzoriek je datované od 70. – 80. rokov 20. storočia (Klíma et al., 1981; Pros a Babuška, 1968), tento typ experimentov nie je vo svete bežný, čo prispieva k jedinečnosti získavaných znalostí. Aparatúra vytvorená na GFÚ AV ČR, v.v.i. umožňovala prežarovanie P vlnami. Tie však dovoľujú len čiastočný popis anizotropie skúmaného materiálu. K úplnému popisu je nutné pridať údaje o šírení S vĺn. Z toho dôvodu Ing. Lokajíček, CSc. navrhol modifikáciu aparatúry tak, aby umožňovala prežarovanie horninového vzorku S vlnami, a to ako za atmosférického, tak aj za pôsobenia hydrostatického tlaku (Lokajíček a Svitek, 2015). Prežarovaním vzoriek pomocou P aj S vĺn v rôznych smeroch je možné získať údaje vedúce k zostrojeniu úplného tenzoru elastických parametrov a interpretácii vlastností hornín. S pôsobiacim hydrostatickým tlakom je možné simulovať zmenu vlastností hornín v zemskej kôre s hĺbkou.

Téma dizertačnej práce je súčasťou grantového projektu riešeného v Geologickom ústave AV ČR, v.v.i.:

- MŠMT Kontakt II – LH13102 – Kinematická a dynamická anisotropie sedimentárních a krystalických hornin: Ultrazvukové, synchrotronní a měření neutronové difrakce (hlavný riešiteľ: T. Lokajíček, obdobie: 2013 – 2015).

Ciele práce je možné stručne zhrnúť v nasledujúcich bodoch:

- Zber nameraných dát a tvorba užívateľského softwaru pre ich prvotné spracovanie a interpretáciu
- Identifikácia vlnových fáz P, S1, S2 na registrovaných vlnových obrazoch ultrazvukových signálov
- Automatizácia procesu merania času príchodu jednotlivých vlnových fáz
- Vytvorenie algoritmu na výpočet elastickej anizotropie z nameraných rýchlostí P, S1 a S2 vĺn
- Syntetický test výpočtu obrátenej úlohy
    - posúdenie vplyvu **typu** vstupných dát na výpočet elastického tenzoru
    - posúdenie vplyvu **nepresnosti** vstupných dát na výpočet elastického tenzoru
    - posúdenie vplyvu **odhadu štartovacieho izotropného modelu** na výpočet elastického tenzoru
- Stanovenie úplného tenzoru elastických parametrov pre vybrané reálne horninové vzorky vrátane chýb
- Zhodnotenie presnosti elastických parametrov pri zanedbaní rozdielov medzi fázovou a grupovou rýchlosťou vĺn v horninových vzorkách

1.2 Štruktúra práce

Doktorská práca pozostáva z troch častí. Prvá časť (kapitola 2) sa venuje študovanej téme elastickej anizotropie hornín, popisuje teoretické postupy stanovenia tenzoru elastických parametrov ako i praktické aspekty laboratórneho získavania dát. Primárne spracovanie nameraných vlnových obrazov a spôsoby určovania času príchodu jednotlivých vlnových fáz je diskutované v kapitole 3. Praktickej realizácii experimentu je venovaná kapitola 4. Hlavnú časť (kapitola 5) práce tvorí súbor šiestich autorových prác publikovaných v recenzovaných časopisoch, pričom prvé štyri práce majú priamy vzťah k téme dizertačnej práce a dve ďalšie publikácie sa študovanej témy dotýkajú okrajovo. Štyri kľúčové práce sú podrobnejšie rozoberané, ďalšia práca je uvedená iba v opublikovanej verzii v prílohe (kapitola 8).

Záverečná časť práce (kapitola 6) zhŕňa publikované poznatky a hodnotí dosiahnutie cieľov dizertačnej práce. Kapitola 7 obsahuje odkazy na použitú literatúru.

Hlavná časť práce sa opiera o nasledujúce publikácie:

1. Lokajíček, T., & **Svitek, T.**, 2015. **Laboratory approach to the study of elastic anisotropy in spheres by simultaneous longitudinal and transverse sounding under confining pressure**. *Ultrasonics,* 56, 294-302. doi:10.1016/j.ultras.2014.08.015
2. **Svitek, T**., Rudajev, V., & Petružalek, M., 2010. **Determination of P–wave arrival time of acoustic events**. *Acta Montan. Slov.*, 15(2), 145–151
3. **Svitek, T.**, Vavryčuk, V., Lokajíček, T., & Petružálek, M., 2014. **Determination of elastic anisotropy of rocks from P- and S-wave velocities: Numerical modelling and lab measurements**. *Geophys. J. Int.*, 199(3), 1682–1697. doi: 10.1093/gji/ggu332
4. Lokajíček, T., Kern, H., **Svitek, T.**, & Ivankina, T., 2014a. **3D velocity distribution of P- and S-waves in a biotite gneiss, measured in oil as the pressure medium: Comparison with velocity measurements in a multi-anvil pressure apparatus and with texture-based calculated data**. *Phys. Earth Planet. Inter*, 231, 1–15. doi:10.1016/j.pepi.2014.04.002
5. Lokajíček, T., Šťastná, A., Petružálek, M., Šachlová, Š., **Svitek, T.** & Přikryl,. R., 2014b. **Quasi-continuous ultrasonic sounding and changes of ultrasonic signal characteristics as a sensitive tool for the evaluation of ongoing microstructural changes of experimental mortar bars tested for their ASR potential**. *Submitted*

Prvá publikácia Lokajíček & Svitek (2015) pojednáva o metodike ultrazvukového merania guľových vzoriek pomocou P a S vĺn a uvádza pokroky dosiahnuté oproti spôsobu merania iba P vĺn.

Druhá publikácia Svitek et al. (2010) sa venuje algoritmu pre automatické určovanie času príchodu P vĺn na vlnových obrazoch javov akustickej emisie a ultrazvukového prežarovania registrovaných v priebehu jednoosových zaťažovacích experimentov na valcových vzorkách. Publikovaný algoritmus je upravený a použitý k analýze signálov registrovaných počas experimentov na guľových vzorkách. Algoritmus tvorí dôležitú súčasť spracovania ultrazvukových dát. Pomocou neho sú zisťované rýchlosti šírenia P vĺn a následne stanovovaná symetria a intenzita ich anizotropie.

Náplňou tretej publikácie Svitek et al. (2014) je preukázanie príspevku laboratórnych ultrazvukových meraní rýchlostí P a S vĺn na guľových vzorkách k poznaniu elastickej anizotropie hornín. Cieľom práce je upozorniť na prínos informácií, ktoré so sebou prináša meranie rýchlostí S vĺn a nutnosť ich znalosti pre výpočet kompletného tenzoru elastických parametrov.

Štvrtá práca Lokajíček et al. (2014a) dokladá použiteľnosť vyvinutej metodiky v porovnaníu s ďalšími spôsobmi určenia elastickej anizotropie hornín. V práci je študovaný materiál z vrtu Outokumpu, Finsko, z ktorého boli vytvorené vzorky tvaru gule a kocky. Guľová vzorka bola testovaná pomocou ultrazvuku a neutronovej difrakcie a kocka iba pomocou ultrazvuku. V článku sú zhrnuté vzájomné porovnania výsledkov.

Posledná publikácia má k téme dizertačnej práce okrajových charakter a nie je detailnejšie popisovaná. Práca Lokajíček et al. (2014b) sa venuje štúdiu procesu porušovania betónu v prostredí alkalicko-silikátových reakcií a popisuje určovanie elastických vlastností betónu pomocou ultrazvukového merania.

2. Anizotropia hornín a tenzor elastických parametrov

Základným prejavom elastickej anizotropie hornín je smerová závislosť rýchlosti elastických vĺn šíriacich sa v hornine. Elastická anizotropia je popísaná tenzorom elastických parametrov c_{ijkl}, tiež nazývaným ako tenzorom tuhosti, ktorý je definovaný ako tenzor 4. rádu a má 81 členov. Avšak vďaka symetrii tenzoru napätia, tenzoru deformácie a vlastnostiam elastickej energie sa počet jeho členov redukuje na 21 nezávislých elastických parametrov. Vo všeobecnom prípade, je pomocou nich definované prostredie s triklinickou anizotropiou. V prípade ďalších symetrií, vyskytujúcich sa v prírode, dochádza k redukovaniu nezávislých parametrov. V najjednoduchšom prípade hovoríme o izotropnom prostredí, ktoré je popísané 2 nezávislými parametrami a v ktorom sú rýchlosti elastických vĺn v každom smere rovnaké.

Pozorovania však ukazujú, že izotropné chovanie hornín je skôr výnimočné a že horniny sú veľmi často anizotropné. K ich anizotropnému chovaniu prispieva mnoho faktorov. Už samotne minerálne zrná tvoriace horninu sú často samé o sebe anizotropné (Aleksandrov a Ryzhova, 1961; Nye, 2001, 1979; Volarovich et al., 1975; Weidner et al., 1975). V dôsledku podmienok pôsobiacich v dobe vzniku horniny dochádza k prednostnej orientácii minerálnych zŕn, hovoríme o „lattice preferred orientation - LPO“. Táto orientácia, ktorá spoločne s tvarovou predispozíciou jednotlivých minerálnych zŕn – „shape preferred orientation – SPO“ prispieva k zvýrazneniu anizotropie (Ildefonse et al., 1992; Kitamura, 2006; Mainprice a Nicolas, 1989; Valcke et al., 2006). Ďalší faktor, ktorý významne prispieva k vzniku anizotropie horninového materiálu, je existencia heterogenít v podobe mikroporušení či pórového priestoru. Hornina je ďalej v priebehu svojho tektonického vývoja vystavená pôsobiacemu tepelnému a napäťovému poľu a vzniknuté mikroporušenie tak získa preferenčnú orientáciu (Dewhurst a Siggins, 2006; Kern et al., 2008; Sayers a Kachanov, 1995). Do akej miery bude mikroporušenie a pórovitosť prispievať k anizotropii daného prostredia závisí aj od toho, či a čím bude tento priestor vyplnený (Bart et al., 2000; Hornby, 1998; Chapman, 2009; Piane et al., 2011; Sayers, 2002; Wang et al., 2012).

Existuje niekoľko spôsobov, ktorými je možné elastické vlastnosti hornín určovať. V podmienkach in-situ sa hojne používajú seizmické metódy. V prípade, že sú k dispozícii vzorky materiálu, je možné podrobiť ich rôznym laboratórnym analýzam. Medzi najpoužívanejšie z nich patria mikroskopické obrazové analýzy, ultrazvukové prežarovanie, neutrónová difrakcia, RTG analýza, statické a dynamické zaťažovacie testy v tlaku či ťahu, a iné. Kombináciou týchto a ďalších metód je možné horninu komplexne popísať. V ďalšom texte sa budeme venovať výhradne laboratórnym ultrazvukovým metódam. Tie sú všeobecne

postavené na princípe určovania času šírenia elastického vlnenia, hovoríme o metóde „Time of flight“ - TOF, (Mattaboni a Schreiber, 1967). Pri znalosti dĺžky dráhy je z času šírenia možné určovať rýchlosť šírenia jednotlivých typov vĺn. V prípade, že sú k dispozícii údaje o šírení vĺn v dostatočnom počte rôznych smerov, je možné spočítať tenzor elastických parametrov. Tenzor elastických parametrov je možné získať aj na základe modálneho zloženia materiálu (Mainprice, 1990) či pomocou neutrónovej difrakcie (Ivankina et al., 2005; Nikitin a Ivankina, 2004; Xie et al., 2003). Tieto nezávislé metódy tak dokážu potvrdiť či doplniť výsledky získané z ultrazvukových meraní.

V začiatkoch laboratórnych meraní sa k interpretácii používali hlavne P vlny, ktoré sú vďaka ich charakteru jednoduchšie generovateľné i registrovateľné (Birch, 1961; Christensen, 1965; Pros a Podroužková, 1974; Pros et al., 1998). Avšak ich informačný potenciál je obmedzený. Meraním rýchlosti S vĺn je možné anizotropiu prostredia lepšie určiť a interpretovať. Prispieva k tomu fakt, že S vlny sa pri prechode anizotropným materiálom rozštiepia na rýchlu (S1) a pomalú (S2) zložku (Obr. 1). S technologickým pokrokom bolo možné vyvinúť laboratórne zariadenia, ktoré sú schopne generovať i registrovať S vlny (Kern, 1982, Siegesmund et al., 1991). Štepenie S vĺn významne prispieva k lepšiemu popisu anizotropie prostredia, ktorým sa elastické vlny šíria (Babuška a Cara, 1991; Crampin a Peacock, 2005; Crampin, 1985; Helbig, 1994) Smer polarizácie rýchlej S vlny (S1) a časový rozdiel medzi príchodmi rýchlej a pomalej fázy δt sú dva základné parametre, z ktorých je možné interpretovať mieru anizotropie prostredia (Obr. 1). Smery polarizácie S1 a S2 vĺn vypovedajú o symetrii anizotropie, parameter δt je možné využiť k určovaniu sily anizotropie (Crampin, 1985).

Meranie a interpretácia S vĺn a ich štiepenia nie sú vždy jednoduché. Sila anizotropie horniny nemusí byť vždy dostatočná, vtedy hovoríme o tzv. „slabej anizotropii“. V takomto prípade môže byť časové oneskorenie δt veľmi malé a je potom obtiažne jednotlivé fázy S1 a S2 identifikovať. Avšak problémy vznikajú aj pre silne anizotropné horniny. Silná anizotropia môže spôsobiť vznik triplikácií S vĺn prejavujúcich sa príchodom mnoho S fáz pozdĺž jedného lúča a existenciou kaustík vo vlnovom poli (Vavryčuk 2003a,b). Zložité chovanie S vĺn je možné pozorovať tiež v blízkosti tzv. akustických ôs (Vavryčuk 2005a,b). K zložitosti interpretácie štiepenia S vĺn prispievajú aj technické faktory spojené s registráciou S vĺn. V prípade, že je prijímač nezatlmený a polarizovaný pod všeobecným uhlom voči orientácii vnútornej štruktúry anizotropného materiálu, bude dochádzať k registrácii rýchlej a pomalej S fázy na jednom vlnovom obraze a k ich interferencii.

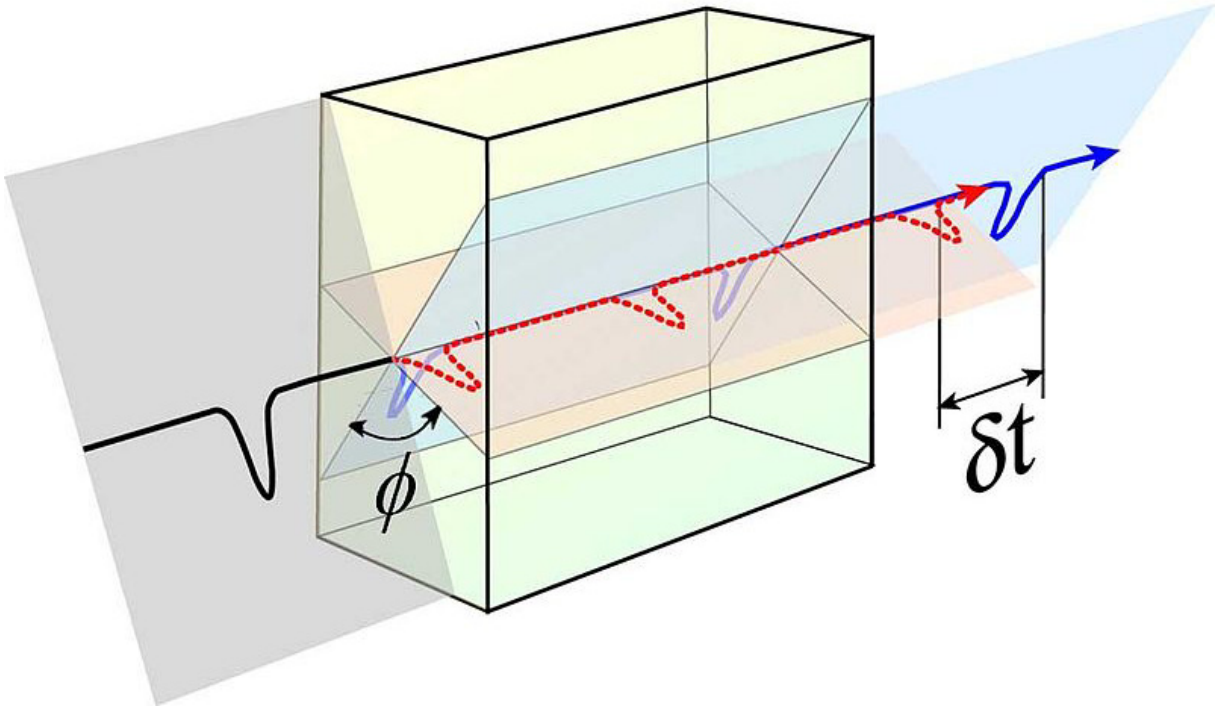

Obr. 1 **Štiepenie S vĺn pri prechode anizotropnou oblasťou; orientácia polarizácie rýchlej fázy - ϕ, časové oneskorenie príchodu rýchlej a pomalej fázy - δt; zdroj http://en.wikipedia.org/wiki/Shear_wave_splitting**

2.1 Fázová a grupová rýchlosť

Výpočet rýchlosti šírenia daného typu vlny sa zakladá na správnom stanovení jej času príchodu (viď Kap. 3). V anizotropii rozlišujeme dva základné typy rýchlostí vĺn. Pri sledovaní rovnakej fázy rovinnej vlny v rôznych smeroch šírenia a určovaní rýchlosti jej šírenia hovoríme o tzv. „fázovej rýchlosti“. Fázová rýchlosť $c(\theta)$ vyjadruje ako rýchlo sa sledovaná fáza rovinnej vlny dostane z bodu A do bodu B (Obr. 2). Naproti tomu o tzv. „grupovej rýchlosti“ hovoríme v súvislosti so šírením energie po dráhe seizmického lúča. Na Obr. 2 je táto dráha vyjadrená úsečkou **CD**.

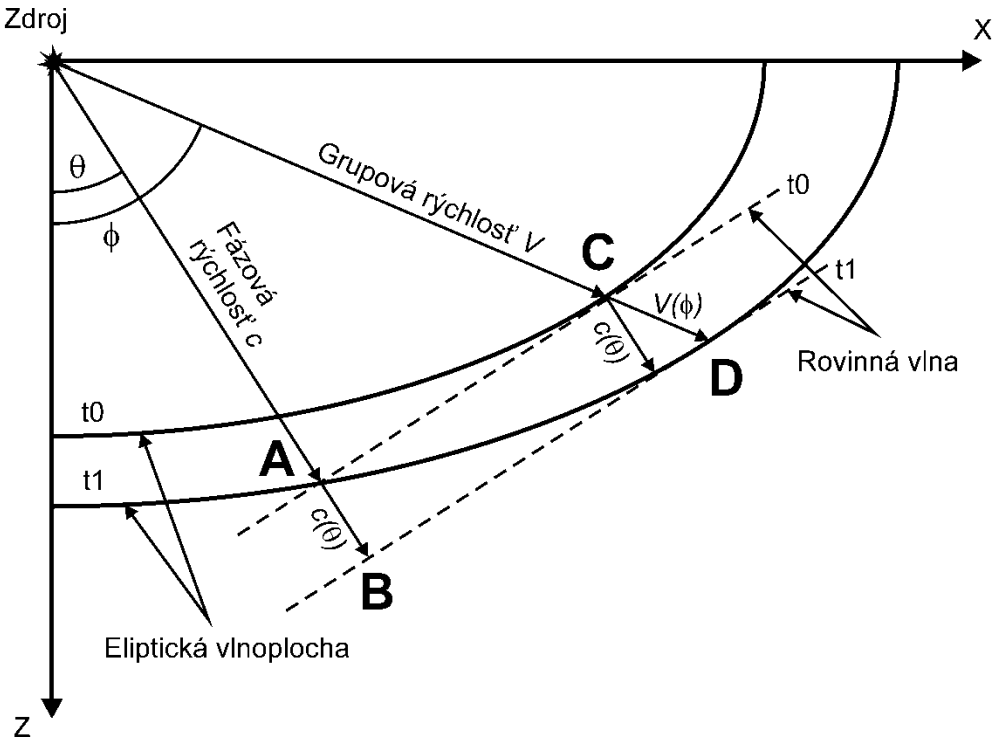

Obr. 2 **Vzťah medzi grupovou a fázovou rýchlosťou v prípade eliptickej vlnoplochy. Os symetrie je v smere *z*; θ - odklon smeru fázovej rýchlosti od osi *z*, ϕ - odklon smeru grupovej rýchlosti od osi *z***

V izotropnom prostredí sú fázová a grupová rýchlosť rovnaké. V anizotropnom prostredí však dochádza k vzájomnému odchyľovaniu týchto rýchlostí. V závislosti na veľkosti zdroja a dĺžke šírenia bude potom v danom smere registrovaná buď fázová alebo grupová rýchlosť (Vestrum, 1994). Do akej miery sa budú fázová a grupová rýchlosť odchyľovať závisí na symetrii anizotropie, jej sile a konkrétnom smere šírenia (Dellinger a Vernik, 1994). Anizotropné prostredie spôsobuje, že normála k vlnoploche si vo všeobecnom smere neodpovedá so smerom lúča (tj. so smerom šírenia elastickej energie, ktorá sa šíri zo zdroja). Táto situácia je znázornená na Obr. 2, kde sú naznačené rozdielne smery šírenia fázovej a grupovej rýchlosti z bodu **C**. V určitých prípadoch je však možné, že aj pre veľmi silnú anizotropiu je grupová a fázová rýchlosť rovnaká. Jedná sa o špeciálne smery šírenia, ktoré odpovedajú osám symetrie daného typu anizotropie a nazývame ich akustickými osami či singularitami (Vavryčuk, 2005a,b).

Fázovú rýchlosť rovinných vĺn šíriacich sa v homogénnom anizotropnom prostredí popisuje Christoffelova rovnica (Helbig, 1994)

$$\det\left(\Gamma_{ij} - c^2\delta_{ij}\right) = 0 \tag{1}$$

kde c je fázová rýchlosť P, S1 alebo S2 vĺn, δ_{ij} je Kroneckerovo delta a Γ_{ij} je Christoffelov tenzor,

$$\Gamma_{jk} = a_{ijkl} n_i n_l . \tag{2}$$

Parametre a_{ijkl} sú komponenty hustotne normalizovaného elastického tenzoru a vektor **n** je fázová normála. V prípade, že poznáme elastické parametre a_{ijkl}, rovnica (1) predstavuje kubickú rovnicu pre výpočet druhej mocniny fázovej rýchlosti *c*. V opačnom prípade, kedy poznáme namerané fázové rýchlosti *c*, rovnica (1) definuje inverzný problém pre výpočet elastických parametrov a_{ijkl}. Táto inverzia predstavuje nelineárny problém a k jej riešeniu používame iteračný postup aplikovaný na teóriu porúch (Jech a Pšenčík, 1989; Jech, 1991; Klíma, 1973; Vavryčuk, 2013).

Poruchová teória vychádza z predpokladu, že anizotropné prostredie definované neznámymi parametrami a_{ijkl} môže byť určené postupnými malými úpravami odchýlok (poruchami) referenčného prostredia

$$a_{ijkl} = a^0_{ijkl} + \Delta a_{ijkl} , \tag{3}$$

kde a^0_{ijkl} definuje referenčné prostredie a Δa_{ijkl} je jeho odchýlka. Tento predpoklad umožní linearizáciu kubickej rovnice výpočtu fázovej rýchlosti *c* (Jech a Pšenčík, 1989; Pšenčík a Vavryčuk, 2002):

$$\Delta\left(c^2\right) = \Delta a_{ijkl} n_i n_l g^0_j g^0_k \tag{4}$$

kde $\mathbf{g^0}$ definuje polarizačný vektor uvažovanej vlny v referenčnom prostredí. Veličina $\Delta\left(c^2\right)$ predstavuje rozdiel medzi štvorcom nameranej a referenčnej fázovej rýchlosti. Rovnica (4) tak predstavuje systém lineárnych rovníc pre neznáme odchýlky Δa_{ijkl}, ktoré sú riešené iteračným postupom. Prvá iterácia predpokladá izotropné referenčné prostredie, ktorého rýchlosti P a S vĺn môžu byť získané ako priemery rýchlostí pozorovaných vo všetkých dostupných smeroch. V prípade, že sú dostupné iba informácie o rýchlostiach P vĺn, je nutné dodať aspoň hrubý odhad rýchlostí S vĺn. Ten je možné získať napríklad pomocou použitia pomeru medzi rýchlosťami P a S vĺn. V prípade Poissonovského prostredia platí, že $\lambda = \mu$ a potom $V_S = V_P / \sqrt{3}$. V následných iteráciách je ako referenčné prostredie považované to, získané z predchádzajúcej iterácie.

Použitím tohto prístupu dokážeme invertovať všetkých 21 elastických parametrov. Avšak nie všetky parametre sú určené s rovnakou presnosťou. V prípade, že máme

k dispozícii iba rýchlosti P vĺn, s dostatočnou presnosťou určíme iba 15 parametrov, pričom zostávajúcich 6, ktoré sú zviazané s vlastnosťami S vĺn, tj. a_{44}, a_{55}, a_{66}, a_{45}, a_{46} a a_{56}, sú určené s menšou presnosťou. V prípade slabej anizotropie nie je možné týchto 6 parametrov zistiť vôbec. To znamená, že k určeniu kompletného tenzoru elastických parametrov je nutné do inverzie dodať taktiež aj meranie rýchlostí S vĺn.

Keďže grupová rýchlosť sa od fázovej rýchlosti v dôsledku vlastností anizotropie prostredia, odlišuje, bude taktiež všeobecne odlišný výpočet tenzoru elastických parametrov, pokiaľ využijeme meranie fázovej či grupovej rýchlosti. Pre slabú anizotropiu je možné považovať fázovú a grupovú rýchlosť za identické (Farra, 2004; Pšenčík a Vavryčuk, 2002; Vavryčuk, 1997). Rýchlosti sa rovnajú aj v smeroch symetrie anizotropie. Avšak čím silnejšia anizotropia je, tým viac sa fázová a grupová rýchlosť budú mimo smery symetrie odlišovať. Z toho dôvodu, keď v experimente registrujeme grupové rýchlosti, je nutné vyššie uvedený postup výpočtu tenzoru elastických parametrov modifikovať.

Vektor grupovej rýchlosti **v** je definovaný nasledovne (Červený, 2001, rovnica 2.4.46)

$$v_i = vN_i = a_{ijkl} p_l g_j g_k , \tag{5}$$

kde **v** je vektor grupovej rýchlosti, **N** je smer lúča, a_{ijkl} sú hustotne normalizované elastické parametre, **p** = **n**/c je vektor pomalosti, **n** je fázová normála, c = 1/p je veľkosť fázovej rýchlosti, p je pomalosť a **g** je polarizačný vektor. Vektory **v** a **p** sú k sebe v nasledujúcom vzťahu,

$$\mathbf{v} \cdot \mathbf{p} = 1 , \tag{6}$$

ktorý vyjadruje ich polárnu reciprocitu (Helbig, 1994). Znamená to, že vektor **v** je normálou k ploche pomalosti a naopak, že vektor **p** je normálou k vlnoploche. Z toho vyplýva, že pokiaľ je grupová rýchlosť určená v dostatočne hustej sieti bodov, je možné získať smerové vektory fázovej rýchlosti ako normály k vlnoploche použitím štandardného postupu diferenciálnej geometrie (Lipschutz, 1969). Následne potom môže byť určená fázová rýchlosť c pomocou vzťahu:

$$c = vN_i n_i \ . \tag{7}$$

Akonáhle určíme smerovú závislosť fázovej rýchlosti, môžeme uskutočniť výpočet elastického tenzoru podľa postupu uvedeného v rovniciach (1–4). Je však potreba zmieniť, že uvedený postup prepočtu má vďaka komplikovanosti S vĺn určité obmedzenia. Vlnoplocha grupových rýchlostí môže byť preto oveľa zložitejšia než povrch plochy pomalosti či plochy

fázových rýchlostí (Musgrave, 1970). So zvyšujúcou sa silou anizotropie sa na vlnoploche môžu objavovať triplikácie a kaustiky (Vavryčuk, 2006) a k určeniu plochy pomalosti či plochy fázových rýchlostí je nutné mať veľmi husté pokrytie smerov grupových rýchlostí. V prípade, že je povrch S vĺn extrémne zložitý, je možné problémom predísť tým, že sa k výpočtu inverzie použijú len hladké časti vlnoplochy. Zrekonštruuje sa tým však len určitá časť povrchu pomalosti či povrchu fázových rýchlostí. Z výsledkov syntetického testu z kapitoly 5.3 ale vyplýva, že inverzia je dostatočne robustná a k uspokojivým výsledkom postačuje meranie smerovej závislosti rýchlosti P vĺn doplniť o meranie rýchlostí S vĺn iba v nevyhnutnom počte smerov.

3. Detekcia času príchodu vlnových fáz

Čas príchodu sledovanej vlny je základný vstupný parameter nutný pre ďalšie spracovanie a interpretáciu úloh týkajúcich sa výpočtu elastickej anizotropie z rýchlostí šírenia seizmických, akustických či ultrazvukových vĺn. Presnosť určenia času príchodu vlny závisí predovšetkým na kvalite signálu. Kvalitu analyzovaného signálu ovplyvňujú konštrukčné vlastnosti snímačov, zložitosť prostredia, ktorým sa vlnenie šíri, a kvalita vzájomného kontaktu snímača a prostredia. To, aké vlastnosti prostredia chceme detegovať a za akých fyzikálnych podmienok, ovplyvňuje vhodnú voľbu snímačov a ich prenosovú charakteristiku. Pre správny popis prostredia, ktorým sa vlnenie šíri, je preto vhodná voľba detegujúceho snímača zásadná. Horninové prostredie vďaka heterogenitám a anizotropii výrazne moduluje počiatočný impulz generovaný zdrojom. Kvalita vlnového obrazu je predovšetkým závislá na kmitočte zdroja, ktorý má byť zvolený tak, aby vysielané vlny zachytili štruktúry požadovanej veľkosti. Platí pritom, že veľkosť hľadanej štruktúry by mala byť väčšia ako niekoľko vlnových dĺžok signálu. V našom prípade boli k meraniu použité piezokeramické snímače s rezonančnou frekvenciou 2 MHz pre generovanie a registráciu P vĺn a 700 kHz pre S vlny.

Aby bolo možné úlohu inverzie anizotropie riešiť, je potrebné mať k dispozícii dostatočný počet vhodných laboratórnych dát. Platí, že čím zložitejšia anizotropia, tým väčšia náročnosť na počet a presnosť dát. S narastajúcim počtom dát vzniká potreba na ich spracovanie. Keďže manuálne spracovanie dát je veľmi časovo náročné, je výhodné k spracovaniu vlnových obrazov signálov a detekcii času príchodu jednotlivých typov vĺn použiť algoritmy na automatické spracovanie. Seizmický, akustický či ultrazvukový signál pozostáva zo šumu a z jednotlivých vlnových fáz, ktoré nesú informácie o zdroji a prostredí,

ktorým sa šíria. Keďže najväčší kontrast medzi signálom a šumom pozorujeme pre P vlny, sú tieto vlny na zázname dobre identifikovateľné a k ich určeniu je možné využiť automatické algoritmy.

Existuje niekoľko metód pre automatické stanovenie času príchodu P vĺn. Vlnový obraz býva, podľa použitej metódy, transformovaný do podoby charakteristickej funkcie, ktorá je následne analyzovaná. Najčastejšie sú používané metódy pomeru priemerovacích okien STA/LTA (Allen, 1982; Svitek et al., 2010), určovanie času príchodu na základe Akaikeho informačného kritéria (Sedlák et al., 2009), či pomocou vyšších štatistických momentov (Lokajíček a Klíma, 2006). V tejto práci, pre účely stanovenia času príchodu P vĺn na záznamoch ultrazvukových signálov z experimentov na guľových vzorkách, je použitý algoritmus, ktorý vychádza z práce (Svitek et al., 2010).

S vlny je vďaka ich charakteru zložitejšie identifikovať s rovnakou presnosťou ako P vlny. Kvalita ich prejavu na vlnovom obraze závisí od konštrukčných vlastností snímača a jeho kmitočtu a ďalej od fyzikálnych podmienok prostredia a geometrie merania. Počas šírenia dochádza na trase od zdroja k prijímaču k lomom a odrazom vĺn rôzneho druhu, tieto vlny môžu taktiež medzi sebou interferovať. To všetko prispieva ku komplikovanosti presného ručného určenia času príchodu S vĺn. Automatické stanovovanie času príchodu je o to náročnejšie. V prípade, že sú si signály vzájomne podobné, je možné k detekcii S vĺn využiť korelačné analýzy, napr. keď sú experimenty na guľových vzorkách realizované pre viac úrovní hydrostatického tlaku.

4. Aparatúra a proces merania

V laboratóriu fyzikálnych vlastností hornín Geologického ústavu AV ČR, v.v.i. bola vyvinutá nová meracia hlava vysokotlakej ultrazvukovej aparatúry, ktorá umožňuje meranie guľových vzoriek a ich prežarovanie P aj S vlnami (Lokajíček a Svitek, 2015). Štandardne merania na guľových vzorkách umožňujú prežarovanie v regulárnej sieti meracích bodov s krokom 15° v smere poludníkov aj rovnobežiek. Vzorka rotuje okolo osi, tj. v rozsahu 0° – 360°, a snímače sa nakláňajú v rozsahu 0° – 75° (Obr. 3). Celkovo sú tak k dispozícii dáta zo 132 nezávislých smerov, čo predstavuje vynikajúce priestorové pokrytie (Pros et al., 1998). Horninové vzorky sú štandardne merané v niekoľkých tlakových úrovniach v rozsahu 0.1 - 400 MPa. To umožňuje sledovať proces uzatvárania prípadných systémov mikrotrhlín a interpretovať tak mieru porušenia a orientáciu vnútorných štruktúr skúmaného materiálu.

Nové experimentálne usporiadanie pozostáva z troch párov piezokeramických snímačov, pričom jeden pár tvoria vysielač a prijímač polarizovaný v pozdĺžnom smere, ktorý je určený k detekcii P vĺn. Ďalšie dva páry pozostávajú z prijímačov a vysielačov polarizovaných priečne, pričom polarizácia jedného páru je orientovaná horizontálne a druhá vertikálne (paralelne s osou rotácie vzorky). Horninová vzorka môže mať rôznu vnútornú štruktúru preto orientácia symetrie anizotropie nie vždy korešponduje s orientáciou polarizácie priečnych snímačov. Je preto potreba uvedomiť si, že polarizácie priečnych snímačov nekorešpondujú s termínmi bežne používanými pre transverzálne izotropné prostredie, kde jedna zložka vlny má označenie ako SH (horizontálna) a druhá SV (vertikálna).

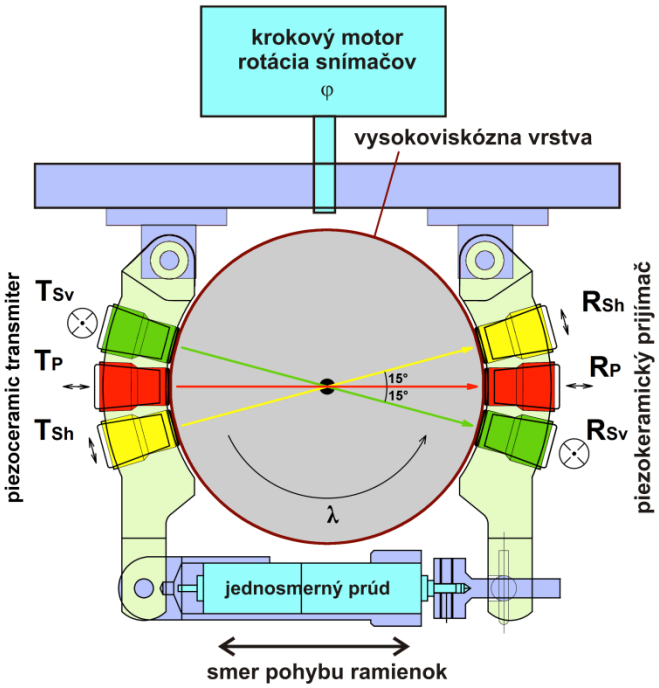

Obr. 3 **Schéma usporiadania snímačov a geometrie merania; λ - uhol rotácie vzorky, φ - uhol rotácie snímačov, T_P, T_{Sv}, T_{Sh}, R_P, R_{Sv}, R_{Sh} sú vysielače a prijímače pozdĺžnej, priečnej vertikálnej a priečnej horizontálnej zložky vlny**

Dôležitým aspektom experimentu je zabezpečenie kvalitných kontaktných podmienok nutných pre dostatočný prenos strižnej energie z vysielača do vzorky a následne zo vzorky do prijímača. V minulosti sa k meraniu P vĺn používali snímače so zaoblenou kontaktnou plochou, ktorej krivosť odpovedala krivosti guľovej vzorky. Tým bol docielený plošný kontakt, ktorý bol po celú dobu experimentu udržiavaný pritláčaním snímačov na povrch vzorky pomocou pružinky. V prípade troch párov snímačov, však nebolo možné použiť rovnakú metódu. Počas experimentu dochádza k rotácii guľovej vzorky a natáčaniu snímačov do aktuálne požadovaných polôh, čo v kombinácii s účinkami hydrostatického tlaku spôsobovalo nedostatočnú kvalitu kontaktu. To viedlo k nedostatočnému prenosu energie

a registrované vlnové obrazy neboli dostatočne kvalitné pre ďalšie spracovanie. Preto sa k meraniu používajú snímače s rovinnou kontaktnou plochou, čo v kombinácii s guľovým povrchom vzorky vytvára bodový kontakt. Ďalším rozdielom oproti minulým meraniam je úprava kontaktných podmienok vzorky a snímača. Pri meraní rýchlostí P vĺn sa pre generovanie hydrostatického tlaku v experimentoch používa transformátorový olej. Keďže sa S vlny týmto médiom nešíria, pokrývame vzorku viskóznym gélom k tomuto účelu určenému (Obr. 4). Látka podobná medu však znemožňuje jednoduché polohovanie snímačov. Preto je nutné po každom meraní snímače od vzorky oddialiť, nastaviť novú polohu a opätovne snímače pritlačiť. To zabezpečuje motor poháňaný jednosmerným prúdom (Obr. 3), ktorý taktiež dokáže obnoviť kontakt s podobným prítlakom vďaka sledovaniu odporu ním pretekajúceho prúdu.

Obr. 4 Viskózny gél („Shear wave“ gél)

Kontaktné podmienky spoločne s intenzitou a symetriou anizotropie vplývajú na spôsob šírenia elastického vlnenia prostredím vzorky. Následne sa od toho odvíja prístup k spracovaniu nameraných dát, ktorý je naznačený v kapitole 2.1. Vzorka je v jednom bode prežarovaná 10x, pričom je v osciloskope týchto 10 signálov priemerovaných. Výsledok priemerovania je následne vyhodnocovaný v ďalšom spracovaní. Vzorkovacia frekvencia záznamu je 100 MHz, tj. časy príchodu je možné určiť s časovým rozlíšením 10 ns.

5. Prehľad dosiahnutých výsledkov

Výsledky práce sú zhrnuté v štyroch celkoch. Postupne je uvedené aké úpravy aparatúry boli vykonané, spôsob určovania príchodov P a S vĺn z nameraných signálov, overenie metodiky výpočtu elastickej anizotropie pomocou syntetických testov a nakoniec sú uvedené výsledky spracovania reálnych experimentálnych dát.

5.1 Publikácia 1:

Lokajíček, T., & Svitek, T., 2015. Laboratory approach to the study of elastic anisotropy in spheres by simultaneous longitudinal and transverse sounding under confining pressure. Ultrasonics, 56, 294-302**.**

Tento článok pojednáva o novom meracom usporiadaní ultrazvukových experimentov za pôsobenia hydrostatického tlaku. Hlavná inovácia systému spočíva v možnosti merať ako P tak aj S vlny. V dobe tvorby publikácie bolo možné zaťažovať vzorky maximálne do úrovne 70 MPa, no po ďalších úpravách je teraz systém schopný merať rýchlosti vĺn na vzorkách zaťažovaných až do 100 MPa. Tak ako je naznačené na Obr. 3, guľová vzorka je prežarovaná jedným párom pozdĺžnych snímačov a dvomi pármi priečne orientovaných snímačov. Ako zdroj prežarovania sú použité piezokeramické tabletky od spoločnosti Noliac, typ-N51 s priemerom 4.5 mm a hrúbkou 0.5 mm pre účely P vĺn a N55 L2.5 – W2.5 – TH1 štvorcového tvaru o hrane 2.5x2.5 mm a hrúbkou 1 mm pre účely S vĺn. Priečne snímače sú umiestnené s nemennou polarizáciou, ktorá je vztiahnutá k osi rotácie vzorky, tj. rozlišujeme vertikálny priečny snímač SV a horizontálny priečny snímač SH. Je potreba uviesť, že toto označenie nesúvisí s pomenovaním typu S vĺn používanom v prípade transverzálnej izotropie. Polarizácia S vĺn nie je preto v priebehu merania orientovaná voči vnútorným štruktúram skúmaného materiálu vždy úplne ideálne. Experimenty sú vykonávané v sieti meracích bodov po 15° v smere rovnobežiek aj poludníkov. Z toho dôvodu sú snímače od seba posunuté taktiež o 15°. Presnosť polohovania sa pohybuje v rozmedzí ±1°. Týmto spôsobom realizujeme 150 meraní v 132 nezávislých smeroch.

V jednej polohe natočenia sú postupne zmerané vlnové obrazy z R_P, R_{Sv} a R_{Sh} snímača. Pre každý typ snímača je zaznamenaných 10 vlnových obrazov, ktoré sú následne priemerované v osciloskope. Pre ďalšie spracovanie je potom uložený finálny priemerovaný signál. To znamená, že v jednom čase sú zmerané tri rôzne smery. Pred ďalším spracovaním sú potom signály preusporiadané tak, aby signály na jednotlivých pozíciách odpovedali rovnakému smeru. Tým je dosiahnuté, že v danom smere merania získame trojzložkový záznam podobne ako je tomu v seizmológii pri meraní trojzložkovým seizmometrom.

Kalibrácia systému

Nová konfigurácia systému bola kalibrovaná na izotropnej vzorke číreho sodno-draselného skla s priemerom 50 mm ± 0.01 mm. Toto meranie ukázalo, že bodový kontakt nemá vplyv na presnosť určenia času príchodu P a S vĺn. Na Obr. 5 je porovnanie vlnových

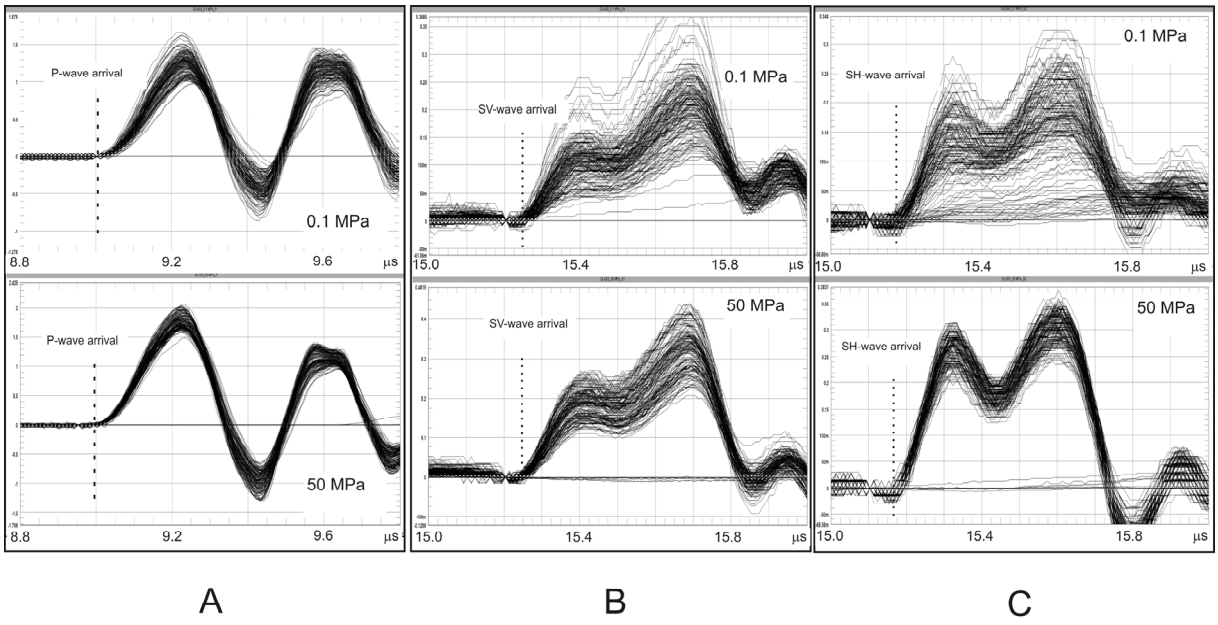

Obr. 5 Vlnové obrazy získané pri kalibračnom meraní na skle pri tlaku 0.1 MPa (hore) a 50 MPa (dole); A – vlnové obrazy registrované pozdĺžne polarizovaným snímačom, B - vlnové obrazy registrované priečnym vertikálne orientovaným snímačom, C - vlnové obrazy registrované priečnym horizontálne orientovaným snímačom

obrazov registrovaných z R_P, R_{Sv} a R_{Sh} snímača pri tlaku 0.1 a 50 MPa.

Obr. 5a ukazuje detail času príchodu 150 signálov P vĺn. Z obrázku vyplýva, že presnosť určenia príchodu P vlny je v rozmedzí jednej vzorky (tj. ±10 ns). Rozptyl amplitúd prvého nasadenia P vĺn je pri tlaku 0.1 MPa okolo ±20 %, pri úrovni tlaku 50 MPa sa zmenší na ±10 %.

Obr. 5b znázorňuje 150 signálov S vĺn registrovaných na priečnom vertikálne orientovanom prijímači. Pre S vlny je charakteristický väčší rozptyl amplitúd (približne 40% pri tlaku 0.1 MPa). Platí však, že s pôsobiacim hydrostatickým tlakom sa rozptyl zníži (na približne 25 % pri tlaku 50 MPa). Väčší rozptyl amplitúd má však za následok horšie určenie času príchodu S vĺn, ktoré sa pohybuje v rozmedzí ±2 vzorkovacie body (±20 ns). Rozptyl amplitúd je možné vysvetliť nestálosťou kontaktných podmienok snímačov so vzorkou v jednotlivých smeroch.

Obr. 5c znázorňuje detail príchodu 150 signálov S vĺn registrovaných na snímači R_{Sh}. Opäť je viditeľný väčší rozptyl amplitúd, kde pri atmosférickom tlaku je to približne 40 % a pri tlaku 50 MPa sa ich rozptyl zmenší na úroveň približne 15 %. Presnosť určenia času príchodu znovu odpovedá intervalu ±2 vzorkovacie body (20 ns).

Pri porovnaní Obr. 5b a 5c je vidieť, že príchody S vĺn na oboch priečnych snímačoch si presne neodpovedajú. Príchod vlny na snímači R_{Sv} je 15.22 µs a na snímači R_{Sh} je 15.18 µs.

Rozdiel 0.04 μs je spôsobený rozdielnymi korekciami na snímače. Po zavedení korekcií boli spočítané rýchlosti šírenia elastických vĺn, pričom rýchlosť P vĺn je 5.57 km/s a rýchlosť S vĺn je 3.28 km/s. Pomer V_P/V_S = 1.70 je hodnota blízka Poissonovskému prostrediu (pomer $\sqrt{3}$). To dokazuje fakt, že na signáloch registrovaných snímačmi R_{Sv} a R_{Sh} bola skutočne registrovaná S vlna.

Kalibračné meranie ukázalo, že nový spôsob súbežného merania P a S vĺn za pôsobenia všesmerného hydrostatického tlaku môže byť použitý k ultrazvukovému prežarovaniu guľových vzoriek za účelom stanovenia rýchlostí šírenia elastických objemových vĺn. Zároveň sa ukázalo, že bude do budúcna nutné zlepšiť kvalitu kontaktu medzi priečnymi snímačmi a vzorkou a to hlavne za účelom stabilného stanovovania amplitúd.

Ďalším krokom k overeniu funkčnosti nového systému merania bol test anizotropnej vzorky kvarcitu, ktorého anizotropia P vĺn pri tlaku 0.1 MPa je približne 34 %. Tento test potvrdil, že je možné registrovať S vlny aj na reálnej hornine. Viac o tomto experimente je možné zistiť priamo z publikácie, ktorá je uvedená v prílohe 2.

5.2 Publikácia 2:

Svitek, T., Rudajev, V., & Petružalek, M., 2010. Determination of P–wave arrival time of acoustic events. Acta Montan. Slov., 15(2), 145–151

Tento článok pojednáva o spôsobe automatického určovania času príchodu P vĺn na vlnových obrazoch signálov akustickej emisie a ultrazvukového prežarovania hornín v priebehu jednoosých zaťažovacích experimentov. Tento druh experimentov generuje veľké objemy dát, vlnových obrazov a parametrických vstupov, ktorých manuálne spracovanie by bolo veľmi časovo náročné. Automatická detekcia času príchodu P vĺn a následný výpočet rýchlosti šírenia je preto nutnosťou pre ďalšie spracovanie dát. Algoritmus v tejto práci uvedený bol aplikovaný aj na ultrazvukové dáta z experimentov na guľových vzorkách.

Základom detekcie času príchodu P vlny je stanovenie tzv. „charakteristickej funkcie“ signálu. Tvar tejto funkcie sa odvíja od metódy použitej k automatickej detekcii času príchodu. Veľmi často používaná metóda je sledovanie pomeru priemerných hodnôt charakteristickej funkcie z krátkeho a dlhého kĺzavého okna, známá ako STA/LTA (Allen, 1982). Okrem tohto spôsobu sa tiež používajú metódy založené na analýze vyšších štatistických momentov - HOS (Lokajíček a Klíma, 2006) či Akaikeho určovacieho kritéria (Sedlák et al., 2009). V článku bolo preukázané, že vyvinutý postup automatického určovania

času príchodu P vĺn je vhodný pre použitie na javoch akustickej emisie a je efektívnejší než doposiaľ používaný spôsob založený na metóde HOS a to ako v porovnaní s manuálne určenými nasadeniami tak aj v porovnaní lokalizačných reziduí. Podklady pre obrazové výsledky bohužiaľ nie sú k dispozícii preto je možné vidieť ich len v grafoch v článku v prílohe 3.

Uplatnenie výsledkov Publikácie 2 pre účely identifikácie času príchodu P a S vĺn registrovaných na guľových vzorkách

Základ metódy, tj. použitie princípu STA/LTA a analýza tvaru signálu, je prevzatý a uplatnený na signály ultrazvukového prežarovania na guľových vzorkách. Táto metóda poskytuje údaje v 132 nezávislých smeroch, ktoré pokrývajú celý povrch vzorky. V praxi je však vykonaných 150 meraní pre danú tlakovú úroveň. Štandardne je meraných 10 tlakových úrovní v intervale 0.1 – 400 MPa (v prípade merania P vĺn) alebo 0.1 – 100 MPa (v prípade merania S vĺn). To je celkom 1500 respektíve 4500 signálov (R_P, R_{Sv} a R_{Sh} snímače), na ktorých je nutné stanoviť čas príchodu niektorého typu vlny. V súčasnosti sú všetky nasadenia P vĺn stanovované automaticky touto metódou, príchody S vĺn sú určované poloautomaticky. Kvalita signálov S vĺn je veľmi závislá na kontaktných podmienkach, ktoré sa zlepšujú s pôsobiacim hydrostatickým tlakom. Preto sú na najvyššej meranej tlakovej úrovni časy príchodu S1 a S2 (rýchlej a pomalej) vlny určené manuálne na všetkých 150 signáloch. Keďže sú merania s narastajúcim tlakom opakované v rovnakých smeroch (presnosť stanovenia polohy merania je ±1°), signály v daných smeroch pre rôzne tlakové úrovne sú si navzájom veľmi podobné. Je preto možné k stanoveniu času príchodu S1 a S2 vĺn na nižších tlakových úrovniach využiť korelačnú analýzu. Korelácia signálov sa používa v cykle cez tlakové úrovne, od najvyššieho tlaku, kde je príchod S vlny určený manuálne, až do najnižšieho tlaku (väčšinou 0.1 MPa). Postupne je porovnávaný tvar aktuálne analyzovaného signálu s tvarom signálu predchádzajúceho. Takto je určený približný príchod S vĺn, ktorý je následne upravený pomocou analýzy tvaru signálu, použitej v Publikácii 2. V prípade veľkých nepresností je nasadenie opravené manuálne. O vplyve nepresností určenia S1 a S2 vĺn na kvalitu stanovenia elastických vlastností študovaného materiálu pojednáva nasledujúca práca.

5.3. Publikácia 3:

Svitek, T., Vavryčuk, V., Lokajíček, T., & Petružálek, M., 2014. Determination of elastic anisotropy of rocks from P and S-wave velocities: Numerical modelling and lab measurements. Geophys. J. Int., 199(3), 1682–1697

Tento článok poukazuje na vplyv merania rýchlostí S vĺn na výpočet tenzoru elastických parametrov c_{ijkl}. Výpočet elastického tenzoru je nelineárna inverzná úloha, ktorej riešením je v najvšeobecnejšom prípade určenie všetkých 21 elastických parametrov stanovených pomocou riešenia Christoffelovej rovnice (rovnice 1 – 2). Údaje vstupujúce do výpočtu, v prípade aproximácie platnej pre elastické homogénne anizotropné prostredie, sú namerané rýchlosti P a S vĺn. Kroky vedúce k výpočtu tenzoru pri použití grupových a fázových rýchlostí sú naznačené v kapitole 2.1.

Článok na príklade syntetických testov hodnotí dopady presnosti vstupných parametrov na presnosť určenia tenzoru elastických parametrov. Kvalita stanovenia tenzoru je posudzovaná skrz presnosť rýchlostí vypočítaných z elastických parametrov získaného tenzoru, ktoré sú porovnávané s teoretickými správnymi hodnotami (Obr. 6). Teoretické rýchlosti sú získané výpočtom fázových rýchlostí pre nasledujúci model anizotropie (Klíma, 1973):

$$C_{ij}^{quartz} = \begin{bmatrix} 86.05 & 4.85 & 10.45 & 18.25 & 0 & 0 \\ 4.85 & 86.05 & 10.45 & -18.25 & 0 & 0 \\ 10.45 & 10.45 & 107.1 & 0 & 0 & 0 \\ 18.25 & -18.25 & 0 & 58.65 & 0 & 0 \\ 0 & 0 & 0 & 0 & 58.65 & 18.25 \\ 0 & 0 & 0 & 0 & 18.25 & 40.6 \end{bmatrix} \quad (8)$$

Hodnoty v rovnici (8) sú uvedené v GPa, hustota je ρ = 2.65 g cm^{-3}. Jedná sa o anizotropiu s trigonálnou symetriou. Sila anizotropie P, S1 a S2 vĺn je 26.6, 29.9 a 27.8 %. V prípade inverzie anizotropie z rýchlostí P vĺn je dobre stanovených 15 parametrov, avšak 6 parametrov, súvisiacich so šírením S vĺn (a_{44}, a_{55}, a_{66}, a_{45}, a_{46} a a_{56}), nie je určených s dostatočnou presnosťou. Navyše v prostredí slabej anizotropie nie je vôbec možné z meraní rýchlostí P vĺn týchto 6 parametrov vôbec určiť. Preto je pre výpočet kompletného tenzoru elastických parametrov nutné merať aj rýchlosti S vĺn. V minulosti sa rýchlosť S vĺn často dopočítavala umelo cez pomer V_P/V_S, ktorý je v Poissonovskom prostredí rovný $\sqrt{3}$.

Ako nástroj k posúdeniu presnosti a robustnosti inverzného výpočtu bol navrhnutý syntetický test, ktorý hodnotil vplyv: 1) nepresnosti určenia rýchlosti S1 a S2 vĺn, 2) rozdielnosť počiatočného rýchlostného modelu, ktorý sa odvíjal od zvolenej hodnoty pomeru V_P/V_S, a 3) metódu výpočtu inverzie podľa typu rýchlostí vstupujúcich do inverzie (P, PS1 alebo PS1S2).

Určovanie času príchodu S1 vĺn je náročný proces, preto sa v jednotlivých variantách uvažovali nepresnosti určenia rýchlosti S1 vĺn z intervalu 0, 0.2, 0.4, 0.6, 0.8, 1, 2, 4, 6, 8, 10, 12, 14, 16, 18, 20, 25, 30, 35 a 40 %.

Určovanie času príchodu S2 vĺn je ešte náročnejšie než pre S1 vlny. V slabej anizotropii nemusia byť vlny S1 a S2 od seba úplne oddelené alebo môže byť príchod S2 vlny ovplyvnený interferenciou s vlnou S1. Preto bola nepresnosť určenia rýchlosti S2 vĺn uvažovaná ako 1.5 krát väčšia než pre S1 vlny. Rýchlosť P vĺn je stanovovaná s veľmi veľkou presnosťou, preto sú nepresnosti uvažované v syntetickom teste veľmi malé, len 0.1 %. Všetky náhodné odchylky simulujúce chyby merania boli vygenerované 100 krát kvôli štatistickému zpracovaniu. Počiatočný rýchlostný model predstavuje prvotný odhad prostredia, ktoré sa v použitej poruchovej metóde pokladá za izotropné. Rýchlosť P vĺn je určená ako priemerná rýchlosť zo všetkých smerov na guľovej vzorke. V prípade, keď nie sú

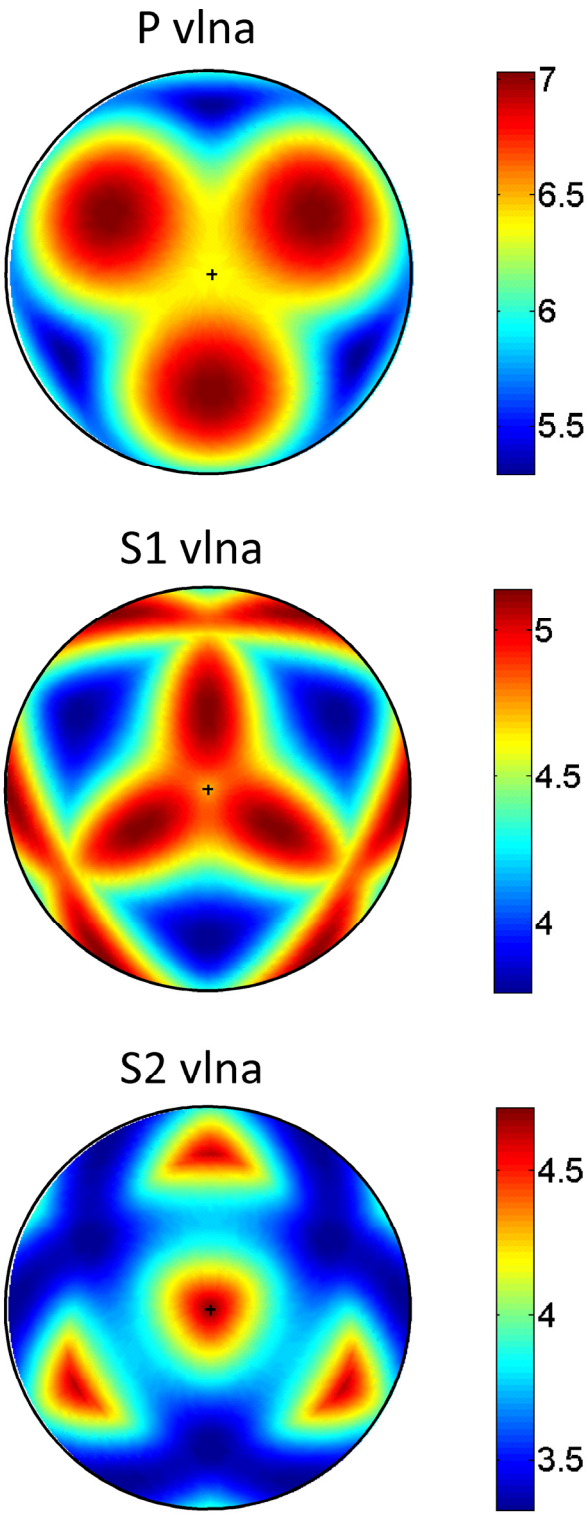

Obr. 6 **Teoretické rýchlosti P, S1 a S2 vĺn monokryštálu kremeňa napočítané z elastických parametrov uvedených v rovnici (8); uvedené hodnoty predstavujú fázové rýchlosti v km/s**

k dispozícii údaje o rýchlosti šírenia S vĺn je nutné túto rýchlosť dodať do výpočtu formou pomeru V_P/V_S. Hodnoty pomeru V_P/V_S boli uvažované z intervalu 1.5 do 2.5. Inverzia bola testovaná pre tri typy vstupných dát: rýchlostí P vĺn, rychlosti P a S1 vĺn a nakoniec rýchlosti P, S1 a S2 vĺn. Kvalita inverzie bola hodnotená na základe porovnania teoretických a predikovaných dát pomocou rovnice:

$$e_{\text{mean}}^{P,S1,S2} = 100\% \cdot \text{mean}\left(\frac{\left|c_{\text{true}}^{P,S1,S2} - c_{\text{predicted}}^{P,S1,S2}\right|}{c_{\text{true}}^{P,S1,S2}}\right),\quad e_{\text{max}}^{P,S1,S2} = 100\% \cdot \max\left(\frac{\left|c_{\text{true}}^{P,S1,S2} - c_{\text{predicted}}^{P,S1,S2}\right|}{c_{\text{true}}^{P,S1,S2}}\right) \tag{9}$$

kde predikované rýchlosti boli vypočítané zo získaných elastických parametrov. Tieto veličiny predstavujú priemer a maximum zo 100 realizácií generovaných pomocou náhodného rovnomerného šumu. Do úvahy boli brané merania zo všetkých 132 smerov.

Výsledky sú zobrazené na Obr. 7 a 8. Os *x* predstavuje nepresnosti určenia rýchlosti S1 vĺn, os *y* znázorňuje interval pomeru V_P/V_S. Farebná škála potom predstavuje percentuálne odchýlky veličín e_{mean}, resp. e_{max}.

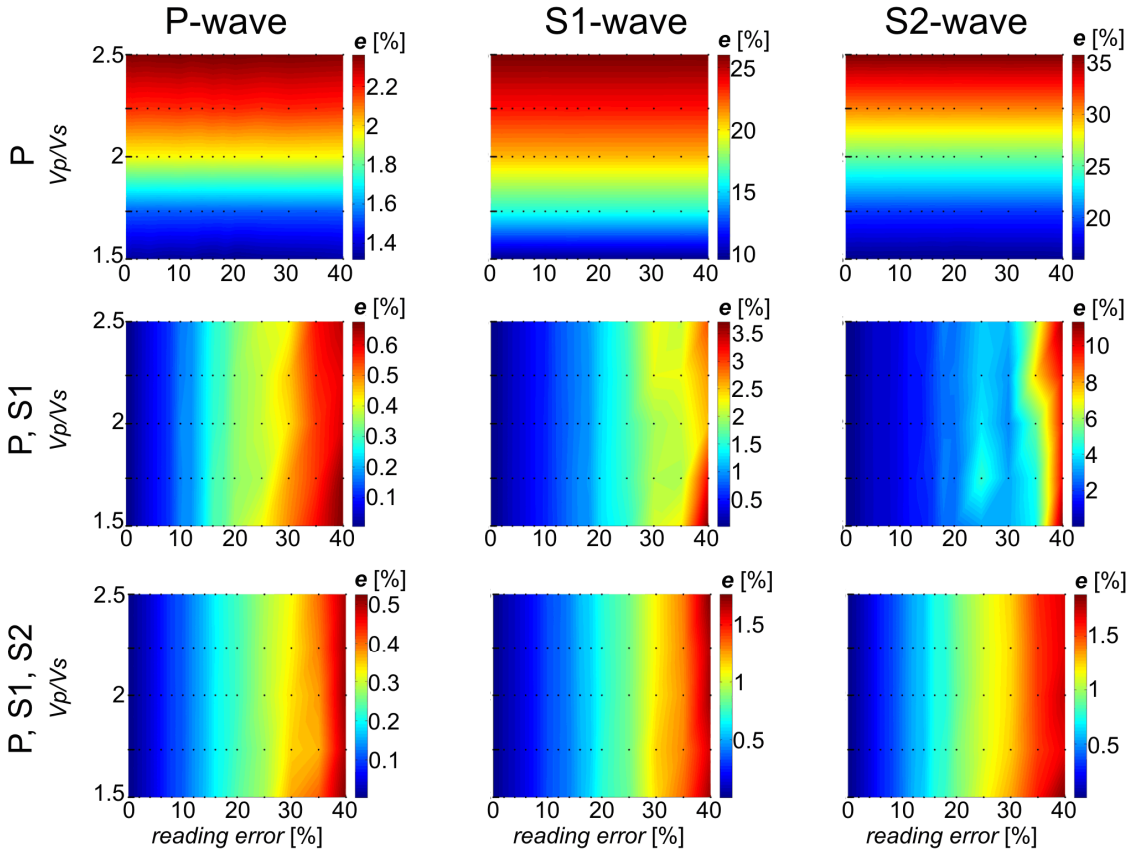

Obr. 7 **Chyba inverzie e_{mean} pre rýchlosti P vĺn (ľavý stĺpec), S1 vĺn (stredný stĺpec) a S2 vĺn (pravý stĺpec) ako funkcia chyby určenia rýchlosti S1 vĺn (stredný riadok) a S1 a S2 vĺn (spodný riadok). Chyby vo vrchnom riadku nie sú závislé na nepresnosti určenia rýchlosti S vĺn, pretože sú invertované len z rýchlosti P vĺn.**

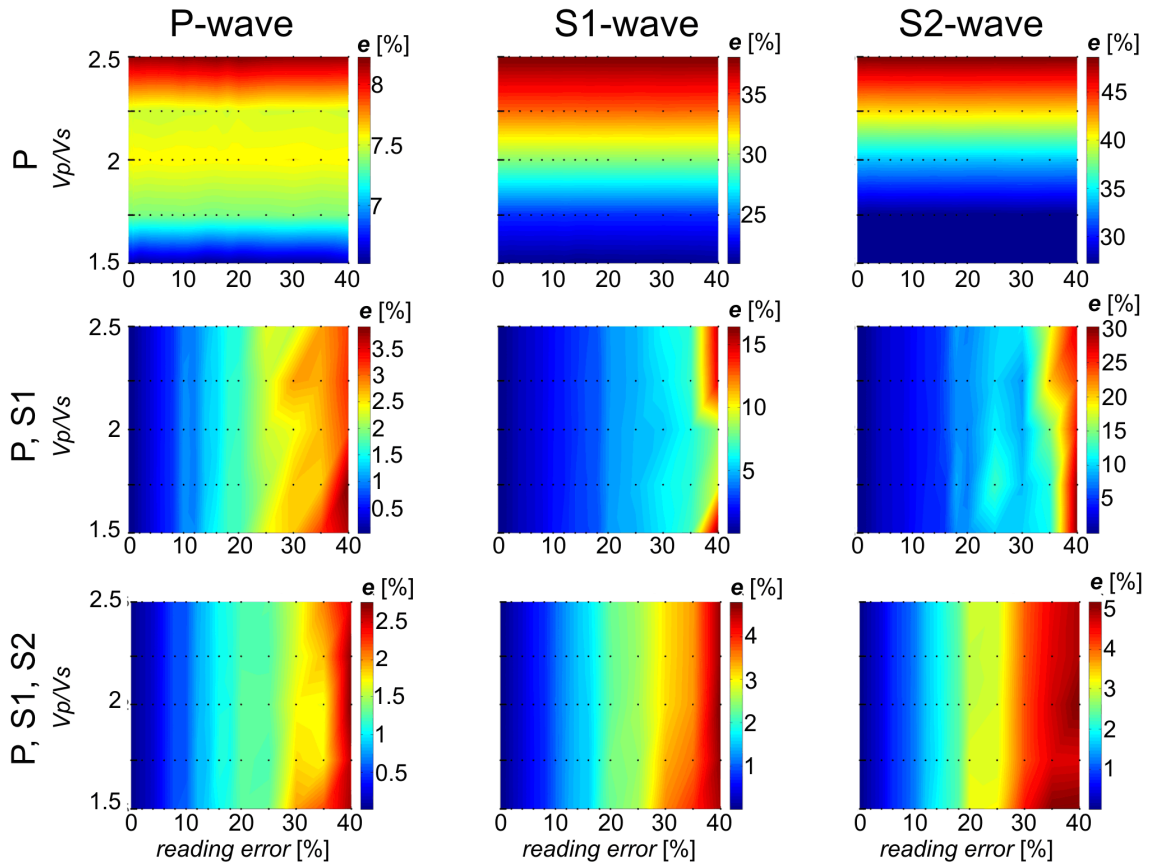

Obr. 8 **Chyba inverzie e_{max} pre rýchlosti P vĺn (ľavý stĺpec), S1 vĺn (stredný stĺpec) a S2 vĺn (pravý stĺpec) ako funkcia chyby určenia rýchlosti S1 vĺn (stredný riadok) a S1 a S2 vĺn (spodný riadok). Chyby vo vrchnom riadku nie sú závislé na nepresnosti určenia rýchlosti S vĺn, pretože sú invertované len z rýchlosti P vĺn.**

Na základe získaných výsledkov je možné urobiť nasledujúce závery:

- Elastický tenzor určený len na základe rýchlostí P vĺn (Obr. 7, Obr. 8 a Obr. 13, ďalej Obr. 19 horný rad) je silne závislý na zvolenom pomere V_P/V_S, ktorý do inverzie vstupuje v prvej iterácii. Získané rýchlosti S1 a S2 vĺn majú výrazne vyššie odchýlky od teoretických rýchlostí než rýchlosti pre P vlny. Priemerná chyba pre S1 a S2 vlny je približne 10-15 krát vyššia než v prípade P vĺn (Obr. 7 horný rad). Z toho dôvodu nie je možné správne interpretovať elastické parametre vztiahnuté k S vlnám a to napriek tomu, že rýchlosti P vĺn sú určené s veľmi dobrou presnosťou (maximálna odchýlka je iba 0.1 %). Interpretované rýchlosti S1 a S2 vĺn sú preto veľmi nepresné.
- Elastický tenzor počítaný z rýchlostí P a S1 vĺn (Obr. 7, Obr. 8 a Obr. 13, ďalej Obr. 19 stredný rad) už vďaka dodaniu informácií o rýchlostiach S1 vĺn nie je citlivý na zvolenom pomere V_P/V_S. Presnosť predikovaných rýchlostí závisí na presnosti určenia rýchlosti S1 vĺn. Za zmienku stojí fakt, že aj pomerne silne zašumené merania S vĺn zlepšia presnosť výpočtu elastického tenzoru (Obr. 7, stredný rad). Zapojenie rýchlostí S vĺn do procesu inverzie výrazne zlepšilo presnosť elastického tenzoru. Dokonca aj

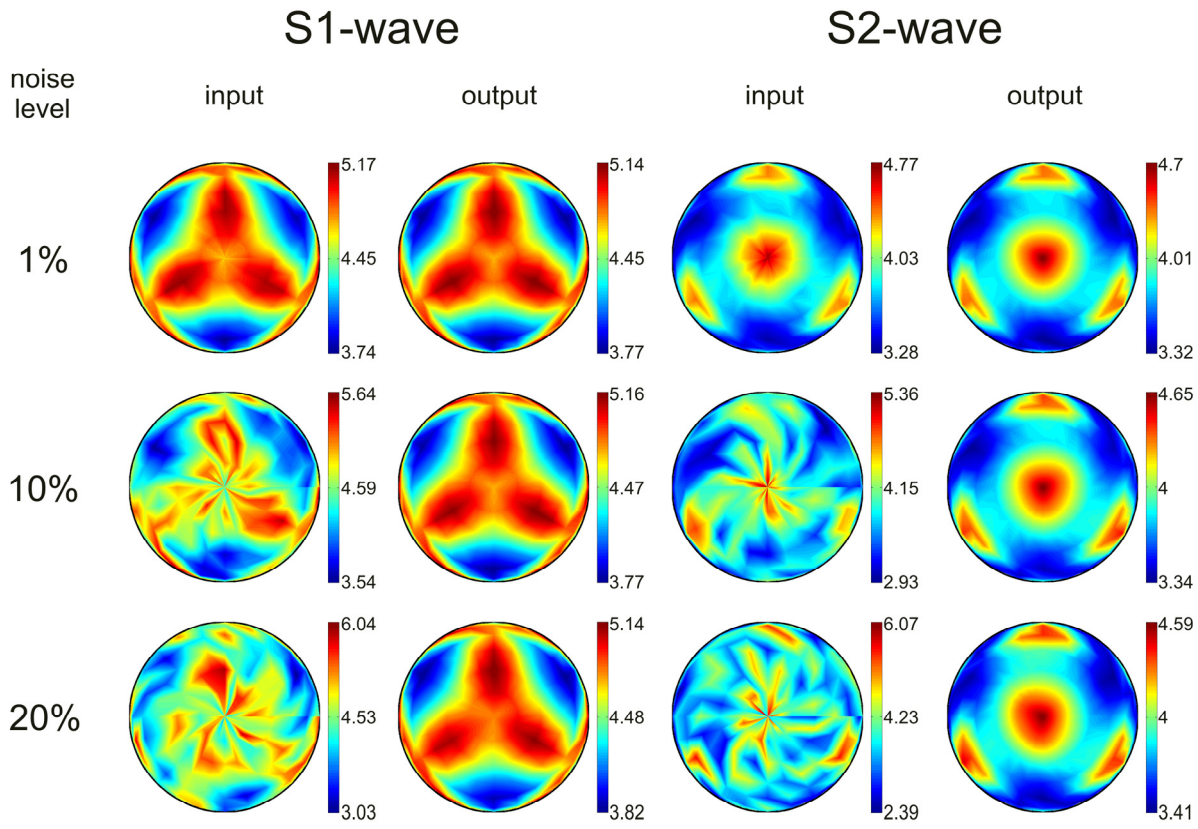

Obr. 9 **Ukážka fázových rýchlostí S1 a S2 vĺn zašumených náhodným rovnomerným šumom vstupujúcich do inverzie a odpovedajúci výstup. Úroveň šumu je 1 % (horný rad), 10 % (stredný rad) a 20 % (spodný rad). Obrázok ukazuje, že použitá metóda inverzie je robustná a stabilná aj pre vysoké úrovne šumu; uvedené hodnoty predstavujú fázové rýchlosti v km/s**

aproximácia rýchlostí P vĺn je lepšia. V prípade, že sú rýchlosti S1 vĺn určené s nepresnosťou menšou než 15 %, je stredná chyba predikovaných P, S1 a S2 vĺn menšia než 0.3 %, 1 % a 3 % pre daný typ vlny.

- Elastický tenzor určený z P, S1 a S2 vĺn (Obr. 7, Obr. 8 a Obr. 13, ďalej Obr. 19 spodný rad) je opäť závislý hlavne od presnosti rýchlostí S1 a S2 vĺn. Pridaná informácia o rýchlosti S2 vĺn má vplyv na interpretáciu rýchlostí S1 a S2 vĺn. Zlepšenie interpretácie rýchlostí P vĺn je len minimálne.

Tento syntetický test na ukážke trigonálnej symetrie kremeňa preukázal, že inverzia elastického tenzoru len za prispenia rýchlostí P vĺn nie je dostačujúca. Elastické parametre súvisiace s P vlnami sú určené s uspokojivou presnosťou, avšak parametre, ktoré majú vzťah k S vlnám vykazujú veľmi nepresné hodnoty. Aby bolo možné získať všetky elastické parametre s odpovedajúcou presnosťou, je potrebné do výpočtu zahrnúť aj rýchlosti S vĺn. Po ich zavedení do výpočtu je dosiahnuté výrazného zlepšenia nie len parametrov vztiahnutých k S vlnám, ale celého elastického tenzoru. V tomto teste do inverzie vstupovalo všetkých 132 nezávislých smerov.

Druhý syntetický test posudzoval množstvo a rozloženie rýchlostí S vĺn vstupujúcich do inverzie. Merania na guľových vzorkách poskytujú informácie o šírení S vĺn v celej škále vzájomných natočení polarizácie S vlny voči orientácii vnútorných štruktúr. Pretože orientácia snímačov je fixná, dochádza k tomu, že tieto orientácie nie sú v každom smere optimálne. Bodový kontakt spoločne s nevhodnou orientáciou prispieva k tomu, že prvé nasadenie S vĺn nie je v každom smere jednoznačne rozpoznateľné (viď Obr. 10).

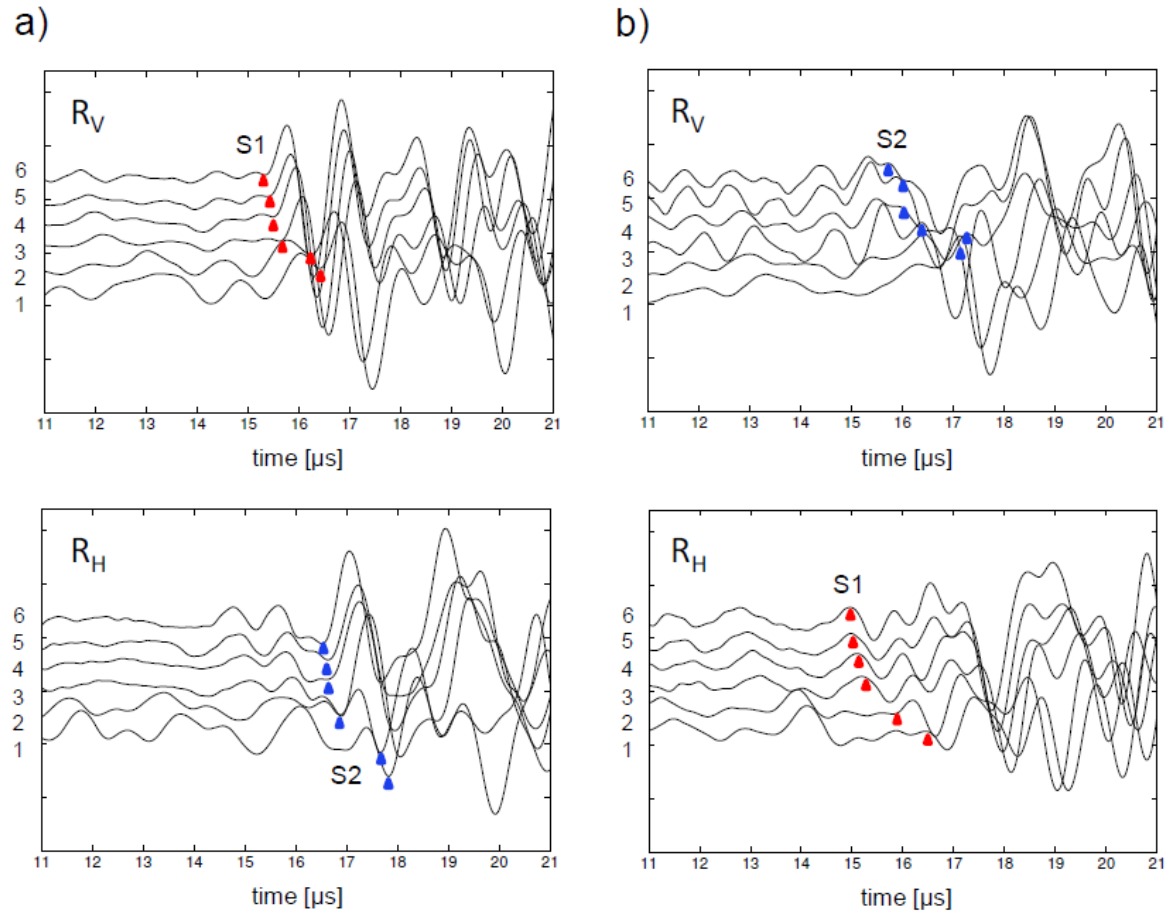

Obr. 10 Príklady vlnových obrazov ultrazvukových signálov registrovaných na vzorke OKU-409 priečnymi snímačmi s vertikálnou (R_V) a horizontálnou (R_H) orientáciou: (a) vlnové obrazy v smere, kde sú nasadenia S vĺn dobre určiteľné, (b) vlnové obrazy v smere, kde sú nasadenia S vĺn určiteľné veľmi obtiažne. Čísla 1-6 určujú tlakové úrovne od 0.1 do 70 MPa. Červené a modré trojuholníky naznačujú časy príchodu rýchlej a pomalej S vlny.

Druhý syntetický test preto hodnotí, do akej miery bude inverzia robustná v prípade, že bude počet vstupných rýchlostí S vĺn menší a priestorové pokrytie nebude optimálne.

Všetky parametre použité v prvom teste boli použité rovnako. Posudzovaná bola presnosť rýchlostí určených z rovnomerne a náhodne rozložených smerov. Rovnomerne rozložené smery boli v sieti po 15°, 30°, 45° a 60°, tj. k dispozícii bolo 132, 30, 12, a 6 smerov S1 alebo S1 a S2 vĺn. Rýchlosti P vĺn boli použité zo všetkých 132 smerov.

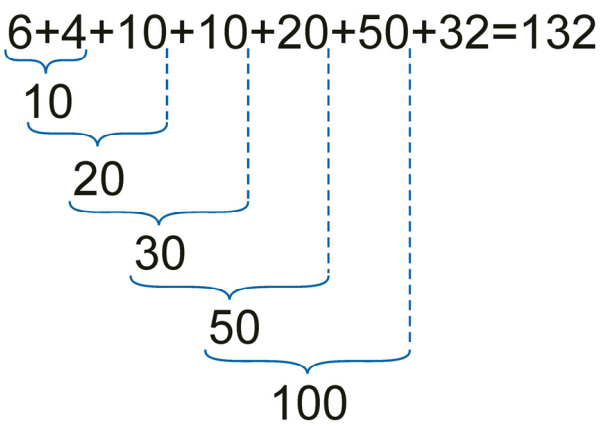

Obr. 11 Schematické vyjadrenie vygenerovania rôzneho počtu náhodných smerov pre účely druhého syntetického testu. Tučne je zvýraznený celkový počet náhodných smerov pre jednotlivé varianty testu.

Pre náhodne rozloženie smerov, bolo postupne vybraných 6, 10, 20, 30, 50, 100 a 132 smerov. Najprv bolo vybratých 6 náhodne orientovaných smerov, ktoré boli postupne doplnené o ďalšie 4 náhodné smery (6+4=10), potom o ďalších 10 náhodných smerov (6+4+10=20) a tak ďalej až do konečného počtu 132 smerov. Schematicky je tento proces vyjadrený na Obr. 11. Prvotná šestica náhodných smerov bola vygenerovaná trikrát, aby bolo možné posúdiť štatistickú hodnovernosť. Pre udržanie rozsahu práce v rozumných medziach však nebudú prezentované všetky získané výsledky.

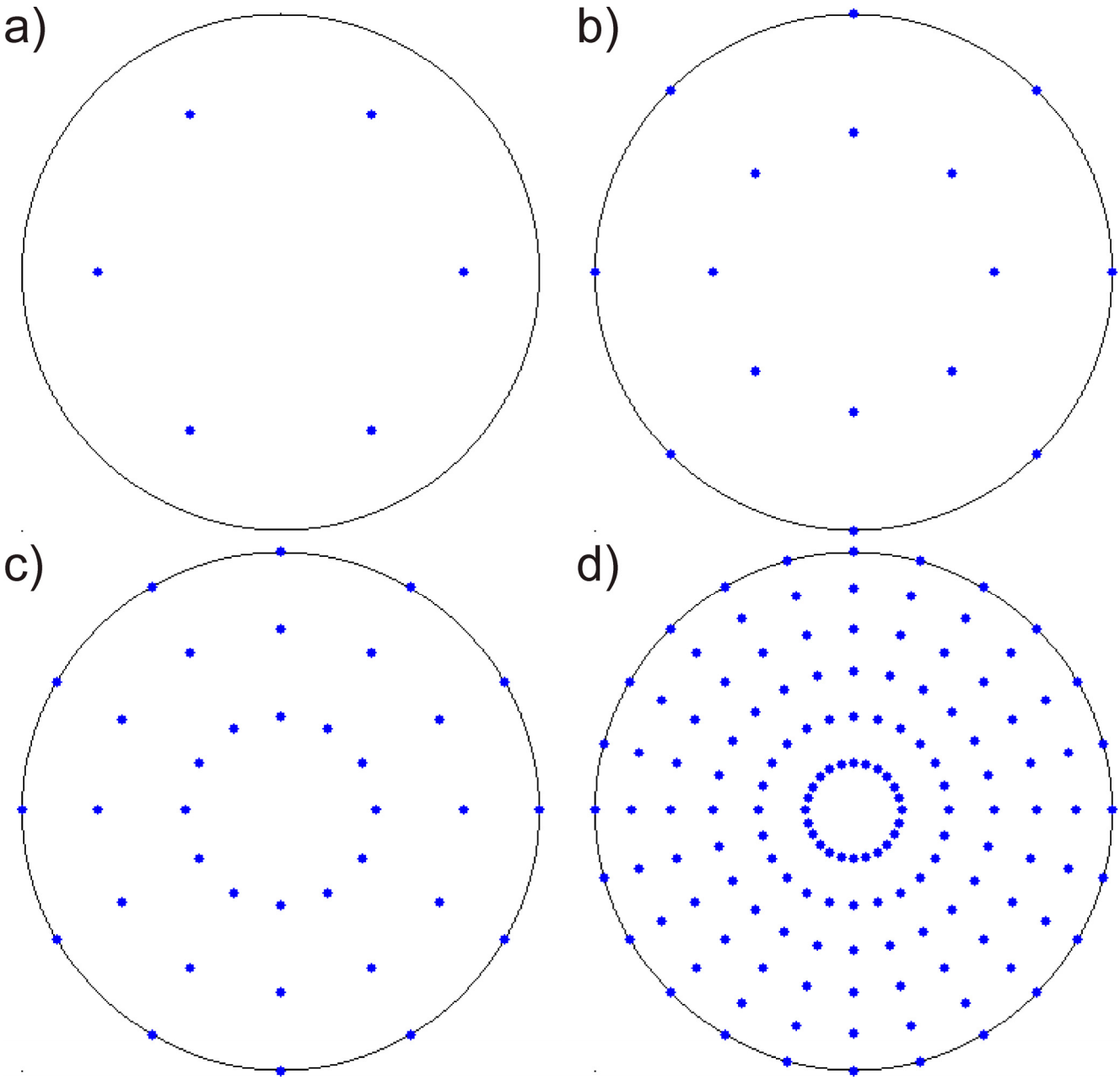

Obr. 12 Rovnoplochá projekcia rovnomerne rozložených smerov do spodnej pologule; a) 6 smerov v sieti po 60°, b) 12 smerov v sieti po 45°, c) 30 smerov v sieti po 30° a d) 132 smerov v sieti po 15°

Na Obr. 12 sú znázornené projekcie rovnomerne rozložených smerov. Variácie pootočených orientácií pravidelnej siete voči vnútornému usporiadaniu štruktúry trigonálnej anizotropie neboli posudzované. Na Obr. 13 – 18 sú na ukážkach hodnôt e_{mean} a e_{max} znázornené prejavy poklesu počtu smerov v pravidelnej sieti vstupujúcich do výpočtu inverzie. Z obrázkov je vidieť trend platný pre všetky typy vĺn, a síce, že znižujúci sa počet smerov má vplyv na presnosť výpočtu tenzoru elastických parametrov. Dôležité je, že pridanie informácie o šírení rýchlostí S vĺn automaticky neznamená zvýšenie presnosti určenia tenzoru. Všeobecne by sa dali zhrnúť nasledujúce závery:

- Pridanie malého počtu nepresne nameraných rýchlostí S1 vĺn zhorší interpretáciu všetkých typov aproximovaných rýchlostí.
- Avšak následné, i minimálne, pridanie informácie o rýchlosti S2 vĺn zlepší aproximáciu a to aj oproti variante, keď nie sú do inverzie uvažované žiadne S vlny.

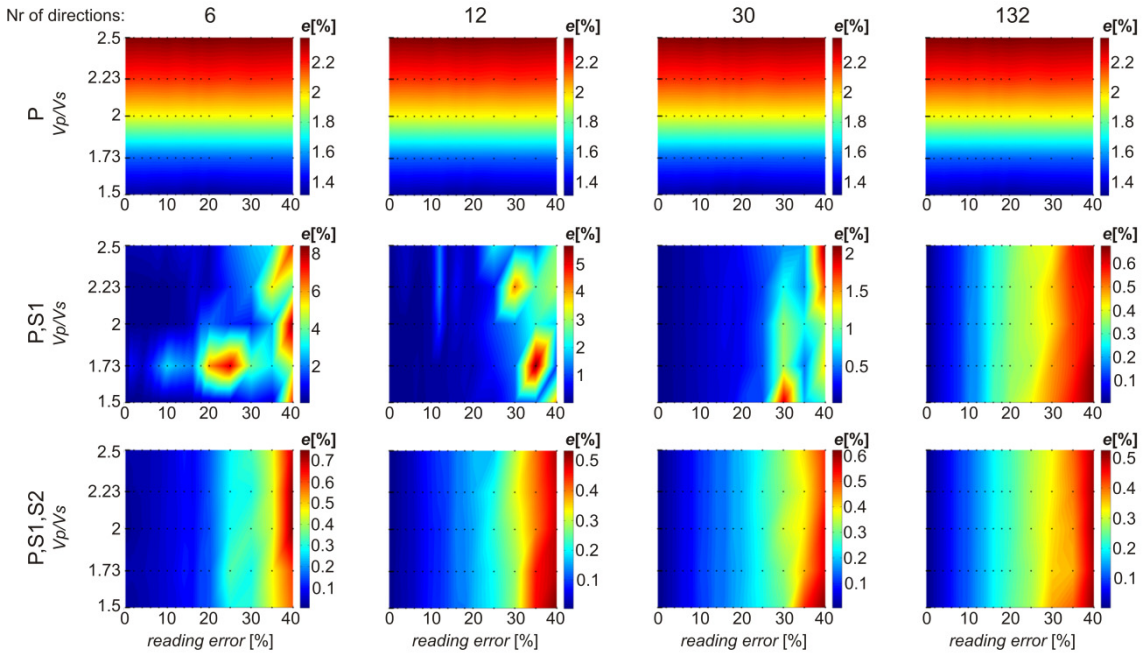

Obr. 13 Odchýlky e_{mean} pre rýchlosti P vĺn napočítané s prispením meraní rýchlostí P vĺn (horný rad), P a S1 vĺn (stredný rad) a P, S1 a S2 vĺn (spodný rad) pre odpovedajúci počet smerov S1 či S2 vĺn; P vlny sú uvažované vo všetkých 132 smeroch

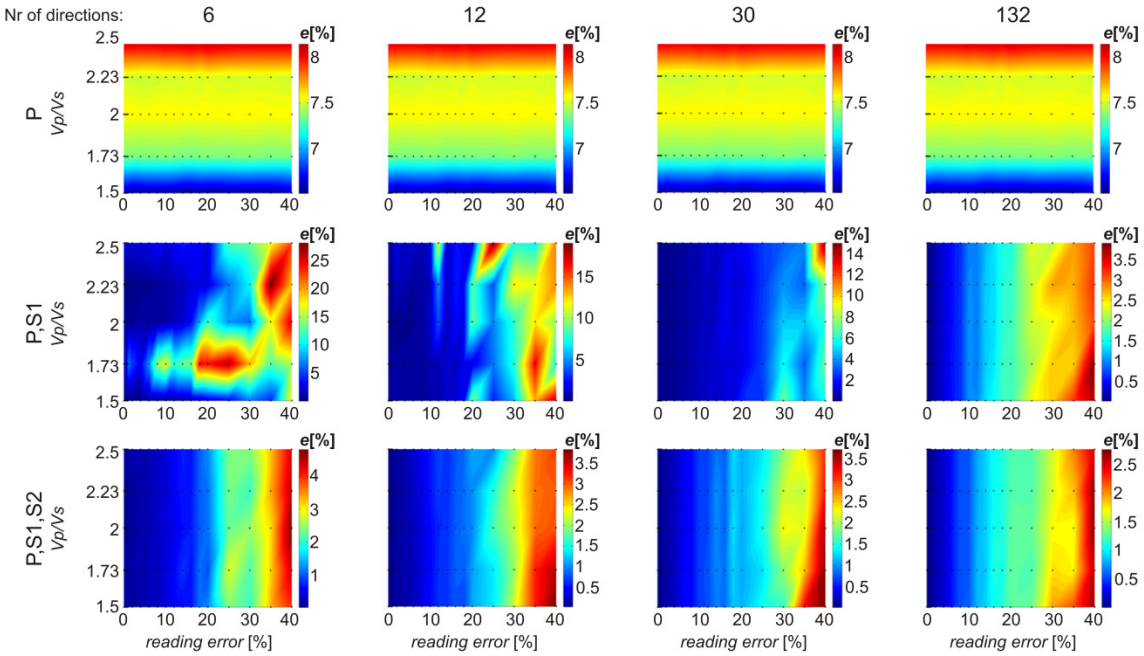

Obr. 14 Odchýlky e_{max} pre rýchlosti P vĺn napočítané s prispením meraní rýchlostí P vĺn (horný rad), P a S1 vĺn (stredný rad) a P, S1 a S2 vĺn (spodný rad) pre odpovedajúci počet smerov S1 či S2 vĺn; P vlny sú uvažované vo všetkých 132 smeroch

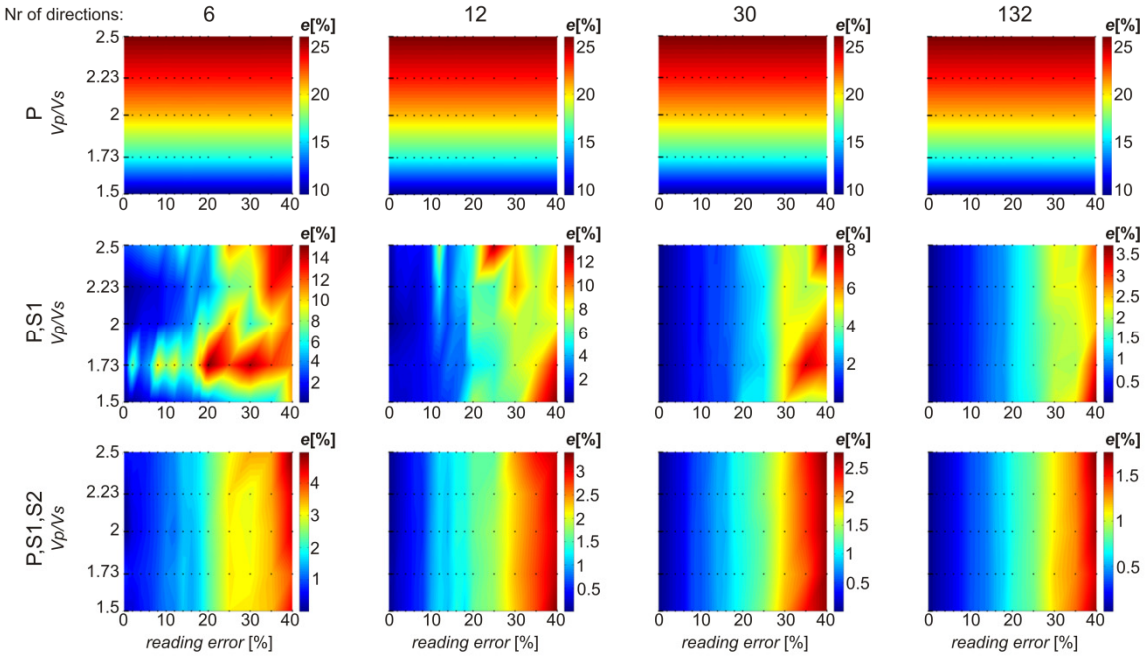

Obr. 15 Odchýlky e_{mean} pre rýchlosti S1 vĺn napočítané s prispením meraní rýchlostí P vĺn (horný rad), P a S1 vĺn (stredný rad) a P, S1 a S2 vĺn (spodný rad) pre odpovedajúci počet smerov S1 či S2 vĺn; P vlny sú uvažované vo všetkých 132 smeroch

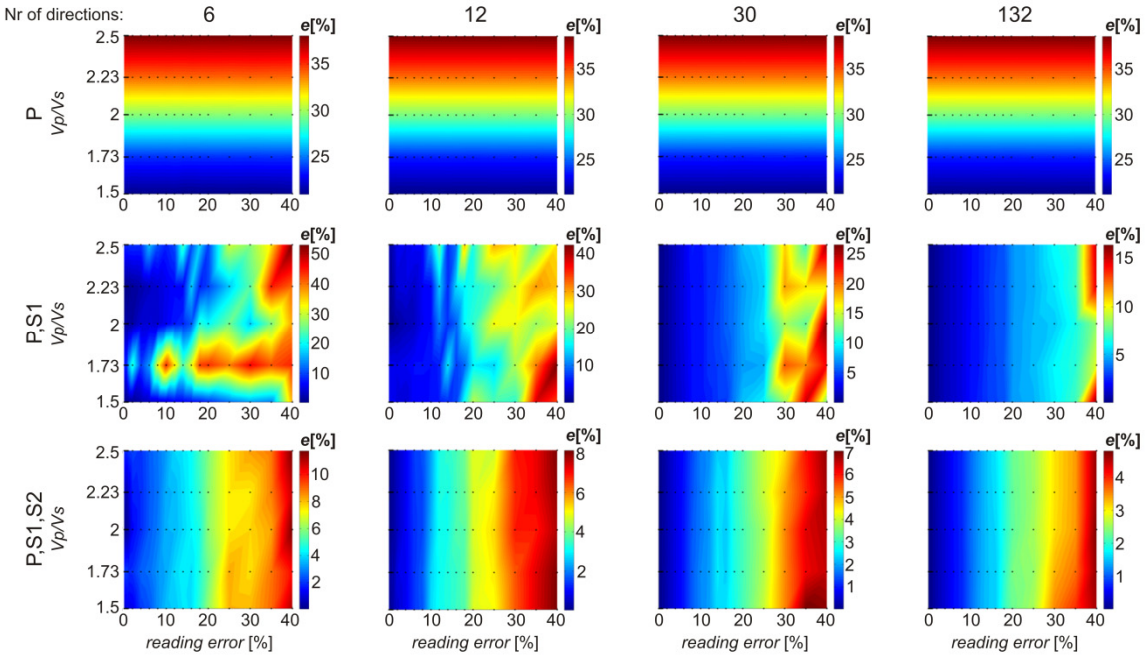

Obr. 16 Odchýlky e_{max} pre rýchlosti S1 vĺn napočítané s prispením meraní rýchlostí P vĺn (horný rad), P a S1 vĺn (stredný rad) a P, S1 a S2 vĺn (spodný rad) pre odpovedajúci počet smerov S1 či S2 vĺn; P vlny sú uvažované vo všetkých 132 smeroch

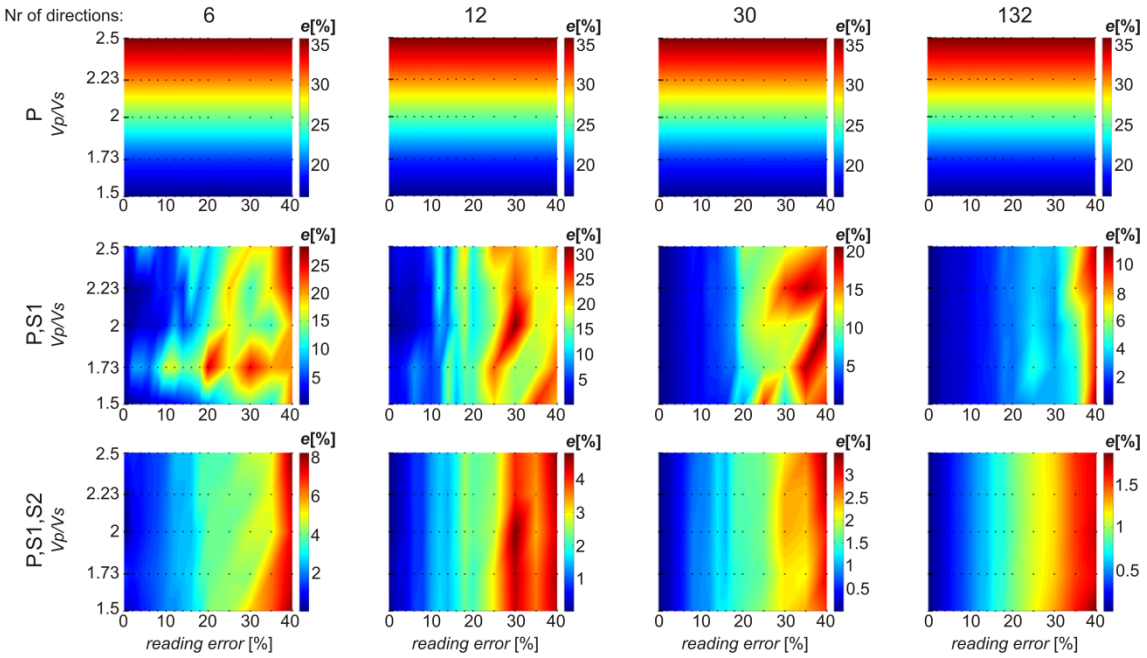

Obr. 17 Odchýlky e_{mean} pre rýchlosti S2 vĺn napočítané s prispením meraní rýchlostí P vĺn (horný rad), P a S1 vĺn (stredný rad) a P, S1 a S2 vĺn (spodný rad) pre odpovedajúci počet smerov S1 či S2 vĺn; P vlny sú uvažované vo všetkých 132 smeroch

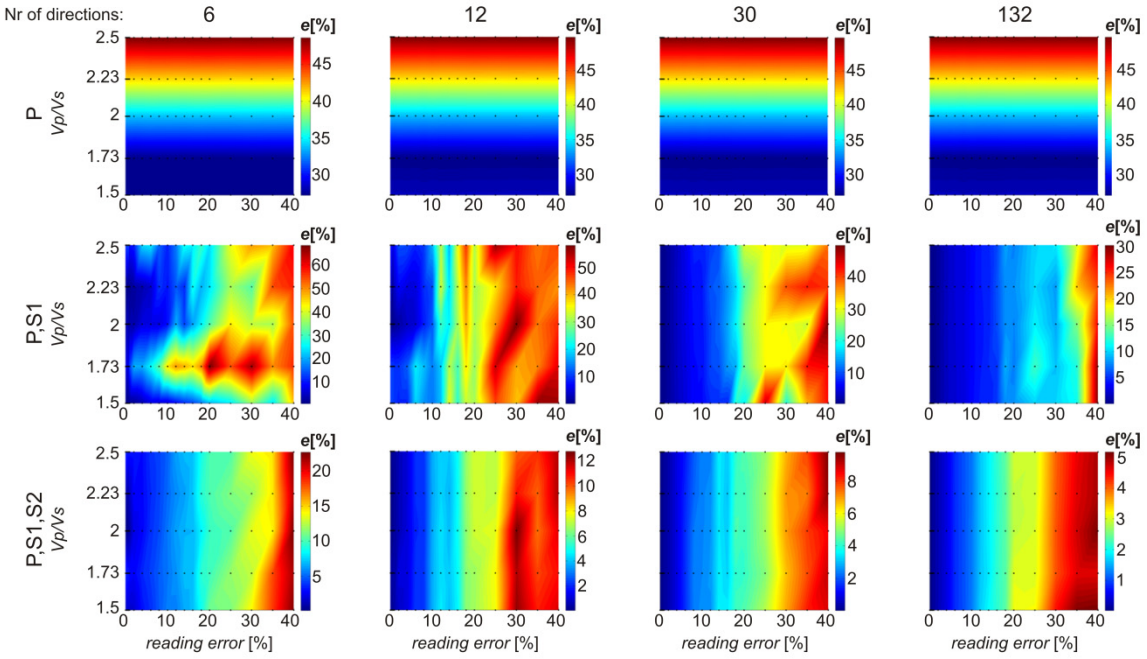

Obr. 18 Odchýlky e_{max} pre rýchlosti S2 vĺn napočítané s prispením meraní rýchlostí P vĺn (horný rad), P a S1 vĺn (stredný rad) a P, S1 a S2 vĺn (spodný rad) pre odpovedajúci počet smerov S1 či S2 vĺn; P vlny sú uvažované vo všetkých 132 smeroch

V prípade použitia náhodne orientovaných smerov má inverzia podobné chovanie ako v prípade rozloženia rýchlostí v pravidelnej sieti smerov. So znižujúcim sa počtom smerov dochádza k väčším nepresnostiam inverzie. Nerovnomerné rozloženie smerov, v prípade zložitej symetrie anizotropie spolu v kombinácii s nízkym počtom smerov orientovaných

v podobných azimutoch môže zhoršiť výsledky inverzie až 2 krát. Porovnanie všetkých možných kombinácií smerov voči orientácii štruktúry by bolo veľmi časovo náročné, ak vôbec realizovateľné. Zo získaných výsledkov sa však javí, že presnosť inverzie je do určitej miery závislá na vzájomnej orientácii vnútornej štruktúry a smerov použitých pre výpočet inverzie.

Posledná časť publikácie pojednávala o uplatnení postupov na reálnych dátach. K analýze bola vybratá vzorka OKU-409 (podrobnejší popis viď v kapitole 5.4), ktorá bola analyzovaná už pre účely Publikácie 4. Na vzorke bol analyzovaný spôsob výpočtu tenzoru elastických parametrov na základe rôzneho typu dát, ktoré do tohto výpočtu vstupovali. Obr. 19 ukazuje rozdiely interpretácie dosiahnutej výpočtom len z rýchlostí P vĺn (horný riadok), z P a S1 vĺn (stredný riadok) a z P, S1 a S2 vĺn (spodný riadok). Na prvý pohľad je zjavné, že rozloženie rýchlostí P vĺn je takmer rovnaké, avšak rozloženie rýchlostí S1 a S2 vĺn sa významne líši pre každý typ výpočtu.

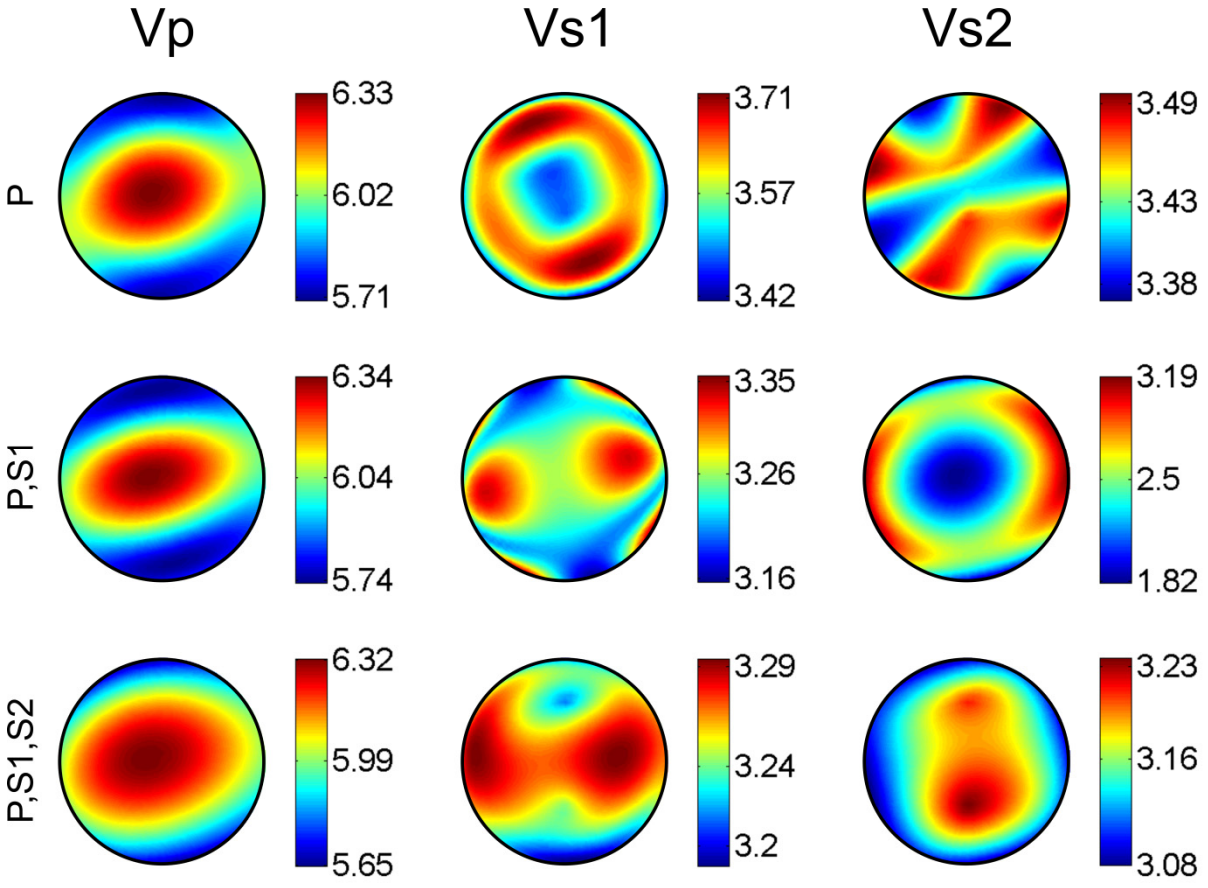

Obr. 19 Porovnanie výpočtu tenzoru elastických parametrov a následnej interpretácie rýchlosti P (ľavý stĺpec), S1 (stredný stĺpec), a S2 vĺn (pravý stĺpec), na základe typu rýchlostí vstupujúcich do výpočtu: len P vlny (horný rad), P a S1 vlny (stredný rad) a P, S1 a S2 vlny (spodný rad); uvedené hodnoty predstavujú fázové rýchlosti v km/s

Na základe výsledkov syntetických testov sa dá usudzovať, že za najvierohodnejšie je možné pokladať výsledky získané z inverzie s prispením rýchlostí P, S1 a S2 vĺn. To

dokladajú aj výsledky konvergencie iteračného výpočtu znázornené na Obr. 20. RMS chyba uvedená na Obr. 20 je počítaná pomocou nasledujúcej rovnice:

$$RMS^{S1,S2} = \sqrt{\sum \frac{\left(c_{obs}^{S1,S2} - c_{pred}^{S1,S2}\right)^2}{n}} \tag{10}$$

kde $c_{obs}^{S1,S2}$ predstavuje namerané rýchlosti, $c_{pred}^{S1,S2}$ sú rýchlosti získané výpočtom z tenzoru elastických parametrov, n je počet smerov, v ktorých sú rýchlosti merané. Z priebehu chovania hodnôt RMS je možné usudzovať nasledujúce závery:

- Výpočet na základe iba rýchlostí P vĺn produkuje stabilné rozloženie rýchlostí S vĺn, ktoré sa s postupným iteračným výpočtom nezlepšujú. Avšak hodnota RMS dosahuje neuspokojivých hodnôt.

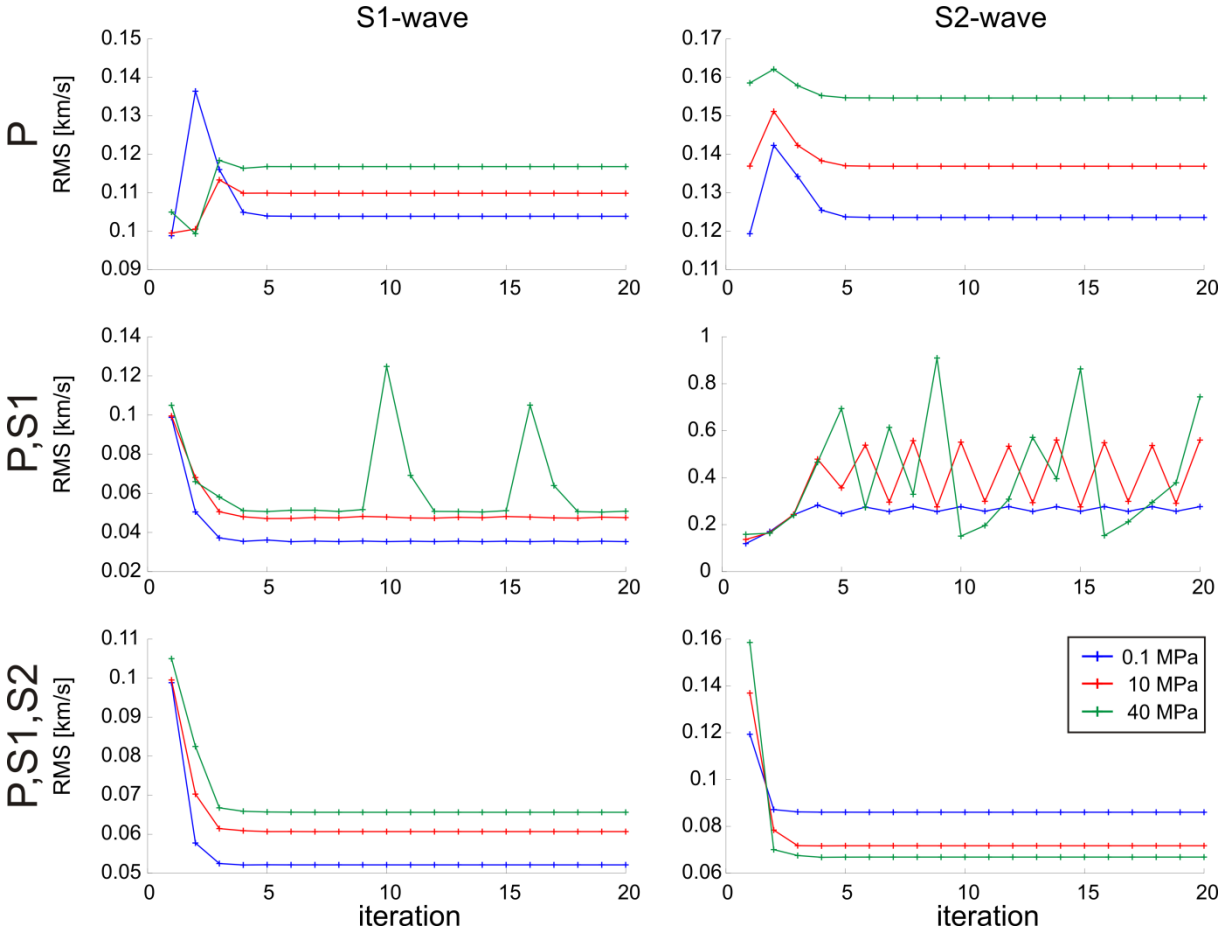

Obr. 20 Konvergencia iteračného postupu inverzie. RMS chyba rýchlostí S1 (ľavý stĺpec) a S2 vĺn (pravý stĺpec). Inverzia len z rýchlostí P vĺn (horný riadok), z rýchlostí P a S1 vĺn (stredný riadok) a z rýchlostí P, S1 a S2 vĺn (spodný riadok). Výsledky uvedené pre 3 tlakové úrovne: 0.1, 10 a 40 MPa.

- Výpočet na základe rýchlostí P a S1 vĺn vykazuje oscilácie oboch rozložení rýchlostí S vĺn v priebehu jednotlivých iteračných krokov. Hodnoty RMS sú opäť neuspokojivo vysoké. Iteračný proces nekonverguje ani po 20 krokoch iterácie.
- Zahrnutie rýchlostí S2 vĺn do inverzie spôsobilo zlepšenie stability výpočtu. Hodnoty RMS sú na akceptovateľnej úrovni. Celý iteračný proces je veľmi robustný a konverguje veľmi rýchlo.

5.4 Publikácia 4:

Lokajíček, T., Kern, H., Svitek, T. & Ivankina, T., 2014. 3D velocity distribution of P and S-waves in a biotite gneiss, measured in oil as the pressure medium: Comparison with velocity measurements in a multi-anvil pressure apparatus and with texture-based calculated data. Phys. Earth Planet. Inter., 231, 1–15

V tomto článku sú prezentované výsledky určovania elastickej anizotropie pomocou rôznych meraní a rôznych prístupov k výpočtu tenzoru elastických parametrov. Merania boli vykonané na vzorke biotitovej ruly z hlbokého vrtu Outokumpu, Fínsko. Jeho výhodou je výborný stav preskúmanosti (Elbra et al., 2011; Kern a Mengel, 2011; Kern et al., 2009, 2008; Kukkonen at al., 2004; Kukkonen et al., 2011; Västi, 2011; Wenk et al., 2012). K meraniu boli použité vzorky pripravené z vrtného jadra z hĺbky okolo 409 m, pričom z neho boli pripravené vzorky tvaru gule (OKU-409) o priemere 50 mm a kocky s hranou 43 mm. Merná hustota materiálu je 2.724 g/cm^3. Vzorka vykazuje zjavnú foliáciu a lineáciu (viď Obr. 21). Pripravené vzorky boli zmerané pomocou ultrazvuku (kocka aj guľa) a neutrónovou difrakciou (guľa).

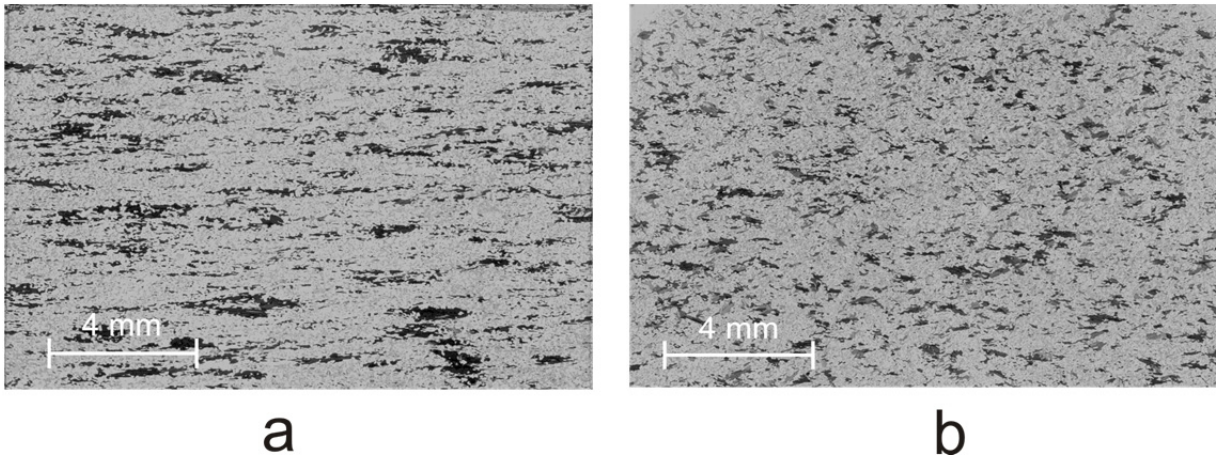

Obr. 21 Optické mikrofotografie ilustrujúce mikroštruktúry biotitickej ruly vzorky OKU-409. Rovinne polarizované svetlo. (a) orientácia paralelne s lineáciou a ± kolmo k rovine foliácie. (b) orientácia kolmo k lineácii

Merania prebiehali na pracoviskách Ústavu geovied Univerzity v Kiele v Nemecku, vo Frankovom laboratóriu neutrónovej fyziky v Spojenom ústave pre nukleárny výskum v Dubne v Rusku a v Laboratóriu fyzikálnych vlastností hornín v Geologickom ústave AV ČR, v.v.i. v Prahe. Meranie na vzorke tvaru kocky bolo vykonané v Kiele v trojosej tlakovej komore, ktorá umožňuje zaťažovať vzorku až do tlaku 600 MPa v troch navzájom nezávislých osách a do teploty až 750°C. V tomto režime je možné vzorku prežarovať P vlnami a dvomi ortogonálne polarizovanými S vlnami. Aby nedošlo k poškodeniu snímačov v dôsledku vysokých pôsobiacich teplôt, snímače sú umiestnené na konci vlnovodov, ktoré sú mimo pôsobenia teploty (viď Obr. 22). Guľová vzorka bola meraná v laboratóriách v Prahe a v Dubne, takže na tú istú vzorku boli aplikované dve odlišné metódy stanovenia elastickej anizotropie – prežarovanie ultrazvukom a neutrónová difrakcia.

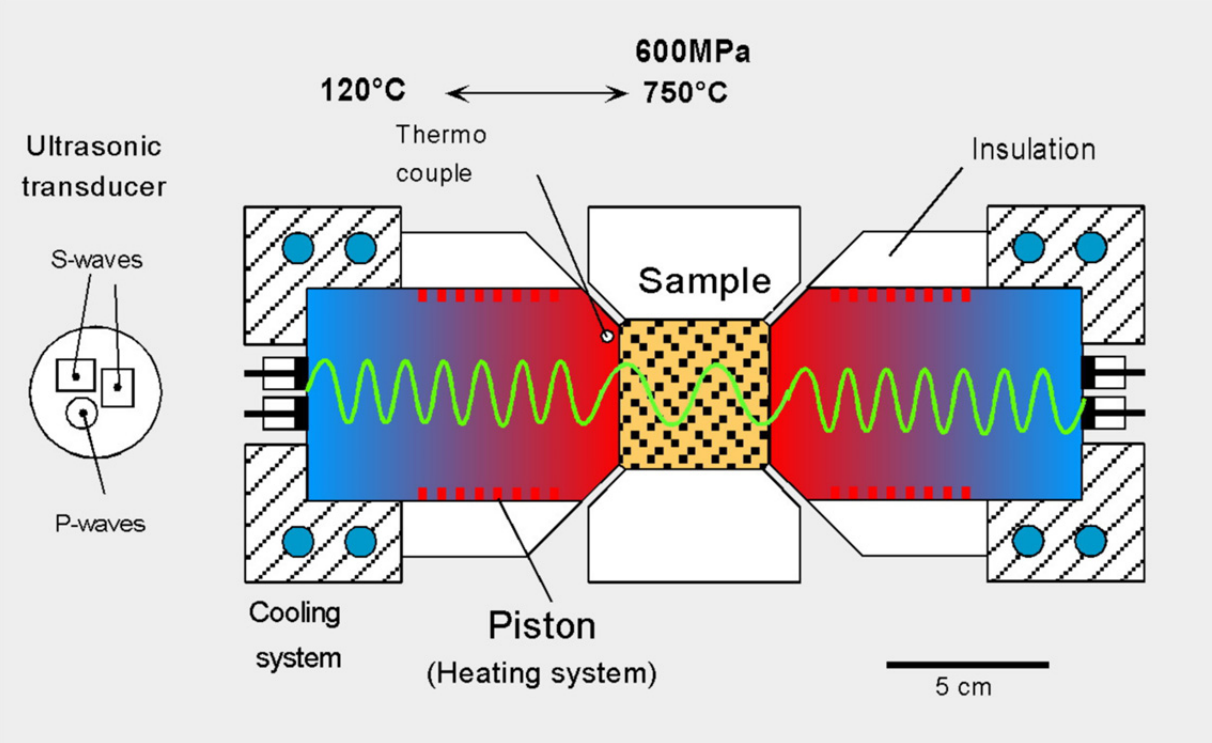

Obr. 22 Schéma geometrie ultrazvukového merania vzoriek tvaru kocky

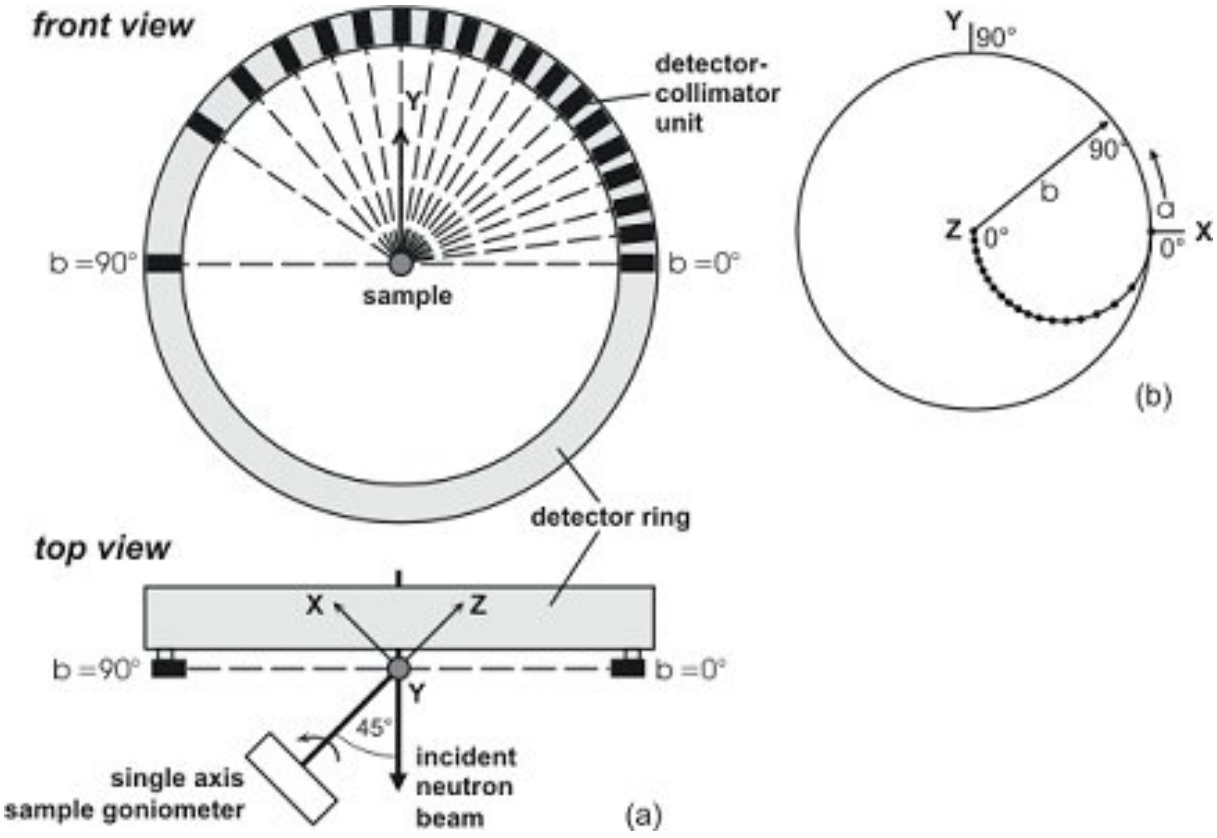

Obr. 23 Schéma geometrie merania vzoriek tvaru gule neutrónovou difrakciou; zdroj http://newuc.jinr.ru/section.asp?id=81

Meranie pomocou neutrónov sa oproti ultrazvuku odlišuje v tom, že nepostihuje mikroporušenia a pórový priestor študovaného materiálu, a vypovedá tak iba o jeho vnútornej textúre. Výsledky tohto merania by sa tak mali blížiť výsledkom ultrazvuku dosiahnutých za pôsobenia vysokého hydrostatického tlaku, kedy sa predpokladá, že je väčšina mikrotrhlín a pórov uzavretá. Geometria merania guľovej vzorky pomocou ultrazvuku je uvedená na Obr. 3, meranie pomocou neutrónov je znázornené na Obr. 23. Porovnanie merania v troch smeroch na vzorke kocky s im odpovedajúcimi smermi na guľovej vzorke sú uvedené na Obr. 24, porovnanie výsledkov ultrazvuku a neutrónovej difrakcii na guli sú potom uvedené na Obr. 25. Na tomto obrázku sú uvedené výsledky dvoch výpočtov merania neutrónovej difrakcie – pomocou metódy GeoMean a GeoMixSelf. Metóda GeoMixSelf sa od metódy GeoMean líši tým, že vo výpočtoch uvažuje tvary minerálnych zŕn a trhlín.

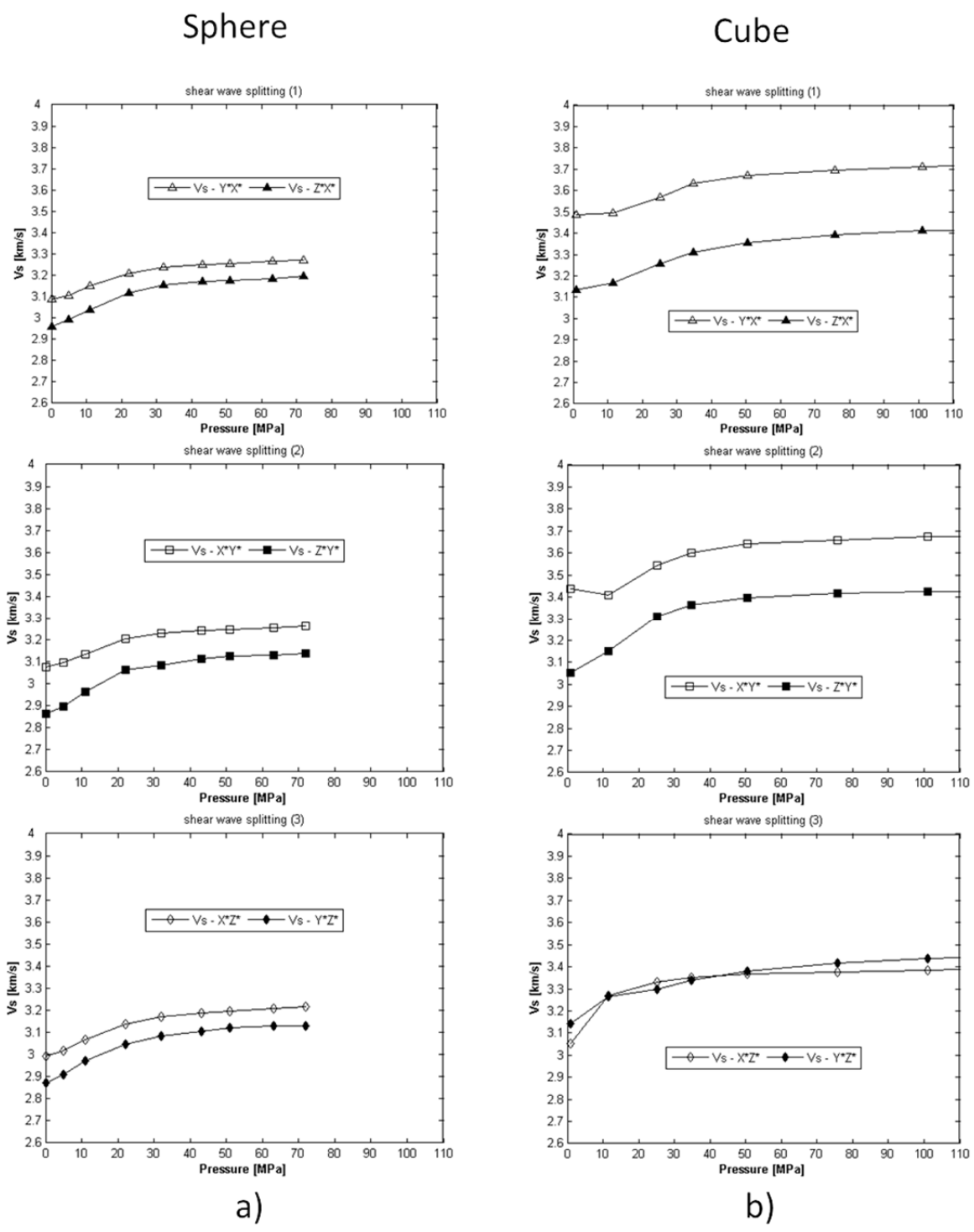

Obr. 24 Porovnanie ultrazvukových rýchlostí S vĺn v troch hlavných smeroch na (a) guľovej vzorke a (b) vzorke tvaru kocky. Dvojindexové značenie (napr. Vs Y*X*) popisuje smer šírenia X a smer polarizácie S vlny Y; X*,Y*,Z* reprezentujú smery maximálnej, strednej a minimálnej nameranej rýchlosti

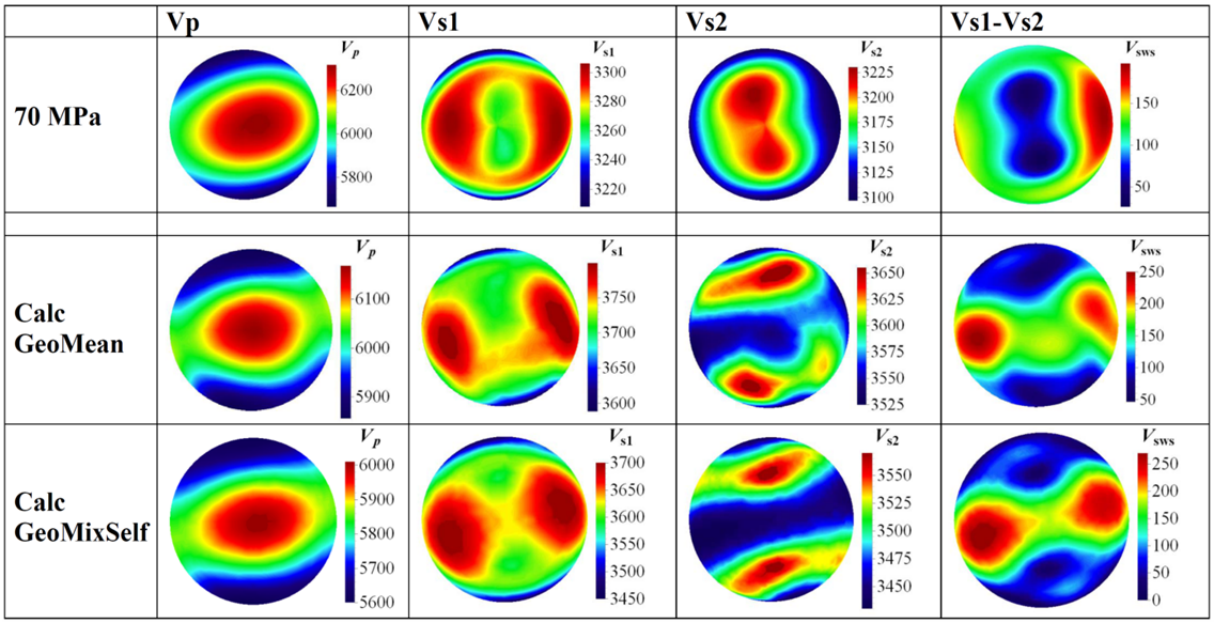

Obr. 25 Rozloženie rýchlostí P, S1 a S2 vĺn a štepenia S vĺn získané ultrazvukom pri tlaku 70 MPa (horný riadok), metódou GeoMean (stredný riadok) a metódou GeoMixSelf (spodný riadok)

Porovnaním výsledkov získaných meraním ultrazvukom na guli a kocke a neutrónovou difrakciou na guli je možné vyvodiť nasledujúce závery:

- Systematicky nižšie rýchlosti merané na guli môžu byť spôsobené epoxidom, ktorým je guľová vzorka pokrytá. Tlak vyvíjaný na guľovú vzorku je generovaný olejom, epoxidová vrstva preto plní funkciu ochrany pred infiltrovaním oleja do pórového priestoru študovaného materiálu. Naproti tomu vzorka tvaru kocky je namáhaná osovými napätiami, ktoré generujú piesty a podobná ochrana tak nie je nutná. Bolo zistené, že epoxidová vrstvička na guľových vzorkách nemá výrazný vplyv na rýchlosť šírenia P vĺn, no ako sa ukazuje rýchlosti S vĺn sú ňou ovplyvnené do značnej miery.
- Neutrónová difrakcia vystihla rozloženie rýchlostí na guli s veľkou mierou podobnosti ako ultrazvukové meranie. Smery hlavných extrémov (maxím a miním) rýchlostí P, S1 aj S2 vĺn korelujú veľmi dobre, napriek tomu, že neutróny nepostihujú rozloženie a orientáciu mikroporušenia, ktoré je vo vzorke prítomné. Neutrónové meranie je porovnávané s ultrazvukovým pri tlaku 70 MPa, kde je pravdepodobné, že nie sú všetky systémy mikroporušenia kompletne uzavreté.

6. Diskusia a záver

Primárnym cieľom práce je štúdium elastickej anizotropie hornín. K tomuto účelu boli použité ultrazvukové merania na guľových horninových vzorkách. V náväznosti na diplomovú prácu bol vytvorený program na automatické určovanie času príchodu P vĺn z ultrazvukových meraní. Program bol ďalej rozšírený o množstvo funkcií vedúcich k analýze, výpočtu a interpretácii tenzoru elastických parametrov. Inovácia aparatúry a možnosť merania S vĺn priniesla veľké množstvo nových informácií, ktoré bolo nutné zapracovať do spracovateľského softwaru. Určenie časov príchodov S vĺn na vlnových

obrazoch získaných zo zaťažovacích experimentov sa uskutočňuje poloautomaticky. Jedna tlaková úroveň, väčšinou tá s najvyšším pôsobiacim hydrostatickým tlakom, je interpretovaná manuálne operátorom. K určeniu časov príchodov S vĺn na nižších tlakových úrovniach je, vďaka podobnosti signálov, využitá korelačná analýza. Nové dáta umožnili porovnať spôsoby určovania elastickej anizotropie. Doposiaľ boli k dispozícii iba merania rýchlostí P vĺn, preto bolo dôležité porovnať, aký vplyv bude mať implementácia merania rýchlostí S1 a S2 vĺn do výpočtu tenzoru elastických parametrov. K posúdeniu, ktorý prístup poskytuje najlepšie výsledky, boli využité syntetické testy. Testy preukázali potrebnosť informácie o rýchlostiach S vĺn pri výpočte tenzoru elastických parametrov. Najlepšie výsledky inverzie boli dosiahnuté v prípade, kedy do výpočtu vstupovali rýchlosti P, S1 aj S2 vĺn. Výpočet je v tomto prípade veľmi robustný a rýchlo konverguje. Vďaka testom bolo tiež zistené, že je potreba merať rýchlosti šírenia S vĺn v dostatočnom počte smerov, ktoré sú rovnomerne priestorovo orientované. Všeobecne platí, že presnosť určenia času príchodu sa môže znižovať pri zvyšujúcom sa množstve použitých dát, tj. čím viac smerov vstupuje do inverzie, tým väčšou chybou môžu byť namerané rýchlosti zaťažené.

Spracovaním ultrazvukových meraní na reálnych horninových vzorkách a porovnaním s výsledkami neutrónovej difrakcie a ultrazvukovými meraniami na inej aparatúre bolo zistené, že získané priestorové rozloženie anizotropie materiálu je dostatočne hodnoverné, no dochádza k systematickému znižovaniu nameraných rýchlostí S vĺn. To naznačuje, že praktická realizácia meraní nie je úplne optimálna. Kvalita nameraných dát, obzvlášť S vĺn, je veľmi závislá na kvalite kontaktu medzi snímačmi a guľovou vzorkou. Kvázibodový kontakt neumožňuje dostatočný prenos strižnej zložky pohybu, preto je registrovaný vlnový obraz dostatočne kvalitný len v špecifických prípadoch (kedy orientácie snímačov a orientácie vnútornej štruktúry študovaného materiálu sú podobné). Kvalitu vlnového obrazu S vĺn do značnej miery ovplyvňuje taktiež epoxidový lak, ktorý slúži ako zábrana proti prenikaniu oleja do vnútra materiálu. Je nutné, aby bol epoxidový lak dostatočne pružný a aby vo vysokých tlakoch nepopraskal. Na druhú stranu však platí, že čím pružnejší lak, tým väčší útlm amplitúd signálu a teda i horšie podmienky pre stanovenie času príchodu S vlny či interpretáciu amplitúd P vĺn. Kvalita registrovaných vlnových obrazov signálov S vĺn je silne závislá na kvalite kontaktu. Zmena bodového kontaktu na plošný by mohla priniesť výrazné zlepšenie kvality registrovaných vlnových obrazov. Toho by mohlo byť dosiahnuté zmenou plochy snímačov z rovinnej na zakrivenú. Ideálne by bolo keby mala plocha snímača rovnakú krivosť ako je krivosť guľového povrchu vzorky. Alternatívou by mohlo byť vyrobiť snímače, ktorých povrch bude mať krivosť o niečo menšiu než je guľový povrch vzorky. Do akej miery to ale bude zlepšenie je momentálne otázne. Ďalšou možnosťou ako zlepšiť kontakt snímača so vzorkou je zmeniť tvar vzorky z guľového na mnohosten. Zbrúsením plôch v miestach merania by došlo k vytvoreniu plošného kontaktu čo by malo priniesť očakávané zlepšenie kvality nameraného signálu. Komplikácie sú v tomto prípade spojené so sieťou meracích bodov, ktorá je redšia na rovníku a hustejšia na póloch (viď Obr. 12d). Alternatívou by mohlo byť vytvoriť mnohosten s menším, avšak pre účely inverzie stále dostatočným, počtom smerov, ktoré by boli po povrchu rozložené rovnomerne, v zmysle plošnom a nie uhlovom.

7. Zoznam citovanej literatúry

Aleksandrov, K.S., Ryzhova, T.V., 1961. The elastic properties of crystals. Sov. Phys. Crystallogr. 6, 228–252.

Allen, R., 1982. Automatic phase pickers: Their present use and future prospects. Bull. Seismol. Soc. Am. 72, S225–242.

Al-Sahawneh, E.I., 2013. Size effect and strength correction factors for normal weight concrete specimens under uniaxial compression stress. Contemp. Eng. Sci. 6, 57–68.

Babuška, V., Cara, M., 1991. Seismic Anisotropy in the Earth. Springer.

Bart, M., Shao, J.F., Lydzba, D., 2000. Poroelastic behaviour of saturated brittle rock with anisotropic damage. Int. J. Numer. Anal. Methods Geomech. 24, 1139–1154. doi:10.1002/1096-9853(20001225)24:15<1139::AID-NAG114>3.0.CO;2-3

Birch, F., 1961. The velocity of compressional waves in rocks to 10 kilobars: 2. J. Geophys. Res. 66, 2199–2224. doi:10.1029/JZ066i007p02199

Crampin, S., 1985. Evaluation of anisotropy by shear-wave splitting. Geophysics 50, 142–152. doi:10.1190/1.1441824

Crampin, S., Peacock, S., 2005. A review of shear-wave splitting in the compliant crack-critical anisotropic Earth. Wave Motion 41, 59–77. doi:10.1016/j.wavemoti.2004.05.006

Červený, V., 2001. Seismic Ray Theory. Cambridge University Press.

Dellinger, J., Vernik, L., 1994. Do traveltimes in pulse-transmission experiments yield anisotropic group or phase velocities? Geophysics 59, 1774–1779. doi:10.1190/1.1443564

Dewhurst, D.N., Siggins, A.F., 2006. Impact of fabric, microcracks and stress field on shale anisotropy. Geophys. J. Int. 165, 135–148. doi:10.1111/j.1365-246X.2006.02834.x

Elbra, T., Karlqvist, R., Lassila, I., Haeggström, E., Pesonen, L.J., 2011. Laboratory measurements of the seismic velocities and other petrophysical properties of the Outokumpu deep drill core samples, eastern Finland. Geophys. J. Int. 184, 405–415. doi:10.1111/j.1365-246X.2010.04845.x

Farra, V., 2004. Improved first-order approximation of group velocities in weakly anisotropic media. Stud. Geophys. Geod. 48, 199–213. doi:10.1023/B:SGEG.0000015592.36894.3b

Helbig, K., 1994. Foundations of Anisotropy for Exploration Seismics. Elsevier Science/Pergamon.

Hornby, B.E., 1998. Experimental laboratory determination of the dynamic elastic properties of wet, drained shales. J. Geophys. Res. 103, 29945. doi:10.1029/97JB02380

Chapman, M., 2009. Models for the elastic properties of rock saturated with multiple fluids., in: 71st EAGE Conference and Exhibition Incorporating SPE EUROPEC 2009. doi:10.3997/2214-4609.201400545

Christensen, N.I., 1965. Compressional wave velocities in metamorphic rocks at pressures to 10 kilobars. J. Geophys. Res. 70, 6147–6164. doi:10.1029/JZ070i024p06147

Ildefonse, B., Launeau, P., Bouchez, J.-L., Fernandez, A., 1992. Effect of mechanical interactions on the development of shape preferred orientations: a two-dimensional experimental approach. J. Struct. Geol. 14, 73–83.

Ivankina, T.I., Kern, H.M., Nikitin, A.N., 2005. Directional dependence of P- and S-wave propagation and polarization in foliated rocks from the Kola superdeep well: Evidence from laboratory measurements and calculations based on TOF neutron diffraction. Tectonophysics 407, 25–42. doi:10.1016/j.tecto.2005.05.029

Jech, J., 1991. Computation of elastic parameters of anisotropic medium from travel times of quasi-compressional waves. Phys. Earth Planet. Inter. 66, 153–159. doi:10.1016/0031-9201(91)90074-R

Jech, J., Pšenčík, I., 1989. First-order perturbation method for anisotropic media. Geophys. J. Int. 99, 369–376.

Kern, H., Ivankina, T.I., Nikitin, A.N., Lokajíček, T., Pros, Z., 2008. The effect of oriented microcracks and crystallographic and shape preferred orientation on bulk elastic anisotropy of a foliated biotite gneiss from Outokumpu. Tectonophysics 457, 143–149. doi:10.1016/j.tecto.2008.06.015

Kern, H., Mengel, K., 2011. P- and S-wave velocities and velocity anisotropy of core samples from the outokumpu 2500 m crustal section: Implications for the nature of seismic reflections, in: Kukkonen, Ilmo, T. (Ed.), Outokumpu Deep Drilling Project 2003–2010. Geological Survey of Finland, Espoo 2011, pp. 83–94.

Kern, H., Mengel, K., Strauss, K.W., Ivankina, T.I., Nikitin, A.N., Kukkonen, I.T., 2009. Elastic wave velocities, chemistry and modal mineralogy of crustal rocks sampled by the Outokumpu scientific drill hole: Evidence from lab measurements and modeling. Phys. Earth Planet. Inter. 175, 151–166. doi:10.1016/j.pepi.2009.03.009

Kitamura, K., 2006. Constraint of lattice-preferred orientation (LPO) on Vp anisotropy of amphibole-rich rocks. Geophys. J. Int. 165, 1058–1065. doi:10.1111/j.1365-246X.2006.02961.x

Klíma, K., 1973. The computation of the elastic constants of an anisotropic medium from the velocities of body waves. Stud. Geophys. Geod. 17, 115–122.

Klíma, K., Pick, M., Pros, Z., 1981. On the problem of equal area block on a sphere. Stud. Geophys. Geod. 25, 24–35. doi:10.1007/BF01613559

Kukkonen, I.T., Rath, V., Kivekäs, L., Šafanda, J., Čermak, V., 2011. Geothermal studies of the Outokumpu Deep Drill Hole, Finland: Vertical variation in heat flow and

palaeoclimatic implications. Phys. Earth Planet. Inter. 188, 9–25. doi:10.1016/j.pepi.2011.06.002

Kukkonen, I.T., the Outokumpu Deep Drilling Working Group, 2004. The Outokumpu Deep Drilling Project – Background, aims and current status of drilling, in: Kukkonen, I.T. (Ed.), Outokumpu Deep Drilling Project. Geological Survey of Finland, pp. 9–10.

Kwasniewski, M., Li, X., Takahashi, M. (Eds.), 2012. True Triaxial Testing of Rocks. CRC Press.

Lipschutz, M.M., 1969. Theory and Problems of Differential Geometry. McGraw-Hill.

Lokajíček, T., Klíma, K., 2006. A first arrival identification system of acoustic emission (AE) signals by means of a high-order statistics approach. Meas. Sci. Technol. 17, 2461–2466.

Lokajíček, T., Svitek, T., 2015. Laboratory measurement of elastic anisotropy on spherical rock samples by longitudinal and transverse sounding under confining pressure. Ultrasonics 56, 294–302. doi:10.1016/j.ultras.2014.08.015

Mainprice, D., 1990. A FORTRAN program to calculate seismic anisotropy from the lattice preferred orientation of minerals. Comput. Geosci. 16, 385–393. doi:10.1016/0098-3004(90)90072-2

Mainprice, D., Nicolas, A., 1989. Development of shape and lattice preferred orientations: application to the seismic anisotropy of the lower crust. J. Struct. Geol. 11, 175–189.

Mattaboni, P., Schreiber, E., 1967. Method of pulse transmission measurements for determining sound velocities. J. Geophys. Res. 72, 5160–5163. doi:10.1029/JZ072i020p05160

Musgrave, M.J.P., 1970. Crystal Acoustics: Introduction to the Study of Elastic Waves and Vibrations in Crystals. Holden-Day.

Nikitin, A.N., Ivankina, T.I., 2004. Neutron diffractometry in geosciences. Phys. Part. Nucl. 35, 193–224.

Nye, J.F., 1979. Physical Properties of Crystals. Clarendon Press.

Nye, J.F., 2001. Elastic Behavior of Single Crystals: Anisotropy, in: Encyclopedia of Materials: Science and Technology. pp. 2415–2422.

Piane, C.D., Dewhurst, D.N., Siggins, A.F., Raven, M.D., 2011. Stress-induced anisotropy in brine saturated shale. Geophys. J. Int. 184, 897–906. doi:10.1111/j.1365-246X.2010.04885.x

Pros, Z., Babuška, V., 1968. An apparatus for investigating the elastic anisotropy on spherical rock samples. Stud. Geophys. Geod. 12, 192–198. doi:10.1007/BF02587847

Pros, Z., Lokajíček, T., Klíma, K., 1998. Laboratory Approach to the Study of Elastic Anisotropy on Rock Samples. Pure Appl. Geophys. 151, 619–629. doi:10.1007/s000240050133

Pros, Z., Podroužková, Z., 1974. Apparatus for investigating the elastic anisotropy on spherical rock samples at high pressure. Veröff Zentralinst Physic Erde 22, 42–47.

Pšenčík, I., Vavryčuk, V., 2002. Approximate relation between the ray vector and the wave normal in weakly anisotropic media. Stud. Geophys. Geod. 46, 793–807. doi:10.1023/A:1021189724526

Sayers, C.M., 2002. Fluid-dependent shear-wave splitting in fractured media. Geophys. Prospect. 50, 393–401.

Sayers, C.M., Kachanov, M., 1995. Microcrack-induced elastic wave anisotropy of brittle rocks. J. Geophys. Res. 100, 4149. doi:10.1029/94JB03134

Sedlák, P., Hirose, Y., Khan, S.A., Enoki, M., Šikula, J., 2009. New automatic localization technique of acoustic emission signals in thin metal plates. Ultrasonics 49, 254–62. doi:10.1016/j.ultras.2008.09.005

Siegesmund, S., Kern, H., Vollbrecht, A., 1991. The effect of oriented microcracks on seismic velocities in an ultramylonite. Tectonophysics 186, 241–251. doi:10.1016/0040-1951(91)90361-U

Stanchits, S., Vinciguerra, S., Dresen, G., 2006. Ultrasonic velocities, acoustic emission characteristics and crack damage of basalt and granite. Pure Appl. Geophys. 163, 975–994. doi:10.1007/s00024-006-0059-5

Svitek, T., Rudajev, V., Petružálek, M., 2010. Determination of P - wave arrival time of acoustic events. Acta Montan. Slovaca 15, 145–151.

Valcke, S.L.A., Casey, M., Lloyd, G.E., Kendall, J.-M., Fisher, Q.J., 2006. Lattice preferred orientation and seismic anisotropy in sedimentary rocks. Geophys. J. Int. 166, 652–666. doi:10.1111/j.1365-246X.2006.02987.x

Västi, K., 2011. Petrology of the drill hole R2500 at Outokumpu , Eastern Finland – the deepest drill hole ever drilled in Finland, in: Kukkonen, Ilmo, T. (Ed.), Outokumpu Deep Drilling Project 2003–2010. Geological Survey of Finland, Espoo 2011, pp. 17–46.

Vavryčuk, V., 1997. Elastodynamic and elastostatic Green tensors for homogeneous weak transversely isotropic media. Geophys. J. Int. 130, 786–800.

Vavryčuk, V., 2003a. Parabolic lines and caustics in homogeneous weakly anisotropic solids. Geophys. J. Int. 152, 318–334.

Vavryčuk, V., 2003b. Behavior of rays near singularities in anisotropic media. Phys. Rev. B 67, 054105. doi:10.1103/PhysRevB.67.054105

Vavryčuk, V., 2005a. Acoustic axes in triclinic anisotropy. J. Acoust. Soc. Am. 118, 647. doi:10.1121/1.1954587

Vavryčuk, V., 2005b. Acoustic axes in weak triclinic anisotropy. Geophys. J. Int. 163, 629–638. doi:10.1111/j.1365-246X.2005.02762.x

Vavryčuk, V., 2006. Calculation of the slowness vector from the ray vector in anisotropic media. Proc. R. Soc. A Math. Phys. Eng. Sci. 462, 883–896. doi:10.1098/rspa.2005.1605

Vavryčuk, V., 2013. Inversion for weak triclinic anisotropy from acoustic axes. Wave Motion 50, 1271–1282. doi:10.1016/j.wavemoti.2012.11.003

Volarovich, M.P., Bayuk, E.I., Efimova, G.A., 1975. Elastic properties of minerals at high pressures. Nauka. (in Russian).

Wang, X.-Q., Schubnel, A., Fortin, J., David, E.C., Guéguen, Y., Ge, H.-K., 2012. High Vp/Vs ratio: Saturated cracks or anisotropy effects? Geophys. Res. Lett. 39, L11307. doi:10.1029/2012GL051742

Weidner, D.J., Swyler, K., Carleton, H.R., 1975. Elasticity of microcrystals. Geophys. Res. Lett. 2, 189–192. doi:10.1029/GL002i005p00189

Wenk, H.-R., Vasin, R.N., Kern, H., Matthies, S., Vogel, S.C., Ivankina, T.I., 2012. Revisiting elastic anisotropy of biotite gneiss from the Outokumpu scientific drill hole based on new texture measurements and texture-based velocity calculations. Tectonophysics 570-571, 123–134. doi:10.1016/j.tecto.2012.06.023

Xie, Y., Wenk, H.-R., Matthies, S., 2003. Plagioclase preferred orientation by TOF neutron diffraction and SEM-EBSD. Tectonophysics 370, 269–286. doi:10.1016/S0040-1951(03)00191-4

8. Prílohy

Príloha 1 – Prehlásenie spoluautorov upresňujúce autorský podiel na jednotlivých publikáciách

- Lokajíčk, T., & **Svitek, T.** (2014). **Laboratory approach to the study of elastic anisotropy in spheres by simultaneous longitudinal and transverse sounding under confining pressure**. *Ultrasonics,* In Press doi:10.1016/j.ultras.2014.08.015

  Autorský podiel (T. Svitek): 40%

  .....
  Ing. Tomáš Lokajíček, CSc.

- **Svitek, T.**, Rudajev, V., & Petružalek, M. (2010). **Determination of P-wave arrival time of acoustic events**. *Acta Montan. Slov.*, 15(2), 145-151.

  Autorský podiel (T. Svitek): 80%

  .....
  Mgr. Matěj Petružálek

- **Svitek, T.**, Vavryčuk, V., Lokajíček, T., & Petružálek, M. (2014). **Determination of elastic anisotropy of rocks from P- and S-wave velocities: Numerical modelling and lab measurements**. *Geophys. J. Int.*, In Press

  Autorský podiel (T. Svitek): 70%

  .....
  RNDr. Václav Vavryčuk, DrSc.

- Lokajíček, T., Kern, H., **Svitek, T.**, & Ivankina, T. (2014). **3D velocity distribution of P- and S-waves in a biotite gneiss, measured in oil as the pressure medium: Comparison with velocity measurements in a multi-anvil pressure apparatus and with texture-based calculated data**. *Phys. Earth Planet. Inter*, 231, 1–15. doi:10.1016/j.pepi.2014.04.002

  Autorský podiel (T. Svitek): 40%

  .....
  Ing. Tomáš Lokajíček, CSc.

- Lokajíček, T., Šťastná, A., Petružálek, M., Šachlová, Š., **Svitek, T.** & Přikryl,. R. (2014). **Quasi-continuous ultrasonic sounding and changes of ultrasonic signal characteristics as a sensitive tool for the evaluation of ongoing microstructural changes of experimental mortar bars tested for their ASR potential**. Submitted to NDTe

  Autorský podiel (T. Svitek): 10%

  .....
  Ing. Tomáš Lokajíček, CSc.

Príloha 2

Publikácia 1:

Lokajíček, T., & **Svitek, T.** (2014). **Laboratory approach to the study of elastic anisotropy in spheres by simultaneous longitudinal and transverse sounding under confining pressure**. *Ultrasonics, In Press*
doi:10.1016/j.ultras.2014.08.015

Ultrasonics xxx (2014) xxx–xxx

Contents lists available at ScienceDirect

Ultrasonics

journal homepage: www.elsevier.com/locate/ultras

Laboratory measurement of elastic anisotropy on spherical rock samples by longitudinal and transverse sounding under confining pressure

Tomáš Lokajíček [a,*], Tomáš Svitek [b,a]

[a] Institute of Geology AS CR, v.v.i. Rozvojová 269, 165 00 Prague 6, Czech Republic
[b] Charles University in Prague, Faculty of Science, Albertov 6, 128 43 Praha, Czech Republic

ARTICLE INFO

Article history:
Received 16 April 2014
Received in revised form 10 August 2014
Accepted 12 August 2014
Available online xxxx

Keywords:
Elastic anisotropy
Hydrostatic pressure
Ultrasonic sounding
High pressure
Longitudinal and shear waves

ABSTRACT

Knowledge of shear wave velocities in loaded rocks is important in describing elastic anisotropy. A new high-pressure measuring head was designed and constructed for longitudinal and traversal ultrasonic sounding of spherical rock samples in 132 independent directions under hydrostatic pressure up to 60 MPa. The velocity is measured using a pair of P-wave sensors and two pairs of S-wave sensors (T_V/R_V and T_H/R_H) with perpendicular polarization. An isotropic glass sphere was used to calibrate the experimental setup. A fine-grained anisotropic quartzite sample was examined using the P- and S-wave ultrasonic sounding. Waveforms are recorded by pairs of T_P/R_P, T_V/R_V and T_H/R_H transducers in a range of confining pressure between 0.1 and 60 MPa. The recorded data showed a shear wave splitting in three basic structural directions of the sample. The measurements proved to be useful in investigating oriented micro-cracks, lattice (LPO) and shape-preferred orientation (SPO) for the bulk elastic anisotropy of anisotropic rocks subjected to hydrostatic pressure.

1. Introduction

Laboratory research into rock samples is focused on understanding the influence of lithology, porosity, confining pressure, anisotropy and degree of fracturing on P- and S-wave velocities.

The anisotropy of rocks may be caused by: (1) lattice (or crystallographic) preferred orientation (LPO), (2) preferred morphological or shape-preferred orientation of inclusions (SPO) [1,2], (3) preferred orientation of micro-cracks/pores, (4) thin layers of isotropic materials with different elastic properties [3], or (5) the combination of the above mentioned parameters. The anisotropy of mechanical properties also depends on the stress level and on the system of acting forces – uniaxial force, confining pressure, etc. [4,5], several methods can be used to study elastic anisotropy experimentally: ultrasonic sounding [1,6], the neutron diffraction method [7], or modal analysis of rock samples which enables calculation of the longitudinal V_P and shear V_S wave velocities of anisotropic rocks based upon experimentally established grain orientation distribution functions [8]. Traditionally, anisotropy of rocks under atmospheric and high pressures has been investigated by means of P-wave ultrasonic sounding in three mutually perpendicular directions on samples in the form of a cube or prism [1,9], or by P- and S-wave sounding [10,11]. Very often, polyhedron-type samples such as octadecahedrons, tetratrioctahedrals [12–14] and/or cubes with beveled edges [15,16] are used. Cylindrical samples are mostly used to determine elastic anisotropy [17–20] and other quantities as well.

The study of the velocity anisotropy of V_P on spherical samples provides more complete information of the velocities in any direction both under atmospheric and high hydrostatic pressures [21–28].

Elastic velocities for many crustal rocks have been determined by ultrasonic experiments using high-pressure apparatus [29–31]. These experimental studies have provided compression and shear wave velocity data to assess the petrological characteristics of the lower parts of the continental crust.

Simultaneous V_P and V_S measurements have been conducted in recent ultrasonic experiments on crustal rocks [32–34]. Elastic moduli of solids have been also calculated by means of resonant ultrasound spectroscopic techniques [35–37]. Nevertheless, such a study requires samples without porosity or fluids.

The purpose of this paper is to describe a new high-pressure system for the laboratory study of rocks by P- and S-wave ultrasonic sounding of spherical samples under confining stress up to 60 MPa.

* Corresponding author.
E-mail address: tl@gli.cas.cz (T. Lokajíček).

http://dx.doi.org/10.1016/j.ultras.2014.08.015
0041-624X/

2. Technical solution

So far, the directional dependence of velocity anisotropy in spherical samples under hydrostatic pressure of 0.1 MPa up to 400 MPa has been studied only by using P-wave velocity sounding, as described in [24].

This paper deals with a significant improvement of this system, which enables measurements also by using two pairs of perpendicularly oriented shear wave transducers. Measurements can presently be made in 132 independent directions under hydrostatic pressure up to 60 MPa.

The mechanical design of the measuring system enables movement of the spherical sample and the transducers by two-step motors. All moving mechanical parts are located inside the pressure vessel. A schematic drawing of the new transducer measuring arrangement is shown in Fig. 1A. Three pairs of transducers (T_P/R_P, T_H/R_H and T_V/R_V) are used for ultrasonic sounding by means of the pulse-transmission method. The angle between the individual transducer pairs is 15 degrees, which corresponds with the measuring step of the high-pressure head. The contact surfaces of the sphere and transducers are covered by a high-viscosity layer (Sonotech, shear wave gel) to transfer the shear-wave energy from the T_H and T_V transducers to the sample and subsequently to R_H and R_V.

The sensor polarization is determined according to the sphere's rotation axis. The measuring system uses one pair of P-wave transducers with flat contact surfaces, denoted by P, which record longitudinal waves. A piezoceramic Noliac pill, N51 4.5 mm in diameter and 0.5 mm thick, is used in the transducer. Their resonant frequency was about 2 MHz. There are also two pairs of perpendicularly oriented shear wave transducers with horizontal T_H and vertical T_V polarization. Noliac tablets, N55, L2.5 – W2.5 – TH1, of size 2.5 × 2.5 mm and 1 mm thick, with 0.8 MHz resonant frequency, are used in flat contact sensors. All transducers have similar point contact with the spherical sample but due to the shear wave gel used; the real contact of the sensors is not point contact but quasi-point one, which may have a diameter of roughly 1 mm or more. Predominant wavelength of recorded signals was about 1–2 mm.

The contact surfaces of the transducers are covered by shear-wave couplant as well. Using two pairs of shear-wave transducers provides better discrimination of the individual shear-wave components propagating through the anisotropic sample. When setting up a new ultrasonic sounding position/direction, due to the high-viscosity layer covering the spherical sample and transducers, the step motors cannot rotate the sphere or the arms fitted with 3 pairs of transducers. To change the position of transducers, the measuring head has to be equipped with one miniature DC motor (Maxon, diameter 8 mm), which is used to eliminate the contact between the sphere and transducers. After setting up a new measuring position, the DC motor re-establishes the contact between the transducers and the sample. As the restoring force of the transducers is controlled by the current of the DC motor, nearly identical contact conditions between the sensors and sample are preserved at all measuring points at one level of acting hydrostatic pressure. The restoring force is given by switching off DC motor current at an identical level. Eliminating the contact between the sample and transducers has several advantages: 1. It enables transducer and sample movement to set up a new transducer positions. 2. It prevents the high-viscosity layer from being wiped off in the course of transducer movement. 3. Calibration measurements proved that the high-viscosity layer remains on the sphere surface during the entire measuring procedure. During sample preparation, the sample and contact surface are carefully covered by shear-wave gel at a temperature of 40 °C to assure very thin and uniform spreading of the shear-wave gel. All measurements are done at 22 °C. Using the Maxon DC motor brings only one limitation it can only be used up to 60 MPa of hydrostatic pressure. As this is a miniature DC motor with a planetary four-stage gear, filling the inner parts of the motor with oil produces high friction of all individual parts, which results in a significant increase in the no-load current, which reaches nearly 80% of the maximum continuous current. Due to this fact, use of the new measuring set up is currently limited to a hydrostatic range between 0.1 MPa and about 60 MPa. As this is the range of hydrostatic pressure at which all cracks close, so that the modified measuring setup records the most important part of this process anyway. At one transducers' position, P, SV and SH waveforms are recorded. Note

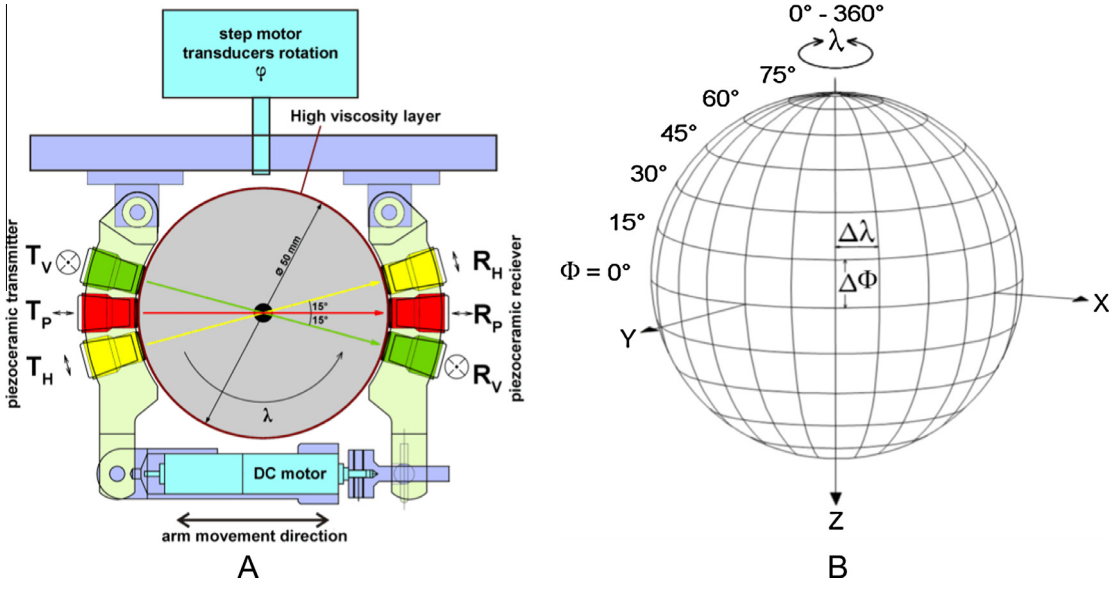

Fig. 1. A: schematic plot of the measuring setup. T_P, R_P – pair of longitudinal piezoceramic transducers (T-transmitter, R-receiver); T_V, R_V – pair of shear-wave transducers with vertical polarization; T_H, R_H – pair of shear-wave transducers with horizontal polarization. λ – angle of sphere rotation, Φ – angle of arm rotation, step motor to rotate arms with transducers, DC motor – motor to eliminate and re-establish contact between the sphere and transducers to enable arm movement and position the sphere and transducers. B: measuring net projection on the sphere surface, arm inclination $\Phi = 0$–$75°$ in steps of 15°, sphere rotation $\lambda = 0$–$360°$ in steps of 15°.

Please cite this article in press as: T. Lokajíček, T. Svitek, Laboratory measurement of elastic anisotropy on spherical rock samples by longitudinal and transverse sounding under confining pressure, Ultrasonics (2014), http://dx.doi.org/10.1016/j.ultras.2014.08.015

that SV and SH are shortcuts used to express waveform polarization and do not correspond with terminology commonly used for transverse isotropy. The SV and SH waveform polarizations are perpendicular and parallel to the sphere rotation axis, respectively. Moreover, we transmit into the sphere shear waves with perpendicular polarization, but anisotropic material influence polarization of recorded waveforms according to the anisotropy symmetry. The spherical sample orientation in high pressure measuring head should be that polarization of one pair shear wave sensors is parallel with the symmetry axis. This measuring arrangement will enable shear wave recording in important structural directions without shear wave polarization.

Fig. 1B shows the schematic arrangement of the measuring set up. The spherical sample can be rotated through angle from $\lambda = 0$–360°, and the arms with transducers through angle from $\Phi = -75°$ to +75°. The sphere's surface is divided into steps of 15°. With the proposed measuring set up, we can make measurements in 132 independent directions. The accuracy of each transducer positioning is ±1°. During one measuring cycle, three signals data set are recorded in steps of 15°. After the measurement, all data sets are transformed/rotated by ±15° to the same angular position. In this way, the measuring set up yields P, SV and SH waveforms at one direction of measurement. This means that at one measuring point on the sphere, three independent wave components (P waveform, SV and SH waveforms) are recorded, very similar to seismic waves recorded by 3-component seismometers.

Captured signals were 40 dB amplified by low noise preamplifier with 10 kHz–10 MHz frequency range. There was developed digitally controlled switching unit, which enables sequential transducers excitation and signal recording by three transducer pairs. Ultrasonic signals were recorded by Agilent digital scope 54601A with a 100 MHz sampling frequency and 8 bit resolution of A/D convertor. Each signal was 10× averaged to improve signal to noise ratio. Each signal was recorded with two different sensitivities. Sensitivity of all captured signals was automatically set up to record full waveform without signal cut off. Second signal recording sensitivity was 10× higher, what enables accurate arrival time reading.

3. System calibration

This new approach to the recording set up with movable shear-wave transducers used under confining stress requires enhanced calibration. To check the quality of the quasi-point contact between the transducers and sphere and to check the accuracy of the entire measuring set up, we used a spherical sample of high quality sodium potassium glass, diameter 50 mm ± 0.01 mm. The glass sample was an isotropic material without any bubbles or cracks, so the arrival times and signals amplitudes were equal in all directions for the P and/or SV and SH components for individual values of acting hydrostatic pressure, as documented by the following measurements. Fig. 2 shows sets of 132 waveforms recorded by the P, SV and SH wave transducers under an atmospheric pressure of 0.1 MPa (upper row) and 50 MPa (lower row). Fig. 2A shows the time details of the P-wave signal arrivals. The arrowed line at about 9 μs marks the P-wave arrival time. As the sampling time interval of the recording system was 10 ns (sampling frequency 100 MHz), the accuracy of P-wave time arrival is ±1 sampling point (i.e. about ± 10 ns). As regards the P-wave amplitude of the first arrival, a slight scattering of amplitudes can be observed at 0.1 MPa, where scattering from the mean amplitude value was ±20%. On the contrary, at an acting hydrostatic pressure of 50 MPa, P-wave amplitude scattering was less than ±10%. No directional dependence of P-wave velocity anisotropy was observed, nor any dependence on amplitude. This result also confirmed the isotropic behavior of the glass sample.

Fig. 2B shows the time details of the signal arrivals of 132 SV waveforms recorded by the T_V pair of S-wave transducers under an atmospheric pressure of 0.1 MPa (upper row) and 50 MPa (lower row).

The arrowed line at the arrival time of about 15.22 μs shows the SV wave arrival. The accuracy of arrival time is about ±2 sampling points (i.e. about ±20 ns). The SV first arrival amplitudes display quite high scatter at atmospheric pressure ±40%. This can be explained by the an imperfect connection of both high-viscosity layers of sphere and sensors in the oil, which results in a larger scatter of the SV first arrival amplitude at a hydrostatic pressure of 0.1 MPa. On the contrary, at 50 MPa we can observe quite stable first arrival amplitudes recorded by the SV transducer; scattering is about 25%. As the glass sample is an isotropic medium without any cracks and with a Young modulus of about 65 GPa, the arrival time of P and S waves is nearly the same at 0.1 and 50 MPa of acting hydrostatic pressure.

Fig. 2C shows the time details of signal arrivals of 132 SH waveforms recorded by the T_H/R_H pair of S-wave transducers under an atmospheric pressure of 0.1 MPa (upper row) and 50 MPa (lower row). The arrowed line at arrival time of about 15.18 μs shows the SH wave arrival. The earlier arrival time at the SH transducer (time difference 0.04 μs) is caused by different transducer time constants according to SV one. As the recording principle of the SH components is identical to that of the SV, we can observe a similar result to the first amplitude recording. The accuracy of the arrival time is about ±2 sampling points (±20 ns). And the scatter of the SH first arrival amplitude at atmospheric pressure is also ±40%, as some signals with very low amplitude should be excluded from the signal processing. On the contrary, at 50 MPa, scattering of SH wave amplitudes is about 15%. Mainly, reduction of shear wave amplitude scatter calls for improvement of amplitude recording stability in the future to use shear waves for ultrasonic signal attenuation studies.

The P wave, SV- and SH-waves were used to determine the real ultrasonic wave velocities. The individual transducer time constants were subtracted. The P-wave velocity was determined to be equal to 5.57 km/s. The SV-, and SH-wave velocities were the same and equal to 3.28 km/s. The ratio between the P- and SV-, SH-waves was calculated and found to be equal to $V_P/V_S = 1.698$, what is close to Poisson's media, $\sqrt{3}$. This result also confirmed that the shear-wave components were recorded by the T_V/R_V and T_H/R_H transducers.

The calibration test indicated that the simultaneous recording of P and S waves under confining stress can be used for ultrasonic sounding of spherical rock samples. The arrival times of the individual waves recorded by the T_P/R_P, T_V/R_V and T_H/R_H transducers can be determined very well. There are some limitations concerning the recording of shear-wave signal amplitudes, mainly at lower values of hydrostatic pressure.

4. Anisotropic sample measurement

The apparatus was tested on a real anisotropic spherical sample – dark gray very fine-grained quartzite–biotite gneisses with macroscopically recognizable ore minerals (py) and mica (bt); biotite forms a minor narrow veins, locality – quarry located 20 km NE of the town of Tábor (Bohemian Massif, Czech Republic) [38]. Modal analysis is given in Table 1. Quartzite mineralogical density is equal to 2.65 g/cm^3.

A spherical sample, 50 ± 0.01 mm in diameter, was made from a quartzite block. The sphere was dried under low pressure of 2 kPa for 24 h at 38 °C to avoid creating any cracks due to higher temperature. After this, several epoxy layers were applied to the sample to prevent the pore space from being filled with oil during the acting of hydrostatic pressure. The sample was then measured by the

Please cite this article in press as: T. Lokajíček, T. Svitek, Laboratory measurement of elastic anisotropy on spherical rock samples by longitudinal and transverse sounding under confining pressure, Ultrasonics (2014), http://dx.doi.org/10.1016/j.ultras.2014.08.015

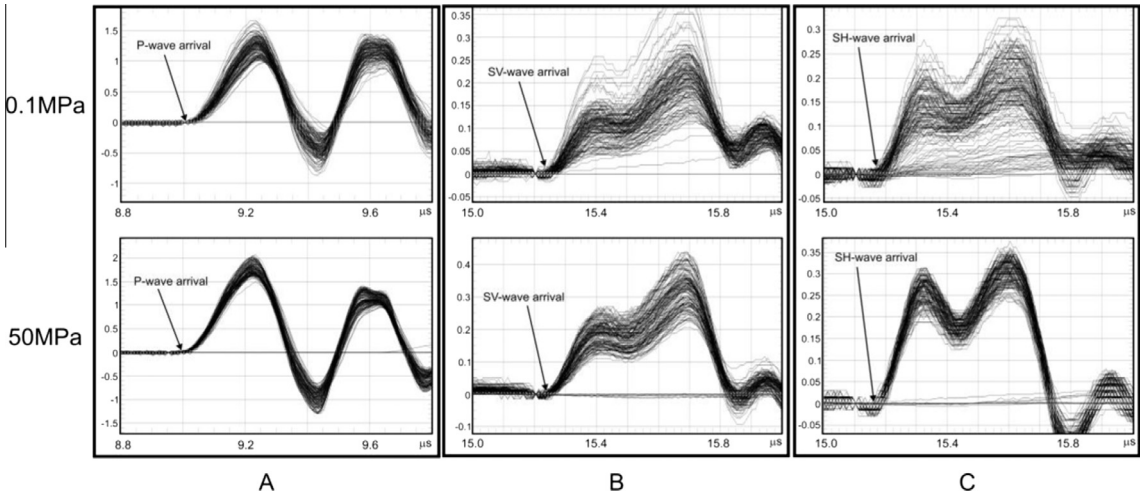

Fig. 2. Glass sample, details of arrival times, upper row – atmospheric pressure 0.1 MPa, lower row – hydrostatic pressure 50 MPa. A – P-wave signal arrival, B – SV-wave signal arrival, SH-wave signal arrival are denoted by arrow.

Table 1
Modal analysis of the quartzite sample.

Minerals	Quartz	Plagioclase	K-feldspar	Biotite	Chlorite
MC (%)	60	15	15	9	1
GS (mm)	0.1	0.1–0.2	To 0.1	0.1–0.2	0.1

MC = mineralogical composition; GS = grain size.

P- and S-wave pulse transmission method, using the transducer configuration shown in Fig. 1A. The samples were measured at 0.1, 10, 20, 30, 40, 50 and 60 MPa. Full waveforms are shown only for the minimum, mean and maximum velocity directions at acting hydrostatic pressure – 0.1 and 60 MPa.

Fig. 3 shows waveforms recorded by the P-wave transducer at 0.1 MPa and 60 MPa. The measuring point of $\lambda = 0°$ is close to the lower arrow and $\lambda = 360°$ is close to the upper arrow of each Φ position denoted by arrowed segments of the line. The same applies to Figs. 3–5. The beginning of the signal at 0 μs is the time of transmitter excitation. Due to the very good quality of first P-wave onset arrival, an automatic algorithm to determine P-wave arrival time can be used. We used the high-order statistic approach [33] to determine the P-wave arrival time. The full line shows the range of P-wave arrival times, i.e. between 11.8 μs and 16.6 μs at 0.1 MPa and between 9.0 μs and 9.8 μs at 60 MPa. We can observe a significant shortening of P-wave arrival time and decreasing time difference between the fastest and slowest first P-wave phase arrival at 60 MPa. Due to the high hydrostatic pressure, the majority of cracks are closed, which results in a decrease of anisotropy and increase in P-wave velocity (shortening of propagation time through the spherical sample in different directions).

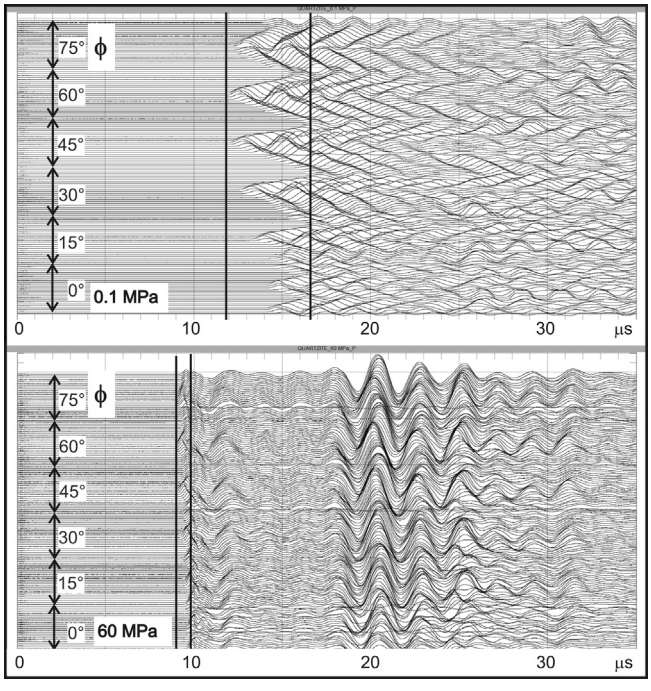

Fig. 3. Quartzite sample: P-wave signals recorded at an atmospheric pressure of 0.1 MPa and hydrostatic pressure of 60 MPa (solid line – P-wave arrival).

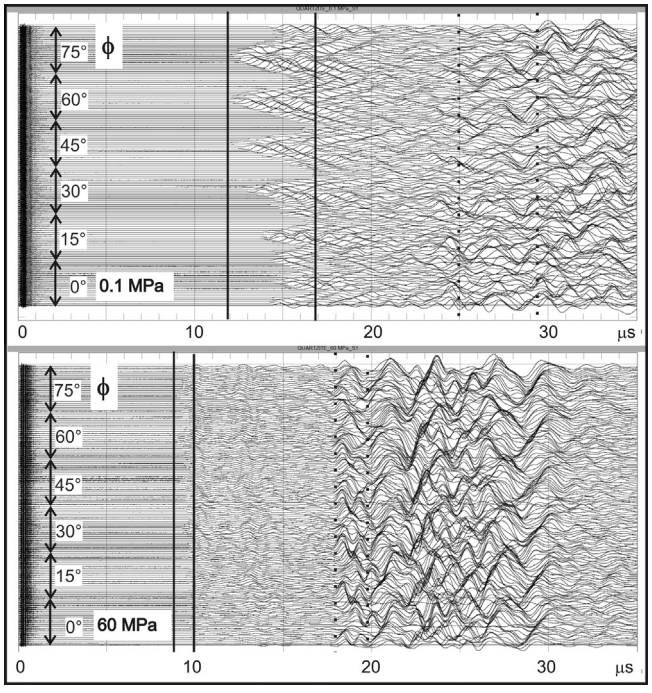

Fig. 4. Quartzite sample: SV-wave signals recorded at an atmospheric pressure of 0.1 MPa and hydrostatic pressure of 60 MPa (solid line – P-wave arrival, dashed line – SV wave arrival).

Please cite this article in press as: T. Lokajíček, T. Svitek, Laboratory measurement of elastic anisotropy on spherical rock samples by longitudinal and transverse sounding under confining pressure, Ultrasonics (2014), http://dx.doi.org/10.1016/j.ultras.2014.08.015

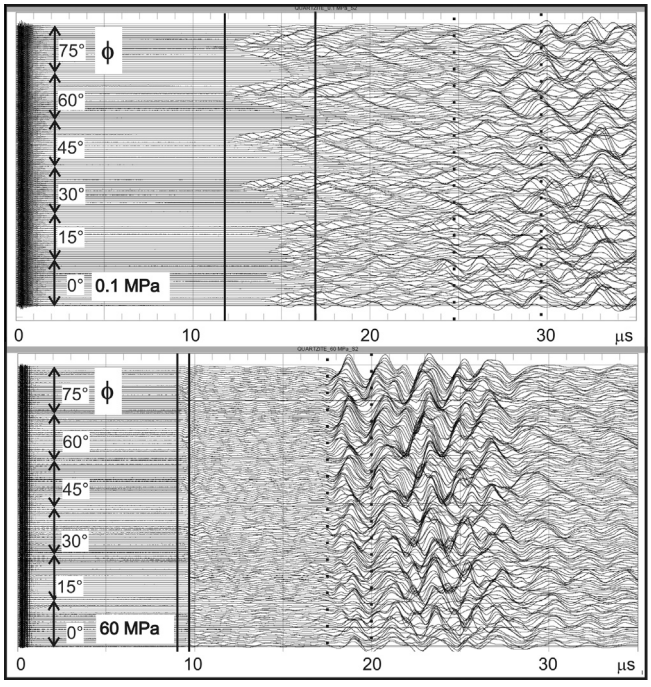

Fig. 5. Quartzite sample: SH-wave signals recorded at an atmospheric pressure of 0.1 MPa and hydrostatic pressure of 60 MPa (solid line – P-wave arrival, dashed line – SH wave arrival).

The anisotropic rock sample with unknown anisotropic symmetry subjected to ultrasonic sounding by a polarized shear wave reflects its inner structure by developing two shear waves with different polarization. These waves are commonly marked as S1 – the fast shear wave component and S2 – the slow shear wave component. Due to the general polarization of the T_V and T_H shear wave transducers, according to the anisotropic symmetry of the quartzite sample, both transducers should detect both components. That is why the following description of S1 and S2 for the fast and slow shear wave components will be used.

Fig. 4 shows waveforms recorded by the R_V receiver. The origin of the signal is again at 0 μs, which coincides with the time of excitation of the T_V transmitter. The two solid lines represent the P-wave arrival, what is a combination of P-wave and shear wave sensor response to compression. In spite of the fact that the shear wave sensor is polarized to record the shear wave component, there will still be "limited" sensitivity of this sensor to the compression wave (this is a feature of piezoceramic material). This P-wave arrival agrees with the arrival time at the pure P-wave transducers. The dashed lines show the arrival times of the S1 and S2 shear-wave components. The shear sensor response is quite pronounced at 60 MPa in the time interval between 18 μs and 30 μs. Due to the more complicated shape of waveforms before shear wave arrival, arrival time is determine manually, based on an operator experience. Very often, a visual correlation is used between waveforms and their shift to shorter arrival times with increasing hydrostatic pressure or vice versa.

Fig. 5 shows waveforms recorded by the T_H/R_H transducers' pair with horizontal polarization of transmitting and recording shear waves. The beginning of the signal is again at 0 μs. The two solid lines again represent the P-wave arrivals at the R_H sensor. The dashed lines show the arrival times of the S1 and S2 shear-wave components at the R_H receiver. The waveforms recorded at 60 MPa show significant attenuation of the P-wave arrival, and shear sensor response is very well pronounced again in the time interval between 18 μs and 30 μs.

Fig. 6 shows 3-D quartzite P-, S1-, S2-wave velocity anisotropy (upper hemisphere projection) at hydrostatic pressures of 0.1 MPa and 60 MPa. Velocity calculation will described in more details in future contributions. At both values of acting hydrostatic pressure we can see P-wave anisotropy with significantly pronounced directions of minimum and maximum velocities. The direction of the maximum velocity at both these values is stable, while the direction of the minimum velocity rotates due to microcracks closure process. At 0.1 MPa symmetry orientation corresponds with the preferred orientation of micro-cracks while at 60 MPa most of the microcracks are already closed, thus symmetry orientation shows effect of aligned mineral grains. From the left-hand image of the 3-D isolines (0.1 MPa) we can determine three basic directions, which are used in rock mechanics studies: X = direction of the maximum velocity (parallel to the lineation within the foliation), Y = direction of the mean velocity (normal to the lineation within the foliation), Z = direction of the minimum velocity (normal to foliation). P and shear wave signals, recorded by the new measuring set up, will only be shown in these selected directions.

Fig. 7 shows the P-wave velocity dependence in the structural directions X (maximum), Y (mean), and Z (minimum) as a function of pressure up to 60 MPa. The main structural directions were determined at an atmospheric pressure of 0.1 MPa. These directions were fixed for all values of hydrostatic pressure. Between 0.1 and 60 MPa we can observe a significant increase of P-wave velocities in all directions. In the maximum velocity direction, the observed velocity increase is 2.1 km/s. On the contrary, in the direction of minimum velocity, a much higher velocity increase of more than 2.9 km/s is observed. This can be explained by the preferred orientation of micro-cracks, which are oriented perpendicular to the minimum velocity direction. This fact is also supported by the partial exponential P-wave velocity/hydrostatic pressure dependence. The black line shows the dependence of the anisotropy strength k of the P-wave velocity. This was calculated using the formula $k\,[\%] = (v_{max} - v_{min})/v_{mean} * 100$ [9]. Anisotropy strength k decreases from 36% at 0.1 MPa to 9% at 60 MPa.

One of the diagnostic phenomenon for determining anisotropy is shear wave splitting when a single shear wave propagating through an anisotropic material splits into two approximately orthogonal polarizations, which travel at different velocities (VS1 fast and VS2 slow) [39]. The following figures show shear waves recorded in three structural directions X, Y and Z, detected by R_V and R_H receivers. Such waveforms are recorded at all of the 132 independent directions.

Fig. 8 shows the waveforms recorded by both pairs of shear-wave transducers with vertical SV and horizontal SH polarization. All signals were recorded in the position of the maximum velocity direction X (red dot in Fig. 6) determined by the P-wave transducers at atmospheric pressure. The left and right columns show the waveforms recorded by the pair of transducers with vertical SV and horizontal SH polarization, respectively.

Waveforms recorded at different values of the confining stress 0.1 (the lowest trace), 10, 20, 30, 40, 50 up to 60 MPa (the uppermost trace) are shown. The time scale ranges from 5 μs to 30 μs. The arrivals of the P-wave can be seen in the time interval between 7 μs and 10 μs. The arrivals of the S1 and S2 shear-wave components occur in the time interval between 16 μs and 25 μs. As the polarization of the T_V/R_V and T_H/R_H transducers does not coincide with the main anisotropy axis, their polarization is not parallel or perpendicular, and that is why we can observe the S1 and S2 arrivals on both the SV and SH waveforms. This fact will help us to determine the individual shear-wave phases with much higher accuracy. Shear-wave arrivals are emphasized by their positive onsets on both SV and SH waveforms.

Fig. 9 shows the SV and SH waveforms recorded in the mean velocity direction – Y (green dot) in Fig. 6.

Please cite this article in press as: T. Lokajíček, T. Svitek, Laboratory measurement of elastic anisotropy on spherical rock samples by longitudinal and transverse sounding under confining pressure, Ultrasonics (2014), http://dx.doi.org/10.1016/j.ultras.2014.08.015

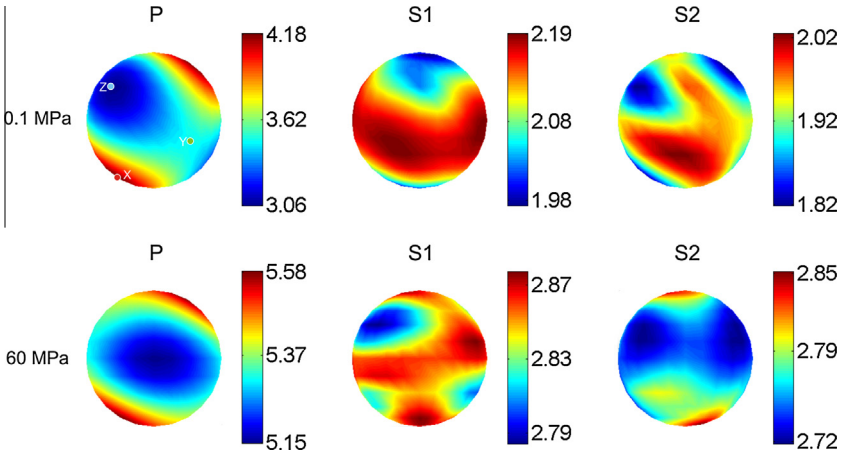

Fig. 6. 3-D P-, S1- and S2-wave velocity anisotropy determined at 0.1 MPa and 60 MPa. The colored velocity scale is in km/s. The red (*X*), green (*Y*) and blue (*Z*) dots denote maximum, mean and minimum velocity direction, respectively. (For interpretation of the references to colour in this figure legend, the reader is referred to the web version of this article.)

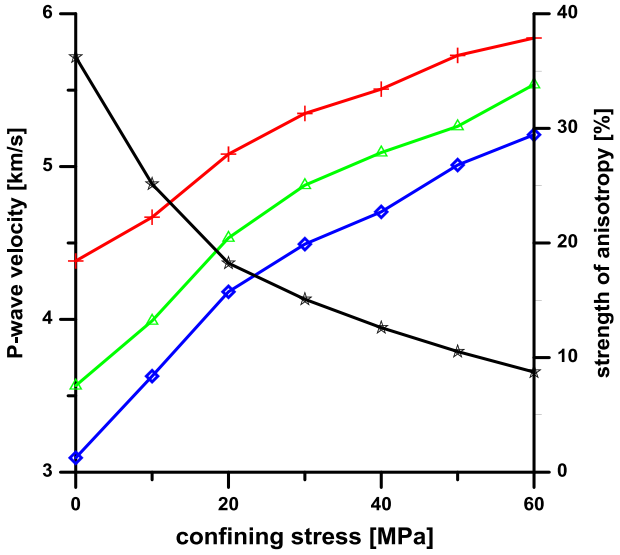

Fig. 7. P-wave velocity dependence at maximum (plus sign, red), mean (triangle, green), minimum (square, blue) velocity directions and strength of anisotropy (asterisk, black). (For interpretation of the references to colour in this figure legend, the reader is referred to the web version of this article.)

Fig. 10 shows the SV and SH waveforms recorded in the minimum velocity direction – *Z* (blue dot) in Fig. 6. All readings of shear wave arrivals cannot be done automatically. The S1 wave component is quite easy to read, as the operator will assign the first significant arrival within the expected range of shear wave arrival time (V_P/V_S = 1.5–2). The S2 wave arrival is much more complicated to determine. Reading this time requires operator skill and some knowledge of the material under study. Better discrimination and determination of S1 and S2 arrivals should be a topic of future investigation. In this regard, more sophisticated methods may be helpful such as particle motion, full waveforms analysis or analysis of polarization vectors of shear wave components calculated by means of elastic stiffness tensor.

Fig. 11 shows the S-wave velocities manually determined in structural directions *X*, *Y*, and *Z* as a function of pressure up to 60 MPa. The S1 and S2 wave arrivals recorded in the three basic directions in the spherical sample *X*, *Y* and *Z* are shown. The plus (+) sign marks the arrival times of the S1 wave component. The triangle marks the arrival times of the S2 wave component.

Fig. 11 shows that shear wave splitting can be observed in all selected structural directions. This can be explained by the fact that at atmospheric pressure, not only crack-preferred orientation, but also lattice (LPO) and shape-preferred orientation (SPO) contribute to quartzite – KVC anisotropy symmetry.

Figs. 4 and 5 indicate, and by comparison with Figs. 8–10 one can see, that the recorded SV and SH shear waveforms display very clear shear-wave arrivals in nearly all directions of the sphere.

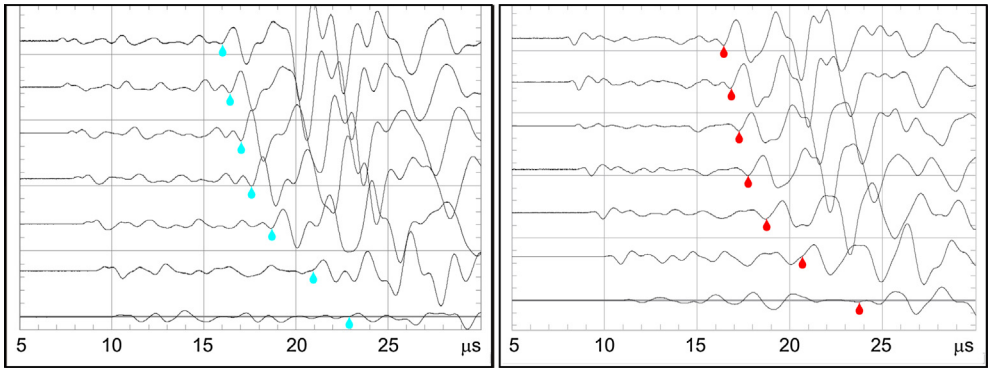

Fig. 8. Maximum velocity direction. Left column – SV signals recorded by the T_V/R_V shear-wave sensors, blue marks denote S-wave arrival. Right column – SH signals recorded by the T_H/R_H shear-wave transducer, red marks denote S-wave arrival. (For interpretation of the references to colour in this figure legend, the reader is referred to the web version of this article.)

Please cite this article in press as: T. Lokajíček, T. Svitek, Laboratory measurement of elastic anisotropy on spherical rock samples by longitudinal and transverse sounding under confining pressure, Ultrasonics (2014), http://dx.doi.org/10.1016/j.ultras.2014.08.015

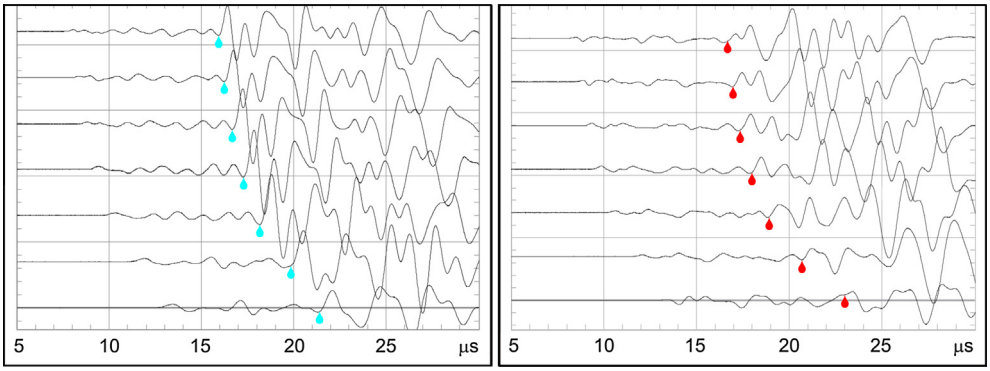

Fig. 9. Mean velocity direction. Left column – SV signals recorded by the T_V/R_V shear-wave sensors, blue marks denote S-wave arrival. Right column – SH signals recorded by the T_H/R_H shear-wave transducers, red marks denote S-wave arrival. (For interpretation of the references to colour in this figure legend, the reader is referred to the web version of this article.)

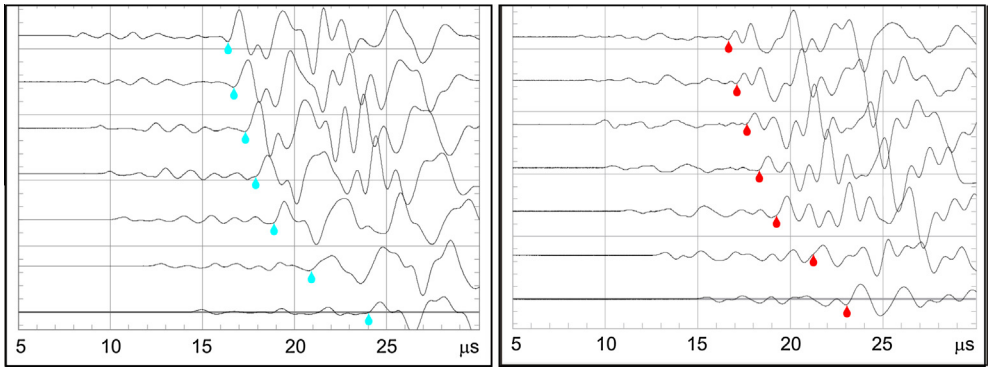

Fig. 10. Minimum velocity direction. Left column – SV signals recorded by the T_V/R_V shear-wave sensor, blue marks denote S-wave arrival. Right column – SH signals recorded by the T_H/R_H shear-wave transducer, red marks denote S-wave arrival. (For interpretation of the references to colour in this figure legend, the reader is referred to the web version of this article.)

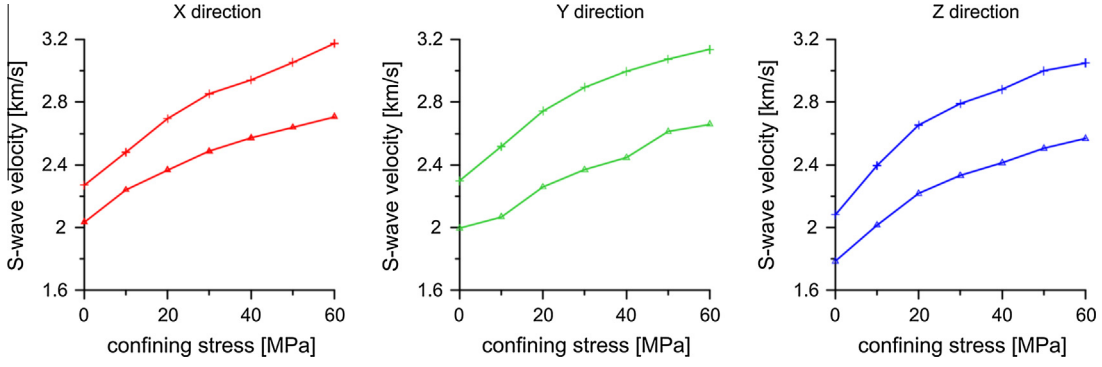

Fig. 11. S1 and S2 velocity dependencies at maximum *X*, mean *Y* and minimum *Z* directions of P-wave velocity surface.

5. Discussion

The scope of his paper was to show technological solution and calibration of multidirectional ultrasonic sounding of spherical rock samples by means of longitudinal and transversal piezoceramic sensors with sliding contact. 3D of P-, S1-, S2-wave velocities are shown as an example. P-arrivals are determined automatically by means of HOS method [40]. On the contrary S1 and S2 time arrivals has to be determined manually, as till now does not exists any automatic procedure for shear wave arrival determination on ultrasonic signals. Very important is existence of two mutually polarized SV and SH waves, what significantly helps for accurate/reliable S1 and S2 wave arrival determination. Reading error of shear wave components is influenced by many parameters, like rock grain size, material heterogeneity, strength of anisotropy, crack size and distribution, spherical shape of the sample and point sensors contact. Multidirectional recording of longitudinal and shear waves evoked many tasks, which have to be solved to correctly determine P, S1 and S2 arrivals and obtain accurate data. These problems included: determination of whether phase or group arrivals are being recorded; ratio between ultrasonic wave length and rock sample inhomogeneity; influence of spherical shape and quasi-point contact on the full waveform; ratio of the diameter of the contact areas of the sensors to the predominant wave length of the signal; proper reading of S1 and S2 arrivals, mainly in directions where possible triplication can be observed;

Please cite this article in press as: T. Lokajíček, T. Svitek, Laboratory measurement of elastic anisotropy on spherical rock samples by longitudinal and transverse sounding under confining pressure, Ultrasonics (2014), http://dx.doi.org/10.1016/j.ultras.2014.08.015

S1 and S2 wave polarization in different directions; manner in which anisotropy strength and its symmetry influence recorded waveforms; number of directions needed to calculate full stiffness tensor properly; whether knowledge of only P and S1 arrivals are sufficient for full tensor calculation; accuracy of retrieved data; mutual orientation of transducers and material structure and structure inhomogeneity itself, etc.

6. Summary

The high-pressure head enhanced by two pairs of perpendicularly oriented shear-wave transducers is very suitable for investigating the contribution of oriented micro-cracks, lattice (LPO) and shape-preferred orientation (SPO) to the bulk elastic anisotropy of rocks of strong anisotropy. All velocity/pressure relations display the well-known initial high-velocity increase with confining pressure. The non-linear rise is due to the progressive closure of micro-cracks, which indicates the pressure sensitivity of P- and S-waves. The contribution of intercrystalline and intracrystalline cracks could also be studied. Such a study could be carried out with the current system under acting hydrostatic pressures between 0.1 and 60 MPa, since most low-aspect ratio cracks close at the high end of this range.

The measuring system has some limitations: This approach is not suitable for measurements above room temperature due to the higher acting temperature; the viscosity of the contact layer will be lower and will not transfer the shear-wave component. Due to the T_P/R_P, T_V/R_V and T_H/R_H transducers pairs being spaced at 15 degrees, the proposed measuring system is suitable for 15-degree measuring nets. At lower values of confining stress, the error in amplitude determination would be higher.

The shear-wave splitting data shown in Fig. 11 proves that the new technical solution will be a suitable tool for enhanced elastic anisotropy studies of rocks subjected to hydrostatic pressure.

A wide range of unique laboratory data of P-, S1- and S2-wave velocities in rocks in up to 132 independent directions shows that the new measuring set up can provide a very important input data for determining full elastic tensor at different values of acting hydrostatic stress. The knowledge of elastic tensor also enables common dynamic modulus derivation including their changes with pressure, as well as the investigation of their differences between drained and saturated rocks and the dependence of the above mentioned parameters on hydrostatic pressure.

By this approach we have sufficient data, inverse iteration process is well over determined, what enables to determine all 21 independent stiffness components for any rock material. Advantage of proposed method is that it does not need any *a priori* assumptions regarding the symmetry class or the orientation of the symmetry axes of rock samples under the study.

Acknowledgements

This work was partially supported by the Grant Agency of the Czech Republic, Project No. MŠMT Kontakt II – LH13102, GA CR P104/12/0915, 13-13967S and by the long-term research development project of the Institute of Geology of the AS CR v.v.i. – RVO67985831. The authors thanks to anonymous reviewers, as their comments significantly improved the quality of the manuscript. Also very appreciated was the help of Mr. V. Filler in constructing the new measuring head, producing the majority of mechanical parts and carrying out the proposed measurements.

References

[1] N.I. Christensen, Elasticity of ultrabasic rocks, J. Geophys. Res. 71 (1966) 5921–5931.
[2] S.E. Tilmann, H.F. Bennett, Ultrasonic shear wave birefringence as a test of homogeneous elastic anisotropy, J. Geophys. Res. 78 (1973) 7623–7629, http://dx.doi.org/10.1029/JB078i032p07623.
[3] V. Babuska, M. Cara, Seismic Anisotropy in the Earth, Kluwer Academic, Dordrecht, 1991.
[4] W.H. Owens, D. Bamford, Magnetic, seismic and other anisotropic properties of rock fabrics, Phil. Trans. R. Soc. Lond., A. 283 (1976) 55–68.
[5] M. Petružálek, J. Vilhelm, T. Lokajíček, V. Rudajev, Assesment of P-wave anisotropy by means of velocity ellipsoid, Acta Geodyn. Geomater. 4 (2007) 23–31.
[6] K.W. Winkler, T.J. Plona, Technique for measuring ultrasonic velocity and attenuation spectra in rocks under pressure, J. Geophys. Res. 87 (1982) 10776, http://dx.doi.org/10.1029/JB087iB13p10776.
[7] A.N. Nikitin, T.I. Ivankina, Neutron Diffractometry Geosci. 35 (2004).
[8] D. Mainprice, A FORTRAN program to calculate seismic anisotropy from the lattice preferred orientation of minerals, Comput. Geosci. 16 (1990) 385–393, http://dx.doi.org/10.1016/0098-3004(90)90072-2.
[9] F. Birch, The velocity of compressional waves in rocks to 10 kbar. Part 2, J. Geophys. Res. 66 (1961).
[10] H. Kern, P- and S-wave velocities in crustal and mantle rocks under the simultaneous action of high confining pressure and high temperature and the effect of the rock microstructure, in: W. Schreyer (Ed.), High-Pressure Res. Geosci., Schreizerbart'tsche Verlagsbuchhandlung, Stuttgart, 1982, pp. 15–45.
[11] M.H.B. Nasseri, A. Schubnel, R.P. Young, Coupled evolutions of fracture toughness and elastic wave velocities at high crack density in thermally treated Westerly granite, Int. J. Rock Mech. Min. Sci. 44 (2007) 601–616, http://dx.doi.org/10.1016/j.ijrmms.2006.09.008.
[12] O. Sano, Y. Kudo, Y. Mizuta, Experimental determination of elastic constants of Oshima granite, Barre granite, and Chelmsford granite, J. Geophys. Res. 97 (1992) 3367, http://dx.doi.org/10.1029/91JB02934.
[13] T. Takemura, Changes in crack density and wave velocity in association with crack growth in triaxial tests of Inada granite, J. Geophys. Res. 110 (2005) B05401, http://dx.doi.org/10.1029/2004JB003395.
[14] Y. Nara, H. Kato, T. Yoneda, K. Kaneko, Determination of three-dimensional microcrack distribution and principal axes for granite using a polyhedral specimen, Int. J. Rock Mech. Min. Sci. 48 (2011) 316–335, http://dx.doi.org/10.1016/j.ijrmms.2010.08.009.
[15] R.J. Arts, P.N.J. Rasolofosaon, B.E. Zinszner, Experimental Determination of the Complete Anisotropic Viscoelastic Tensor In Rocks, 1992 SEG Annu. Meet, 1992.
[16] R.J. Arts, A Study of General Anisotropic Elasticity in Rocks by Wave Propagation: Theoretical and Experimental Aspects, 1993.
[17] P.M. Douglass, B. Voight, Anisotropy of granites: a reflection of microscopic fabric, Géotechnique 19 (1969) 376–398, http://dx.doi.org/10.1680/geot.1969.19.3.376.
[18] M.H.B. Nasseri, A. Schubnel, P.M. Benson, R.P. Young, Common evolution of mechanical and transport properties in Thermally cracked Westerly Granite at elevated hydrostatic pressure, Pure Appl. Geophys. 166 (2009) 927–948, http://dx.doi.org/10.1007/s00024-009-0485-2.
[19] S. Stanchits, S. Vinciguerra, G. Dresen, Ultrasonic velocities, acoustic emission characteristics and crack damage of basalt and granite, Pure Appl. Geophys. 163 (2006) 975–994, http://dx.doi.org/10.1007/s00024-006-0059-5.
[20] M. Petružálek, J. Vilhelm, V. Rudajev, T. Lokajíček, T. Svitek, Determination of the anisotropy of elastic waves monitored by a sparse sensor network, Int. J. Rock Mech. Min. Sci. 60 (2013) 208–216, http://dx.doi.org/10.1016/j.ijrmms.2012.12.020.
[21] Z. Pros, V. Babuška, A method for investigating the elastic anisotropy on spherical rock samples, Zeitschrift Fur Geophys. 33 (1967) 289–291.
[22] Z. Pros, V. Babuška, An apparatus for investigating the elastic anisotropy on spherical samples, Stud. Geophys. Geod. 12 (1968) 192–198.
[23] R.J. Arts, P.N.J. Rosolofosaon, B.E. Zinszner, Experimental and theoretical tools for characterizing anisotropy due to mechanical defects in rocks and varying pore and confining pressure, in: E. Fjær, F. Rune, J.S. Holt (Eds.), Seism. Anisotropy, Soc. explor. Geophys, Tulsa, 1996, pp. 384–432.
[24] Z. Pros, T. Lokajíček, K. Klíma, Laboratory approach to the study of elastic anisotropy on rock samples, Pure Appl. Geophys. 151 (1998) 619–629, http://dx.doi.org/10.1007/s000240050133.
[25] D. Nadri, A. Bóna, M. Brajanovski, T. Lokajíček, Estimation of stress-dependent anisotropy from P-wave measurements on a spherical sample, Geophys. 76 (2011) WA91–WA100, http://dx.doi.org/10.1190/1.3552703.
[26] A. Bóna, D. Nadri, M. Brajanovski, Thomsen's parameters from p-wave measurements in a spherical sample‡, Geophys. Prospect. 60 (2012) 103–116, http://dx.doi.org/10.1111/j.1365-2478.2010.00917.x.
[27] R. Přikryl, T. Lokajíček, Z. Pros, K. Klíma, Fabric symmetry of low anisotropic rocks inferred from ultrasonic sounding: implications for the geomechanical models, Tectonophysics 431 (2007) 83–96, http://dx.doi.org/10.1016/j.tecto.2006.05.031.
[28] M. Martinkova, Z. Pros, K. Klima, T. Lokajicek, J. Kotkova, Experimentally determined P-wave velocity anisotropy for rocks related to the Western Bohemia seismoactive region, Stud. Geophys. Geod. 44 (2000) 581–589, http://dx.doi.org/10.1023/A:1021871819408.
[29] N.I. Christensen, W.D. Mooney, Seismic velocity structure and composition of the continental crust: a global view, J. Geophys. Res. 100 (1995) 9761, http://dx.doi.org/10.1029/95JB00259.
[30] K. Ito, Y. Tatsumi, Measurement of elastic wave velocities in granulite and amphibolite having identical H_2O-free bulk compositions up to 850 °C at

Please cite this article in press as: T. Lokajíček, T. Svitek, Laboratory measurement of elastic anisotropy on spherical rock samples by longitudinal and transverse sounding under confining pressure, Ultrasonics (2014), http://dx.doi.org/10.1016/j.ultras.2014.08.015

1 GPa, Earth Planet. Sci. Lett. 133 (1995) 255–264, http://dx.doi.org/10.1016/0012-821X(95)00074-M.

[31] H. Kern, B. Liu, T. Popp, Relationship between anisotropy of P and S wave velocities and anisotropy of attenuation in serpentinite and amphibolite, J. Geophys. Res. 102 (1997) 3051, http://dx.doi.org/10.1029/96JB03392.

[32] Y. Kono, M. Ishikawa, M. Arima, Laboratory measurements of P- and S-wave velocities in polycrystalline plagioclase and gabbronorite up to 700 & #xB0; C and 1 GPa: implications for the low velocity anomaly in the lower crust, Geophys. Res. Lett. 33 (2006) L15314, http://dx.doi.org/10.1029/2006GL026526.

[33] S. Nishimoto, M. Ishikawa, M. Arima, T. Yoshida, J. Nakajima, Simultaneous high *P–T* measurements of ultrasonic compressional and shear wave velocities in Ichino-megata mafic xenoliths: their bearings on seismic velocity perturbations in lower crust of northeast Japan arc, J. Geophys. Res. 113 (2008) B12212, http://dx.doi.org/10.1029/2008JB005587.

[34] H. Kern, K. Mengel, K.W. Strauss, T.I. Ivankina, A.N. Nikitin, I.T. Kukkonen, Elastic wave velocities, chemistry and modal mineralogy of crustal rocks sampled by the Outokumpu scientific drill hole: evidence from lab measurements and modeling, Phys. Earth Planet. Inter. 175 (2009) 151–166, http://dx.doi.org/10.1016/j.pepi.2009.03.009.

[35] A. Migliori, J.L. Sarrao, W.M. Visscher, T.M. Bell, M. Lei, Z. Fisk, et al., Resonant ultrasound spectroscopic techniques for measurement of the elastic moduli of solids, Phys. B Condens. Matter 183 (1993) 1–24, http://dx.doi.org/10.1016/0921-4526(93)90048-B.

[36] G. Kaplan, T.W. Darling, K.R. McCall, Resonant ultrasound spectroscopy and homogeneity in polycrystals, Ultrasonics 49 (2009) 139–142, http://dx.doi.org/10.1016/j.ultras.2008.08.001.

[37] T. Watanabe, Y. Shirasugi, K. Michibayashi, A new method for calculating seismic velocities in rocks containing strongly dimensionally anisotropic mineral grains and its application to antigorite-bearing serpentinite mylonites, Earth Planet. Sci. Lett. 391 (2014) 24–35, http://dx.doi.org/10.1016/j.epsl.2014.01.025.

[38] M. Hoerbe, Final Report of Geological Research: Calculation of Aggregate Resources in Těchobuz Quarry Near Pacov, Report No. FZ006900 2005 (in Czech), 2005.

[39] S. Crampin, Geological and industrial implications of extensive-dilatancy anisotropy, Nature 328 (1987) 491–496, http://dx.doi.org/10.1038/328491a0.

[40] T. Lokajíček, K. Klíma, A first arrival identification system of acoustic emission (AE) signals by means of a high-order statistics approach, Meas. Sci. Technol. 17 (2006) 2461–2466, http://dx.doi.org/10.1088/0957-0233/17/9/013.

Please cite this article in press as: T. Lokajíček, T. Svitek, Laboratory measurement of elastic anisotropy on spherical rock samples by longitudinal and transverse sounding under confining pressure, Ultrasonics (2014), http://dx.doi.org/10.1016/j.ultras.2014.08.015

Príloha 3

Publikácia 2:

Svitek, T., Rudajev, V., & Petružalek, M. (2010). **Determination of P–wave arrival time of acoustic events**. *Acta Montan. Slov.*, 15(2), 145–151.

Determination of P – wave arrival time of acoustic events

Tomáš Svitek[1], Vladimír Rudajev[2] and Matěj Petružálek[3]

The new approach to the P-wave arrival time determination based on acoustic emission data from loading experiments is tested. The algorithm used in this paper is built on the STA/LTA function computed by a convolution that speeds up the computation process very much. The picking process makes use of shifting of temporary onset until certain conditions are fulfill and as a main decision criterion on the threshold exceeding of the STA/LTA derivation function is used. The P-wave onset time is determined in a selected interval that corresponds to the theoretical propagation of elastic wave in the rock sample. Results obtained by our algorithm were correlated with data acquired manually and a high order statistic software as well.

Key words: *Onset detection, Automatic picker, Acoustic emission, Loading experiments, STA/LTA*

Introduction

The evaluation of stability of underground engineering structures is one of significant tasks of geomechanics. For the development and verification of effective methods of assessing the deformation characteristics, it is advisable to carry out their research under laboratory conditions, which enable us to simulate the process of stress state growth up to the level of their own strength. As to the rocks, representing a heterogeneous discontinuous medium with primary cracks and places of different mechanical strength, the distribution of the stress field is inhomogeneous with higher local values especially in the vicinity of so-called "stress concentrators". During the loading of rock specimens, the local strength will be exceeded in these places and brittle ruptures will be created, which leads to the elastic wave emission. These points of brittle ruptures are sources (foci) of elastic wave radiation ranging from acoustic to ultrasonic frequencies. Events like these are referred to as the "acoustic emission" (AE). The observation of the acoustic emission process is based on the monitoring via a geophone net, located on the surface of the studied rock specimen. The location of acoustic foci and the monitoring of their migration during loading until a final destruction of the rock specimen provides a significant information about foci clustering within the areas of predisposed places of future final rupture. Acoustic emissions and the location of their foci was studied by Lockner (1993), Lockner and Byerlee (1977), Vilhelm et al. (2008), Veverka J., Rudajev V. (2004). The accuracy of the location depends on the knowledge of the velocity model as well as on the accuracy of determining the P – wave onset time. Therefore, the accuracy of determining the time of the onset is very important and often poses a difficult problem.

This paper is concerned with the determination of the time of the first arrivals of P – waves important for localizing acoustic events occurring during the rock specimens loading. This topic is also involved in many publications, based on different principles. The methods most frequently used for the P – wave time determination are, for example: the STA/LTA ratio (short-term average/long-term average) by Allen, R. (1982), Baer, M., Kradolfer, U. (1987), SNR (signal-to-noise ratio) by Zuolin Chen (2005), HOS (high - order statistics) by Lokajicek, T., Klima, K. (2006), and the AIC criterion (Akaike Information Criterion) by Sedlak et al. (2009).

Background of the Pick – Tester (PT) Method

In general, it always stands good that signal is transformed to a characteristic function (CF) which creates the signal envelope. The time of the first arrival is then determined on this envelope by using specified criteria.

The procedure presented in this paper is based on the STA/LTA principle (Allen, 1982). The characteristic function is computed using the following equation

[1] *Mgr. Tomáš Svitek*, Charles University in Prague, Faculty of Science, Albertov 6, 128 43 Praha 2 also Institute of Geology Academy of Sciences of the Czech Republic, v.v.i., Rozvojová 269, 165 00 Praha 6 - Lysolaje, Czech Republic, svitek@gli.cas.cz

[2] *RNDr. Vladimír Rudajev DrSc.*, Institute of Geology Academy of Sciences of the Czech Republic, v.v.i., Rozvojová 269, 165 00 Praha 6 - Lysolaje, Czech Republic

[3] *Mgr. Matěj Petružálek*, Charles University in Prague, Faculty of Science, Albertov 6, 128 43 Praha 2 also Institute of Geology Academy of Sciences of the Czech Republic, v.v.i., Rozvojová 269, 165 00 Praha 6 - Lysolaje, Czech Republic

(Review and revised version 20. 10. 2010)

$$CF(i) = y(i)^2 + K\left(y(i) - y(i-1)\right)^2$$

where y is the input signal and the second part of the equation is its derivative. K is the weight constant, which reflects the sampling frequency and the noise characteristic of the seismic receiver,

$$K(i) = \frac{\sum_{i=1}^{n} |y(i)|}{\sum_{i=1}^{n} |y(i) - y(i-1)|} \quad ,$$

where *n* is the number of signal samples. The STA/LTA ratio was chosen as the detector. It is the average of the CF amplitude in the short- (long-) time window. The calculation of the real STA and LTA values then yields an average of the values of the characteristic function in a time window of a certain length. These windows have shifted subsequently along the characteristic function. For this operation, it is necessary to use cyclic algorithms repeated depending on the quantity of the data (number of traces), when the first arrival time is determined. All algorithms were realized in the Matlab software. Therefore, this software is not optimized for using cyclic operations; the convolution was used for computing the STA and LTA functions.

The convolution is defined by the equation $y(t) = \int_{-\infty}^{\infty} s_1(t-\tau)s_2(\tau)d\tau$ and is noted as $y(t) = s_1(t) * s_2(t)$, where s_1 is the rectangular signal with the length STA or LTA and s_2 is the acoustic (ultrasonic) signal. The signal s_2 is a discrete series of numbers and the convolution equation can then be expressed in the following form; $y(k) = \sum_j s_1(k-j)s_2(j)$; $k - j > 0$. Replacing the cyclic algorithms by the convolution accelerates the calculation. Consequently, the criteria for determining the times of the first arrivals enter the computation process. Figure 1 shows a simplified block diagram of particular steps of this process.

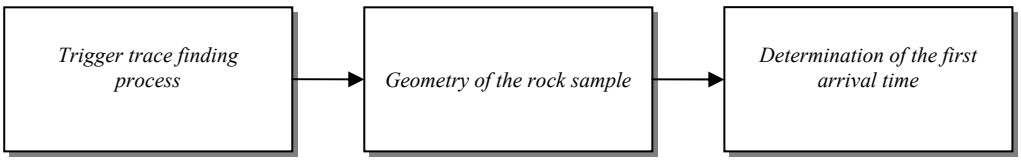

Fig. 1. Block diagram of the arrival time assessment.

During our loading experiments, the acoustic emission data were recorded by an 8-channel piezoceramic system. For this reason, the first step of the computation process is to find the trace on which the acoustic event was first registered. Based on this fact, it is possible to apply considerations of rock specimen geometry and then to determine the P–wave time arrival. The whole process is based on the values and shape of the STA/LTA ratio function, whereas the length of the LTA window is 100 points (10 μs) and the length of the STA window is 10 points (1 μs).

In the following, the criteria of determining the arrival time will be described in a more detail.

Step 1 – STA/LTA level determination

The first step is the dynamical determination of the STA/LTA level. When this level is exceeded, the raw arrival time is assessed. For this purpose the median of the maxima of all eight traces is computed. The STA/LTA level is then established as 15 % of the median value. Two extreme cases can occur:

Strong event – The STA/LTA level is higher than the smallest maximum of any STA/LTA function. In this case the decision level is established as the smallest value of maxima of the STA/LTA function.

Weak event – The STA/LTA level of 15 % of the median is not high enough so that the decision level is established by a predefined empirical value.

The value of the level then reflects the magnitude of the registered AE event.

Step 2 – STA/LTA derivation and its peaks

In this step, the STA/LTA function is derived (hereinafter called "Derivation") and its maximum is determined again. Consequently, the level of the Derivation is determined for every trace. In this case, the decision level is established as 1/3 of the Derivation maximum.

Step 3 – P – wave pick allocated to the main or local maximum of Derivation

Points whose amplitudes of the STA/LTA and Derivation functions exceed their levels determine the peaks which indicate a certain increase of the signal.

Next in the process, only the peaks of the Derivation whose maxima are higher than or equal to a half of the main maximum are considered. According to the number of peaks which satisfy this criterion, the following cases can be identified:

a. Only one peak found; raw P – wave pick is placed to the point of Derivation maximum,
b. More than one peak found and at once STA/LTA ratio in the place of the local maximum of previous peak is higher or equal to STA/LTA level and at once distance between last two peaks is shorter than 100 samples (10 μs); raw P – wave pick is placed to the point of the local Derivation maximum of the previous peak (Fig. 2c),
c. None of the previous cases applies; raw P – wave pick is placed to the point of the main Derivation maximum.

Using this procedure we assessed the raw P – wave picks, which are placed to a certain Derivative maximum.

Step 4 – Trigger trace determination

All these steps (Steps 1 – 3) lead up to the best possible determination of the trace, where the signal was recorded as the first, so-called, trigger trace. Once the trigger trace is known, the parameters of the specimen geometry can be applied in the computation.

Step 5 – Determination of the theoretical signal propagation time in the rock specimen

With a view to the mutual distance of sensors, we can compute the theoretical propagation time of elastic waves in the rock specimen and determine the travel-time limits, in which the signal has to reach the sensor. Using the 8-channel system, we obtain 28 mutual sensor distances from the following equation:

$$r_{ij} = \sqrt{(x_i - x_j)^2 + (y_i - y_j)^2 + (z_i - z_j)^2} \quad , i = j = 1 \ldots 8,\ i \neq j,$$

We then compute the theoretical time of propagation from the reference (trigger) sensor (S_R) to the other sensors (S_i) using the equation $t_{S_R S_k} = \frac{r_{Ri}}{v}$, $i=1, 2,\ldots 7,$ where $t_{SRSK} = t_{SR} - t_{SK}$ and v is the P – wave velocity in the rock specimen. This formula is, in general, valid in an isotropic medium. Hence, since most rocks are more or less anisotropic, the previous formula needs to be modified with respect to the real value of rock anisotropy. The problem of anisotropy is discussed in more detail for example in Petružálek et al. 2007. With regard to the anisotropy, we can express the previous equation in the following form:

$$t_{S_R S_k} = \frac{r_{Ri}}{v} P$$

where P is the parameter of the anisotropic velocity ellipsoid represented by a 3 x 3 matrix of semi-axis vectors of this ellipsoid. We thus obtain the theoretical propagation times for every sensor and can determine the time interval (Fig. 2c - red part of STA/LTA) on every trace, for which the relation $t_{S_k} < \left(t_{S_R S_k} + t_{S_R}\right) \cdot 1{,}2$, where t_{Sk} is the time measured at the *k-th* sensor and t_{SR} is the arrival time at the reference sensor, is valid. The lower value of the time interval is limited by the arrival time on the trigger trace. The real time of the signal has to be looked for in the interval defined by these rules. Of course, we need to know the velocity model of the specimen under examination perfectly. This model is obtained from the ultrasound radiation. During the loading, the parameters of the velocity model can vary; hence the coefficient 1.2 was applied in the previous relation. This coefficient was determined empirically.

Step 6 – Possible pick shift

In this part of the algorithm, the shape of the STA/LTA function will be analyzed and the pick can be possibly shifted to the previous peak. This step is applied in situations when the signal is rising very slightly. If this situation occurs, it is possible that the main Derivation maximum is not at the first peak but on any following peak of STA/LTA. If any peak of STA/LTA exists before the point of the Derivation maximum, and the mutual distance of these two peaks is less than 25 samples (2.5 μs), it is recognized by the procedure in this step and the pick is shifted to the previous STA/LTA peak (Fig. 2c). Repeating of this shifting procedure depends on the number of relevant STA/LTA peaks.

Steps 7 – Final pick determination

In the last step, we analyze the shape of the real signal in the vicinity of the temporary raw pick and, if necessary, the pick is again shifted to one of the characteristic points of the signal (maximum, minimum or plateau) and the final P – wave arrival time is determined.

Figure 2 shows the individual steps of the algorithm mentioned above for a better understanding.

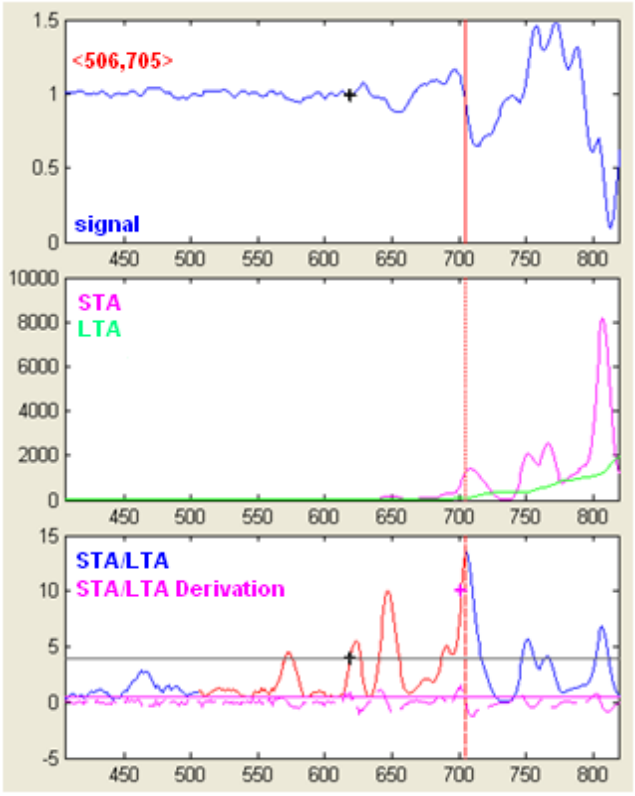

Fig. 2 Procedure explanation (A – recorded signal, B – STA and LTA functions, C – STA/LTA and its Derivation; x-axis units [samples]

- Grey horizontal line – STA/LTA level calculated according to the Step 1 (Fig. 2c)
- Purple horizontal line - Derivation level calculated according to the Step 2 (Fig. 2c)
- According to the Derivation function we find the raw P – wave pick whereas we assume that the arrival time does not occur after the main Derivation maximum (purple cross) calculated according to the Step 3 (Fig. 2c).
- Red part of STA/LTA calculated according to the Step 5 (Fig. 2c)
- The figure indicates that the Derivation maximum (purple cross) is the incorrect determination of the arrival time. For this reason, the shape of the STA/LTA function is analyzed (Step 6). This function has larger peaks in comparison with the Derivation function. As peaks of the STA/LTA function, we consider only peaks whose amplitudes are higher than the estimated STA/LTA level (grey line). If the distance between two neighboring peaks is less than 25 samples (2,5 μs), the P – wave pick shifts to the place where the previous peak crosses the STA/LTA level;
- Black cross calculated according to the Step 7

Results and discussion

The algorithm of Pick-Tester (PT) program is tested on a data file, obtained during the loading of a migmatite rock specimen. The 950 AE events (7600 traces) were chosen from the data recorded during this experiment. The P- wave arrival times were manually picked from these traces. These data served as a model data file to develop the algorithm for the automated arrival time determination in the PT program.

The P – wave arrival time difference is the main criterion for the resultant evaluation. The quality of the picks will be evaluated by comparing the times manually determined by a human operator. We assume these picks to be correct. Another criterion is a comparison with times obtained using the HOS method (Lokajíček, Klíma, 2006). The correctness of the picks determination is reflected in the location residuum of the individual AE events.

In the following figure 3, one can see a general view of the user interface of the Pick-Tester program. This figure shows the comparison of P – wave arrival times determined by different methods. In the main graph (left side), there are 8 records of one AE event. The manual pick on each signal is marked in the red color, the HOS pick in blue and the PT pick in black. The green cross indicates the trigger trace. The right-hand side of the figure shows a detail of the selected trace (upper graph), its STA and LTA functions (middle graph) and the STA/LTA function with its Derivation function (bottom graph). In the upper part of the interface are situated control buttons which can be used to set the length of the STA and LTA windows and allow the movement in the data sets.

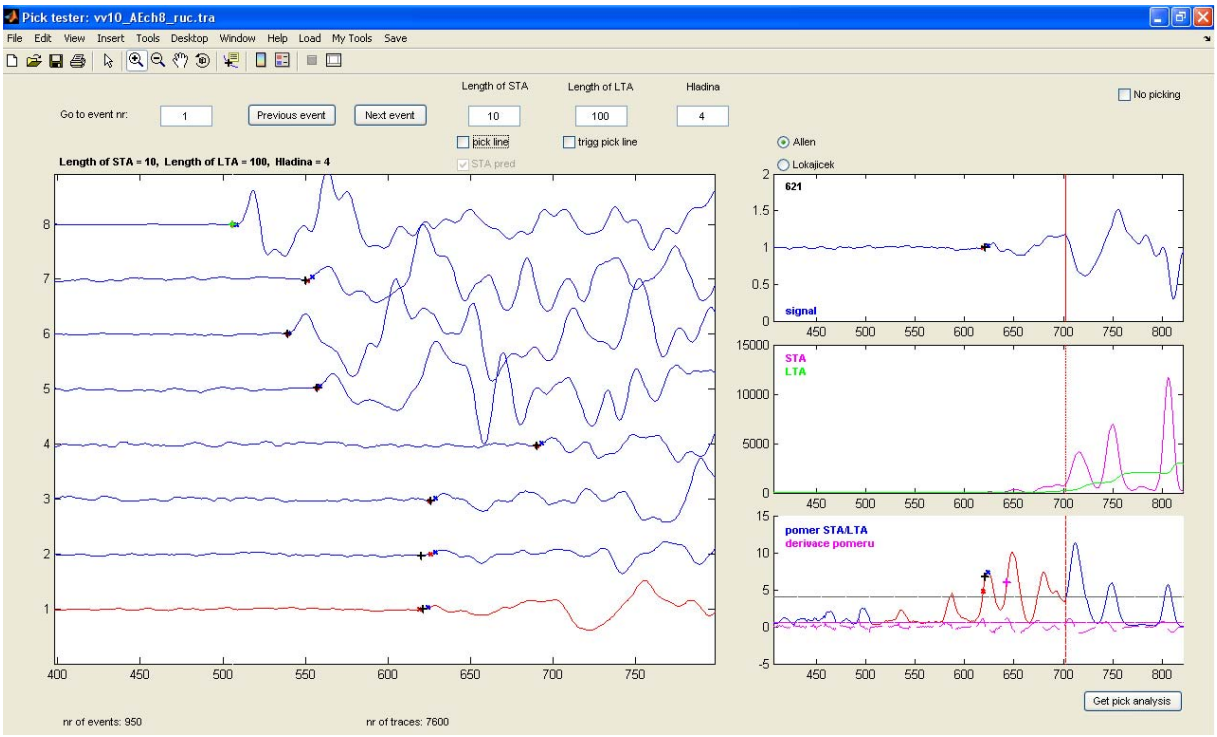

Fig. 3. Preview of picking program Pick-tester.

Figure 4 shows the results of the whole data set (950 AE events ~ 7600 traces). Histograms in this figure represent the absolute value of the arrival time difference determined manually, by the HOS software and by the PT program. The measure of the "x" axis is in the samples; 1 sample ~ 0.1 μs (sampling frequency 10 MHz).

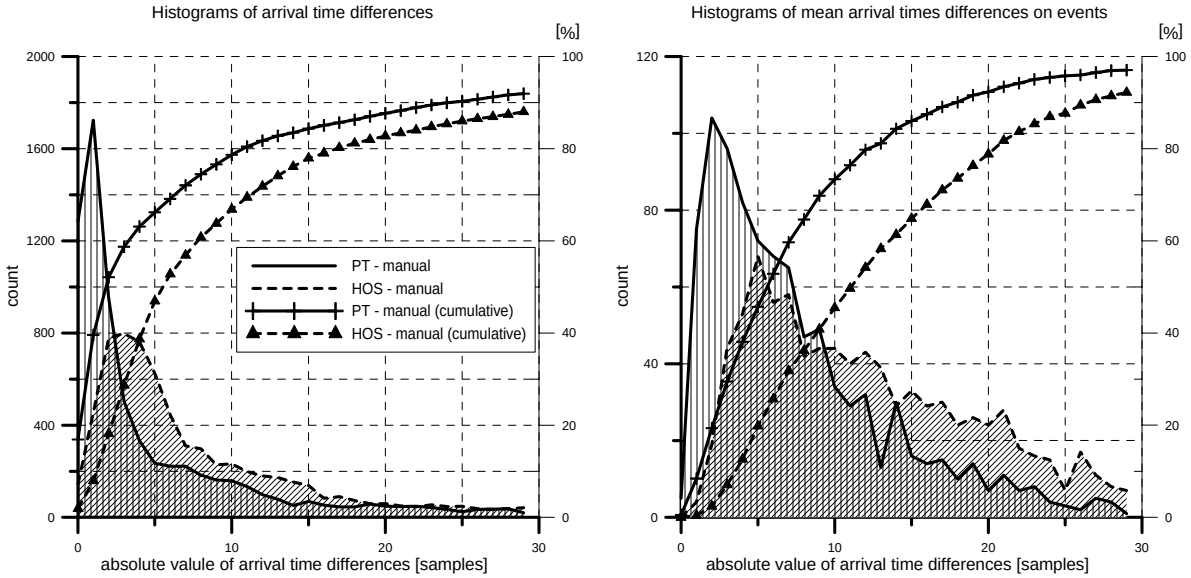

Fig. 4. Histograms of absolute values of arrival time differences assessed by HOS software, PT and manual; x-axis units [samples], legend is valid for both graphs.

The histograms in Fig. 4a represent the absolute value of the time difference individually for each signal. The histograms in Fig. 4b represent the absolute value of the mean time difference for 8 records of one AE event. The cumulative curves indicate that the PT picks agree better with the manual picks (78.7 % picks with 10 samples error) than the HOS method picks (only 66.8 % picks with 10 samples error).

One advantage of the PT method is its computation speed. Computation of the dataset used, i.e. 7600 signals, takes only 75 seconds.

Another parameter that can be used to evaluate the accuracy of the automated picks is the location residuum of the AE events. The location algorithm is based on a simple and reliable grid search method. The modified location method with the L1 norm was used, i.e. the minimum sum of the power of time differences is replaced by the minimum sum of the absolute values of time residues. By comparing the residual times of the manual, HOS and PT picks, one can find how accurate the individual kinds of picks are. The comparison is shown in Fig 5.

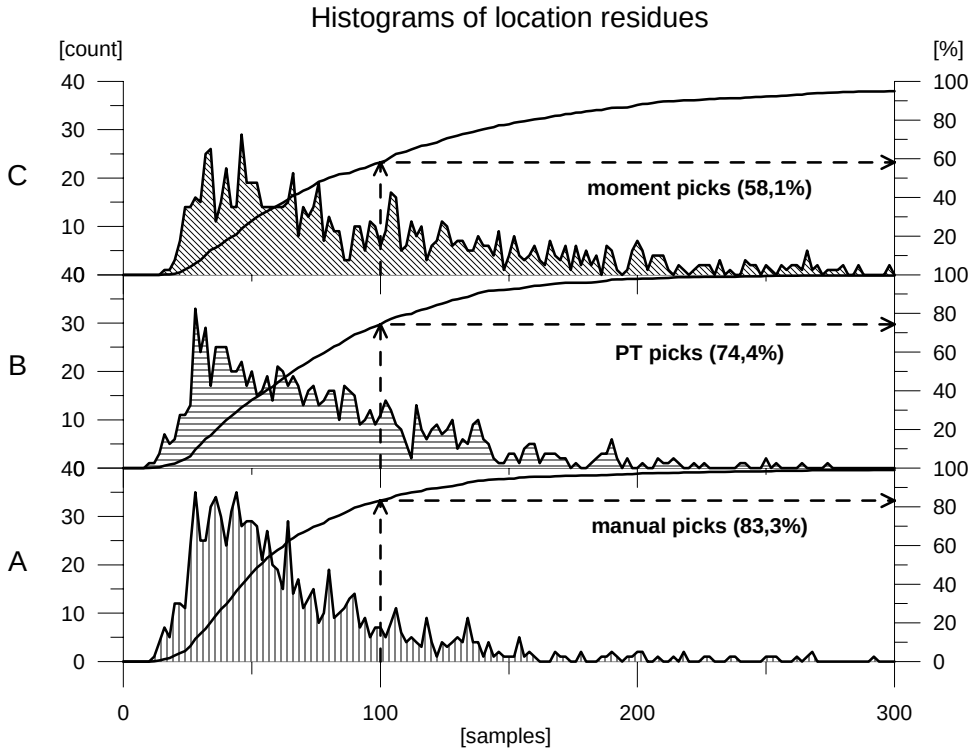

Fig. 4. Histograms of location residues of manual (A), PT (B) and HOS (C) picks.

The residues computed from the manual picks are shown in Fig. 5A, the HOS (moment) residues in Fig. 5C and the PT residues in Fig. 5B. The comparison of location residues displays a similarly successful sequence as in the case of the time difference comparison. If the value of 100 samples (10 μs) is taken to be the criterion of the pick's quality, the manual picks fit this criterion in 83.3 % of the cases, the PT picks in 74.4 % and, finally, the HOS picks fit only in 58.1 % of all AE events.

Conclusions

In this paper, a new derived method for determining the P-wave time arrivals is presented, and its application is demonstrated on the acoustic signals occurring during the rock specimen loading. This method of automated picking by the Pick-Tester program allows to analyse large volumes of data in a relative short time. The accuracy of the automated picks is in a very good agreement with the manually determined picks. The time values determined by both methods differ by less than 1 μs in 78 % cases. The final locations of the AE events display a similar agreement. However, manual processing of such large data files is very time-consuming and practically unworkable. It has been found that the approach used in the Pick-Tester program yields better results than the high-order statistics (HOS) method which is able to work automatically as well.

Acknowledgment

This paper was partially supported by the Grant Agency of the Academy of Sciences of the Czech Republic, Project No. IAA300130906, by the Institutional Research Plan No. AVOZ 30130516 of the Institute of Geology, AS CR, v.v.i. and by the Research Project of the Ministry of Education No. MSM 0021620855. We are grateful to RNDr. Tomáš Fischer PhD. and Ass. Prof. RNDr. Jan Vilhelm, CSc. for their help with creating of PT algorithm and Ing. Tomáš Lokajíček, CSc. for providing data from HOS software.

References

Allen, R.: Automatic phase pickers: their present use and future prospects. *Bulletin of the Seismological Society of America, Vol. 72, No. 6, 1982, p. S225-S242*.

Baer, M., and Kradolfer, U.: An automatic phase picker for local and teleseismic events. *Bulletin of the Seismological Society of America, Vol. 77, 1987, p. 1437-1445*.

Chen, Z.: A multi-window algorithm for automatic picking of microseismic events on 3-C data. *SEG Expanded Abstracts 24, 2005, p. 1288*.

Lockner, D.A., and Byerlee, J.D.: Acoustic emission and creep in rock at high confining pressure and differential stress. *Bull. of the Seismological Society of Amer., Vol. 67, 1977, p. 247-258*.

Lockner, D.: The role of acoustic emission in the study of rock fracture. *Int. J. Rock Mech. Min. Sci. Geomech. Abstr., Vol. 30, No. 7, 1993, p. 883–899*.

Lokajícek, T., Klíma, K.: A first arrival identification system of acoustic emission (AE) signals by means of a high-order statistics approach. *Measurement Science and Technology, Vol. 17, No. 9, 2006, p. 2461-2466*.

Petružálek, M., Vilhelm, J., Lokajíček, T. and Rudajev, V.: Assessment of p-wave anisotropy by means of velocity ellipsoid, *Acta Geodyn. Geomater., Vol. 4, No. 3, 2007, p. 23-31*.

Sedlak, P., Hirose, Y., Khan, S.A., Enoki, M., and Sikula, J.: New automatic localization technique of acoustic emission signals in thin metal plates. *Ultrasonics, Vol. 49, 2009, p. 254–262*.

Veverka, J., Rudajev, V.: Evaluation of ultrasound emission foci in loading rock samples. *Acta Geodynamica et Geomaterialia, Vol. 1, No. 1 (123), 2004, p. 103-110*.

Vilhelm, J., Rudajev, V., Lokajíček, T., Veverka, J.: Correlation analysis of ultrasound emission from loaded rock samples – the study of interaction of microcracking nucleation centers. *Rock Mechanics and Rock Engineering, Vol. 41, No. 5, 2008, p. 695-714*.

Príloha 4

Publikácia 3:

Svitek, T., Vavryčuk, V., Lokajíček, T., & Petružálek, M. (2014). **Determination of elastic anisotropy of rocks from P- and S-wave velocities: Numerical modelling and lab measurements**. *Geophys. J. Int.*, 199(3), 1682–1697.
doi: 10.1093/gji/ggu332

Geophysical Journal International

Geophys. J. Int. (2014) **199,** 1682–1697 doi: 10.1093/gji/ggu332
GJI Seismology

Determination of elastic anisotropy of rocks from *P*- and *S*-wave velocities: numerical modelling and lab measurements

Tomáš Svitek,[1,2] Václav Vavryčuk,[3] Tomáš Lokajíček[2] and Matěj Petružálek[1,2]

[1]*Faculty of Science, Charles University in Prague, Albertov* 6, 128 43 *Praha, Czech Republic*
[2]*Institute of Geology, Academy of Sciences, Rozvojová* 269, 165 00 *Praha, Czech Republic*
[3]*Institute of Geophysics, Academy of Sciences, Boční* II/1401, 141 00 *Praha, Czech Republic. E-mail: vv@ig.cas.cz*

Accepted 2014 August 29. Received 2014 August 13; in original form 2014 February 16

SUMMARY

The most common type of waves used for probing anisotropy of rocks in laboratory is the direct *P* wave. Information potential of the measured *P*-wave velocity, however, is limited. In rocks displaying weak triclinic anisotropy, the *P*-wave velocity depends just on 15 linear combinations of 21 elastic parameters, called the weak-anisotropy parameters. In strong triclinic anisotropy, the *P*-wave velocity depends on the whole set of 21 elastic parameters, but inversion for six of them is ill-conditioned and these parameters are retrieved with a low accuracy. Therefore, in order to retrieve the complete elastic tensor accurately, velocities of *S* waves must also be measured and inverted. For this purpose, we developed a lab facility which allows the *P*- and *S*-wave ultrasonic sounding of spherical rock samples in 132 directions distributed regularly over the sphere. The velocities are measured using a pair of *P*-wave sensors with the transmitter and receiver polarized along the radial direction and using two pairs of *S*-wave sensors with the transmitter and receiver polarized tangentially to the spherical sample in mutually perpendicular directions. We present inversion methods of phase and ray velocities for elastic parameters describing general triclinic anisotropy. We demonstrate on synthetic tests that the inversion becomes more robust and stable if the *S*-wave velocities are included. This applies even to the case when the velocity of the *S* waves is measured in a limited number of directions and with a significantly lower accuracy than that of the *P* wave. Finally, we analyse velocities measured on a rock sample from the Outokumpu deep drill hole, Finland. We present complete sets of elastic parameters of the sample including the error analysis for several levels of confining pressure ranging from 0.1 to 70 MPa.

Key words: Geomechanics; Microstructures; Body waves; Seismic anisotropy; Wave propagation; Acoustic properties.

1 INTRODUCTION

Laboratory measurements as well as in situ observations confirm that majority of real rocks are anisotropic. Elastic anisotropy can be intrinsic if formed by anisotropic mineral grains, but also effective if produced by the presence of layers, preferentially oriented small scale inhomogeneities or joints, cracks and microcraks. Intrinsic rock anisotropy origins either in the preferential arrangement of anisotropic mineral grains being called the 'lattice-preferred orientation (LPO)' anisotropy or 'crystallographic-preferred orientation (CPO)' anisotropy (Karato 2008), or it can origin in a shape predisposition of individual mineral grains being called the 'shape-preferred orientation (SPO)' anisotropy (Mainprice & Nicolas 1989; Ildefonse *et al.* 1992; Kitamura 2006; Valcke *et al.* 2006). Anisotropy of a rock is very often produced by defects such as cracks, microcracks or pores created during tectonic evolution of the rock when exposed to temperature–pressure conditions of a surrounding environment. Consequently, rock is damaged and becomes full of systems of pervasive cracks or microcracks of various scales and orientations (Sayers & Kachanov 1995; Dewhurst & Siggins 2006; Kern *et al.* 2008). Parameters of anisotropy depend also on whether or not and what content saturates the free space of these defects (Hornby 1998; Sayers 2002; Piane *et al.* 2011; Wang *et al.* 2012).

Anisotropic properties of rocks can be measured in laboratory on rock samples or in situ. The laboratory methods are, for example, the microscopic image analyses, ultrasonic sounding, neutron diffraction (Xie *et al.* 2003; Nikitin & Ivankina 2004; Ivankina *et al.* 2005), static and dynamic loading tests in pressure or tense regimes. In *in situ* conditions like in gas and oil reservoirs, anisotropy of rocks

is measured by the multi-offset multi-azimuthal vertical seismic profiling (Okaya *et al.* 2004; Asgharzadeh *et al.* 2013) or by the shear-wave splitting analysis (Crampin 1985; Savage 1999; Peng & Ben-Zion 2004). In general, acoustic and/or seismic methods are based mainly on the determination of the traveltime of elastic waves, well known as the 'time-of-flight' measurements. As we know the distance between the source and a receiver, it is possible to determine the propagation velocity of individual waves in the respective propagation direction and consequently to invert the directionally dependent velocity for anisotropic parameters.

The most common type of waves used for probing anisotropy of rocks in the laboratory is the direct *P* wave (Christensen 1966; Pros *et al.* 1998; Bóna *et al.* 2012; Lokajíček *et al.* 2013). This wave can easily be generated and recorded, and its interpretation is simpler than that of waves coming at later times including the *S* waves. The information potential of the measured *P*-wave velocity, however, is limited. In rocks displaying weak triclinic anisotropy, the *P*-wave velocity depends just on 15 linear combinations of 21 elastic parameters, called the weak-anisotropy parameters (Mensch & Rasolofosaon 1997; Pšenčík & Gajewski 1998; Vavryčuk 2009). The remaining elastic parameters cannot be retrieved. In strong triclinic anisotropy, the *P*-wave velocity depends on all 21 elastic parameters, but inversion for six of them is ill-conditioned and these parameters are retrieved with a low resolution. This deficiency can be removed only by incorporating the *S*-wave velocities. The measurement of the *S*-wave velocities is, however, more difficult; it requires equipping special transmitters and sensors for generating and recording the *S* waves, and the interpretation of recorded signals is also more involved (Kern 1982; Siegesmund *et al.* 1991).

In this paper, we present an approach of measuring the *P*- and *S*-wave velocities on rock samples and inverting them for elastic anisotropy. In order to be able to analyse a general anisotropy of no symmetry, we developed a new high pressure apparatus that allows measuring the *P*- and *S*-wave velocities on spherical rock samples. The velocities are measured in 132 independent directions which provide good spatial coverage (Pros *et al.* 1998) needed for a reliable determination of anisotropy parameters. The waveforms are recorded with radial as well as two mutually perpendicular transverse sensors in order to identify the two *S* waves and to measure their arrivals accurately. We present inversion schemes for determining anisotropy parameters using phase as well as ray velocities and test their robustness on synthetic models. We show how the accuracy of the parameters is improved if the *S*-wave measurements are incorporated. Finally, we exemplify our approach on real measurements obtained for a strongly foliated fine-grained biotite gneiss from the Outokumpu deep drill hole, Finland (Kern *et al.* 2009) exposed to various confining pressure conditions.

2 THEORY

2.1 Determination of anisotropy from phase velocities

The phase velocity describes the propagation of plane waves and is directed along the phase normal (i.e. the normal to the wave front). The phase velocity of plane waves propagating in a homogeneous anisotropic medium is described by the Christoffel equation (Musgrave 1970; Helbig 1994):

$$\det\left(\Gamma_{ij} - c^2\delta_{ij}\right) = 0, \tag{1}$$

where c is the phase velocity of the *P*, *S*1 or *S*2 waves, δ_{ij} is the Kronecker delta and Γ_{ij} is the Christoffel tensor,

$$\Gamma_{jk} = a_{ijkl}n_i n_l. \tag{2}$$

Parameters a_{ijkl} are the components of the elastic (stiffness) tensor normalized to density, and vector $\mathbf{n}$ is the phase normal. If elastic parameters a_{ijkl} are known, eq. (1) is the cubic equation for the squared phase velocity c. If the phase velocity c is known from measurements, eq. (1) defines an inverse problem for calculating elastic parameters a_{ijkl}. This inversion is non-linear and usually solved by iterations using perturbation theory (Klíma 1973; Jech & Pšenčík 1989; Jech 1991; Vavryčuk 2013).

In perturbation theory, we assume that the anisotropic medium defined by unknown parameters a_{ijkl} can be obtained by a small perturbation of a known reference medium

$$a_{ijkl} = a^0_{ijkl} + \Delta a_{ijkl}, \tag{3}$$

where a^0_{ijkl} defines the reference medium and Δa_{ijkl} its perturbation. Under this assumption, the cubic equation for phase velocity c can be linearized as follows (Jech & Pšenčík 1989; Pšenčík & Vavryčuk 2002):

$$\Delta(c^2) = \Delta a_{ijkl}n_i n_l g^0_j g^0_k, \tag{4}$$

where $\mathbf{g}^0$ defines the polarization vector of the analysed wave in the reference medium, $\Delta(c^2)$ is the misfit between the measured velocity in the studied anisotropic medium and the velocity in the reference medium. Eq. (4) represents a system of linear equations for unknown perturbations, Δa_{ijkl}, which can be solved in iterations. In the first iteration, the reference medium is assumed to be isotropic. Its *P*- and *S*-wave velocities can be obtained by averaging the observed directionally dependent velocities over all directions. If only *P*-wave velocities are measured and inverted, a rough estimate of the *S*-wave velocity in the isotropic reference medium must also be supplied. We can use, for example, a value obtained from the Poisson ratio between the *P* and *S* velocities, $V_S = V_P/\sqrt{3}$. In higher iterations, the reference medium is the result of the previous iteration.

Using the above approach, we can invert for all of 21 elastic parameters. However, not all of them are retrieved with the same accuracy. In the case of the *P*-wave velocity inversion, 15 parameters are well resolved but six parameters related to the *S*-wave propagation (hereafter the *S*-wave related parameters) a_{44}, a_{55}, a_{66}, a_{45}, a_{46} and a_{56} are less accurate. Under weak anisotropy, these six parameters cannot be determined from the *P*-wave velocities at all. Hence, in order to determine the complete elastic tensor accurately, measurements of the *S*-wave velocities must be utilized in the inversion.

2.2 Determination of anisotropy from ray velocities

The ray velocity defines the signal propagation and energy transport and is directed along a ray. If anisotropy under study is weak, we do not need to distinguish between the phase and ray velocities. Their magnitudes are approximately equal and directions differ by a small angle (Vavryčuk 1997; Pšenčík & Vavryčuk 2002; Farra 2004). However, if anisotropy is strong, the phase and ray velocities are different. For this reason, it is important to understand which velocity is measured in the field or lab experiments. If the waves used for determining anisotropy are generated by point sources, the ray velocity is usually measured and the procedure of the inversion for elastic anisotropy described in Section 2.1 must be modified.

The ray velocity vector **v** is defined as (Červený 2001, his eq. 2.4.46):

$$v_i = vN_i = a_{ijkl} p_l g_j g_k, \tag{5}$$

where v is the ray velocity, **N** is the ray direction, a_{ijkl} are the density-normalized elastic parameters, $\mathbf{p} = \mathbf{n}/c$ is the slowness vector, **n** is the phase normal, $c = 1/p$ is the phase velocity, p is the slowness and **g** is the polarization vector. Vectors **v** and **p** are related by the following equation,

$$\mathbf{v} \cdot \mathbf{p} = 1 \tag{6}$$

expressing the polar reciprocity of the slowness and wave surfaces (Helbig 1994). This condition means that vector **v** is normal to the slowness surface $p = p(\mathbf{n})$ and vector **p** is normal to the wave surface $v = v(\mathbf{N})$. Hence, if ray velocity v is measured in a sufficiently dense grid of ray directions **N**, we can calculate vectors **n** as normals to the wave surface using standard formulae of differential geometry (Lipschutz 1969). Subsequently, phase velocity c can be calculated for vectors **n** using the following formula

$$c = vN_i n_i. \tag{7}$$

Having computed $c = c(\mathbf{n})$ we can invert for anisotropic parameters using the procedure described in Section 2.1. Obviously, if we combine several types of waves in the inversion, which were measured for the same set of ray directions **N**, the sets of phase normals **n** are different for individual wave types.

It should be noted that the above approach has some limitations. The geometry of the wave surface can be much more complicated than that of the slowness or phase velocity surface (Musgrave 1970). For *S* waves, the wave surface can be multivalued with triplications and cusp edges (Vavryčuk 2006). In general, the complexity of the wave surface increases with strength of anisotropy. So, it can happen under strong anisotropy that the complete slowness or phase velocity surface can be constructed only using velocity measurements on a very fine grid of ray directions and by identifying and interpreting also later arrivals of waves. If the wave surface of *S* waves is extremely complicated, we can avoid problems with the triplications and the cusp edges by calculating the wave normals (and corresponding phase velocities) only for smooth parts of the wave surface. In this way, we will not be able to reconstruct the complete slowness or phase velocity surfaces of the *S* waves but only their isolated patches. Fortunately, this is not critical for the inversion for anisotropic parameters. As will be shown in synthetic tests, the inversion can work robustly even when measurements of the *P*-wave velocities are supplemented by a limited number of measurements of the *S*-wave velocities.

The above approach is advantageous, because it is a simple generalization of the inversion of the phase velocities described in Section 2.1. First, we pre-process the input data by transforming the ray velocities to the phase velocities, and then we apply the standard inversion scheme. However, anisotropic parameters can also be calculated using other approaches, for example, if ray velocities are measured together with polarization vectors (Bóna *et al.* 2008).

3 SYNTHETIC TESTS

In this section, the robustness of the inversion of phase velocities for elastic anisotropy is studied using numerical modelling. For synthetic anisotropy, we adopted elastic parameters of quartz published

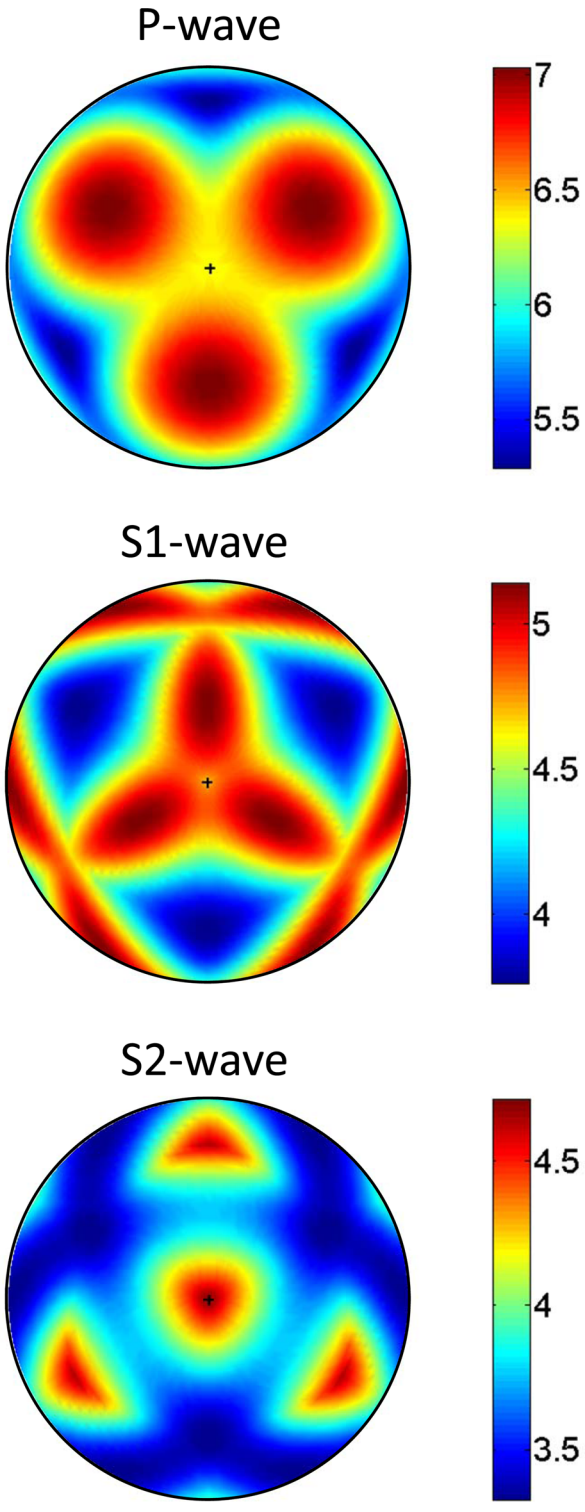

Figure 1. The *P*-, *S*1- and *S*2-wave phase velocities of anisotropy used in the synthetic tests. The colour-coded velocities are in km s^{-1}.

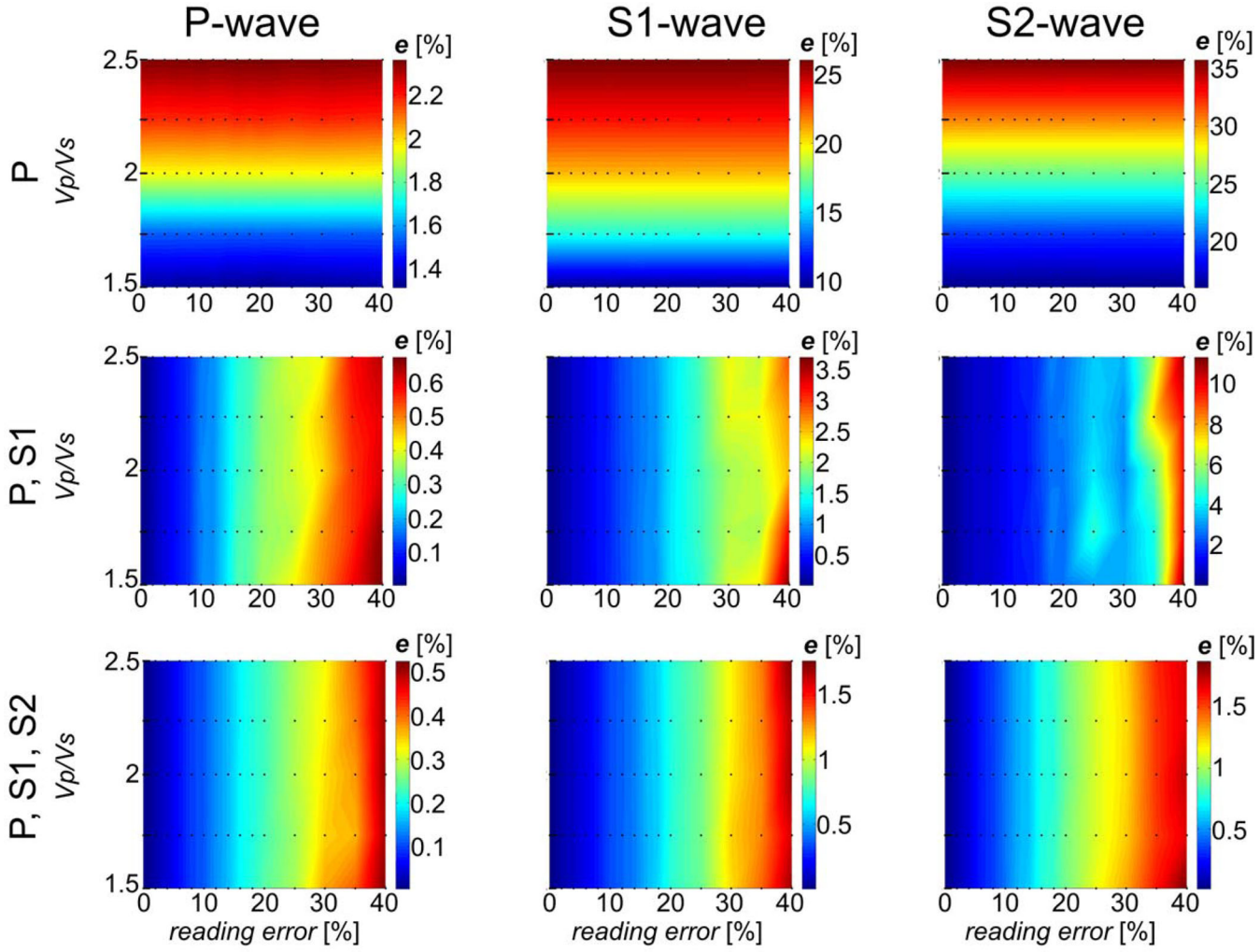

Figure 2. Error e_{mean} of the predicted *P*-wave (left-hand panel), *S*1-wave (middle panel) and *S*2-wave (right-hand panel) velocities as a function of the reading error of the measured *S*1-wave velocities (middle row) and *S*1- and *S*2-wave velocities (bottom row). The inversion is performed using velocities measured in all 132 directions. The errors in the top row panels are independent of the reading error of the *S*-wave velocities, because only the *P*-wave velocities are inverted. The dots indicate points in which error e_{mean} is calculated.

by Klíma (1973):

$$C_{ij}^{\text{quartz}} = \begin{bmatrix} 86.05 & 4.85 & 10.45 & 18.25 & 0 & 0 \\ 4.85 & 86.05 & 10.45 & -18.25 & 0 & 0 \\ 10.45 & 10.45 & 107.1 & 0 & 0 & 0 \\ 18.25 & -18.25 & 0 & 58.65 & 0 & 0 \\ 0 & 0 & 0 & 0 & 58.65 & 18.25 \\ 0 & 0 & 0 & 0 & 18.25 & 40.60 \end{bmatrix}. \quad (8)$$

The values in eq. (8) are in GPa and the density of quartz is $\rho = 2.65$ g cm^{-3}. Anisotropy displays a trigonal symmetry. Strength of the *P*-, *S*1- and *S*2-wave anisotropy is 26.6, 29.9 and 27.8 per cent, respectively. For the directional variation of the *P*-, *S*1- and *S*2-wave phase velocities, see Fig. 1. The velocities used in the inversion are calculated in a regular grid of directions with latitude ranging from –75° to 75° in step of 15° and longitude from 0° to 360° in step of 15°. This represents a set of 132 independent directions covering the whole sphere surface.

3.1 Test 1

In this test, we study the robustness of the inversion with respect to the following factors: (1) starting model, that is the estimate of the *S*-wave velocity of the isotropic reference medium needed in the first iteration, (2) noise in input data (i.e. in the measured velocities) and (3) types of waves used in the inversion. The *S*-wave velocity of the isotropic reference model is defined by the V_P/V_S ratio ranging from 1.5 to 2.5. The errors of the phase velocities are assumed to be 0.1 per cent at most for the *P* wave. The errors of the *S*1-wave velocities are assumed to achieve values: 0, 0.2, 0.4, 0.6, 0.8, 1, 2, 4, 6, 8, 10, 12, 14, 16, 18, 20, 25, 30, 35 and 40 per cent. The errors of the *S*2-wave velocities are 1.5 times larger than those for the *S*1 wave. A uniform random distribution was chosen for all noise levels. Every noise value was generated 100 times to get statistically relevant results. The limits of noise selected for the *P*, *S*1 and *S*2 waves are based on the analysis of real data presented in Section 4. The accuracy of the *P*-wave velocity is very high, because the *P* wave has a sharp onset with no noise before its arrival and thus picking of arrival times is quite accurate. A significantly lower accuracy of the *S*1 and *S*2 waves originates in the fact that the *S* waveforms are generally more complex and their interpretation

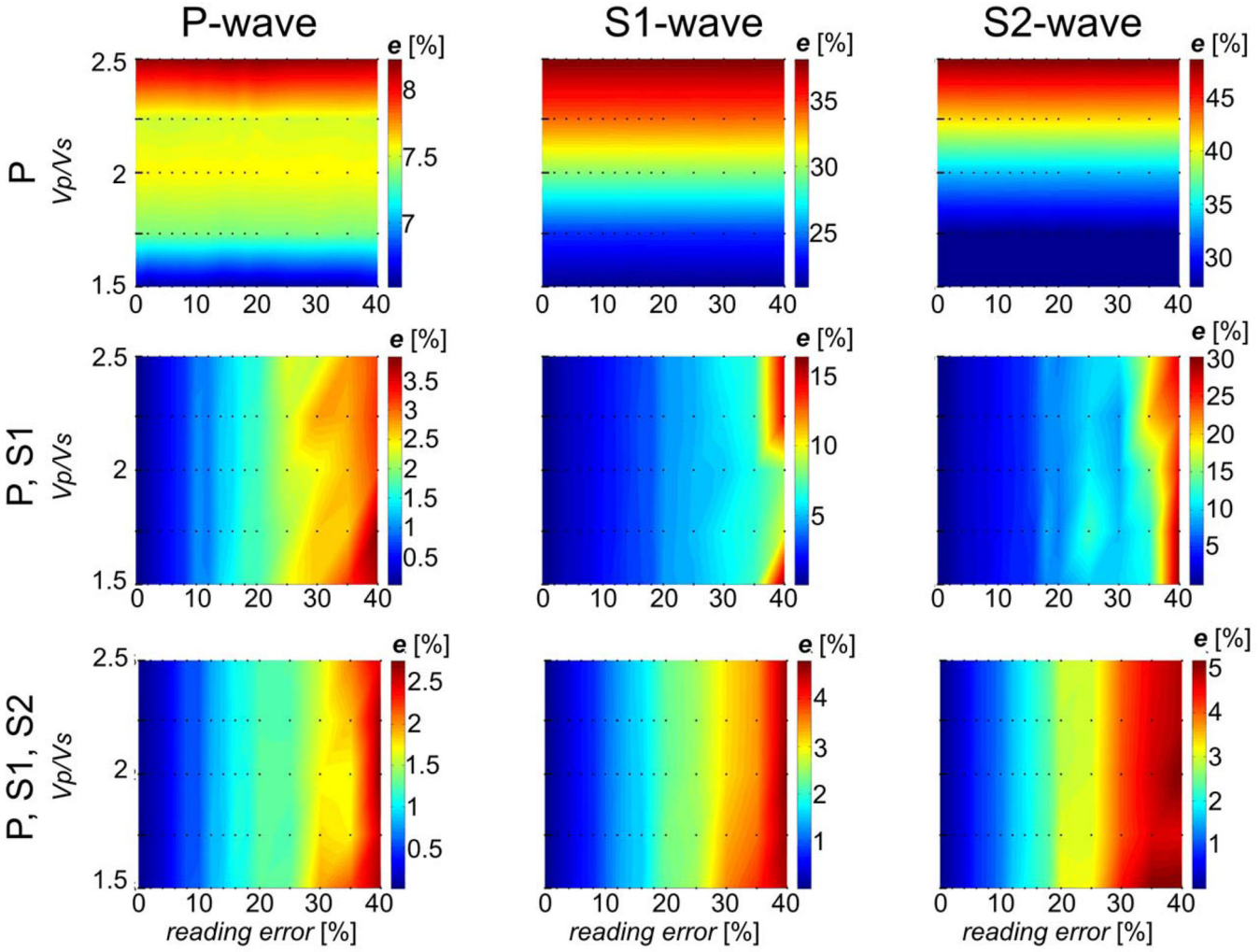

Figure 3. Error $e_{\max}$ of the predicted *P*-wave (left-hand panel), *S*1-wave (middle panel) and *S*2-wave (right-hand panel) velocities as a function of the reading error of the measured *S*1-wave velocities (middle row) and *S*1- and *S*2-wave velocities (bottom row). The inversion is performed using velocities measured in all 132 directions. The errors shown in the top row panels are independent of the reading error of the *S*-wave velocities because only the *P*-wave velocities are inverted. The dots indicate points in which error $e_{\max}$ is calculated.

is often difficult. Moreover, in the case of weak anisotropy, the two *S* waves need not be well separated; they can interfere and their reliable distinguishing is not always possible. This particularly complicates identifying the slow *S* wave. Therefore, the slow *S*-wave velocity is assumed to have systematically higher errors than the fast *S*-wave velocity. Finally, we studied the robustness of the inversion for three different input data sets. We tested inversion for anisotropy using the *P*-wave velocities only, the *P*- and *S*1-wave velocities, and the *P*-, *S*1- and *S*2-wave velocities. The success of the inversion is quantified by a relative difference between true and predicted velocities:

$$e^{P,S1,S2}_{\text{mean}} = 100\ \text{per cent} \cdot \text{mean}\left(\frac{\left|c^{P,S1,S2}_{\text{true}} - c^{P,S1,S2}_{\text{predicted}}\right|}{c^{P,S1,S2}_{\text{true}}}\right),$$

$$e^{P,S1,S2}_{\text{max}} = 100\ \text{per cent} \cdot \max\left(\frac{\left|c^{P,S1,S2}_{\text{true}} - c^{P,S1,S2}_{\text{predicted}}\right|}{c^{P,S1,S2}_{\text{true}}}\right), \qquad (9)$$

where the predicted velocity is calculated from the retrieved anisotropic parameters. These quantities are averaged over all directions and over 100 realizations of random noise.

The results of the synthetic tests are shown in Figs 2–4. According to the results we arrive at the following conclusions:

(1) The elastic tensor computed from the *P*-wave velocities only (top rows in Figs 2 and 3) strongly depends on the V_P/V_S ratio supplied in the first iteration. The predicted velocities of the *S*1 and *S*2 waves have significantly higher errors than those for the *P* wave. The mean errors for the *S*1 and *S*2 waves are about 10 and 15 times higher than for the *P* waves, respectively. Thus the *S*-wave related parameters cannot be reliably retrieved even if the accuracy of the *P*-wave velocities is quite high (0.1 per cent at most). Consequently, the *S*1- and *S*2-wave velocities calculated from the retrieved elastic tensor are highly inaccurate.

(2) The elastic tensor computed from the *P*- and *S*1-wave velocities (middle rows in Figs 2 and 3) is insensitive to the V_P/V_S ratio supplied in the first iteration. The accuracy of the predicted velocities depends on the picking accuracy of the *S*1-wave onsets. Interestingly, including quite inaccurate measurements of the *S*-wave velocities still improves the accuracy of the elastic tensor (Fig. 4, bottom row). Even the fit between the predicted and true *P*-wave velocities is better. If the *S*1-wave velocities are measured with the mean errors less than

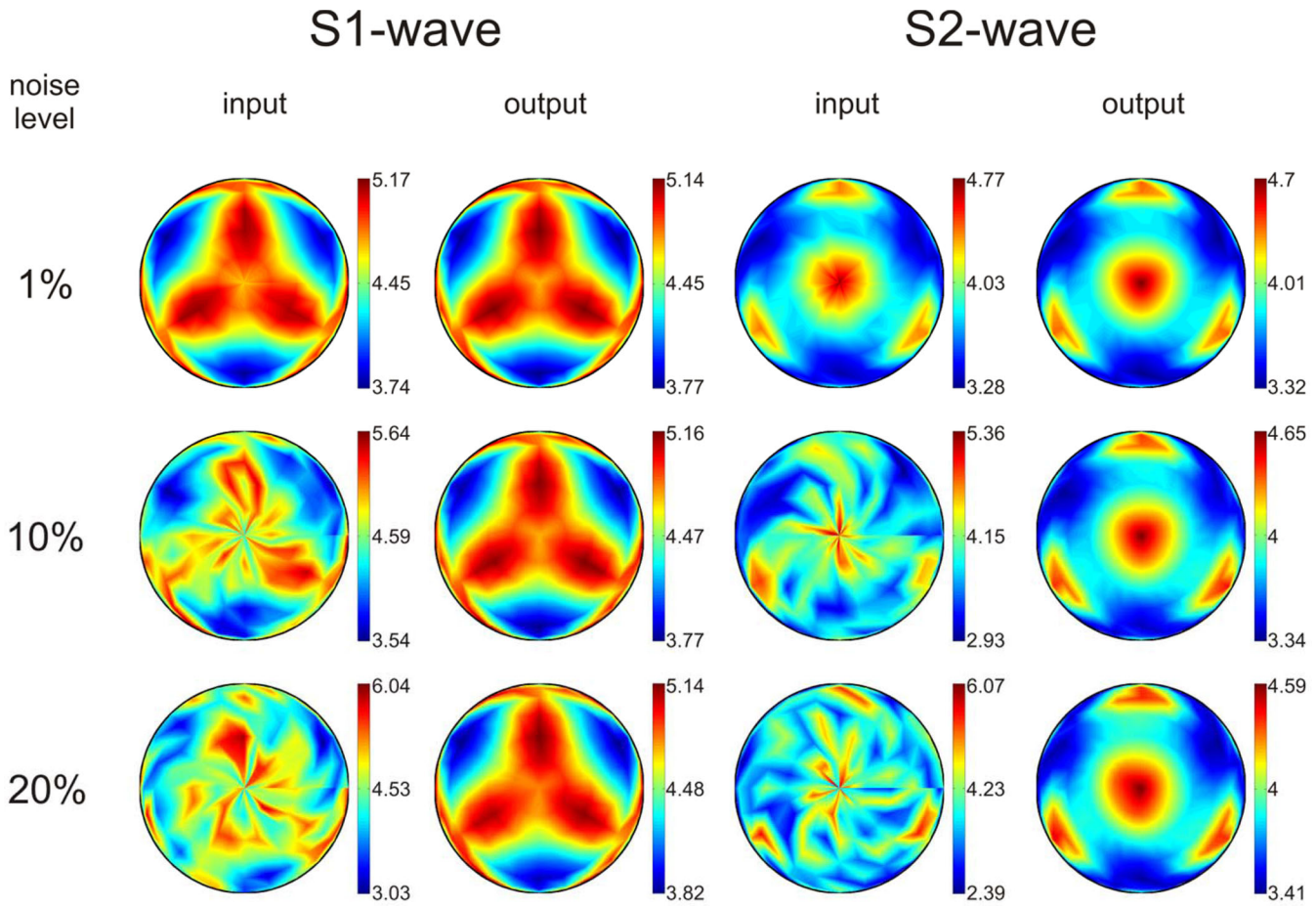

Figure 4. Examples of input noisy *S*1- and *S*2-wave velocities used in the inversion and the corresponding output velocities predicted from the retrieved elastic parameters. The noise levels of the *S*1-wave velocities are: 1 per cent (top row), 10 per cent (middle row) and 20 per cent (bottom row), respectively. The colour-coded velocities are in km s^{-1}. The figure demonstrates that the inversion is robust and stable even for a high level of noise.

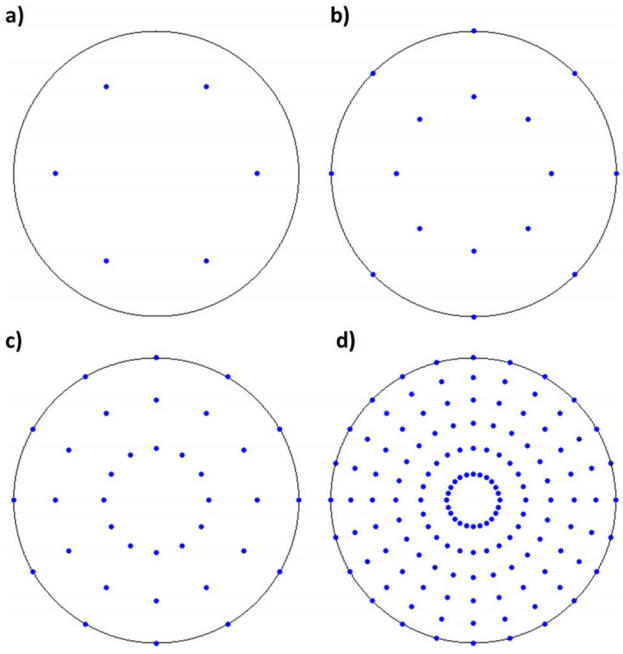

Figure 5. The stereographic projection of directions with velocity measurements used in the synthetic tests: the regular grid of (a) 6 directions (60° step), (b) 12 directions (45° step), (c) 30 directions (30° step) and (d) 132 directions (15° step).

15 per cent, the mean errors of the predicted *P*-, *S*1- and *S*2-wave velocities are less than 0.3, 1 and 3 per cent, respectively.

(3) The elastic tensor computed from the *P*-, *S*1- and *S*2-wave velocities (bottom rows in Figs 2 and 3) is mainly dependent on the accuracy of the inverted *S*1- and *S*2-wave velocities. The additional information on the *S*2-wave velocities improves the accuracy of the predicted *S*1- and *S*2-wave velocities. The accuracy of the *P*-wave velocities is not further improved.

In summary, the performed synthetic tests indicate that the components of the elastic tensor inverted from the *P*-wave velocities only are determined with a reasonable accuracy except for the *S*-wave related parameters. These parameters should be viewed as very approximate and rather unreliable. The complete elastic tensor characterizing trigonal (or more general) anisotropy can be computed only when including the *S*-wave velocities into the inversion. Including the *S*-wave velocities leads to increasing the accuracy of the *S*-wave related parameters but also of the complete elastic tensor.

3.2 Test 2

Including information on the *S*-wave velocities into the inversion is not always an easy task. The *S* waves can be contaminated by the *P*-wave generated noise. Also, the two *S* waves do not often separate. In addition, the *S* waves can interfere in a complicated way near the *S*-wave singularities (Vavryčuk 2005a,b). In such cases, it is not

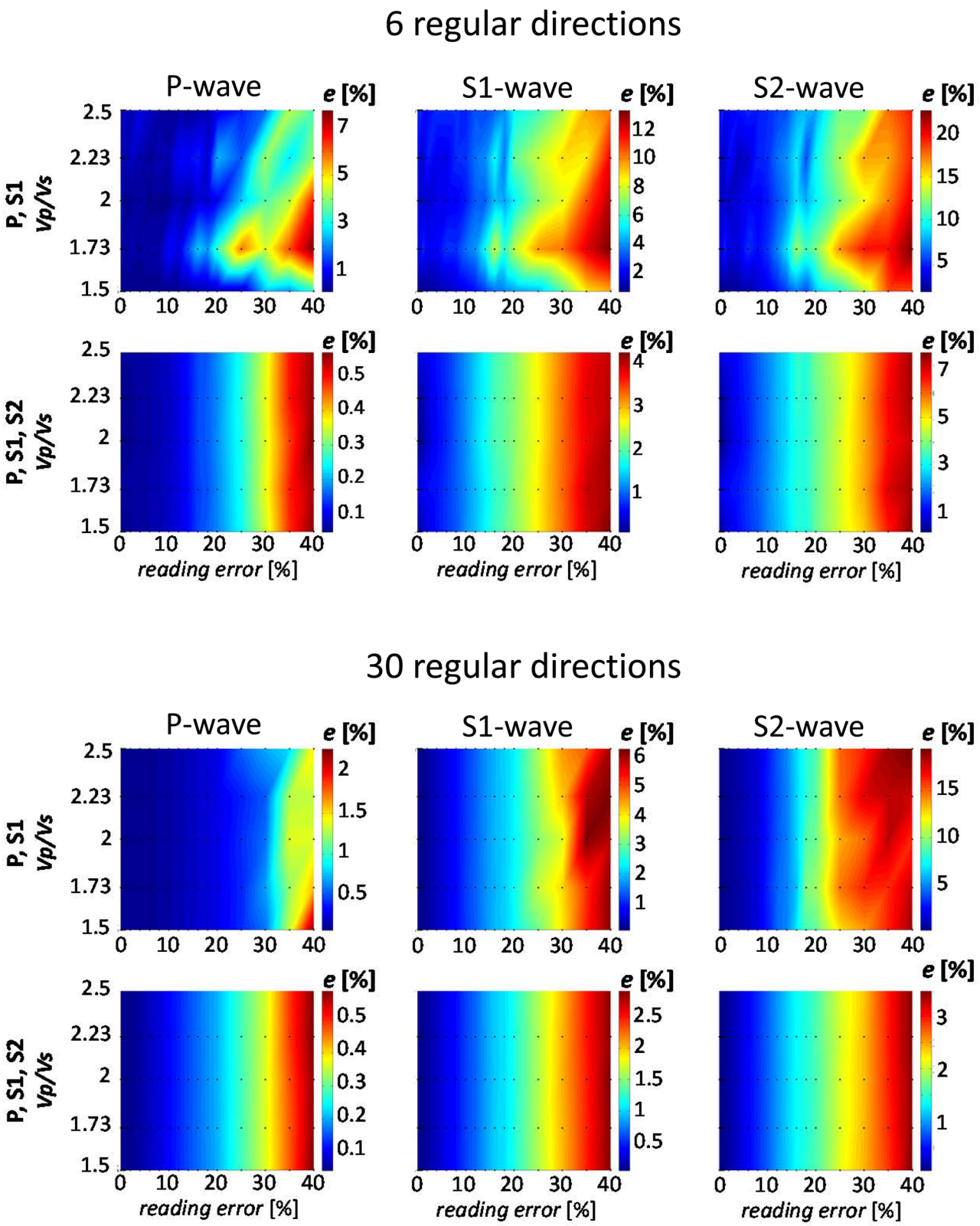

Figure 6. Error e_{mean} of the *P*-, *S*1- and *S*2-wave velocities as a function of the reading error of the measured *S*1-wave velocities (top row of each composite plot) and *S*1- and *S*2-wave velocities (bottom row of each composite plot). The inversion is performed using the *P*-wave velocities in all 132 directions and the *S*-wave velocities for a regular grid of six directions (upper plots) and 30 directions (lower plots). The dots indicate points in which error e_{mean} is calculated.

Table 1. Error e_{mean} as a function of the number of regular directions with the measured *S*-wave velocities used in the inversion. The *P*-wave velocities are measured in all 132 directions with error of 0.1 per cent. The errors of the measured *S*1- and *S*2-wave velocities are 40 and 60 per cent, respectively.

Error e_{mean}	*P*, *S*1 data Number of *S* directions		*P*, *S*1, *S*2 data Number of *S* directions	
	6	132	6	132
*S*1 wave	15 per cent	3.5 per cent	4.5 per cent	1.6 per cent
*S*2 wave	27 per cent	11 per cent	8 per cent	1.7 per cent

possible to measure reliably arrivals of one or both of the two *S* waves in some directions. For these reasons, we designed another synthetic test in which we analysed the accuracy of the inverted elastic tensor in dependence on the number of directions in which the *S*-wave velocities could be measured reliably.

Similarly as in Test 1, the errors were evaluated using eq. (9) being averaged over 100 realizations of random noise. The noise level of the measured *P*-wave velocity was 0.1 per cent as in Test 1. The inversion was performed with the *P*-wave velocities measured in all 132 directions (see Fig. 5d) and with the *S*-wave velocities measured in 6, 12, 30 and 132 regularly distributed directions (see Fig. 5). The accuracy of the *S*-wave velocities due to picking errors of the *S*-wave arrivals is the same as in Test 1.

The results of the test for 6 and 30 regular directions of the *S*-wave velocities are shown in Fig. 6. The errors of the inversion with the 6 and 132 regular directions of the *S*-wave velocities are summarized in Table 1. The synthetic tests indicate that including six directions with accurately measured *S*1-wave velocities is sufficient for a reliable determination of the complete elastic tensor. If the *S*1-wave velocity errors reach values of 20 per cent or more then the inversion is not improved with respect to the inversion of the

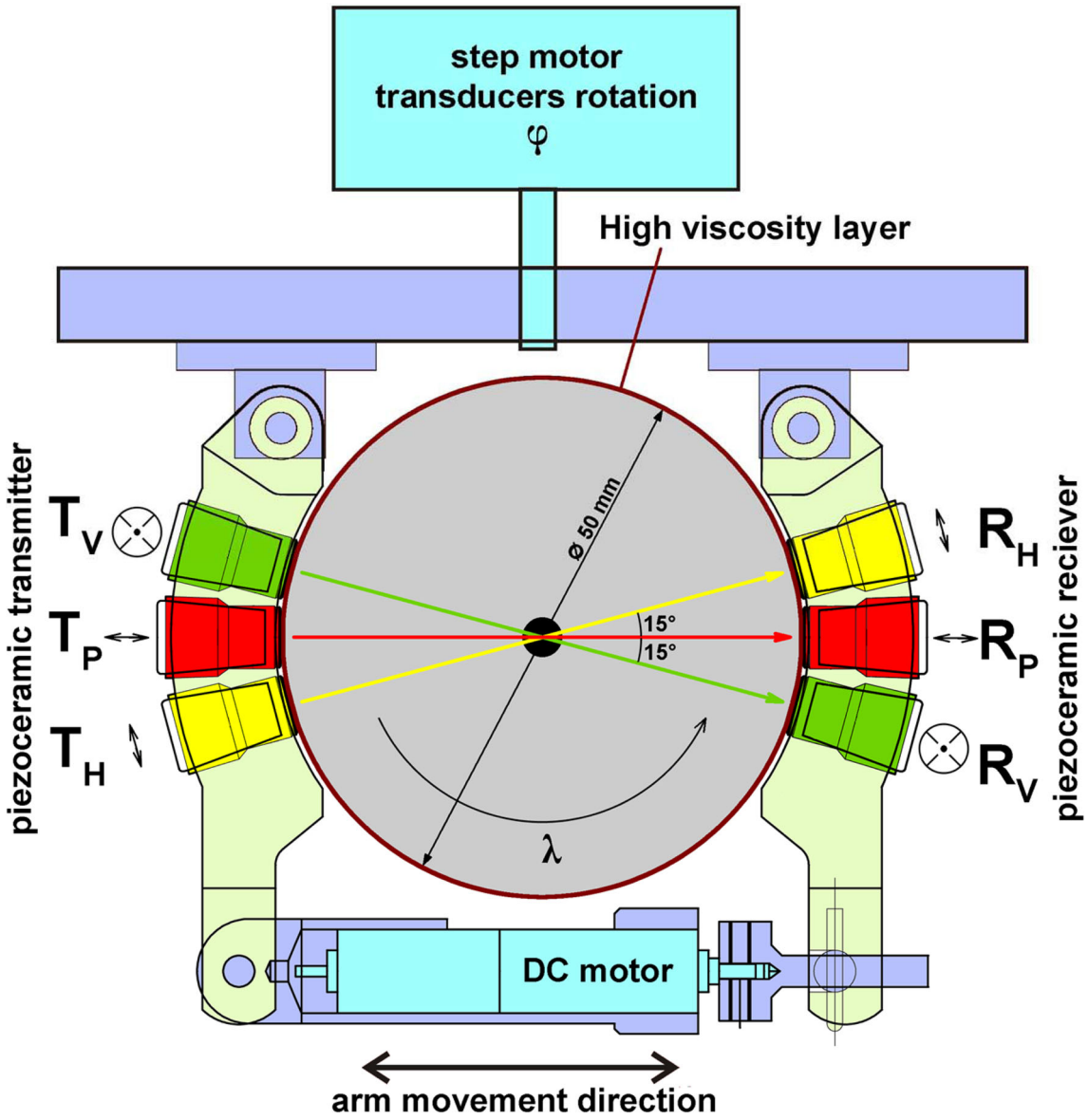

Figure 7. The experimental setup and measurement geometry; T_P and R_P are the radial transmitter and receiver, respectively (mostly generating and sensitive to the *P* waves), T_V and T_H are the transverse transmitters (mostly generating the *S* waves), and R_V and R_H are the transverse receivers (mostly sensitive to the *S* waves) lying in the vertical and horizontal planes, respectively. The axis of rotation is vertical. Modified from Lokajíček *et al.* (2014).

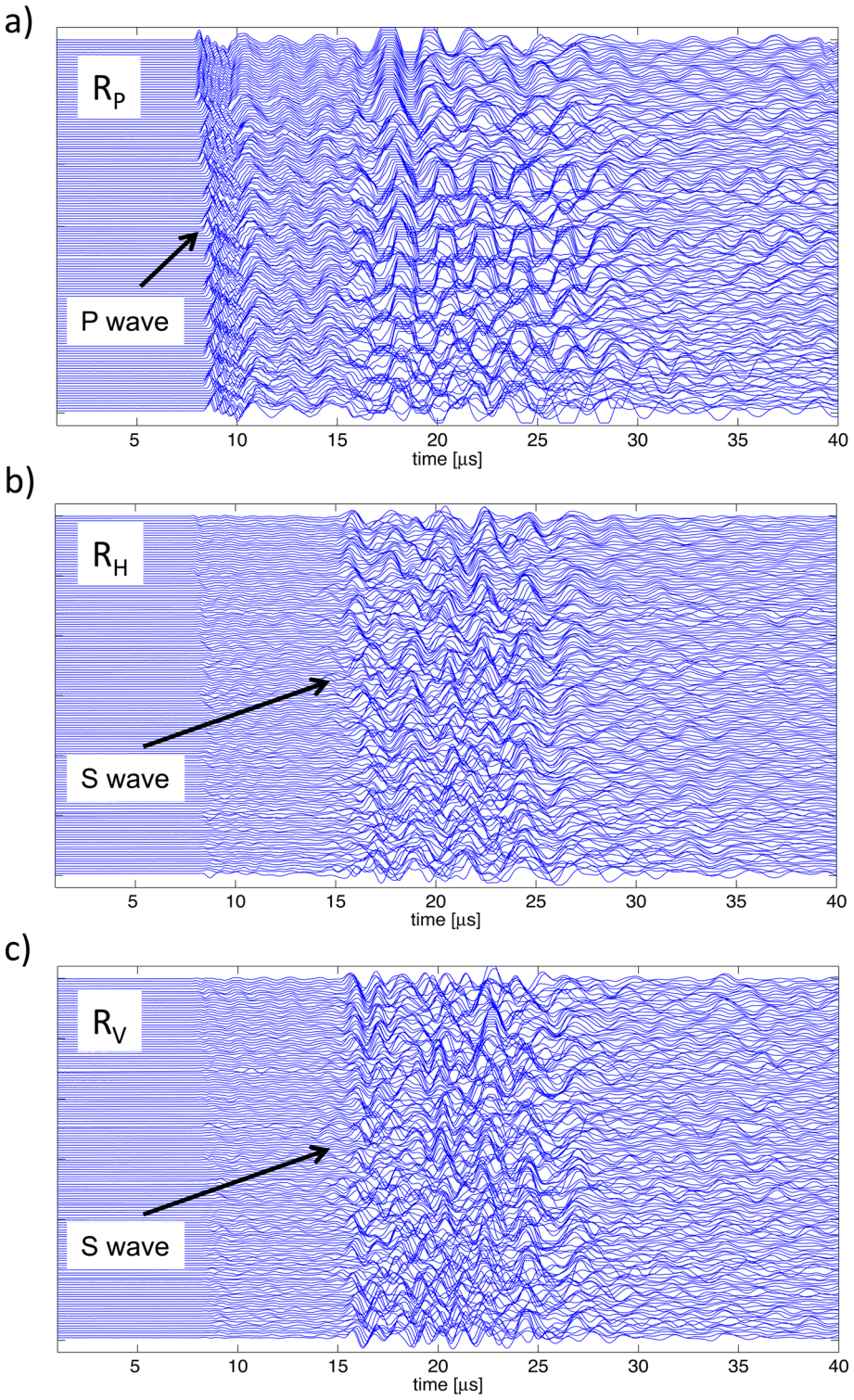

Figure 8. Waveforms of ultrasonic signals observed for the OKU-409 sample at confining pressure of 70 MPa. The waveforms are recorded in all directions at the *P*-wave sensor R_P (a), the *S*-wave sensor R_H (b) and the *S*-wave sensor R_V (c). The origin of the timescale corresponds to the excitation time of the signal.

P-wave velocities only. The results show that a much higher accuracy of the predicted *P*-wave velocities is obtained if we include the *S*2-wave velocities even for a minimum number of directions. A further increase of directions with the measured *S*2-wave velocities is not essential for improving the predicted *P*-wave velocities but significantly improves the accuracy of the predicted *S*1- and *S*2-wave velocities.

For completeness, we also performed synthetic tests with inverting the *S*-wave velocities measured in directions with an irregular distribution over the sphere. The tests revealed that the accuracy of results is two to three times lower than if the inversion is performed with a regular distribution of directions. This emphasizes the necessity of uniform coverage of the sphere by velocity measurements for the inversion to work efficiently.

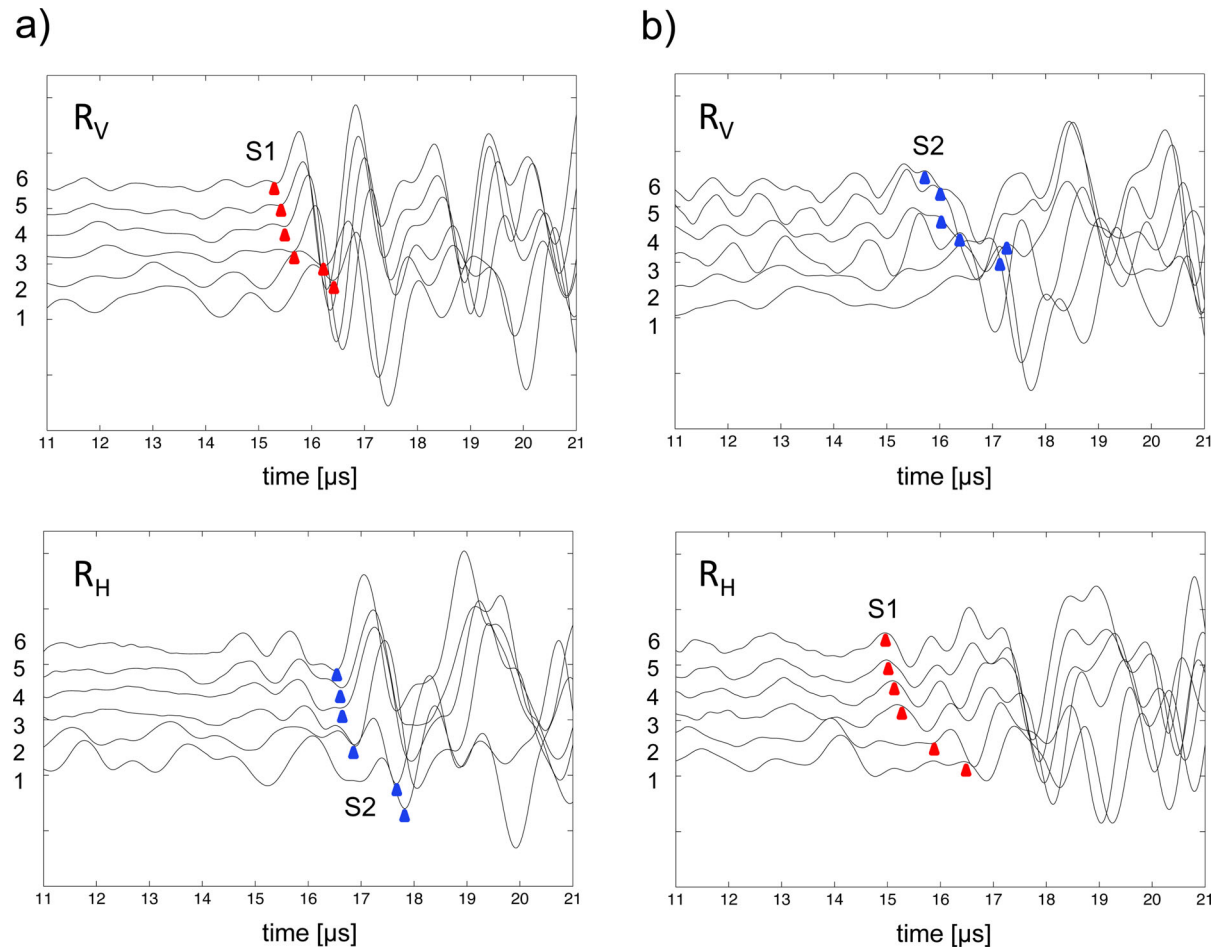

Figure 9. Examples of waveforms of ultrasonic signals observed for the OKU-409 sample on the transverse receivers: (a) waveforms in a direction in which clear *S*-wave onsets are observed, (b) waveforms in a direction in which rather unclear and disturbed *S*-wave onsets are observed. The waveforms in the individual panels are recorded under six different pressure levels with an increasing order: label 1 corresponds to 0.1 MPa, and label six corresponds to 70 MPa. The red and blue triangles mark the *S*1- and *S*2-wave arrival times, respectively. The origin of the timescale corresponds to the excitation time of the signal.

4 EXPERIMENTAL DATA

4.1 Setup of the experiment

The determination of elastic anisotropy is exemplified using an experimental facility allowing a measurement of the *P*- and *S*-wave ray velocities on spherical samples with a diameter of 50 mm. The sample was exposed to the following six confining pressure levels: 0.1, 5, 10, 20, 40 and 70 MPa. The acoustic signals are excited and recorded by three piezoceramics sensor couples with a resonant frequency of 2 MHz. The equipment allows an ultrasonic sounding of spherical rock samples in 132 independent directions by using a pair of the *P*-wave sensors (the transmitter and receiver polarized along the radial direction) and two pairs of the *S*-wave sensors (the transmitter and receiver polarized tangentially to the spherical sample, see Fig. 7). The waveforms of ultrasonic signals were recorded using an A/D convertor with the dynamic range of 8 bits and with the sampling frequency of 100 MHz. Each waveform was recorded 10 times and then averaged in order to reduce noise. The sensitivity of the convertor was set up to record individual signals without any distortion and with the maximum possible dynamics. For the *S*-wave velocity measurements, the spherical sample and contact planes of all transducers were covered by a viscous gel to allow transferring shear wave energy. Due to this gel, the sensors are not at a point contact with the sample as for the *P*-wave sensors, but may have a diameter of 1 mm or more. During the measurement, the contact between the spherical sample and the transducers was repeatedly eliminated and re-established by a miniature DC motor.

4.2 Rock sample

The measurements were performed on rock sample OKU-409 from the Outokumpu deep drill hole, Finland (Kern *et al.* 2009; Kukkonen *et al.* 2011). The sample sphere was prepared from a core segment recovered from depth of 409 m. The sample is a homogeneous biotite gneiss with pronounced foliation and lineation. The modal composition is 39.6 vol.-per cent quartz, 36.9 vol.-per cent plagioclase, 23.4 vol.-per cent biotite (Kern *et al.* 2009). The foliation and lineation are defined by platy and elongated biotite minerals exhibiting a strong shape preferred orientation. The bulk density of the rock sample as calculated from mass and dimensions of the sphere is 2.724 g cm^{-3}. Various properties of this rock as the texture pattern, the petrophysical and elastic properties have been studied and described by many authors (Kern *et al.* 2008, 2009; Elbra *et al.* 2011; Wenk *et al.* 2012). In particular, the focus was put on elastic anisotropy determined using various methods. It was measured on a spherical sample using the apparatus described in this paper, on

a cube sample using a multi-anvil pressure apparatus, and it was also calculated from the texture-based data. A detailed review of the results can be found in Lokajíček *et al.* (2014).

4.3 Data processing

Processing of waveforms provides the *P*-, *S*1- and *S*2-wave onset times in 132 independent directions (see Fig. 8). Since the *P*-wave onset is usually noise-free and well distinguished, the determination of the *P*-wave arrivals is rather easy and can be performed automatically (Allen 1982; Lokajíček & Klíma 2006; Sedlák *et al.* 2009; Svitek *et al.* 2010). The *S* waveforms, however, are often complex and their arrivals can be unclear and hidden in noise. For this reason, the *S*1- and *S*2-wave arrivals were determined manually after a careful inspection of an analyst. The quality of the waveforms recorded in different directions is exemplified in Fig. 9. The figure shows that finding the onsets of the *S* waves is not always obvious. Waveforms from the vertically and horizontally polarized receivers are shown on the top and bottom of the figure, respectively. Six signals at each plot represent ultrasonic sounding in the same direction but under different confining pressures. Fig. 9(a) shows signals of a very good quality where onsets of the *S* waves can be determined quite accurately, whereas Fig. 9(b) shows signals of a worse quality. All picks were found manually. The accuracy of picking can be increased if waveforms at all pressure levels are plotted and interpreted simultaneously as shown in Fig. 9. Since the waveforms are often similar, the delay times between the *S*-wave arrivals at different pressure levels could also be determined automatically by cross-correlating the waveforms.

Under increasing confining pressure, the propagation velocities are increased but also anisotropy strength is changed. For example, strength of anisotropy is almost 21.4, 5.3 and 5.1 per cent at atmospheric pressure but only 11.2, 3.2 and 4.8 per cent at 70 MPa for the *P*, *S*1 and *S*2 waves, respectively.

4.4 Results

First, we focus on determining anisotropic parameters of the rock sample at pressure of 70 MPa. We calculate phase velocities from the measured ray velocities according to Section 2.2 and then we run the inversion of the phase velocities for anisotropic parameters according to Section 2.1.

Fig. 10 shows the predicted *P*-, *S*1- and *S*2-wave phase velocities when the elastic tensor was inverted from the *P*-wave velocities only, the *P*- and *S*1-wave velocities, and finally from the *P*-, *S*1- and *S*2-wave velocities. Interestingly, the predicted *P*-wave velocity pattern is very similar for all three data sets but the predicted *S*-wave velocity pattern is remarkably different. This applies to both *S*1 and *S*2 waves. The most accurate result is presented at the bottom row of Fig. 10 when the *P*-, *S*1- and *S*2-wave velocities have been inverted.

Second, we analyse an iteration process of the inversion. Fig. 11 shows the rms values of the *S*1- and *S*2-wave velocities through iterative cycles at three confining pressure levels: 0.1, 10 and 40 MPa.

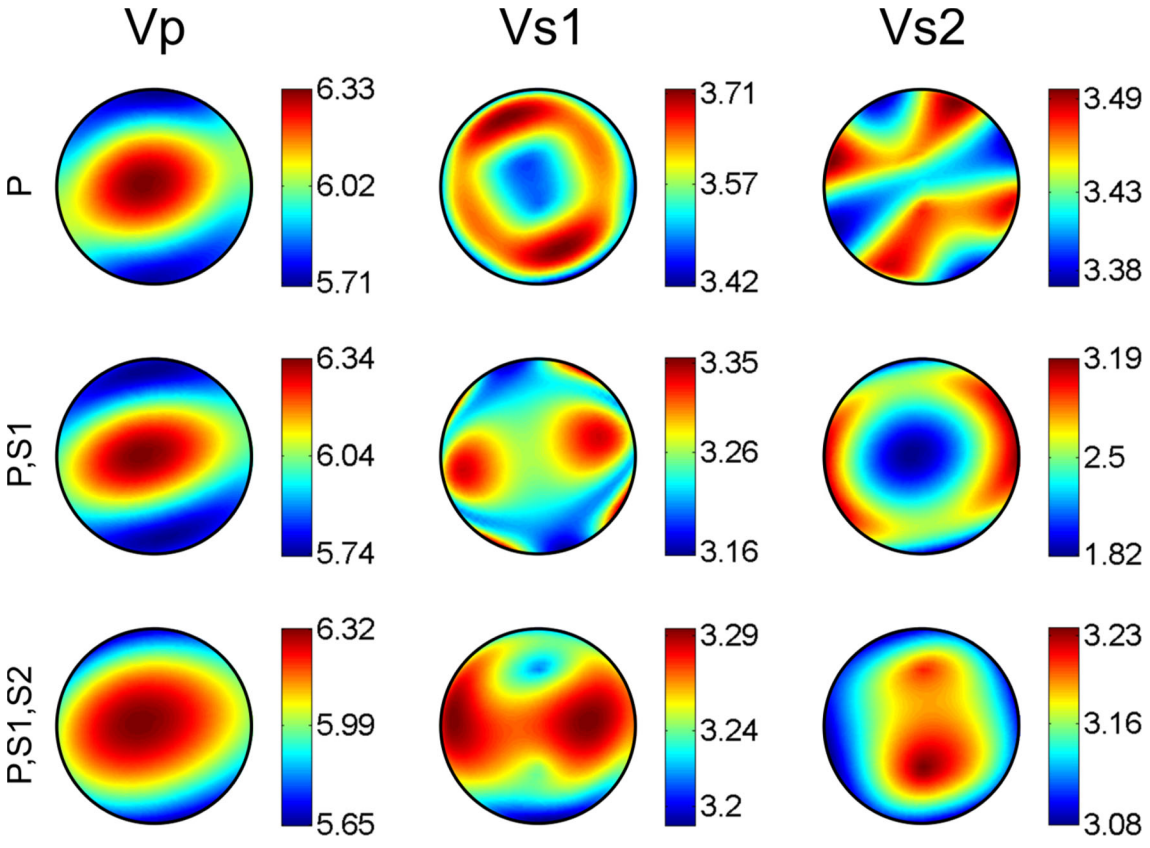

Figure 10. Phase velocities of the *P* (left-hand column), *S*1 (middle column) and *S*2 (right-hand column) waves corresponding to the elastic parameters retrieved by inverting three different data sets: the *P*-wave velocities only (top row), the *P*- and *S*1-wave velocities (middle row), and the *P*-, *S*1- and *S*2-wave velocities (bottom row). The confining pressure is 70 MPa. The colour-coded velocities are in km s^{-1}. Note a stable pattern of the *P*-wave velocities but a rather variable pattern of the *S*1- and *S*2-wave velocities, when different data sets are inverted. The most reliable and stable results are in the bottom row, where all available data are inverted.

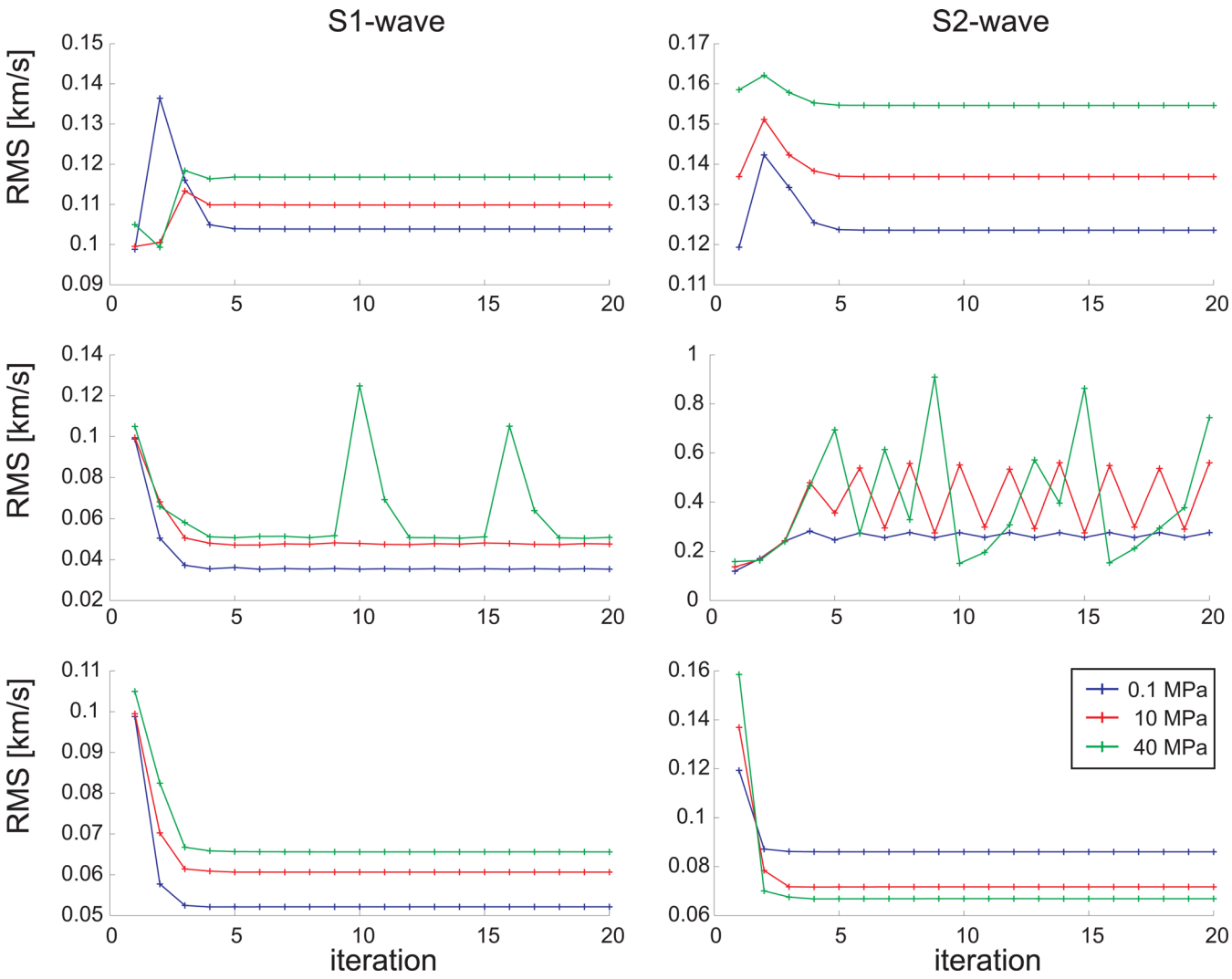

Figure 11. Convergence of iterations of the inversion for three selected confining pressure levels: 0.1 MPa (blue line), 10 MPa (red line) and 40 MPa (green line). Left-hand column: rms of the *S*1-wave velocities, right-hand column: rms of the *S*2-wave velocities, both calculated using three data sets: the *P*-waves velocities only (top row), the *P*- and *S*1-wave velocities (middle row), and the *P*-, *S*1- and *S*2-wave velocities (bottom row).

These plots demonstrate convergence of the iterations. The rms values are calculated as follows:

$$\mathrm{rms}^{S1,S2} = \sqrt{\sum \frac{\left(c_{\mathrm{obs}}^{S1,S2} - c_{\mathrm{pred}}^{S1,S2}\right)^2}{n}}, \tag{10}$$

where $c_{\mathrm{obs}}^{S1,S2}$ are the measured velocities, $c_{\mathrm{pred}}^{S1,S2}$ are the velocities calculated from the retrieved elastic tensor and n is the number of directions in which the velocities are measured. According to the behaviour of the rms values we arrive at the following conclusions:

(1) The calculation based on the '*P*-wave velocities only' method produces stable shear velocities which are not further improved through the iterative process. However, the rms value is rather high and mostly unacceptable.

(2) The calculation based on the '*P*- and *S*1-wave velocities' method produces oscillations of both predicted *S*-wave velocities among several velocity models and the rms level is unacceptable as well. The iterative process does not converge even after 20 iterations for some confining pressure values.

(3) Including measurements of the *S*2-wave velocities improves the stability of the iteration process. The predicted shear velocities converge and the rms level reaches the lowest value. The iterative process is robust and converges very quickly.

4.5 Pressure dependence of anisotropy

For distinguishing different origins of anisotropy it is important to analyse elastic properties of the rock sample as a function of confining pressure. With increasing pressure, strength of anisotropy can be changed as well as its symmetry. Since anisotropy of the sample is not weak at some of pressure levels (e.g. *P*-wave anisotropy is 21.4 per cent at the atmospheric pressure), we cannot simply neglect the differences between the ray and phase velocities. First, the ray velocities must be recalculated to the phase velocities according to Section 2.2 and then inverted according to Section 2.1.

Table 2 summarizes the elastic stiffness coefficients calculated by the iterative inversion from the *P*- and *S*-wave velocities measured at pressures of 0.1, 5, 10, 20, 40 and 70 MPa. Fig. 12 presents the calculated *P*-, *S*1- and *S*2-wave phase velocities from the retrieved elastic parameters of the sample exposed to individual pressure levels. The patterns of the *P*- and *S*-wave phase velocities indicate the commonly observed increase of velocities with confining pressure

Table 2. Elastic parameters of rock sample OKU-409 retrieved using measurements of the *P*-, *S*1- and *S*2-wave velocities at six individual levels of confining pressure.

Elastic tensor (GPa)	Pressure (MPa)					
	0.1	5	10	20	40	70
c11	80.3 ± 2.3	83.7 ± 2.0	86.6 ± 1.8	93.7 ± 1.3	96.7 ± 1.5	97.7 ± 1.6
c22	65.1 ± 0.2	70.0 ± 0.4	75.5 ± 0.5	83.0 ± 0.9	86.0 ± 0.8	87.3 ± 0.8
c33	98.3 ± 1.3	98.8 ± 1.3	101.0 ± 1.2	105.3 ± 1.1	107.1 ± 1.0	108.5 ± 1.2
c44	24.6 ± 0.7	24.8 ± 0.7	25.6 ± 0.8	26.8 ± 0.7	27.6 ± 0.8	27.9 ± 0.7
c55	25.8 ± 1.1	26.1 ± 1.1	27.1 ± 1.1	28.2 ± 0.9	29.0 ± 1.0	29.2 ± 1.0
c66	22.4 ± 0.5	22.9 ± 0.5	23.6 ± 0.7	25.0 ± 0.5	25.9 ± 0.7	26.0 ± 0.6
c12	27.1 ± 0.2	30.2 ± 0.4	32.7 ± 0.7	37.7 ± 0.6	38.9 ± 0.9	39.9 ± 0.6
c13	37.3 ± 0.8	37.9 ± 0.7	39.1 ± 0.8	42.7 ± 0.8	43.5 ± 0.7	44.1 ± 0.5
c14	0.3 ± 1.9	0.4 ± 1.5	0.1 ± 0.7	0.1 ± 0.9	−0.1 ± 0.5	−0.1 ± 0.2
c15	−0.7 ± 1.1	−0.6 ± 0.7	−0.3 ± 0.5	−0.4 ± 0.7	−0.4 ± 0.7	−0.6 ± 1.1
c16	2.5 ± 2.4	2.2 ± 2.1	1.8 ± 1.7	1.4 ± 1.6	1.5 ± 1.5	1.5 ± 1.5
c23	31.8 ± 1.3	33.0 ± 1.2	35.0 ± 1.2	38.5 ± 0.8	39.2 ± 1.2	40.2 ± 1.1
c24	0.9 ± 1.7	0.8 ± 1.8	0.5 ± 1.3	0.2 ± 0.9	0.1 ± 0.7	−0.0 ± 0.6
c25	−0.7 ± 1.1	−0.5 ± 0.7	−0.7 ± 0.9	−0.6 ± 0.9	−0.72 ± 1.10	−1.0 ± 1.5
c26	1.9 ± 2.1	1.6 ± 1.7	1.2 ± 1.4	0.8 ± 1.2	1.0 ± 1.3	1.0 ± 1.3
c34	1.9 ± 3.9	1.5 ± 3.0	1.3 ± 2.3	1.1 ± 1.8	0.7 ± 1.2	0.7 ± 1.2
c35	−1.1 ± 1.6	−1.0 ± 1.4	−0.9 ± 1.2	−0.9 ± 1.2	−0.9 ± 1.4	−1.1 ± 1.7
c36	1.6 ± 2.3	1.5 ± 2.1	1.3 ± 1.6	1.0 ± 1.5	1.3 ± 1.5	1.4 ± 1.5
c45	−0.3 ± 0.3	−0.2 ± 0.3	−0.1 ± 0.4	−0.1 ± 0.4	0.0 ± 0.4	0.1 ± 0.4
c46	0.2 ± 0.2	0.1 ± 0.1	0.4 ± 0.3	0.3 ± 0.1	0.2 ± 0.1	0.2 ± 0.2
c56	0.5 ± 0.9	0.1 ± 0.5	−0.02 ± 0.28	−0.0 ± 0.1	−0.1 ± 0.1	−0.0 ± 0.1

pointing to a progressive closure of microcracks (Pros *et al.* 1998; Nadri *et al.* 2011; Piane *et al.* 2011; Lokajíček *et al.* 2013). At pressure of 70 MPa, the effect of microcracks with a low-aspect ratio is minimized and the respective velocity surfaces reflect rather the velocity distribution of the crystallographic-preferred orientation (CPO) anisotropy. Importantly, the nearly orthorhombic symmetry of the velocity patterns observed at low pressures is preserved as pressure is increased. This indicates that crack- and CPO-related fabrics are symmetrically disposed.

Note that a pressure dependence of anisotropy was analysed for the same sample also by Lokajíček *et al.* (2014, their fig. 10). Comparing the predicted phase velocities obtained by both approaches for identical pressure levels (0.1, 20 and 70 MPa), we find that they are slightly different. These inconsistencies are produced by a less accurate inversion applied by Lokajíček *et al.* (2014) in which the differences between the ray and phase velocities were ignored.

5 CONCLUSIONS

The accuracy of the retrieved elastic tensor depends on the following factors:

(1) If only the *P*-wave velocities are measured and inverted for the elastic tensor, some value of the V_P/V_S ratio of the reference isotropic medium must be supplied in the first iteration of the inversion. In next iterations, no such information is needed and the inversion can modify all elastic parameters including those responsible mainly for values of the *S*-wave velocities. Nevertheless, if the starting value is very roughly estimated or completely incorrect, the iteration process does not converge to the true values. In this case, only a part of the elastic tensor is well retrieved and the *S*-wave related parameters C_{44}, C_{45}, C_{46}, C_{55}, C_{56} and C_{66} are inaccurate.

(2) If the *P*- and *S*1-wave velocities are measured and inverted for the elastic tensor, the problem with the artificial value of the V_P/V_S ratio supplied in the first iteration is removed. The synthetic tests show that additional information on the *S*1-wave velocities remarkably increases the accuracy of the inversion and decreases its sensitivity to the starting value of the V_P/V_S ratio. However, if a small number of measurements of the *S*1-wave velocity is included or if the measurements suffer from high picking errors, the fit between the true and predicted *P*-wave velocities can become even worse than if only the accurate *P*-wave velocities are inverted.

(3) If the *P*-, *S*1- and *S*2-wave velocities are available, the inversion results display the highest accuracy. This applies even to the case when the *S*1- and *S*2-wave velocities are measured with a significantly less accuracy than the *P*-wave velocities, for example with the *S*-wave velocity errors of 10–15 per cent compared to the *P*-wave velocity errors of 0.1 per cent. The synthetic tests as well as the processing of real data confirm that the *S*2-wave velocities included into the inversion stabilize the iterative cycle and produce the smallest deviations from observations.

(4) If the *S*1- and *S*2-wave velocities are measured in a small number of directions (6 or 30 directions), the inversion yields results with almost twice higher accuracy for regularly distributed directions than for randomly distributed directions. The more directions are inverted, the higher accuracy of the elastic tensor is obtained. Hence, measurements with a limited number of independent directions are better to carry out in a regular arrangement.

(5) The accuracy of the measured *P*-wave velocities obtained by ultrasonic measurements on spherical samples under confining loading is about 50 m s^{-1}. Based on the rms comparison of the measured and predicted *S*1- and *S*2-wave velocities it is shown that the most accurate elastic parameters are obtained if velocities of all three wave types are inverted. The rms value of real data reached a satisfactory level of 50–70 m s^{-1} and 70–90 m s^{-1} for the *S*1- and *S*2-wave velocities, respectively.

(6) If ray velocities are measured in a lab experiment and strength of anisotropy of a rock is higher than about 10 per cent, we recommend transforming the ray velocities to the phase velocities before the inversion. This transform is rather simple and improves the accuracy of the retrieved anisotropic parameters.

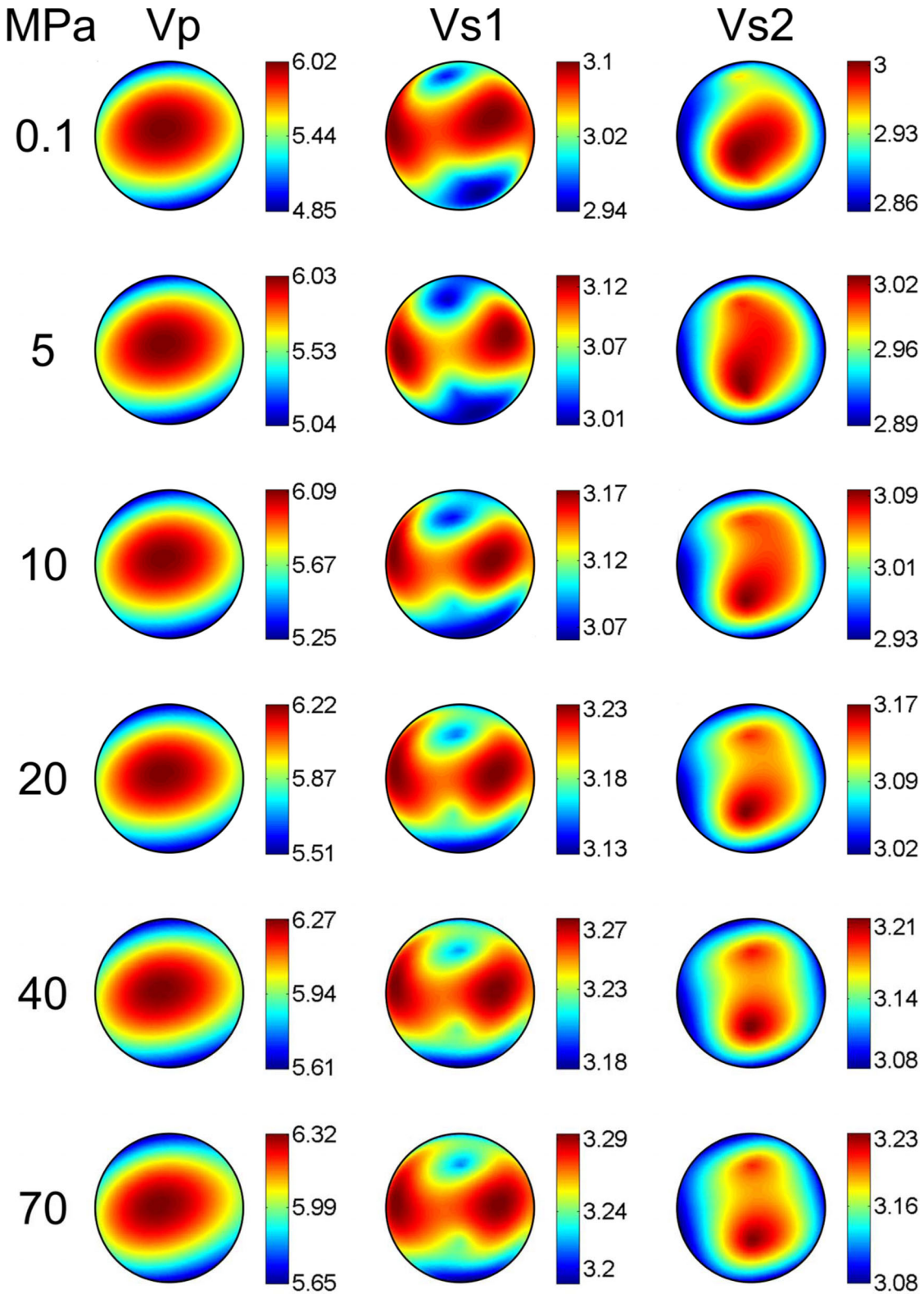

Figure 12. The *P*-, *S*1- and *S*2-wave phase velocities corresponding to the retrieved elastic parameters (see Table 2) under six levels of confining pressure. The colour-coded velocities are in km s^{-1}.

ACKNOWLEDGEMENTS

We wish to thank Andrej Bóna and an anonymous reviewer for their helpful reviews. This study was supported by the Academy of Sciences of the Czech Republic, project RVO 67985831, by the Ministry of Education, project Kontakt II LH13102, and by the Grant Agency of the Czech Republic, projects P104/12/0915, P210/12/1491 and 13–13967S.

REFERENCES

Allen, R., 1982. Automatic phase pickers: their present use and future prospects, *Bull. seism. Soc. Am.,* **72**(6), S225–S242.

Asgharzadeh, M., Bóna, A., Pevzner, V, Urosevic, M. & Gurevich, B., 2013. Reliability of the slowness and slowness-polarization methods for anisotropy estimation in VTI media from 3C walkaway VSP data, *Geophysics,* **78**(5), WC93–WC102.

Bóna, A., Bucataru, I. & Slawinski, M.A., 2008. Inversion of ray velocity and polarization for elasticity tensor, *J. appl. Geophys.,* **65**(1), 1–5.

Bóna, A., Nadri, D. & Brajanovski, M., 2012. Thomsen's parameters from P-wave measurements in a spherical sample, *Geophys. Prospect.,* **60**(1), 103–116.

Červený, V., 2001. *Seismic Ray Theory,* Cambridge Univ. Press.

Christensen, N.I., 1966. Elasticity of ultrabasic rocks, *J. geophys. Res.,* **71**(24), 5921–5931.

Crampin, S., 1985. Evaluation of anisotropy by shear-wave splitting, *Geophysics,* **50**(1), 142–152.

Dewhurst, D.N. & Siggins, A.F., 2006. Impact of fabric, microcracks and stress field on shale anisotropy, *Geophys. J. Int.,* **165**(1), 135–148.

Elbra, T., Karlqvist, R., Lassila, I., Hæggström, E. & Pesonen, L.J., 2011. Laboratory measurements of the seismic velocities and other petrophysical properties of the Outokumpu deep drill core samples, eastern Finland, *Geophys. J. Int.,* **184,** 405–415.

Farra, V. 2004. Improved first-order approximation of group velocities in weakly anisotropic media, *Stud. Geophys. Geod.,* **48,** 199–213.

Helbig, K., 1994. *Foundations of Anisotropy for Exploration Seismics,* Pergamon.

Hornby, B.E., 1998. Experimental laboratory determination of the dynamic elastic properties of wet, drained shales, *J. geophys. Res.,* **103**(B12), 29 945–29 964.

Ildefonse, B., Launeau, P., Bouchez, J.-L. & Fernandez, A. (1992). Effect of mechanical interactions on the development of shape preferred orientations: a two-dimensional experimental approach, *J. Struct. Geol.,* **14**(1), 73–83.

Ivankina, T.I., Kern, H.M. & Nikitin, A.N., 2005. Directional dependence of P- and S-wave propagation and polarization in foliated rocks from the Kola superdeep well: evidence from laboratory measurements and calculations based on TOF neutron diffraction, *Tectonophysics,* **407**(1–2), 25–42.

Jech, J., 1991. Computation of elastic parameters of anisotropic medium from travel times of quasi-compressional waves, *Phys. Earth planet. Inter.,* **66**(3–4), 153–159.

Jech, J. & Pšenčík, I., 1989. First-order perturbation method for anisotropic media, *Geophys. J. Int.,* **99,** 369–376.

Karato, S., 2008. *An Introduction to Rheology of Solid Earth,* Cambridge Univ. Press.

Kern, H., 1982. Elastic-wave velocity in crustal and mantle rocks at high pressure and temperature: the role of the high-low quartz transition and of dehydration reactions, *Phys. Earth planet. Inter.,* **29**(1), 12–23.

Kern, H., Ivankina, T.I., Nikitin, A.N., Lokajíček, T. & Pros, Z., 2008. The effect of oriented microcracks and crystallographic and shape preferred orientation on bulk elastic anisotropy of a foliated biotite gneiss from Outokumpu, *Tectonophysics,* **457**(3–4), 143–149.

Kern, H., Mengel, K., Strauss, K.W., Ivankina, T.I., Nikitin, A.N. & Kukkonen, I.T., 2009. Elastic wave velocities, chemistry and modal mineralogy of crustal rocks sampled by the Outokumpu scientific drill hole: evidence from lab measurements and modeling, *Phys. Earth planet. Inter.,* **175**(3–4), 151–166.

Kitamura, K., 2006. Constraint of lattice-preferred orientation (LPO) on Vp anisotropy of amphibole-rich rocks, *Geophys. J. Int.,* **165**(3), 1058–1065.

Klíma, K., 1973. The computation of the elastic constants of an anisotropic medium from the velocities of body waves, *Stud. Geophys. Geod.,* **17**(2), 115–122.

Kukkonen, I.T., Rath, V., Kivekas, L., Šafanda, J. & Čermák, V., 2011. Geothermal studies of the Outokumpu Deep Drill Hole, Finland: vertical variation in heat flow and palaeoclimatic implications, *Phys. Earth planet. Int.,* **188,** 9–25.

Lipschutz, S., 1969. *Theory and Problems of Differential Geometry,* McGraw-Hill.

Lokajíček, T. & Klíma, K., 2006. A first arrival identification system of acoustic emission (AE) signals by means of a high-order statistics approach, *Measur. Sci. Technol.,* **17**(9), 2461–2466.

Lokajíček, T., Goel, R.K., Rudajev, V. & Dwivedi, R.D., 2013. Assessment of velocity anisotropy in rocks, *Int. J. Rock Mech. Min. Sci.,* **57,** 142–152.

Lokajíček, T., Kern, H., Svitek, T. & Ivankina, T., 2014. 3D velocity distribution of P- and S-waves in a biotite gneiss, measured in oil as the pressure medium: comparison with velocity measurements in a multi-anvil pressure apparatus and with texture-based calculated data, *Phys. Earth planet. Inter.,* **231,** 1–15.

Mainprice, D. & Nicolas, A., 1989. Development of shape and lattice preferred orientations: application to the seismic anisotropy of the lower crust, *J. Struct. Geol.,* **11**(1), 175–189.

Mensch, T. & Rasolofosaon, P., 1997. Elastic-wave velocities in anisotropic media of arbitrary symmetry—generalization of Thomsen's parameters ε, δ and γ, *Geophys. J. Int.,* **128,** 43–63.

Musgrave, M.J.P., 1970. *Crystal Acoustics,* Holden-Day.

Nadri, D., Bona, A., Brajanovski, M. & Lokajíček, T., 2011. Estimation of stress-dependent anisotropy from P-wave measurements on a spherical sample, *Geophysics,* **76**(3), WA91–WA100.

Nikitin, A.N. & Ivankina, T.I., 2004. Neutron diffractometry in geosciences, *Phys. Particle Nucl.,* **35**(2), 193–224.

Okaya, D., Rabbel, W., Beilecke, T. & Hasenclever, J., 2004. P wave material anisotropy of tectono-metaorphic terrane: an active source seismic experiment at the KTB super-deep drill hole, southeast Germany, *Geophys. Res. Lett.,* **31,** L24620, doi:10.1029/2004GL020855.

Peng, Z. & Ben-Zion, Y., 2004. Systematic analysis of crustal anisotropy along the Karadere-Düzce branch of the north Anatolian fault, *Geophys. J. Int.,* **159,** 253–274.

Piane, C.D., Dewhurst, D.N., Siggins, A.F. & Raven, M.D., 2011. Stress-induced anisotropy in brine saturated shale, *Geophys. J. Int.,* **184**(2), 897–906.

Pros, Z., Lokajíček, T. & Klíma, K., 1998. Laboratory approach to the study of elastic anisotropy on rock samples, *Pure Appl. Geophys.,* **151**(2–4), 619–629.

Pšenčík, I. & Gajewski, D., 1998. Polarization, phase velocity and NMO velocity of qP waves in arbitrary weakly anisotropic media, *Geophysics,* **63,** 1754–1766.

Pšenčík, I. & Vavryčuk, V., 2002. Approximate relation between the ray vector and wave normal in weakly anisotropic media, *Stud. Geophys. Geod.,* **46,** 793–807.

Savage, M.K., 1999. Seismic anisotropy and mantle deformation: What have we learned from shear wave splitting?, *Rev. Geophysics,* **37,** 65–106.

Sayers, C.M., 2002. Fluid-dependent shear-wave splitting in fractured media, *Geophys. Prospect.,* **50**(4), 393–401.

Sayers, C.M. & Kachanov, M., 1995. Microcrack-induced elastic-wave anisotropy of brittle rocks, *J. geophys. Res.,* **100**(B3), 4149–4156.

Sedlák, P., Hirose, Y., Khan, S.A., Enoki, M. & Sikula, J., 2009. New automatic localization technique of acoustic emission signals in thin metal plates, *Ultrasonics,* **49**(2), 254–262.

Siegesmund, S., Kern, H. & Vollbrecht, A., 1991. The effect of oriented microcracks on seismic velocities in an ultramylonite, *Tectonophysics,* **186**(3–4), 241–251.

Svitek, T., Rudajev, V. & Petružálek, M., 2010. Determination of P–wave arrival time of acoustic events, *Acta Montan. Slov.,* **15**(2), 145–151.

Valcke, S.L.A., Casey, M., Lloyd, G.E., Kendall, J.-M. & Fisher, Q.J., 2006. Lattice preferred orientation and seismic anisotropy in sedimentary rocks, *Geophys. J. Int.,* **166**(2), 652–666.

Vavryčuk, V., 1997. Elastodynamic and elastostatic Green tensors for homogeneous weak transversely isotropic media, *Geophys. J. Int.,* **130,** 786–800.

Vavryčuk, V., 2005a. Acoustic axes in triclinic anisotropy, *J. Acoust. Soc. Am.,* **118,** 647–653.

Vavryčuk, V., 2005b. Acoustic axes in weak triclinic anisotropy, *Geophys. J. Int.,* **163,** 629–638.

Vavryčuk, V., 2006. Calculation of the slowness vector from the ray vector in anisotropic media, *Proc. Roy. Soc. A,* **462,** 883–896.

Vavryčuk, V., 2009. Weak anisotropy-attenuation parameters, *Geophysics,* **74**(5), WB203–WB213.

Vavryčuk, V., 2013. Inversion for weak triclinic anisotropy from acoustic axes, *Wave Motion,* **50**(8), 1271–1282.

Wang, X.-Q., Schubnel, A., Fortin, J., David, E.C., Guéguen, Y. & Ge, H.-K., 2012. High Vp/Vs ratio: Saturated cracks or anisotropy effects?, *Geophys. Res. Lett.,* **39**(11), L11307, doi:10.1029/2012GL051742.

Wenk, H.-R., Vasin, R.N., Kern, H., Matthies, S., Vogel, S.C. & Ivankina, T.I., 2012. Revisiting elastic anisotropy of biotite gneiss from the Outokumpu scientific drill hole based on new texture measurements and texture-based velocity calculations, *Tetonophysics,* **570–571,** 123–134.

Xie, Y., Wenk, H.-R. & Matthies, S., 2003. Plagioclase preferred orientation by TOF neutron diffraction and SEM-EBSD, *Tectonophysics,* **370**(1–4), 269–286.

Príloha 5

Publikácia 4:

Lokajíček, T., Kern, H., **Svitek, T.**, & Ivankina, T. (2014). **3D velocity distribution of P- and S-waves in a biotite gneiss, measured in oil as the pressure medium: Comparison with velocity measurements in a multi-anvil pressure apparatus and with texture-based calculated data**. *Phys. Earth Planet. Inter*, 231, 1–15.
doi:10.1016/j.pepi.2014.04.002

Physics of the Earth and Planetary Interiors 231 (2014) 1–15

Contents lists available at ScienceDirect

Physics of the Earth and Planetary Interiors

journal homepage: www.elsevier.com/locate/pepi

3D velocity distribution of P- and S-waves in a biotite gneiss, measured in oil as the pressure medium: Comparison with velocity measurements in a multi-anvil pressure apparatus and with texture-based calculated data

T. Lokajíček [a,*], H. Kern [b], T. Svitek [c,a], T. Ivankina [d]

[a] Institute of Geology AS CR, v. v. i., Rozvojová 269, 165 00 Prague 6, Czech Republic
[b] Institute of Geosciences, University of Kiel, Olshausenstr., 40, D-24098 Kiel, Germany
[c] Charles University in Prague, Faculty of Science, Albertov 6, 128 43 Prague 2, Czech Republic
[d] Joint Institute for Nuclear Research, Frank Laboratory of Neutron Physics, 141980 Dubna, Russia

ARTICLE INFO

Article history:
Received 23 November 2013
Received in revised form 6 April 2014
Accepted 13 April 2014
Available online 24 April 2014

Keywords:
Velocity measurements
Neutron diffraction
3D-velocity calculation
Seismic anisotropy
Measured and calculated elastic properties

ABSTRACT

Ultrasonic measurements of the 3D velocity distribution of P- and S-waves were performed on a spherical sample of a biotite gneiss from the Outokumpu scientific drill hole. Measurements were done at room temperature and pressures up to 400 and 70 MPa, respectively, in a pressure vessel with oil as a pressure medium. A modified transducer/sample assembly and the installation of a new mechanical system allowed simultaneous measurements of P- and S-wave velocities in 132 independent directions of the sphere on a net in steps of 15°. Proper signals for P- and S-waves could be recorded by coating the sample surface with a high-viscosity shear wave gel and by temporal point contacting of the transmitter and receiver transducers with the sample surface during the measurements. The 3D seismic measurements revealed a strong foliation-related directional dependence (anisotropy) of P- and S-wave velocities, which is confirmed by measurements in a multi-anvil apparatus on a cube-shaped specimen of the same rock. Both experimental approaches show a marked pressure sensitivity of P- and S-wave velocities and velocity anisotropies. With increasing pressure, P- and S-wave velocities increase non-linearly due to progressive closure of micro-cracks. The reverse is true for velocity anisotropy. 3D velocity calculations based on neutron diffraction measurements of crystallographic preferred orientation (CPO) of major minerals show that the intrinsic bulk anisotropy is basically caused by the CPO of biotite constituting about 23 vol.% of the rock. Including the shape of biotite grains and oriented low-aspect ratio microcracks into the modelling increases bulk anisotropy. An important finding from this study is that the measurements on the sample sphere and on the sample cube displayed distinct differences, particularly in shear wave velocities. It is assumed that the differences are due to the different geometries of the samples and the configuration of the transducer–sample assembly. On the spherical sample with a point source and point receiver the first break at the velocity arrival time is suggested to define group velocities in most cases, whereas the receivers in the multi-anvil apparatus recorded the flat part of the wavefront, that is, phase velocities.

1. Introduction

During the past, numerous measurements of the 3D velocity distribution of P-waves were performed on sample spheres of crustal and mantle rocks at the Institute of Geology of the Academy of Sciences in Prague (Pros et al., 2003; Kern et al., 2008). Measurements were done at room temperature in a pressure vessel up to 400 MPa with oil as the pressure medium. Up to now, measurements of S-wave velocities were not possible with this device, because the transducers and the 3D positioning system were placed in oil, and fluids do not transmit S-waves. We have modified this high pressure system initially developed by Pros et al. (1998), and supplemented the set of P-wave transducers by two pairs of S-wave transducers, and by installation of a mechanism allowing temporal point contact with the sample without any disturbance by the fluid during the measurements (for details see Lokajíček, 2013).

* Corresponding author. Tel.: +420 603439096; fax: +420 224239102.
E-mail address: tl@gli.cas.cz (T. Lokajíček).

http://dx.doi.org/10.1016/j.pepi.2014.04.002
0031-9201/

In this contribution we will show that both, P- and S-wave velocities, can be measured simultaneously with this device at pressures up to 400 and 70 MPa, respectively. Here we report data of the 3D velocity distribution of P- and S-waves measured for the first time on a sample sphere of biotite gneiss. We will rely, in particular, on the directional dependence of compressional and shear wave propagation and their relationship to the crystallographic (CPO) and shape preferred orientation (SPO) of major rock-forming minerals.

The results obtained on the spherical sample are compared with data measured on a cube-shaped specimen of the same rock in a multi-anvil pressure apparatus at the Institute of Earth Sciences, University of Kiel (Germany) in order to verify that the system works properly. Measurements on the sample sphere and cube were done on dry samples using the ultrasonic pulse transmission technique. In addition, comparison is made with texture-based 3D velocity calculations with and without taking into account the effect of grain shape (SPO) and of low-aspect ratio microcracks. The analysis for CPO was performed on the same sample sphere used for the ultrasonic velocity measurements. The measurements were done at the Joint Institute for Nuclear Research (JINR) in Dubna (Russia), with the SKAT texture diffractometer at the pulse reactor IBR-2.

2. Experimental methods

The equipment for the measurement of the 3D velocity distribution of sample spheres at the Institute of Geology in Prague consists of a pressure vessel connected to a two-step pressure generator, a sample positioning unit equipped with the ultrasonic piezoceramic transducers, a device for generating ultrasonic pulses and travel time measurement and data acquisition (Pros et al., 1998). All moving mechanical parts are located inside the pressure vessel. Details of the device are shown in Fig. 1a.

The assembly of transducers comprise one set of longitudinal (P) and two pairs of shear wave (SV and SH) transducers (transmitter and receiver) with parallel and perpendicular polarization of the shear wave transducers, namely T_V, R_V and T_H, R_H, respectively. Isolation of the sample with 50 mm ± 0.01 mm in diameter from oil within the pressure vessel is achieved by coating the sample surface with a thin layer of epoxy. An additional thin cover of a high-viscosity shear wave gel provides the necessary point contact of the transducers with the sample during the measurements without any disturbance by the fluid. The measuring head allows to rotate the spherical sample around its vertical axis by 360° and to move the piezosensor assembly around a horizontal axis over the sample surface in the range from −75° to +75°. A stepwise contacting of the spherical sample during the measurement is achieved by the direct current DC motor moving the transducers to and from the sample surface. All data sets recorded during one measuring cycle for SV (recorded by R_V) and SH (recorded by R_H) deviate by +15° and −15° from the direction of V_p measurement. They are transformed/rotated to the same angle position after the measurement. Velocities are obtained in 132 directions. For the analysis of the 3D distribution of P- and S-wave velocities we used an angular grid of 15°.

The geometry of the piston–sample arrangement in the multi-anvil pressure apparatus of the Institute of Earth Sciences at Kiel allows simultaneous measurements of compressional and two orthogonally polarized shear wave velocities (S_V, S_H) in the three perpendicular directions of a sample cube at pressure (up to 600 MPa) and temperature (up to 750 °C) (Kern et al., 1997). A sketch illustrating the transducer–piston–sample assembly is shown in Fig. 1b. A state of near-hydrostatic stress is achieved by pressing six pyramidal pistons in the three orthogonal directions onto the cube-shaped specimen with edge length of 43 mm. Because the apparatus was constructed for measurements under pressure and temperature, the transducers are placed at the low-temperature side of the pistons to prevent problems with the Curie temperature of the transducers. Both pairs of S-wave transducers (transmitter and receiver) have the same polarization. The travel time of the pulses through the specimen is obtained by subtracting the calibrated time needed for the pulse to travel to and from the specimen through the pistons from the total time measured by the transducers. A complete set of experimental data comprises three P-wave velocities, six S-wave velocities and the length change (volume change) of the sample as derived from the piston displacement.

The texture measurements at the Frank Laboratory of Neutron Physics at JINR (Dubna, Russia) were done with the time-of-flight texture (TOF) diffractometer SKAT. Neutrons were produced by the pulsed nuclear reactor IBR-2 (e.g., Walther et al., 1995). Texture measurements by neutron diffraction are most suitable for investigations of large sample volumes, because of the high penetration depth and low absorption of neutrons for most elements.

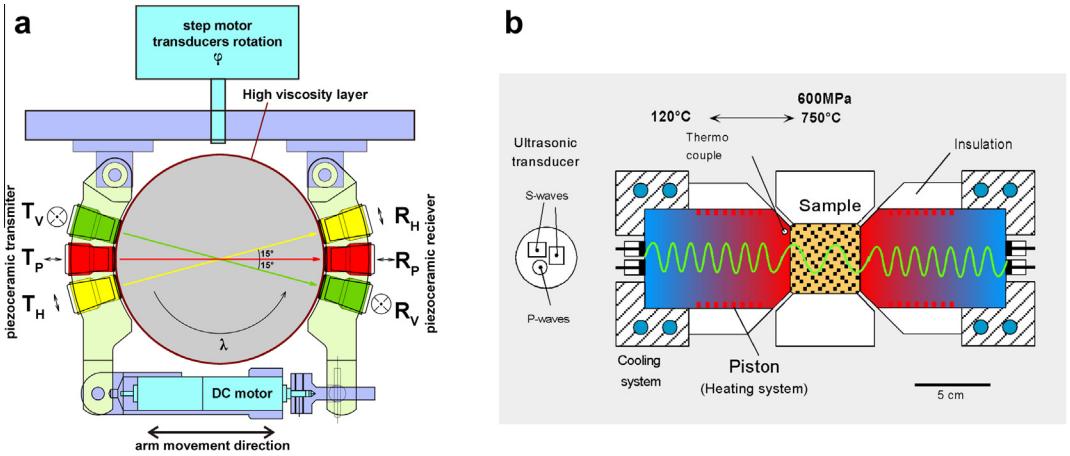

Fig. 1. Schematics of the transducer–sample arrangement. (a) Positioning unit of the pressure vessel at the Institute of Geology in Prague. P – couple of longitudinal piezoceramic transducers, T_V, R_V – pairs of shear wave transducer with vertical polarization, T_H, R_H – pairs of shear wave transducers with horizontal polarization. Rotations of the sphere and arms are indicated by arrows, DC motor – motor for arm movement to enable positioning of sphere and transducers. (b) Transducer–piston–sample assembly in the multi-anvil pressure apparatus at the Institute of Earth Sciences, Kiel University, for velocity measurements in three orthogonal directions of a sample cube at pressure and temperature.

Compared to previous measurements (Kern et al., 2009; Ivankina et al., 2005), the experimental conditions for the texture measurements of geomaterials by means of the diffractometer SKAT have been optimized by modernization of the reactor (2007–2011) and the neutron guide system, and by installation of two more detector systems at scattering angles of $2\theta = 65°$ and 135°, respectively. For the current measurements we used a detector system at the scattering angle of $2\theta = 90°$.The sample was rotated to 36 positions in 10° increments, producing 684 spectra. The exposition time at one sample position was 60 min., so the whole measuring time for the sample was 36 h. By reducing the number of sample directions to be measured we improved counting statistics at the same beam time. We applied the Rietveld method (Lutterotti et al., 1997; Wenk et al., 2010), which relies on full diffraction spectra, to separate overlapping peaks and to provide quantitative orientation distributions of rock forming minerals (Wenk et al., 2012)

3. Rock sample, mineral composition and rock fabric

Sample sphere and cube-shaped sample were prepared from a core segment (about 10 cm in length, 10 cm diameter) of the Outokumpu scientific drill hole (Kukkonen, 2011) recovered from 409 m depth (Kern et al., 2009). The sample cube (43 mm on edge) as well as the sample sphere (50 mm in diameter) were taken from the center of the upper and lower half of the core, respectively, ensuring that disturbance of the microstructure by drilling was minimized. Bulk density of the rock sample as calculated from mass and dimensions of the cube is 2.724 g/cm^3.

The sample is homogeneous biotite gneiss with pronounced foliation and lineation. The modal composition is 39.6 vol.% quartz, 36.9 vol.% plagioclase, 23.4 vol.% biotite, as determined by mass balance calculations (Kern et al., 2009, Table 2). Foliation and lineation are defined by platy and elongated biotite minerals exhibiting strong shape preferred orientation (SPO). The biotite grains are elongated subparallel to the lineation direction, ranging in length from 0.4 to 2 mm (Fig. 2a). Normal to lineation, lengths are between 0.4 and 1 mm (Fig. 2b). The thickness of the biotite platelets perpendicular to foliation is about 5–300 μm (Fig. 2b). Quartz and plagioclase are more or less equiaxed with an average grain size of 0.1 mm. The platy biotite minerals are almost isolated and do not form compositional layers. The structural reference frame X, Y, Z is defined by foliation and lineation. XY is foliation, X is lineation and Z is the foliation normal.

Whereas the foliation is clearly contoured by its traces on the section cut parallel to lineation (Fig. 2a), the traces of the foliation are only weakly evident on the section cut normal to lineation (Fig. 2b).This is particularly due to the fact that the biotite minerals exhibit disk-like shapes rotated to some degree around X, so that proper tracing of the foliation plane (XY) was difficult.

The crystallographic preferred orientation (CPO) of the major minerals was obtained by analyzing the time-of flight neutron diffraction data with the Rietveld method. Fig. 3 presents selected pole figures for biotite, plagioclase and quartz, recalculated from the orientation distribution functions (ODFs) applying the WIMV method (Matthies, 2002). The alignment of platy biotite minerals give rise to strong crystallographic preferred orientation (CPO). In an equal area projection, the (001) pole figure of biotite shows a strong single maximum almost perpendicular to the foliation plane with an angular spread towards the Y direction. The poles of the (010) and (100) planes are concentrated on great circles parallel to the foliation plane indicating a quasi-axial symmetry. The CPOs of plagioclase and quartz are weak and within experimental uncertainties. Their patterns are asymmetric relative to foliation and lineation.

4. Experimental P- and S-wave velocities and velocity anisotropy

In foliated gneisses, P-wave velocities are generally highest within the foliation plane with maximum values parallel to lineation (X). Lowest velocities are almost always measured normal to foliation (parallel Z) (e.g., Kern et al., 2009; Ji and Salisbury, 1993). Fig. 4 shows the 3D velocity surface for P-waves obtained by the measurements on the sample sphere projected onto the core segment from which the sample sphere was prepared. The directions of maximum [X], intermediate [Y] and minimum velocities [Z], are considered to properly define the structural frame of the rock sample under study. The minimum velocity direction [Z] is found to be subparallel to the core axis and the foliation plane (XY) subnormal to it. With respect to the foliation-related principal directions of the velocity surface derived from the measurements on the sample sphere, the three orthogonal directions of the sample cube X*, Y*, Z* prepared for the measurements in the multi-anvil pressure apparatus are not completely in accordance with the structural reference frame. Whereas X* is parallel to X, the Y* and Z* directions deviate from Y and Z by about 20°, that is, compared to the spherical sample, the reference frame of the sample cube is tilted by about 20° around the lineation X (Fig. 4).

The measurements of P-wave velocities in the pressure vessel and in the multi-anvil pressure apparatus were done at pressures up to 400 MPa. Fig. 5 compares the velocity–pressure relations for P-waves measured in X*, Y*, and Z* of the sample sphere (Fig 5a) with those obtained by the measurements on the sample cube (Fig. 5b). Both set of curves correspond fairly well with respect to the slopes of the curves. The velocity–pressure relations display

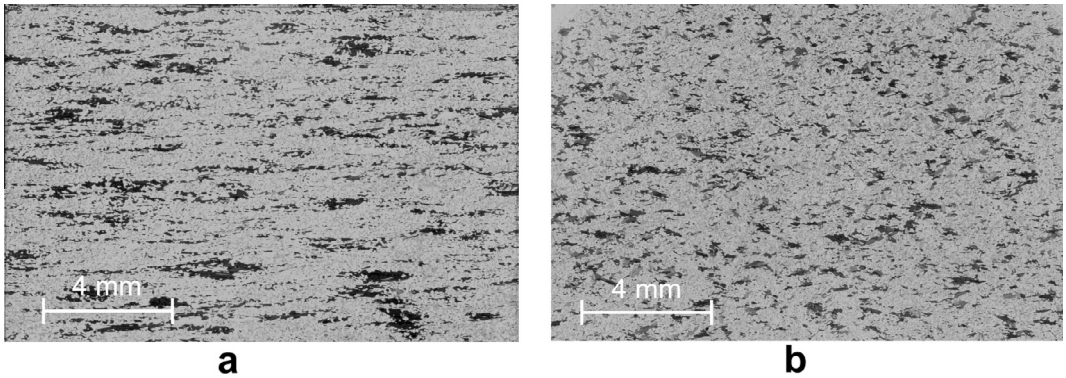

Fig. 2. Optical microphotographs illustrating microstructures of biotite gneiss sample 409. Plane-polarized light. (a) Section cut parallel to lineation and +/− normal to foliation. (b) Section cut normal to lineation.

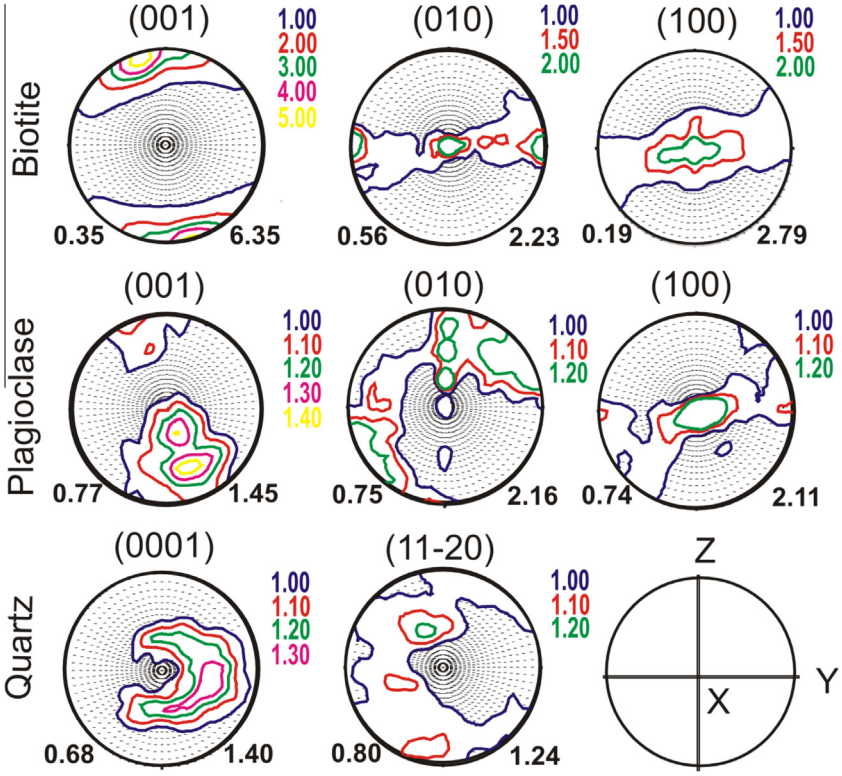

Fig. 3. Recalculated pole figures for biotite, plagioclase and quartz based on neutron diffraction measurements. Equal area projection onto the ZY-plane, lower hemisphere. Contours in multiples of random distribution (m.r.d.).

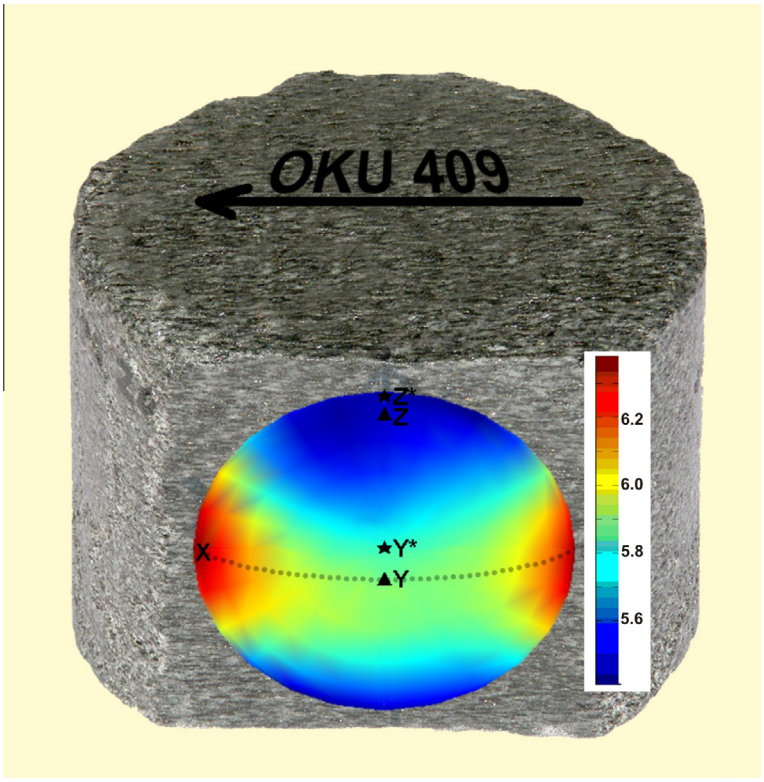

Fig. 4. Lower hemisphere equal area projection of the P-wave velocities measured on the sample sphere onto the OKU409 core segment. Note that the directions of maximum (X), intermediate (Y) and minimum velocities (Z) defining the structural reference frame of the sample sphere are not strictly in accordance with the three orthogonal measuring directions X*, Y*, Z* of the sample cube.

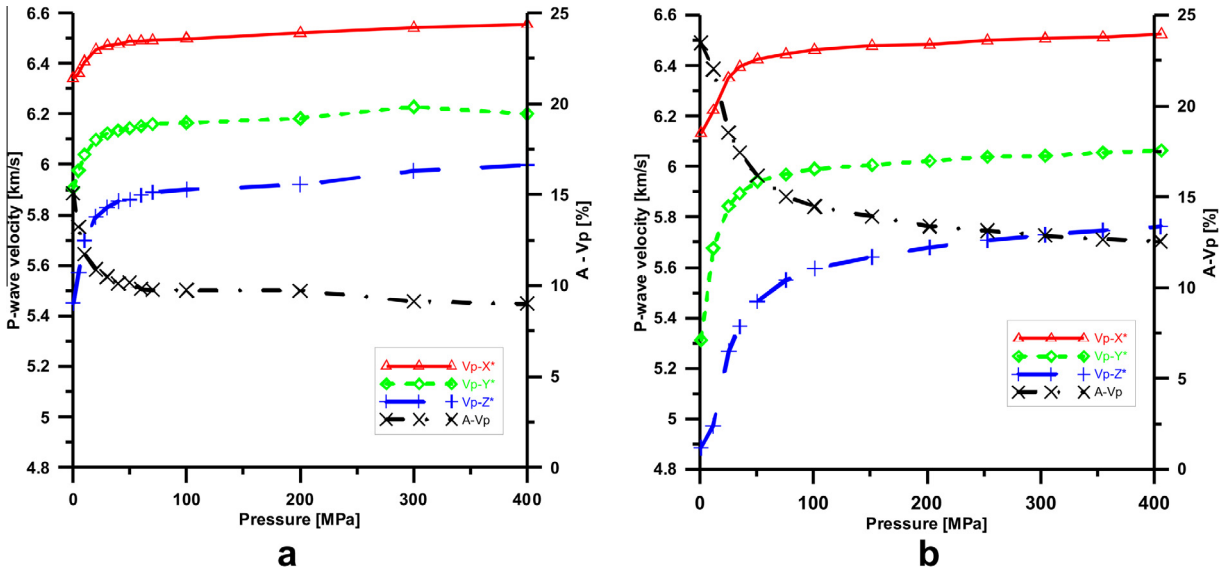

Fig. 5. Experimental ultrasonic P-velocities in X*, Y*, and Z* directions and P-wave anisotropy as function of pressure (a) sample sphere (b) sample cube.

the well-known non-linear velocity increase with confining pressure due to progressive closure of microcracks resulting from sample compaction, which is highest normal (subnormal) to the foliation plane. At pressures above 100 MPa the slopes tend to become linear indicating that most of the low-aspect ratio cracks are closed. V_p is highest parallel to X*, intermediate parallel to Y* and lowest parallel to Z*. However, there are differences in the absolute values of P-wave velocities measured on the spherical and cube-shaped sample. Whereas V_p measured in the X* and Y* direction of the sphere and cube are nearly identical, velocities measured on the sphere are lower in the Z* direction. Maybe that the fast paths that avoid cracks were over-represented in the first arrivals at the point receivers for the measurements on the sphere. Nevertheless, the differences of P-wave velocities measured in the three orthogonal directions X*, Y*, Z* of the sample sphere as well as on the sample cube indicate a strong velocity anisotropy defined by the percent differences between maximum and minimum velocity with respect to mean velocity as defined by Birch (1961): [$A = (Vmax - Vmin)/(Vmean)100\%$]. From the pressure dependence, it is concluded that oriented microcracks are a major contribution to velocity anisotropy at low pressure. Increasing pressure reduces the effect of cracks in a non-linear slope approaching nearly constant values at high pressures. Thus, the almost pressure-independent part of bulk anisotropy is mainly caused by CPO and anisotropy of the component minerals. Bulk velocity anisotropy of P-waves as derived from the measurements in X*, Y*, Z* at 400 MPa on the sample sphere and sample cube is about 9.8% and 12.55%, respectively.

The overall volume change at 400 MPa as determined by the piston displacement is about 1.2%.

It is important to note that P- and S-waves travelling through an anisotropic body are only "pure" waves when their propagation direction is parallel or perpendicular to the symmetry axis (Nishizawa and Kanagawa, 2010.). In off-axis directions, they are not the true P and S waves but quasi-P (qP) and quasi-S waves (qS). Consequently, in the present experiments V_p is generally a quasi-compressional and V_{S1} and V_{S2} are generally quasi-shear waves since particle motion is neither parallel or perpendicular to the symmetry axis in most cases. This means that shear wave velocities recorded by the two receiving transducers R_V and R_H do represent only vector components of the fast and slow split shear waves. Only when propagating along the symmetry axis or in the symmetry plane of transversally isotropic polycrystals, the two shear waves are the true S waves polarized perpendicular to the propagation direction. In case of transvers isotropy (TI) the two shear wavespeeds are equal for propagation along the symmetry axis. Thus, for shear waves propagating through anisotropic media the vibration directions are as important as the propagation directions (Christensen, 1985).

An important diagnostic of seismic anisotropy is shear wave splitting, the elastic equivalent of the birefringence phenomenon in optics. When a seismic shear wave travels through an elastically anisotropic medium, its energy is split into two orthogonally polarized components that travel at different velocities The polarization direction of the fastest wave is called fast direction and the lag of the slower wave is the delay time.

For a proper identification of the first S-wave arrival, the signal wave forms of different pressures were gathered. Figs. 6 and 7 presents the wave forms (S1, S2) measured in the three directions X*, Y*, Z* for selected pressures on the sample sphere (up to 70 MPa) and on the sample cube (up to 100 MPa), respectively. Whereas the first arrivals of S-waves are well-defined on the diagrams obtained from the measurements on the sample cube, the respective patterns of the spherical sample are more complex so that a proper reading of the first S-wave arrival is not as easy. Nevertheless, gathering of the wave forms allowed a proper pick up of the first S-wave arrivals in most cases.

In Fig. 8 we compare the S-wave velocities of the sample sphere for the X*, Y*, Z* directions (Fig. 8a) as derived from the velocity surfaces shown in Fig. 10 (lower line) with those of the sample cube (Fig. 8b) The non-linear increase of the S-wave velocities reflects again progressive closure of microcracks with increasing pressure. Shear wave splitting is highest in the X*Y*-plane, and lowest normal to it. Fast S-waves are generally polarized parallel to X*Y*. However, there is a marked difference to be observed when comparing the absolute values of S-wave velocities measured on the sphere and on the cube. Velocities of the spherical sample are found to be systematically lower than those of the sample cube. This also holds for shear wave splitting.

5. Calculation of the 3D velocity surfaces from measured P- and S-wave velocities

In order to calculate the 3D velocity distribution from measured P- and S-wave velocities measured on the sample sphere, we

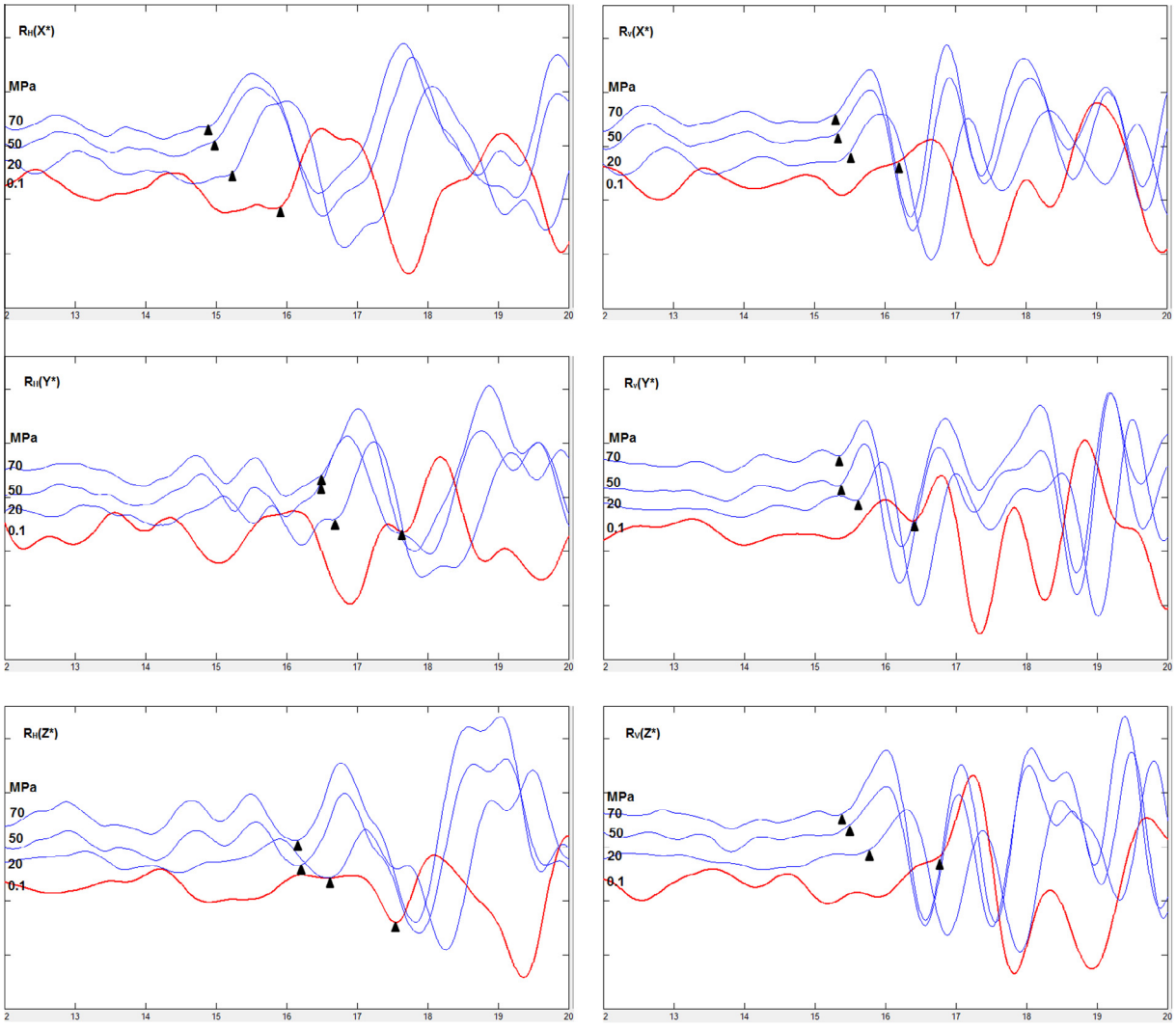

Fig. 6. S-wave forms (S1, S2) measured in the three orthogonal directions X*, Y*, Z* on the sample sphere for selected pressures up to 70 MPa. Arrival times are shown by black triangles.

determined the stiffness coefficients by means of the Christoffel equation (Červený, 2001).

$$\det\left(\Gamma_{ij} - c^2\delta_{ij}\right) = 0 \tag{1}$$

where c is the phase velocity of the P, S1 or S2 waves, δ_{ij} is the Kronecker delta, and Γ_{ij} is the Christoffel tensor,

$$\Gamma_{ij} = a_{ijkl}N_kN_l. \tag{2}$$

Parameters a_{ijkl} are the components of the tensor of density-normalized elastic (stiffness) parameters, and vector N is the phase normal. If elastic parameters a_{ijkl} are known, Eq. (1) is the cubic equation for the squared phase velocity c. If the phase velocity c is known from measurements, Eq. (1) defines an inverse problem for calculating elastic parameters a_{ijkl}.

For the determination of the complete elastic tensor (21 elastic parameters) it is necessary to know at least 15 P-wave velocities and 6 S-waves velocities in different directions with exact precision. The calculation of the elastic tensor parameters represents a non-linear inverse problem that is linearized by an iterative process using perturbation theory (Jech and Pšenčík, 1989; Jech, 1991; Klíma and Červený, 1973; Vavryčuk, 2013); see Eq. (3) and Eq. (8). From measured velocities of P-, S1- and S2-waves ($V_t^{P,S1,S2}$) differences of individual parameters Δa_{ijkl} were calculated and, subsequently, the complete tensor of elastic parameters, i.e., 21 elastic coefficients A_{IJ}, $I,J = 1\ldots6$, is obtained through the generalized inversion. We assume that phase velocities are measured. Matrix A_{IJ} represents reduced form of a 4th rank tensor a_{ijkl}. Mutual transformation is given by Voigt notation (Mavko et al., 2009) as:

$$11 \to 1, 22 \to 2, 33 \to 3, 23 \to 4, 13 \to 5, 12 \to 6$$

Tensor computation comes from an assumption of homogeneous isotropic media characterized by matrix $A_{[0]}$, see Eq. (4) that represents initial approximation.

$$A_{[n]} = A_{[n-1]} + \left(\Delta a_{ijkl}\right)_{[n]} \tag{3}$$

$$A_{[0]} = \begin{bmatrix} \alpha^2 + \Delta a_{11} & \frac{\alpha^2}{Q^2} + \Delta a_{12} & \frac{\alpha^2}{Q^2} + \Delta a_{13} & \Delta a_{14} & \Delta a_{15} & \Delta a_{16} \\ & \alpha^2 + \Delta a_{22} & \frac{\alpha^2}{Q^2} + \Delta a_{23} & \Delta a_{24} & \Delta a_{25} & \Delta a_{26} \\ & & \alpha^2 + \Delta a_{33} & \Delta a_{34} & \Delta a_{35} & \Delta a_{36} \\ & & & \frac{\alpha^2}{Q^2} & 0 & 0 \\ & & & & \frac{\alpha^2}{Q^2} & 0 \\ & & & & & \frac{\alpha^2}{Q^2} \end{bmatrix} \tag{4}$$

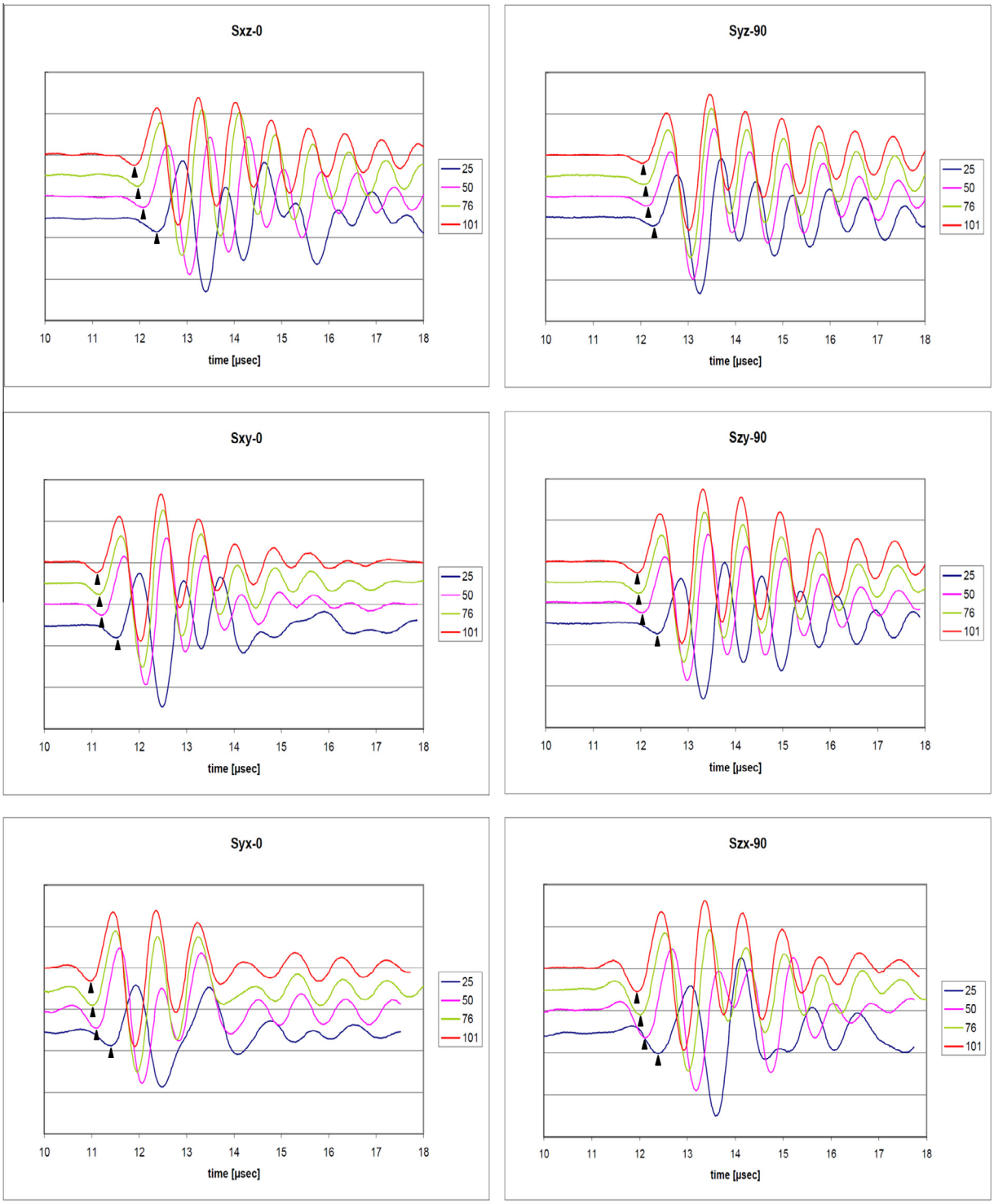

Fig. 7. S-wave forms (S1, S2) measured in the three orthogonal directions X*, Y*, Z* of the sample cube for selected pressures up to 100 MPa. Arrival times are shown by black triangles.

Matrix $A_{[0]}$ is determined from mean velocity of P-waves measured in 132 independent directions on sphere surface (α), while velocity of S-waves is artificially calculated through given P/S velocity ratio (Q). Velocity model is in the 1st iteration step calculated by:

$$\left(c^{P,S1,S2}\right)^2 = a_{ijkl}N_iN_jN_kN_l; i,j,k,l = 1,2,3 \quad (5)$$

where $c^{P,S1,S2}$ is calculated phase velocity of P-, S1- and S2-waves, respectively and $N = [\cos\theta\ \cos\varphi;\ \cos\theta\ \sin\varphi;\ \sin\theta]$ is directional vector of the elastic wave propagation, where θ and φ represent elevation and azimuth, respectively. Other iterations (2^{nd}–20th) calculate with homogeneous anisotropic media. Beside directional vectors N and velocities of P-, S1- and S2-waves from all given directions also polarization vectors g of individual waves enter the calculation of the velocity model:

$$\left(c^{P,S1,S2}\right)^2 = a_{ijkl}N_iN_lg_jg_k; i,j,k,l = 1,2,3 \quad (6)$$

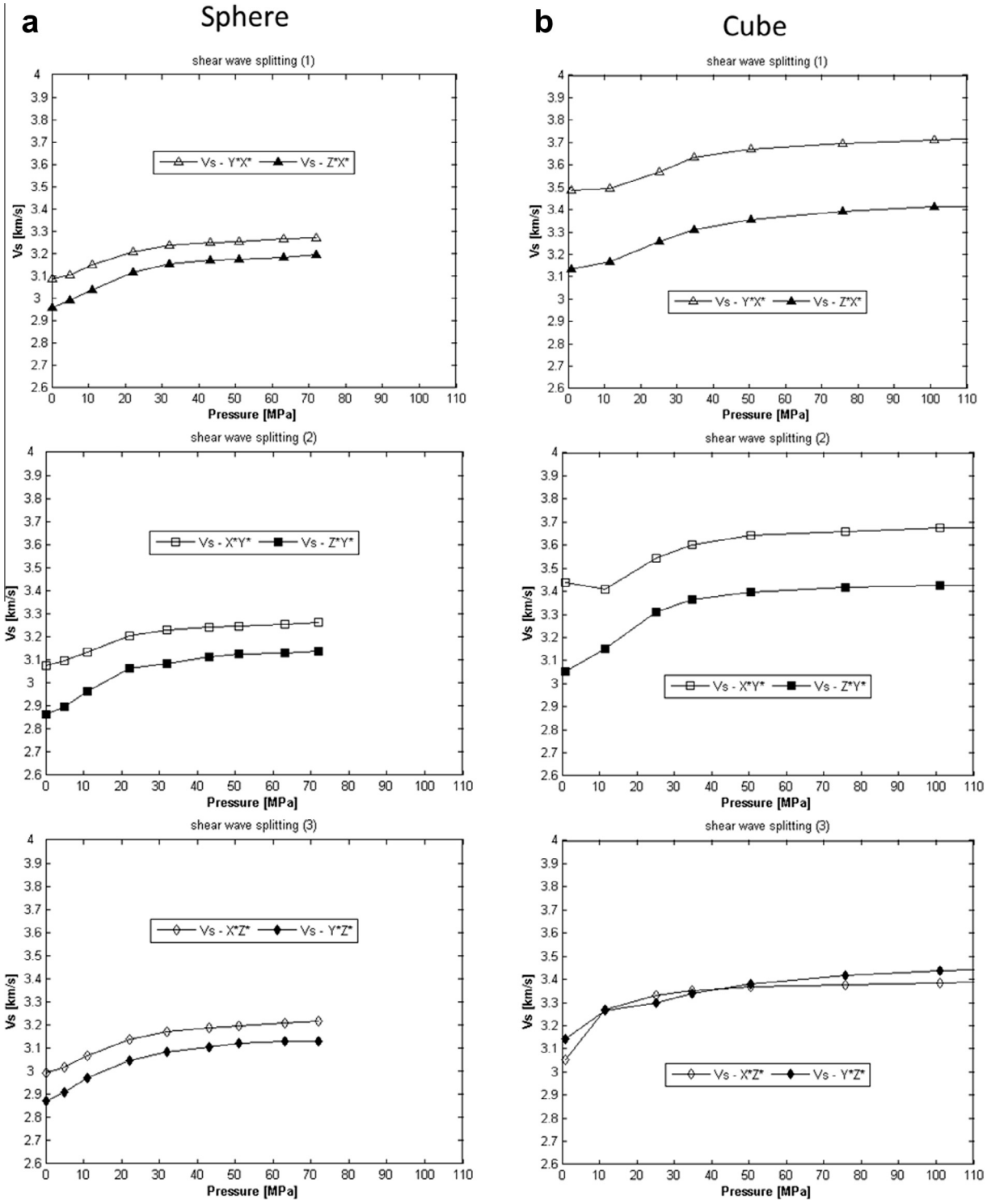

Fig. 8. Pressure dependence of shear wave velocities in X*, Y*, Z* directions. The shear wave velocities are denoted by V-*ij*. For example, Vs_{-Y*X*} indicates the shear wave propagating in the X* direction with a transverse Y*-direction polarization. (a) Spherical sample at pressures up to 70 MPa, (b) cubic sample at pressures up to 100 MPa.

Polarization vectors *g* are determined from Christoffel tensor as its eigenvectors. Subsequent data inversion for 1st iteration step is given by:

$$(\Delta a_{ijkl})_{[n]} = \overline{N}^{-g} \cdot \left[\left(V_t^{\mathrm{P}} \right)^2 - \alpha^2 \right] \tag{7}$$

where Δa_{ijkl} are differences of individual density-normalized elastic parameters, n is an iteration step – in this case $n = 1$, $\overline{N}^{-g}$ is generalized inversion of direction cosines matrix, V_t^{P} is measured P-wave velocity in direction t and α is a mean velocity of P-waves measured in 132 independent directions at sphere surface. For further iteration steps the inversion is calculated through:

$$(\Delta a_{ijkl})_{[n]} = \overline{N}^{-g} \cdot \left[\left(V_t^{\mathrm{P,S1,S2}} \right)^2 - \left(c_t^{\mathrm{P,S1,S2}} \right)^2_{[n-1]} \right] \tag{8}$$

where symbols Δa_{ijkl}, n and $\overline{N}^{-g}$ are same as in Eq. (6), $V_t^{\mathrm{P,S1,S2}}$ are measured P-, S1- and S2-wave phase velocities, respectively in direction t and $c_t^{\mathrm{P,S1,S2}}$ are approximated velocities at the same

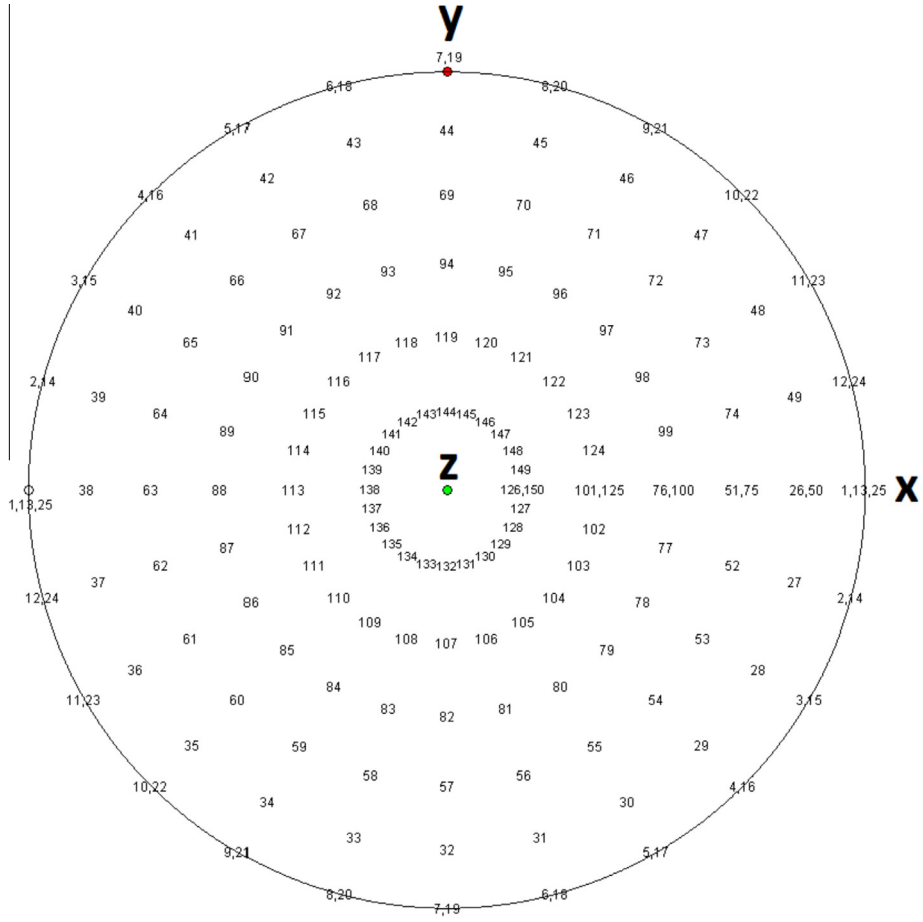

Fig. 9. Equal area projection to the lower hemisphere of 132 independent measuring directions of the spherical sample. The orientation with respect to the structural reference frame X, Y, Z is indicated.

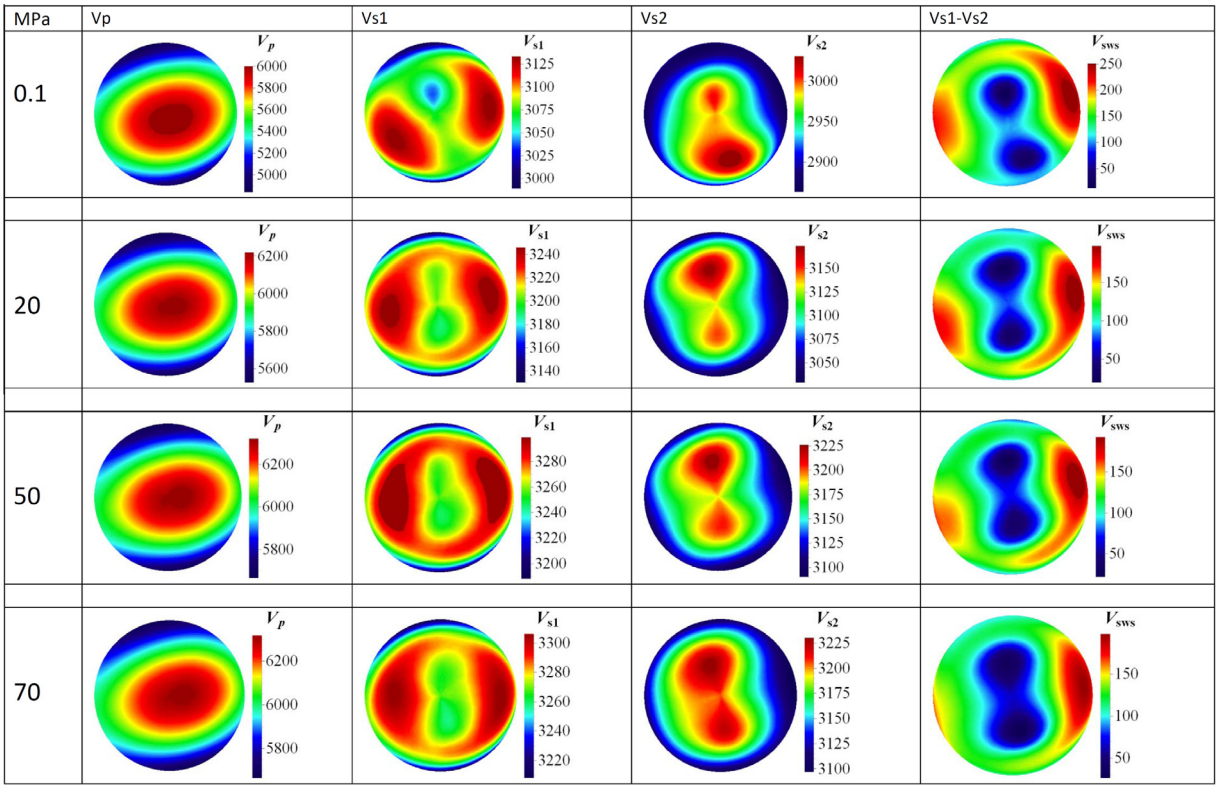

Fig. 10. Pressure dependence of P, S1, S2 and shear wave splitting (S1–S2) for selected pressures up to 70 MPa as calculated from ultrasonic measurements on the spherical sample. Lower hemisphere projection. Coordinates are the same as in Fig. 3.

direction t that are computed from Christoffel tensor as its eigenvalues at previous iteration step. Convergence of the algorithm is quite fast, twenty iteration steps are sufficient to reach final full elastic tensor.

As an example, V_p, V_{S1}, V_{S2} measured at 70 MPa in the 132 directions (m) are tabulated in Table 1 and compared with the

Table 1
Measured (m) and calculated (c) velocities (m/s) of V_p, V_{S1}, V_{S1} at 70 MPa for 132 directions of the sample sphere. Order of measurements is indicated in the spherical projection – Fig. 9.

Order	Direction nr.	70 MPa					
		P		S1		S2	
		m	*c*	*m*	*c*	*m*	*c*
1	'1,13,25'	6024	5997	3297	3268	3252	3120
2	'2,14'	5981	5937	3270	3256	3095	3129
3	'3,15'	5879	5854	3251	3240	3071	3128
4	'4,16'	5834	5769	3240	3222	3073	3118
5	'5,17'	5807	5702	3268	3208	3075	3108
6	'6,18'	5780	5667	3257	3202	3084	3110
7	'7,19'	5737	5674	3312	3205	3177	3120
8	'8,20'	5774	5727	3249	3217	3038	3129
9	'9,21'	5817	5814	3219	3234	2977	3127
10	'10,22'	5945	5909	3306	3252	3178	3117
11	'11,23'	6035	5983	3303	3265	3218	3109
12	'12,24'	6053	6015	3300	3271	3135	3111
13	'26,50'	6013	6033	3272	3286	3094	3122
14	'27'	5952	5976	3240	3280	3030	3132
15	'28'	5855	5896	3209	3268	3090	3133
16	'29'	5821	5814	3109	3255	3014	3125
17	'30'	5787	5747	3113	3243	3060	3117
18	'31'	5760	5711	3096	3236	3075	3118
19	'32'	5760	5714	3092	3236	3069	3127
20	'33'	5767	5759	3215	3241	3088	3137
21	'34'	5828	5836	3226	3250	3115	3137
22	'35'	5931	5920	3281	3262	3207	3128
23	'36'	6031	5985	3303	3271	3199	3121
24	'37'	6046	6012	3307	3274	3199	3121
25	'38'	6031	5994	3285	3270	3243	3129
26	'39'	5938	5936	3253	3261	3062	3136
27	'40'	5875	5856	3236	3250	3032	3135
28	'41'	5807	5774	3232	3239	3049	3127
29	'42'	5787	5711	3220	3229	3085	3121
30	'43'	5760	5682	3197	3224	3133	3124
31	'44'	5747	5697	3183	3226	3062	3132
32	'45'	5774	5756	3230	3235	3079	3136
33	'46'	5869	5846	3232	3248	3209	3131
34	'47'	5952	5942	3277	3263	3240	3119
35	'48'	6061	6016	3300	3277	3240	3110
36	'49'	6068	6049	3294	3286	3179	3112
37	'51,75'	6061	6099	3249	3305	3167	3135
38	'52'	5995	6052	3211	3305	3147	3145
39	'53'	5917	5983	3201	3302	3109	3150
40	'54'	5862	5910	3143	3298	3109	3147
41	'55'	5821	5851	3119	3293	3102	3144
42	'56'	5787	5817	3117	3287	3069	3146
43	'57'	5780	5818	3123	3281	3121	3154
44	'58'	5787	5852	3177	3277	3135	3161
45	'59'	5848	5911	3179	3277	3167	3160
46	'60'	5952	5976	3277	3283	3228	3151
47	'61'	6031	6025	3281	3288	3262	3143
48	'62'	6039	6043	3285	3291	3234	3141
49	'63'	6002	6024	3270	3290	3224	3147
50	'64'	5952	5973	3266	3288	3232	3153
51	'65'	5875	5904	3406	3286	3111	3155
52	'66'	5834	5834	3374	3284	3066	3154
53	'67'	5800	5783	3111	3281	3094	3153
54	'68'	5767	5763	3100	3277	3058	3155
55	'69'	5754	5785	3085	3274	3081	3158
56	'70'	5800	5844	3127	3272	3111	3157
57	'71'	5889	5929	3179	3276	3131	3148
58	'72'	5988	6015	3218	3284	3215	3134
59	'73'	6090	6081	3262	3294	3213	3124
60	'74'	6098	6111	3268	3302	3211	3126
61	'76,100'	6158	6185	3321	3305	3243	3155
62	'77'	6112	6152	3230	3306	3189	3167
63	'78'	6053	6103	3215	3306	3139	3175
64	'79'	5981	6050	3226	3307	3135	3179
65	'80'	5931	6005	3264	3305	3125	3182
66	'81'	5910	5978	3245	3300	3129	3187
67	'82'	5889	5975	3240	3293	3030	3192
68	'83'	5924	5996	3175	3287	3016	3195
69	'84'	5967	6031	3195	3288	3169	3189
70	'85'	6031	6070	3232	3293	3220	3178
71	'86'	6083	6098	3274	3300	3220	3168
72	'87'	6090	6106	3279	3305	3218	3165
73	'88'	6075	6089	3259	3307	3228	3169
74	'89'	6002	6051	3255	3308	3205	3176
75	'90'	5945	6001	3183	3309	3137	3184
76	'91'	5903	5952	3169	3309	3125	3189
77	'92'	5862	5919	3127	3307	3094	3193
78	'93'	5841	5911	3117	3301	3060	3196
79	'94'	5862	5934	3108	3294	3056	3195
80	'95'	5910	5984	3175	3288	3139	3189
81	'96'	5988	6050	3181	3288	3141	3174
82	'97'	6083	6116	3257	3292	3203	3158
83	'98'	6150	6167	3232	3298	3220	3147
84	'99'	6180	6191	3305	3303	3232	3147
85	'101,125'	6281	6266	3316	3289	3256	3176
86	'102'	6258	6250	3294	3286	3281	3187
87	'103'	6211	6224	3318	3282	3257	3199
88	'104'	6180	6195	3311	3278	3251	3210
89	'105'	6143	6169	3327	3272	3243	3219
90	'106'	6112	6152	3318	3266	3277	3227
91	'107'	6112	6146	3303	3263	3287	3230
92	'108'	6127	6152	3296	3268	3277	3223
93	'109'	6158	6165	3300	3278	3245	3210
94	'110'	6180	6180	3274	3288	3266	3197
95	'111'	6196	6189	3298	3296	3262	3188
96	'112'	6203	6189	3300	3301	3266	3186
97	'113'	6188	6177	3320	3303	3262	3189
98	'114'	6150	6155	3318	3303	3277	3197
99	'115'	6090	6129	3274	3300	3222	3207
100	'116'	6046	6105	3294	3294	3230	3218
101	'117'	6024	6091	3303	3286	3245	3228
102	'118'	6010	6092	3262	3275	3257	3234
103	'119'	6046	6109	3327	3269	3251	3232
104	'120'	6098	6141	3277	3271	3209	3218
105	'121'	6143	6181	3277	3277	3253	3199
106	'122'	6219	6220	3283	3283	3251	3183
107	'123'	6274	6250	3303	3287	3245	3173
108	'124'	6289	6266	3318	3289	3266	3171
109	'126,150'	6402	6315	3332	3273	3319	3192
110	'127'	6394	6312	3351	3270	3272	3196
111	'128'	6361	6305	3353	3267	3279	3203
112	'129'	6345	6295	3347	3263	3277	3210
113	'130'	6329	6286	3327	3260	3292	3216
114	'131'	6321	6279	3318	3259	3309	3219
115	'132'	6321	6274	3320	3261	3303	3218
116	'133'	6329	6271	3316	3266	3287	3213
117	'134'	6329	6271	3313	3272	3281	3208
118	'135'	6329	6271	3313	3278	3287	3203
119	'136'	6329	6270	3311	3282	3289	3199
120	'137'	6321	6267	3313	3284	3309	3199
121	'138'	6297	6261	3333	3285	3289	3201
122	'139'	6274	6254	3351	3283	3226	3205
123	'140'	6266	6247	3349	3280	3255	3211
124	'141'	6242	6242	3338	3274	3268	3218
125	'142'	6242	6240	3333	3268	3277	3223
126	'143'	6250	6243	3311	3263	3272	3226
127	'144'	6258	6252	3294	3262	3279	3223
128	'145'	6281	6265	3296	3264	3279	3215
129	'146'	6321	6279	3305	3268	3294	3206
130	'147'	6361	6294	3289	3271	3274	3198
131	'148'	6394	6306	3294	3273	3266	3192
132	'149'	6402	6313	3324	3274	3307	3190

Table 2
Bulk elastic stiffness coefficients c_{ij} [GPa] based on ultrasonic measurements at 0.1, 20, 50, 70 MPa. (ρ = 2.724 g/cm^3). The column on the right presents corresponding coefficients obtained by the GeoMixSelf approximation.

Elastic stiffnesses (GPa)	Pressure (MPa)				Calc GeoMixSelf
	0.1	20	50	70	
c11	80.11 ± 2.35	93.95 ± 1.48	98.26 ± 1.46	97.94 ± 1.67	98.35
c22	64.68 ± 0.18	83.53 ± 0.96	87.71 ± 0.85	87.69 ± 0.83	85.55
c33	97.64 ± 1.31	105.29 ± 1.18	108.74 ± 1.07	108.56 ± 1.13	92.86
c44	24.23 ± 0.72	26.59 ± 0.77	27.65 ± 0.80	27.97 ± 0.73	32.76
c55	25.71 ± 1.06	28.02 ± 0.90	28.84 ± 1.00	29.10 ± 1.00	35.90
c66	22.50 ± 0.43	25.11 ± 0.61	26.34 ± 0.53	26.55 ± 0.44	32.44
c12	26.61 ± 0.22	38.02 ± 0.66	40.07 ± 0.70	39.67 ± 0.40	20.60
c13	35.61 ± 0.80	42.03 ± 0.52	44.26 ± 0.75	43.52 ± 0.45	21.22
c14	−0.74 ± 1.80	1.15 ± 2.83	0.17 ± 1.01	0.15 ± 0.65	−0.09
c15	−0.77 ± 1.09	−0.48 ± 0.78	−0.55 ± 1.04	−0.60 ± 1.17	−0.28
c16	2.32 ± 2.42	1.19 ± 1.66	1.25 ± 1.62	1.33 ± 1.56	0.30
c23	27.73 ± 1.35	36.65 ± 0.73	38.50 ± 1.19	38.25 ± 1.14	22.14
c24	0.61 ± 1.69	0.52 ± 1.20	0.35 ± 0.88	0.25 ± 0.69	−0.19
c25	−0.30 ± 1.04	−0.80 ± 1.35	−0.79 ± 1.49	−0.91 ± 1.70	−0.04
c26	1.96 ± 2.05	0.67 ± 1.20	0.77 ± 1.29	0.88 ± 1.30	−0.01
c34	2.09 ± 3.95	0.69 ± 1.47	0.57 ± 1.27	0.43 ± 1.09	1.65
c35	−1.05 ± 1.56	−0.68 ± 1.16	−0.92 ± 1.69	−0.99 ± 1.82	−0.05
c36	2.23 ± 2.30	1.15 ± 1.46	1.33 ± 1.60	1.52 ± 1.52	−0.10
c45	0.09 ± 0.33	0.19 ± 0.40	0.21 ± 0.34	0.26 ± 0.33	0.07
c46	0.07 ± 0.20	0.21 ± 0.33	0.17 ± 0.38	0.12 ± 0.28	−0.22
c56	0.96 ± 0.86	−0.26 ± 0.66	−0.03 ± 0.23	−0.04 ± 0.16	0.53

corresponding velocities calculated by the iterative approach (*c*). The equal area projection shown in Fig. 9 indicates the order of measuring directions (1. . ..132). (The full data sets for the measurements at 0.1, 20, 50 MPa are available on request). Differences between measured and calculated velocities may be small or relatively large for particular directions, probably due to the fact that the respective velocities recorded by the transducers are closer or farther to phase velocities. However, the great number of measurements recorded in the 132 independent directions and the robust algorithm suggests that the position of maxima and minima and corresponding anisotropies are properly reflected on the velocity surfaces calculated for V_p and V_s.

In Table 2 we present the elastic stiffness coefficients derived from the P- and S-wave velocities measured at pressures of 0.1, 20, 50, and 70 MPa as obtained by the iterative process, together with CPO-based calculated data using the GeoMixSelf algorithm.

Fig. 10 presents the calculated velocity surfaces of P, S1 and S2 wave velocities for selected pressures up to 70 MPa derived from the measurements on the spherical sample. The patterns for P- and S-wave velocities indicate an increase of velocities with pressure pointing to progressive closure of microcracks. At 70 MPa the effect of low-aspect ratio microcracks is minimized so that the respective velocity surfaces reflect the almost CPO-related 3D velocity distribution. Importantly, the near-rhombic symmetry of the patterns observed at low pressures is preserved as pressure is increased, indicating that crack- and CPO-related fabrics are symmetrically disposed.

6. Calculation of the 3D velocity distribution based on neutron diffraction CPO patterns

The orientation distribution functions for biotite, quartz and plagioclase components of Outokumpu biotite gneiss, reconstructed from the neutron diffraction measurements, provided the basis for the calculation of the elastic properties of the bulk aggregate. Compared to previous calculations (Ivankina et al., 2005; Kern et al., 2009), where the simplest Voigt approach was applied, we used, in a first step, the geometric mean (GeoMean) approximation (Morawiec, 1989; Matthies and Humbert, 1995) for the calculation of elastic properties of mineral components. Bulk elastic properties were obtained by averaging the single crystal tensors over corresponding orientation distributions, based on the CPO's presented in Fig. 3 and by subsequent combining the averages for each phase according to their volume fractions, then we calculated V_p, V_{S1}, V_{S2} and shear wave splitting for the bulk sample by solving Christoffel's equation. For the modeling we used the elastic stiffness tensors for phlogopite (biotite), quartz and albite (plagioclase) as reported in Wenk et al., 2012.

Fig. 11 shows velocity surfaces of the P-wave velocities and the fast (V_{S1}) and slow (V_{S2}) S-waves velocities calculated from the geometric mean (GeoMean) average. The velocity surfaces for the aggregates (100 vol.%) of biotite, quartz and plagioclase, display most distinctly that, compared to quartz and plagioclase, the biotite minerals contribute most to the intrinsic anisotropy in the investigated gneiss sample (Fig. 5). The directions of minimum and maximum V_p as well as directions of minimum and maximum shear wave splitting (V_{S1}–V_{S2}) of the bulk rock correspond to the slow [0 0 1] and fast ([1 0 0] and [0 1 0]) directions of the biotite single crystal.

It should be noted that CPO-based approximations (Voigt, Reuss or geometric mean) ignore the effect of crystal shape (SPO) and microporosity. In order to explore the possible effect of grain shape and microcracks on bulk elastic properties of the biotite gneiss sample we applied, in a second step, the GEO–MIX–SELF algorithm (GMS) described by Matthies (2010) for modelling the 3D velocity distribution. Using this algorithm, Wenk et al. (2012) have recently shown that grain shape and low-aspect ratio cracks may have a significant impact on bulk elasticity of strongly foliated biotite gneiss from Outokumpu. The GMS method combines the self-consistent approach and the geometric mean approximation. We used similar microstructural data as listed in (Wenk et al., 2012). Our calculation refers to aspect ratios of 1:0.2:0.05 for the biotite platelets and to 1:0.2:0.02 for oriented microracks (0.1% by volume), in addition to the CPO's of biotite, quartz and plagioclase (Fig. 3). Microcracks are considered to be parallel to biotite platelets, and grain shapes of quartz and plagioclase to be spherical. Again, we used elastic stiffnesses of phlogopite, quartz and albite reported in (Wenk et al., 2012).

In Fig. 12 and Table 3 the 3D velocity distributions of P- and S-waves (S1, S2) calculated according to the GMS-algorithm are compared with those of the GeoMean calculation and the respective velocity surfaces derived from the measurements at 70 MPa.

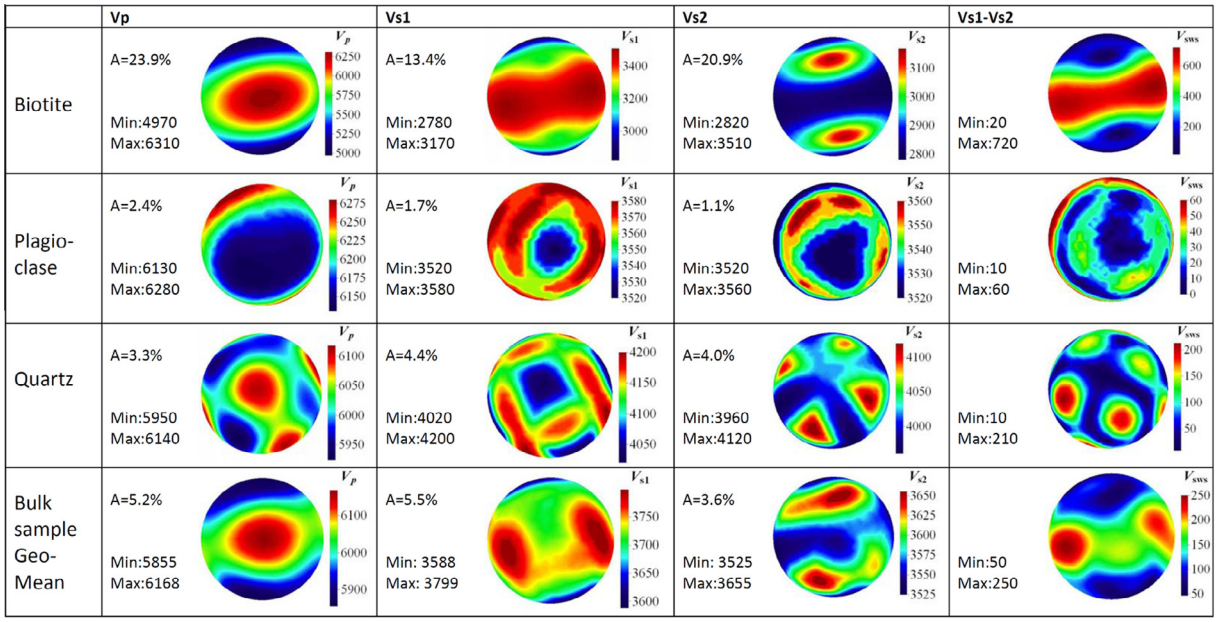

Fig. 11. CPO-based calculated velocity surfaces for P waves of mineral aggregates (100 vol.%) for biotite, plagioclase and quartz along with calculated velocity surfaces for V_p, V_{S1}, V_{S2} and V_{S1}–V_{S2} of the bulk rock, according to mineral proportions. (GeoMean approximation).

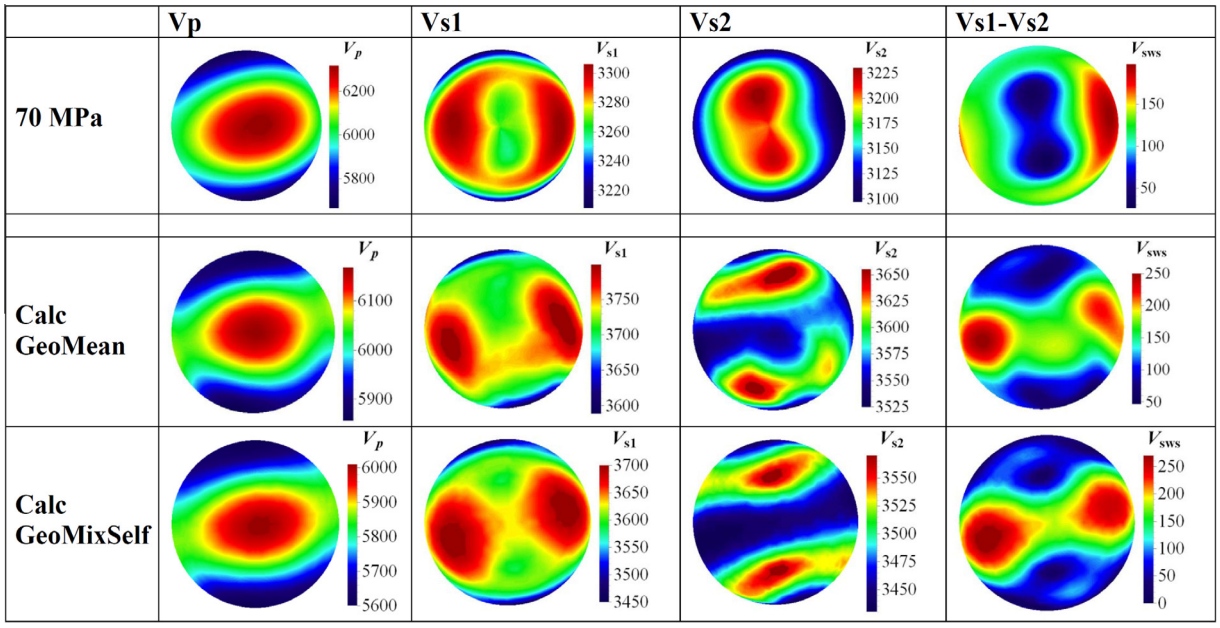

Fig. 12. 3D velocity distributions of V_p, V_{S1}, V_{S2}, and V_{S1}–V_{S2} derived from measurements (at 70 MPa) and from calculations, based on the GeoMean and GeoMixSelf approximation.

In addition, V_p- and V_S-velocities measured on the sample cube are listed in Table 3.

Fig. 13 presents velocity profiles for V_p, V_{S1} and V_{S2} along the ZX-, YZ- and XY-sections of the velocity surfaces derived from the velocity measurements at 70 MPa and the CPO-based GeoSelfMix calculation (Fig. 12). From the sections along the symmetry planes of the reference frame it is clear that V_p is highest subparallel to X. Maximum differences in shear wave velocities (shear wave splitting) occur almost for shear waves propagating parallel to the YX-plane, whereas shear wave splitting is found to be lowest for shear waves propagating within the ZX-plane. However the directions of minimum shear wave splitting derived from the experiments deviate from those obtained by the GeoMixSelf approximation.

7. Discussion

The 3D velocity distributions of P- and S-wave velocities have been measured on a spherical sample of fine-grained, homogeneous biotite gneiss recovered from the Outokumpu Scientific Drill hole. The specimen exhibits strong crystallographic (CPO) and shape preferred orientation (SPO) of the biotite minerals. A main purpose of the present study is to show that the improved and

Table 3
Experimental (sphere-70 MPa and cube-400 MPa) maximum, mean and minimum values of V_p, V_s, velocity anisotropies and shear wave splitting along with respective data obtained by the GeoMix and GeoMixSelf approximation.

V_p, V_s		Exp sphere 70 MPa	Exp cube 400 MPa	Calc GeoMean	Calc GeoMixSelf
V_p, *m/s*	min	5664	5762	5855	5600
	max	6317	6522	6168	6010
	mean	5980	6116	5991	5776
	A, %	10.9	9.8	5.2	7.1
V_{S1}, *m/s*	min	3208	3497	3588	3450
	max	3306	3723	3799	3700
	mean	3270	3641	3723	3608
	A,%	3.0	6.2	5.5	6.9
V_{S2}, *m/s*	min	3097	3424	3525	3430
	max	3230	3460	3655	3570
	mean	3147	3443	3584	3489
	A,%	4.2	1.1	3.6	4.0
V_{S1}–V_{S2}, *m/s*	min	26	73	50	10
	max	198	263	250	270

modified equipment at Prague allows simultaneous measurements of the 3D compressional and shear wave velocity distribution on a sample sphere placed in oil as the pressure medium. For three particular orthogonal directions of the spherical sample the P- and S-wave velocities are compared with respective data measured in a multi-anvil apparatus on a sample cube prepared from the same core segment. In addition, comparison is made with calculated texture-based 3D velocity distributions of P- and S-waves.

The V_p–pressure relations measured in the three orthogonal directions of the cube-shaped sample compare reasonably well with those measured in the same directions on the sample sphere. Both set of curves show a strong pressure sensitivity of wave velocities and velocity anisotropy (Fig. 5). The non-linear steep velocity increase as well as the decrease of anisotropy with increasing pressure are clearly a result of progressive closure of low-aspect ratio microcracks. Importantly, in the biotite gneiss, microcracks are closely related to the biotite CPO fabric. Thus, they occur mainly parallel to the morphologic sheet plane (0 0 1) of the biotite minerals (see Fig. 2a). The close relationships between aligned microcracks and crystallographic preferred orientation (CPO) of biotite are also reflected by the velocity surfaces presented in Fig. 10. The symmetries of the patterns for Vp are not significantly changed as pressure is increased, indicating that the crack fabric and crystallographic fabric are symmetrically disposed. The quasi-linear behavior above about 70–100 MPa seen on the velocity–pressure curves (Fig. 5) gives also evidence that most of the aligned flat cracks are closed at higher pressures and that the elastic properties of the rock are basically controlled by the rock matrix, that is, by the elastic properties of major minerals and their CPO. Consequently, the directional dependence of V_p and V_S at high pressures is mainly caused by the CPO of major minerals, in particular by the CPO of biotite. The role of the biotite CPO is also documented by the similarities between the shapes of the velocity surfaces (V_p, V_{S1}, V_{S2}, V_{S1}–V_{S2}) derived from the measurements on the spherical sample (Fig. 10) and the respective 3D velocity calculations (GeoMean approximation) based on the neutron diffraction texture measurements (Fig. 11). The 3D projections of measured V_p (70 MPa) and calculated V_p compare fairly well with both, the GeoMean and GeoMixSelf approximation (Fig. 12), whereas for V_{S1} better agreement between measured and calculated velocities is observed for the GeoMixSelf approximation. There is reasonable agreement with respect to the position of the maxima and minima on the measured and calculated 3D velocity surfaces for V_{S2} obtained by the GeoMixSelf modelling, although the overall shapes of the velocity surfaces are slightly different. The same holds for shear wave splitting (V_{S1}–V_{S2}).

The comparison of the velocity profiles for V_p, V_{S1} and V_{S2} along the ZX-, YZ- and XY-sections of the velocity surfaces derived from the velocity measurements (70 MPa) with those obtained by the CPO-based GeoSelfMix calculation (Fig. 13) shows that V_p is highest subparallel to X, and maximum differences in shear wave velocities (shear wave splitting) occur almost for shear waves propagating parallel to the YX-plane. Shear wave splitting is found to be lowest for shear waves propagating within the ZX-plane. Directions of lowest shear wave splitting values are oblique to foliation and basically due to the angular spread of the biotite (0 0 1) single maximum towards the Y direction (Fig. 3). However, the positions of shear wave splitting minima derived from the experiments deviate from those obtained by the GeoMixSelf approximation. Finally, the comparison shows again that the CPO-based calculated shear waves velocities are systematically higher than those derived from the measurements on the spherical sample

Calculated bulk elastic properties (Table 3) considering the effect of grain shapes and low-aspect ratio cracks (GMS approximation) revealed an increase of anisotropy of P-waves (A–V_p = 7.1%) compared to A–V_p = 5.2%, calculated without consideration of grain shapes and cracks (GeoMean approximation). Compared to V_p-anisotropies derived from the experimental data, the CPO-based calculated anisotropies (GMS approximation) are markedly lower. The differences may be due, at least in part, to the fact that the aspect ratios for the biotite platelets and oriented microcracks assumed in the calculation were not close enough to reality.

Most important, however, are the striking differences in the shear wave velocities recorded by the transducers for the measurements on the sample sphere (Fig. 8a) and on the sample cube (Fig. 8b). S-wave velocities measured in the three orthogonal directions on the cube-shaped specimen are markedly higher than those measured on the sphere. Presently, we do not have a convincing explanation for the differences. We suggest that the differences are due to the different geometries of the samples and the different configurations of transducers relative to the samples. In the multi-anvil apparatus the travel distance of elastic waves is about 160 mm. In this distance, elastic waves are almost equal to phase velocities (Dellinger and Vernik, 1994). By contrast, in the pressure vessel, the spherical shape of the sample and the point contacting of the sensors on the sample surface may give rise that the measured velocities are closer to group velocities than to phase velocities. With a point source and point receiver, the first break (Fig. 6a) probably define the vertical group-velocity arrival time (Dellinger and Vernik, 1994). Group velocities are generally lower than phase velocities. This hypothesis is also supported by the observation that the texture-based velocity surfaces calculated for the S-wave

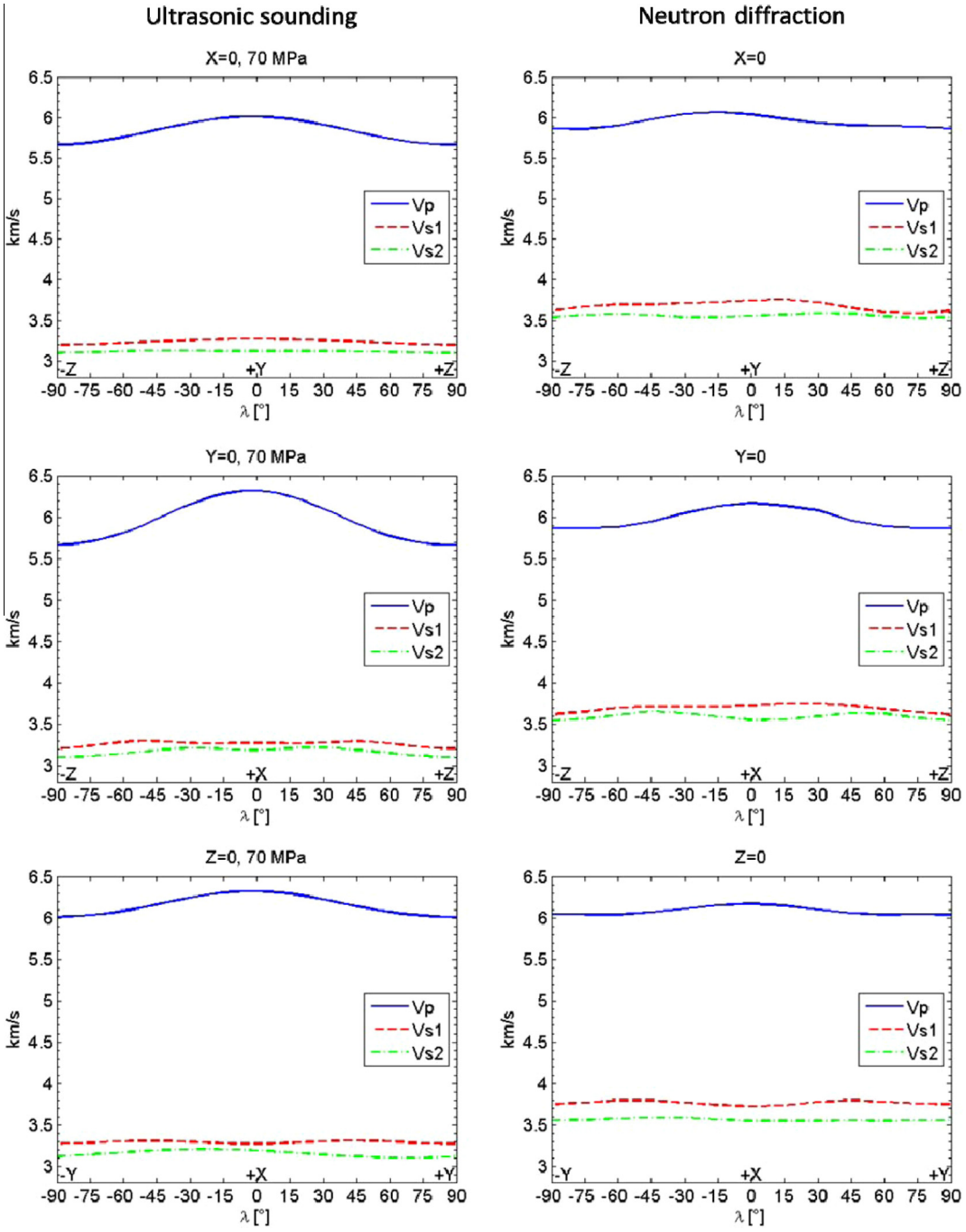

Fig. 13. Velocity profiles for V_p, V_{S1} and V_{S2} along the ZY-, ZX-, and YX –planes across derived from the experiments (70 Ma) and CPO-based calculated (GeoMixSelf) velocity surfaces. Lamda is the propagation angle.

velocities of the bulk rock (Figs. 11 and 12) display, in contrast to Vp, markedly higher Vs than those derived from measurements on the spherical sample at 70 MPa confining pressure (Fig. 10). At pressures above about 70–100 MPa the effect of aligned low-aspect ratio cracks on wave velocities is almost eliminated in the biotite sample and the bulk elastic properties are close to intrinsic.

8. Conclusions

An important finding from this study is that the measurements on the sample sphere and on the sample cube of the foliated biotite gneiss from Outokumpu displayed distinct velocity–pressure behaviors under the same experimental conditions. Whereas the V_p–pressure curves for the three orthogonal directions of the cube-shaped sample agree reasonably well with those for corresponding directions of the sample sphere, marked differences are observed, in particular, for the respective V_S vs pressure relationships. Shear wave velocities measured on the sphere are systematically lower than those measured on the cube. We assume that the differences are mainly due to the differences in the geometry of the samples and the configuration of transducer-sample assembly. In the multi-anvil pressure apparatus the travel distance of the elastic waves is wide and the receiver samples the flat central part of the

wavefront. Thus, we can assume that the measured velocities correspond to phase velocities. On the sample sphere in the pressure vessel, however, with a point source and point receiver the first break at the velocity arrival time is suggested to define group velocities in most cases.

The velocity–pressure relationships of the cube-shaped specimen as well as of the sample sphere confirm a marked pressure sensitivity and strong directional dependence of P- and S-wave velocities. At low pressures, oriented microcracks contribute largely to the measured bulk anisotropy. At high pressures, most of aligned cracks are closed and the residual anisotropy is mainly caused by crystallographic preferred orientation (CPO) of major minerals. The calculation of the 3D velocity distribution of P- and S-wave velocities based on neutron diffraction texture measurements is a powerful means to investigate the relative contribution of the crystallographic preferred orientation of major minerals to the CPO-related bulk anisotropy. The comparison of the velocity surfaces calculated for the mineral aggregates of the biotite gneiss with those of the bulk rock clearly demonstrates that the CPO-related seismic anisotropy and shear wave splitting is dominated by the CPO of the biotite minerals defining the foliation, whereas the contribution of the CPOs of the constituent quartz and plagioclase minerals to bulk anisotropy is weak. The GeoMean approximation considering the influence of volume fractions, single crystal elastic properties, CPO of major minerals as well as the GeoMixSelf approximation, considering in addition, grain shape and volume and shapes of microcracks provide powerful means to calculate elastic bulk properties of the foliated biotite gneiss. Both, the experimentally-derived and texture-based calculated velocity surfaces of the bulk rock compare reasonably well with respect to symmetry and position of P-wave velocity maxima and minima and their relation to the foliation plane.

The comparison of the experimental data obtained by the two different techniques gives evidence that the configuration of the sample/transducer assembly is important to assess what kind of velocities (phase vs group velocities) are measured in pulse transmission experiments.

Acknowledgements

This work was partially supported by the Grant Agency of the Czech Republic, Project No. MŠMT Kontakt II – LH13102, GA CR P104/12/0915, 13-13967S and by the long-term research development project of the Institute of Geology of the AS CR v.v.i. – RVO67985831. H.K. thanks D. Schulte-Kortnack and R. Hinges for help with the experiment in the multi-anvil apparatus an A. Fehler for preparing the sample cube and thin sections. We are appreciative for Grants from the Plenipotentiary of the Government of the Czech Republic in the Joint Institute of Nuclear Research (order no. 328 (May 28, 2013), item 19); and from the Scientific Program JINR-Czech Republic (order no. 291 (May 16, 2013), item 26). We thank R. Vasin for help in texture analysis using MAUD software and for calculation based on GMS approximation. The authors would like to thank H.-R. Wenk for his comments on an earlier version of the manuscript and Ian Jackson and Yuji Higo for thoughtful comments that helped to improve this manuscript.

References

Birch, F., 1961. The velocity of compressional wave velocities in rocks to 10 kbar, part 2. J. Geophys. Res. 66, 2199–2224.

Christensen, N.I., 1985. Measurements of dynamic properties of rocks at elevated pressures and temperatures. In: Pincus, H.J., Hoskins, E.R. (Eds.), Measurements of Rock Properties at elevated Pressures and Temperatures, ASTM Spec. Tech. Publ., vol. STP869, pp. 93–107.

Červený, V., 2001. Seismic Ray Theory. Cambridge University Press, New York.

Dellinger, J., Vernik, L., 1994. Do travel times in pulse-transmission experiments yield anisotropic group or phase velocities? Geophysics 59, 1774–1779.

Ivankina, T.I., Kern, H., Nikitin, A.N., 2005. Directional dependence of P- and S-wave propagation and polarization in foliated rocks from the Kola superdeep well: evidence from laboratory measurements and calculations based on TOF neutron diffraction. Tectonophysics 407, 25–42.

Jech, J., Pšenčík, I., 1989. First-order perturbation method for anisotropic media. Geophys. J. Int. 99, 369–376.

Jech, J., 1991. Computation of elastic parameters of anisotropic medium from travel times of quasi-compressional waves. Phys. Earth Planet. Inter. 66 (3–4), 153–159. http://dx.doi.org/10.1016/0031-9201(91)90074-R.

Ji, S., Salisbury, M.H., 1993. Shear wave velocities, anisotropy and splitting in high-grade mylonites. Tectonophysics 211, 453–473.

Kern, H., Liu, B., Popp, T., 1997. Relationship between anisotropy of P- and S-wave velocity and anisotropy of attenuation in serpentinite and amphibolite. J. Geophys. Res. 102, 3051–3065.

Kern, H., Ivankina, T.I., Nikitin, A.N., Lokajíček, T., Pros, Z., 2008. The effect of oriented microcracks and crystallographic and shape preferred orientation on bulk elastic anisotropy of a foliated biotite gneiss from Outokumpu. Tectonophysics, 143–149.

Kern, H., Mengel, K., Strauss, K.W., Ivankina, T.I., Nikitin, A.N., Kukkonen, I.T., 2009. Elastic wave velocities, chemistry and modal mineralogy of crustal rocks sampled by the Outokumpu scientific drill hole: evidence from lab measurements and modeling. PEPI 175, 151–166.

Klíma, K., Červený, V., 1973. The computation of the elastic constants of an anisotropic medium from the velocities of body waves. Stud. Geophys. Geod. 17 (2), 115–122.

Kukkonen, I., 2011. Outokumpu Deep Drilling Project 2003–2010. Geological Survey of Finland, Special Paper 51, 252 pages.

Lokajíček, T., 2013. Laboratory approach to the study of elastic anisotropy on spheres by simultaneous longitudinal and transvers sounding under confining pressure. Submitted to Ultrasonics.

Lutterotti, L., Matthies, S., Wenk, H.-R., Schultz, A.J., Richardson, J.W., 1997. Combined texture and structure analysis of deformed limestone from time-of-flight neutron diffraction spectra. J. Appl. Phys. 81, 594–600.

Matthies, S., Humbert, M., 1995. On the principle of a geometric mean of even-rank symmetric tensors for textured polycrystals. J. Appl. Cryst. 28 (3), 254–266.

Matthies, S., 2002. 20 years WIMV, history, experience and contemporary developments. Mater. Sci. Forum 408–412, 95–100.

Matthies, S., 2010. On the combination of self-consistent and geometric mean elements for the calculation of the elastic properties of textured multi-phase samples. Solid State Phenom. 160, 87–93.

Mavko, G., Mukerji, T., Dvorkin, J., 2009. The Rock Physics Handbook. Cambridge University Press, New York.

Morawiec, A., 1989. Calculation of polycrystal elastic constants from single crystal data. Phys. Status Solidi (b) 154, 535–541.

Nishizawa, O., Kanagawa, K., 2010. Seismic velocity anisotropy of phyllosilicate-rich rocks: characteristics inferred from experimental and crack-model studies of biotite rich schist. Geophys. J. Int. 182, 375–388.

Pros, Z., Lokajíček, T., Klíma, K., 1998. Laboratory approach to the study of elastic anisotropy on rock samples. Pure Appl. Geophys. 151, 619–629.

Pros, Z., Lokajíček, T., Přikryl, R., Klíma, K., 2003. Direct measurement of 3D elastic anisotropy on rocks from the Ivrea zone (Southern Alps, NW Italy). Tectonophysics 370, 31–47.

Vavryčuk, V., 2013. Inversion for weak triclinic anisotropy from acoustic axes. Wave Motion 50 (8), 1271–1282.

Walther, K., Heinitz, J., Ullemeyer, K., Betzl, M., Wenk, H.-R., 1995. TOF texture analysis of limestone standard: Dubna results. J. Appl. Cryst. 28, 503–507.

Wenk, H.-R., Lutterotti, L., Vogel, S.C., 2010. Rietveld texture analysis from TOF neutron diffraction data. Powder Diffr. 25, 283–296.

Wenk, H.-R., Vasin, R.N., Kern, H., Matthies, S., Vogel, S.C., Ivankina, T.I., 2012. Revisiting elastic anisotropy of biotite gneiss from the Outokumpu scientific drill hole based on new texture measurements and texture-based velocity calculations. Tectonophysics 570–571, 123–134.

Príloha 7

Publikácia 6:

Lokajíček, T., Šťastná, A., Petružálek, M., Šachlová, Š., **Svitek, T.** & Přikryl,. R. (2014). **Quasi-continuous ultrasonic sounding and changes of ultrasonic signal characteristics as a sensitive tool for the evaluation of ongoing microstructural changes of experimental mortar bars tested for their ASR potential**. *Submitted*

Elsevier Editorial System(tm) for Cement and Concrete Research
Manuscript Draft

Manuscript Number:

Title: Quasi-continuous ultrasonic sounding and changes of ultrasonic signal characteristics as a sensitive tool for the evaluation of ongoing microstructural changes of experimental mortar bars tested for their ASR potential

Article Type: Research Paper

Keywords: Alkali-Aggregate Reaction; Thermal Treatment; Physical Properties; Mortar bar; Ultrasonic sounding

Corresponding Author: Dr. Tomas Lokajicek, Ph.D.

Corresponding Author's Institution: Institute of Geology, Academy of Sciences of the Czech Republic, v.v.i.

First Author: Tomas Lokajicek, Ph.D.

Order of Authors: Tomas Lokajicek, Ph.D.; Aneta Šťastná, Ph.D.; Matěj Petružálek, Mgr.; Šárka Šachlová, Ph.D.; Tomáš Svitek, Mgr.; Richard Přikryl, Prof.

Abstract: Ultrasonic testing was used to determine material mechanical changes due to the alkali silicate reaction (ASR). Heating chamber was constructed to enable ultrasonic sounding of mortar bars, stored in accelerating solution. Regular ultrasonic sounding reveals significant dependence of signal longitudinal velocity, energy, amplitude and frequency. Mortar bars were stored in cold or warm water and in an accelerating warm medium. Ultrasonic results showed good correlation with results of ASTM standard expansion tests and much higher sensitivity to ASR-induced concrete deterioration. Whilst length changes did not exceed 0.51 % of original length of mortar bars, P-wave velocity and signal characteristics exhibited 50 (80 resp.) % change. This result shows that ultrasonic sounding seems to be more sensitive to microstructutral changes due to ongoing deterioration of concrete microstructure by ASR than the dimensional changes and thus can provide improved tool for the characterization of ASR-related processes in standard testing procedures.

Suggested Reviewers: Michael D. A. Thomas Dr., P.Eng.
University of New Brunswick, Fredericton, CA
mdat@unb.ca
ASR

Oğuzhan Çopuroğlu
Delft University of Technology
O.Copuroglu@tudelft.nl
ASR

Nicolas Robeyst
Magnel Laboratory for Concrete Research, Ghent University
Nicolas.Robeyst@UGent.be
ultrasonic testing

1. Introduction:

The high number of deteriorated concrete structures and excessive costs associated with their replacements point out the importance of laboratory methods that minimize risk due to alkali-silica reaction (ASR) which has been recognized as one of the most deleterious defects of concrete structures [1, 2, 3]. The most effective way seems to be to mitigate the use of alkali-reactive aggregates in concrete [4, 5, 6].

The accelerated mortar bar test is the most common laboratory method which facilitates recognition of the ASR potential of aggregates based on the expansion values of mortar bars [7, 28, 29]. Mortar bars are prepared using tested aggregates and stored in an accelerating solution at 80°C (60°C resp.). The expansion of mortar bars is measured for fourteen days according to ASTM C1260 [7]. The main disadvantage of the expansion test is the process of length measurement during which the mortar bars are removed from the solution and measured with a length comparator [8].

Ultrasonic testing was applied to the concrete structures with the aim of measuring the degree of concrete deterioration and cracking [9, 10, 11, 12] correlated the results of ultrasonic pulse velocity with the strength parameters of concrete. There was also discussion of the effectiveness of laboratory and in situ non-destructive methods such as electric, seismic, and acoustic testing to evaluate structures affected by internal swelling reactions. [13] applied non-linear ultrasonic testing with resonant and pulse velocity parameters to recognize early damage. Various approaches have been used to automate the ultrasonic testing procedure [14, 15].

An innovative method is discussed in this paper combining the standard accelerated mortar bar test with quasi-continuous ultrasonic sounding. The ASR potential of quartzite aggregates is tested in a newly designed heating chamber which enables ultrasonic sounding of submerged mortar bars with any frequency of reading of ultrasonic signal. The results

obtained are compared with the expansion values measured with a standard length comparator.

2. Methodology

2.1 Experimental aggregate

The experimental aggregate used in this study was taken from the Těchobuz quarry located 20 km NE of the town of Tábor (Bohemian Massif, Czech Republic). The exploited sequence of metamorphic rocks represents mixture of intimately interlayered quartzite, quartzite paragneiss, and biotite paragneiss, with minor interlayers of calc-silicate rocks (erlans) and amphibolites [16].

The Těchobuz quarry produces crushed aggregate representing a mixture of the rock types mentioned above. The aggregate is used in the construction industry as a filler for concrete, asphalt mixtures, and for unbound gravel basements [17]. For this study, the tested rock material was represented by fine-grained plagioclase-rich quartzite. This massive (non-foliated) rock is composed of dominant quartz, accompanied with plagioclase and some minor mafic minerals.

2.2 Accelerated mortar bar test

To conduct accelerated mortar bar testing according to ASTM standard C1260, aggregate is crushed and sieved, mortar bar specimens are prepared and then tested. The mortar bars were prepared using a fraction of 0.125/5 mm, cement CEM I 42.5 and distilled water at a ratio of 2.25/1/0.47. A total of twelve different mortar bars were prepared using the same type of aggregate. After 24 hours of hardening and 24 hours of tempering: (1) two mortar bars were

stored in 1M NaOH solution at 80°C (MB80NaOHL) for expansion tests, (2) two mortar bars were stored in water at 80°C (MB80WL) and (3) two mortar bars were stored in water at 20°C (MB20WL). The expansion of mortar bar specimens was measured after a total of forty days (in contrast to fourteen days for ASTM C1260) using a length comparator. Final expansion data were calculated as the average value of two mortar bars measured under the same conditions. Another six mortar bars were measured by ultrasonic testing in a temperature-controlled chamber (see section 2.3).

2.3 Ultrasonic sounding in a temperature-controlled chamber.

Ultrasonic testing presents an important non-destructive method used to investigate material properties and qualities. Changes in ultrasonic velocity propagation, signal attenuation and frequency content can be used as parameters to describe mechanical/elastic changes as a result of concrete deterioration from ASR [11, 12].

Numerous experimental tests were carried out to find a commercially viable means of sensor protection given a 1M NaOH solution at 80 °C. During these time-consuming tests (more than a year) no ultrasonic sensor protection was found resistant to NaOH for more than 1 week. Due to this fact, 316L steel waveguides were used between mortar bar specimens and the ultrasonic sensor. Figure 1 shows the newly constructed experimental set up for the ultrasonic testing of mortar bars.

The experimental arrangement was based on a temperature-controlled heating chamber (20°C – 90 °C) designed for the ultrasonic testing of the same samples used during the accelerated mortar bar test (according to ASTM C1260). The chamber is capable of accommodating two mortar bars. As testing solution, both distilled water and 1M NaOH solution were used.

Unfortunately, this arrangement did not enable expansion measurement of mortar bars during the experiment. In this case, mortar bar expansion could be measured before or after storage. The above mentioned waveguides, sealed in the chamber walls, enabled transmission of ultrasonic waves between the tested mortar bars and piezoceramic transducers. The waveguides had fixed position in the chamber walls. For each mortar bar, a pair of ultrasonic sensors were used. Wide-band, high-temperature-resistant sensors (40 days at 80 °C) manufactured by the 3S Sedlak Company were used as ultrasonic sensors. Ultrasonic sounding was done by means of a Vallen AMSY5 multichannel automatic recording system. This system enables the use of any ultrasonic sensor as a transmitter and remaining ones as receivers. The system has a 16-bit resolution and a sampling frequency of 10 MHz for each channel. The recorded signal duration was 16,384 points, which corresponds to a time duration of 1.6384 ms. Automatic ultrasonic sounding was carried out every 10 minutes throughout the experiment. In all experiments, two mortar bars were measured simultaneously. Each mortar bar, elongated by two steel waveguides, was located between two ultrasonic sensors. Each sensor was successively excited by a high-voltage pulse (100 V), while the second sensor acted as a receiver. Using this approach, two pairs of reciprocal signals were acquired every 10 minutes for each of the mortar bars being tested together. The Vallen automatic recording system produced two independent data sets. One data set automatically stored the basic parameters of all recorded ultrasonic waveforms, like arrival time of all waveforms, their energy, maximum amplitude, duration, etc. The second data set consists of all waveforms transmitted and received. Both data sets enabled time and frequency domain analysis of recorded signals. Significant recorded waveform features are given in Figure 2.

Further analysis used the following waveform parameters for non-destructive evaluation of mortar bar state and integrity:

In the time domain range:

1. The time difference between transmitting time and the first arrival of the ultrasonic signal was used to calculate the travel time through the sample (Fig.2). Arrival times were determined automatically by the Vallen system (basic parameter data set available online) and also offline by the automatic processing of captured waveforms. P wave velocity was calculated from this time and measured mortar bar length. Time corrections for the steel waveguides and sensors themselves were applied.
2. Duration of captured signal, which was measured as the time interval between crossing of setup threshold level by signal arrival and fall under this level at the tail of the signal (basic parameter data set available online).
3. Maximum amplitude of the entire recorded waveform (basic parameter data set available online). Nevertheless, this value could also be influenced by cross-talk between sensors or ultrasonic waves which propagate along a different path, such as chamber walls, the testing solution, second mortar bar, etc.
4. The true energy of recorded signals is calculated directly as an integral value of the squared signal. This parameter can be recorded directly by the Vallen multichannel system, which is equipped with an ASP-SQ module.
5. First arrival amplitude was determined from full waveforms by special offline software.

The frequency domain range includes:

1. Magnitude of frequency spectrum of the very beginning of recorded waveform.
2. Time-frequency content of the recorded signal, analyzed by Vallen wavelet analysis.

Experimental measurements in the heating chamber were performed on three pairs of identical mortar bars with the same aggregate, but under different testing condition, as follows: (1) two mortar bars were stored in 1M NaOH solution at 80°C (MB80NaOHU), (2)

two mortar bars were stored in water at 80°C (MB80WU), and (3) two mortar bars were stored in water at 20°C (MB20WU). All ultrasonic data presented are averaged values of four data sets – two reciprocal sets from each mortar bar.

3. Results

3.1 Expansion of mortar bar specimens

Two types of aggregates are generally distinguished according to the accelerated mortar bar test (following ASTM C1260): non-reactive (aggregates indicating expansion of mortar bars < 0.10 % after a fourteen-day testing period); and reactive (aggregates indicating expansion of mortar bars > 0.10 % after a fourteen-day testing period).

The investigated mortar bars tested in 1 M NaOH solution at 80°C (MB80NaOHL) exceeded the limit of 0.10 %, i.e. achieved 0.18 % after fourteen and 0.51 % after forty days of testing, respectively (Fig. 3). The expansion values of MB20WL and MB80WL mortar bars stored in water solution (at both 20°C and 80°C) were both in a narrow range, between -0.01 and 0.02 % after fourteen, as well as forty days of testing (Fig. 3). The shape of the expansion curves indicated a continuous increase of expansion values of the MB80NaOHL mortar bars after the end of measurement. On the other hand, stagnating expansion data of MB20WL and MB80WL mortar bars can be expected.

3.2 Time domain analysis - analysis of the basic parameters of recorded signals

Figure 4 shows experimental data of three independent sample types. Each dependence/curve is an average of four data sets (two tested samples and transmitter/receiver interchangeability). Fig. 4A shows P wave velocity-time dependence of three samples.

MB20WU (blue trace) exhibits a continuous increase of longitudinal wave velocity from 3.2 km/s. After about 10 days, the velocity stabilizes at about 4.8 km/s. Due to the influence of high temperature (80°C) and faster sample hardening, MB80WU (red trace) exhibits a much faster increase of P-wave velocity from 3.2 km/s to 4.2 km/s. After 3 days of testing, the velocity reached 4.2 km/s and remained at this level until the end of the experiment. On the contrary, MB80NaOHU exhibits a rapid increase of longitudinal velocity within about the first 2 days. After this time, we can observe a gradual decrease of longitudinal propagation velocity in the sample.

In Fig. 4B, we can see ultrasonic signal duration-time dependence. With respect to MB20WU, we can observe a gradual increase of signal duration over time. On the contrary, both heated samples exhibit a rapid decrease of signal duration during the first stage of the test. During this period, the sample should stiffen quickly due to the influence of higher temperature. After this time, we see constant signal duration in sample MB80WU and a slow decrease of signal duration in sample MB80NaOHU.

Fig. 4C presents maximum ultrasonic signal amplitude over time. Again, a continual increase in maximum signal amplitude over time is seen in sample MB20WU. Similarly, we see a rapid change of maximum signal amplitude over time in sample MB80WU. High temperature quickens mortar bar hardening in any type of bath. After some time the signal amplitude stabilizes to a constant value. In sample MB80NaOHU, there is a rapid rise of signal amplitude rise (1-2 days). After this time, there is a gradual decrease in amplitude. There are some amplitude fluctuations from the second to the tenth day of the experiment. We believe such fluctuations to be due to local stiffness conditions in the sample under the study. These fluctuations may be caused by the fixed unmovable waveguides, resulting in an increase in stress over the course of ASR. Because two mortar bars are placed in a single heating chamber, maximum ultrasonic signal amplitude may be affected by cross-talk between

individual channels or a different propagation path from transmitter to receiver (chamber walls, testing solution and second mortar bar).

Fig. 4D shows signal energy dependence of all three samples over time. The blue line again displays a continuous increase of transmitted energy. The red and green lines again show rapid energy increase within 1 – 5 days. After this time, we can observe fluctuations in recorded signal energy. After the 10^{th} day of the experiment, we see a continual decrease in signal energy. We can say that the energy of recorded signals partly reflects the stiffening or deterioration of samples. Nevertheless, like the maximum signal amplitude dependence shown in Fig. 4C, this is affected by many parameters not directly related to the state of the sample.

3.3 Full waveform analysis

The Vallen system obtains full waveforms through a multichannel transient recording system. Figure 5 shows the waveforms of ultrasonic sounding for three different samples. The lower trace of each frame is the first day of the experiment and the upper trace represents the last. Fig. 5A – the MB20WU sample was measured for 20 days. Here we see a continual shortening of arrival time, resulting in increasing propagation velocity in the sample during sample hardening. A continuous increase in first arrival amplitude can also be observed. Fig. 5B – red traces show the MB80WU sample which was measured for 26 days. Here we can see rapid shortening of arrival time in 1 or 2 days. First signal amplitude also increases during the first two days of the experiment. After that, the amplitude and arrival time remains practically constant. Fig. 5C – green traces show the MB80NaOHU sample. Signals exhibit significant delay in all arrival times (except for the first two days). Also, there is a significant decrease in first arrival amplitude, beginning on the second day of the test.

The arrival times and first onset amplitude of signals shown in Figure 5 were subjected to precise arrival time determination. A two-step AIC picker was used to identify the onset times [18]. Based on the arrival times determined by an AIC picker, longitudinal propagation velocity was calculated. These time courses are shown in Figure 6A. We see behavior similar to that shown in Fig. 4A; continual increase of velocity in the sample at 20°C, increase of velocity within 5 days in the sample at 80°C and rapid increase of velocity within 2 days, followed by continual velocity decrease. Starting from day 10, velocity decrease is much closer to a linear dependence, which is not the case for velocity dependence shown in Fig. 4A. The faster velocity decrease after day 25 can be explained by the Vallen system determining arrival time based on the signal crossing some threshold value. At the end of the experiment, the signal is quite weak and the first onset amplitude can be missed. According to our knowledge, amplitude of the signal's first arrival is very sensitive to sample integrity. Based on precise arrival times obtained by an AIC picker, the first onset amplitude was determined, which is depicted in Figure 6B. There is a marked amplitude increase in sample MB20WU, as well as an amplitude increase in the MB80WU sample. On the contrary, the MB80NaOHU sample exhibits a rapid increase in first onset amplitude, followed by amplitude decrease with some fluctuations. Starting from day 15, continuous amplitude decrease is observed.

3.4 Frequency domain analysis

Waveforms obtained by the transient recorder part of the AMSY5 system were also subjected to frequency domain analysis. All signals were recorded with a pre-triggering setup of 200 points, 0.02 ms. An example of a recorded signal is shown in Figure 2. Two different signal parts were analyzed: 1. The initial part of the signal; 2. The entire recorded signal.

1. For frequency domain analysis, the first 20 μs was selected after signal arrival (200 points. The signal time series values were corrected using a Hanning window. The corrected part of the signal was extended by adding zero values to have a total of 16384 points. Fast Fourier Transform analysis was applied to this part of the data set, see Figure 7A. An example of the signal spectrum is shown in Figure 7B. Figure 8 shows results of frequency domain analysis. Figure 8A shows the frequency where the spectrum reached its maximum, as shown in Fig. 7B. We can see that the frequency of the initial part of recorded signals starts at 72- 73 kHz range for all samples. Sample MB20WU (blue color) displays a continuous increase of frequency up to about 81 kHz after 20 days of measurement. Sample MB80WU (red color) shows an increase of signal frequency. The frequency maximum at 92 kHz is reached after 3 days of measurement. After this day, the value is stable for about 5 days. Then, a continual decrease of frequency can be observed. On the contrary, sample MB80NaOHU displays a low value of frequency change up to only 78 kHz, but with a high slope – in 2 days. After this, the value fluctuates for about 13 days. Starting on day 15 day, there is generally a continual decrease in frequency. Figure 8B shows changes in the maximum values of spectrum frequency in the early part of the signal (see. Fig. 7A). These dependencies should display similar dependencies as the first amplitudes of signals (see Fig. 6B). In this type of analysis we analyze about 1.5 of the signal waveform period. Sample MB20WU shows a continuous increase in signal amplitude during the entire test duration. Sample MB80WU exhibits amplitude increase during the first 8 days, followed by a very slow amplitude decrease with minor fluctuations. For MB80NaOHU we see a rapid amplitude increase during the first 3 days. After this time, we notice a quick amplitude decrease for 5 days followed by a small amplitude increase. Starting from the 15^{th} day we see a continual decrease in amplitude very similar to Fig. 6B dependences.

Figure 9 shows examples of AGU-Vallen wavelet analysis [19] together with signal waveforms. The analyzed parts of waveforms are shown in green. The wavelet diagram shows the magnitudes of wavelet transform in rainbow colors. Lower magnitudes (zero) correspond to pink while peak magnitudes correspond to red. The wavelet data of three various signals acquired at different time points from each of the three measured samples are shown. Signals acquired at the beginning of the experiment (first row) are shown for all three samples. The second row demonstrates wavelet analysis of signals acquired at the time when maximum P-wave velocity is reached (see Fig.8A). An exception is the column of Fig. 9A of the sample at 80°C where velocity continues to increase. A regular time interval of 10 days was selected for this sample. The bottom row shows signals obtained at the end of experiment. Figure 9A (sample MB20WU) shows that at the beginning of experiment there is low frequency content only. This frequency content is maintained during the entire experiment. Over time there is an increase in higher frequency due to the increasing stiffness of the sample. The MB20WU sample was kept at 20°C for the entire experiment. Fig.9B shows wavelet analysis of sample MB80WU. Here we see higher frequency content at the beginning of experiment, as the high temperature of 80°C results in a rapid increase in mortar bar stiffness. Fig. 9C shows wavelet analysis of sample MB80NaOHU. At the beginning of storage, wavelet signal analysis is very similar for the sample at 80°C. On the second day of the experiment when maximum propagation velocity is observed, there is significant movement of frequencies towards the initial parts of the recorded signal. This can be explained by contact improvement between individual mortar bar aggregates due to the initiation of the ASR process. Wavelet analysis of signals recorded after 35 days shows significant damping of signals with low frequency content, which is significantly pronounced at the central part of the signal. Higher frequencies, closer to first signal arrival, can be explained by cross-talk and misrecording of transmitted signals, which also propagate through the bath and temperature chamber walls.

4.0. Discussion

Laboratory extension tests are a standard method of assessing the suitability of aggregate for concrete with respect to ASR. During testing, mortar bars are placed in a warm NaOH solution for 14 days at 80°. The mortar bars are repeatedly taken out of this bath (at least 5 times) and any change in length indicates susceptibility of the aggregate to ASR. Ultrasonic testing (UT) is one of the basic non-destructive methods for testing and researching qualitative and mechanical properties of materials. Over the past decade it has been used to test the setting and hardening of concrete mixtures [20, 21, 22, 23], but with respect to UT testing of aggregate susceptibility to ASR, this work is novel.

A chamber was developed and constructed for UT testing which allows for the long-term storage of mortar bars in 1M NaOH at 80° as well as their automatic, periodic ultrasound radiation directly in the chamber without any handling of the sample.

Detailed analysis of recorded UT signals and the data describing their character should enable us to determine whether ultrasound testing is a suitable method for detecting aggregate susceptibility to ASR. If so, the next task is to select a suitable form of UT data and manner of processing it, particularly with respect to ASR sensitivity, to enable automatic monitoring during testing.

For this purpose we assessed the primary data provided online by the Vallen measurement system, which required no further processing and also enabled direct monitoring.

Recorded waveforms were analyzed with respect to both time and frequency. In both cases UT parameters were monitored over time which depend on the velocity of propagation, attenuation and frequency filtering of the test environment. To determine the effect of

concrete setting and hardening and high temperatures and ASR on ultrasound parameters, measurements from different baths are compared to each other:

(1) water 20°, normal conditions, should reflect the process of setting and hardening - MB20WU

(2) water 80°, effect of temperature - MB80WU

(3) NaOH 80°, effect of ASR - MB80NaOHU.

The mortar bars were prepared in the same way with the same reactive aggregate for all experiments.

The results of the ultrasound test were compared with the extension tests which were carried out on identically prepared bars under the same physical conditions.

At the beginning of the experiment, the tested samples are in the initial phase of hardening. The measured initial velocity of approx. 4 km corresponds to the published velocity at a time of roughly 30 hours after the mixing of concrete [20, 24]. During the course of hardening there is an increase in the strength and stiffness (elastic constant) of the concrete. Along with increasing concrete stiffness there is an increase in the velocity of elastic waves. A sharp rise in velocity during the first few days was seen in all tested samples, independent of the type of bath and also described in the literature [22, 25]. For the MB20WU sample (blue line), the increase in velocity continues more slowly and corresponds to the process of concrete hardening under ideal conditions (quote). An increase in temperature results in a quickening of the hardening process and thus a steeper increase in velocity [26]. In the 80° bath (MB80WU, red trace and MB80NaOHU – green trace) the hardening process is complete within 4 days of the experiment. The velocity is then nearly constant in this sample and after a brief plateau begins to drop in MB80NaOHU sample. The drop in velocity begins around the 4^{th} day of the experiment and since we also begin to see expansion in the sample from the 5^{th}

day on, we ascribe the behavior of ultrasound parameters in MB80NaOHU sample between day 4 and 40 to the effects of ASR.

During the hardening process there is an increase in velocity, reduction of attenuation (increase in amplitude, signal length, energy) and reduction of high-frequency filtration, which results in a shift of spectra to higher frequencies. This type of behavior was recorded in all samples in the first 4 days of the experiment and in the blue sample it continued for the entire duration of the experiment. In contrast, ASR should have an entirely opposite effect, i.e. drop in velocity, increase of attenuation and shift of spectra to lower frequencies. This type of behavior was seen in MB80NaOHU sample, beginning on day 4 and continuing to the end of the experiment.

Even if all tested UT parameters reacted to ASR, their sensitivity and susceptibility to errors differed, presenting us with different informational values.

The parameters from the Vallen apparatus (arrival time determined by exceeding a threshold, maximum amplitude, energy, duration of signal, Fig. 4) have the advantage of being determined automatically and available online. At first glance, the most suitable parameter for describing ASR would seem to be signal energy, where a 0.5% change in length after 40 days corresponds to a drop in energy of 80%. Energy, along with duration and maximum amplitude are influenced by sample properties, as well as sample shape, chamber construction and potential cross-talk between channels. Of the parameters offered by the Vallen system, the most suitable is arrival time (direct P wave propagating primarily through the sample) and from this the velocity of P wave propagation. Even when using velocitys determined in this manner to assess ASR potential, waveforms should be recorded to enable such data to be checked.

The velocities obtained by processing waveforms correspond with minor differences to the velocities determined by the Vallen automated system. Prolongation of 0.5 percent

corresponds to a drop in velocity of 400 m/s (approx. 9% of maximum value). The amplitudes of first onset and maximum signal amplitude (Fig. 4 and 6) are similar in character but the first onset is much more sensitive to material change (80% compared to 10%). This is because the amplitude of first onset, just like arrival time, corresponds directly to wave propagation, which is affected only by the state of the test material. The amplitude of first onset is also 10 times more sensitive that the velocity of P wave propagation, which is given by the integral character of the sensor (sensor area). Even though the amplitude of first onset is very sensitive to ASR, dependence on the type of sensor, waveguide, nature of contact, and the difficulty in determining corrections make the comparison of amplitude measurement between individual laboratories very complicated. In MB80WU sample, there is a marked difference in first onset amplitudes between two adjacent dependencies. This jump was caused by chamber manipulation (visual checking of water level during the experiment). In MB80NaOHU sample, on days 6 to 11 there was a break in the steady drop, seen in all data but especially first onset amplitudes and energies. These excited states may reflect local disruptions and hardening due to local stiffness caused by ASR. If these excitations arise as a consequence of brittle failure, then these changes may be accompanied by increased AE activity.

The frequency content of the initial signal also behaves as expected, the hardening processes is accompanied by a shift to higher frequencies, while ASR results in a shift to lower frequencies. This behavior is depicted in the wavelet analysis pictures. The size of spectral peak at the initial phase of the signal (1.5 periods) correlates well with the first onset amplitude.

5.0 Comparison of ultrasonic sounding results with expansion values of mortar bars

The expansion values of mortar bars only indicated ASR in the mortar bars accelerated in 1 M NaOH (MB80NaOHL). Expansion values after 14 days reached 0.18 % (see Fig. 3). An increasing tendency was observed for the entire testing period. Almost no expansion was observed in mortar bars accelerated in water at 20°C and 80°C (MB20WL and MB80WL). These results are in line with long-year ASR laboratory testing [8]. Both high temperature and alkaline solution are essential factors for determining ASR impact.

The same conclusions were found employing ultrasonic sounding. ASR originating in a mortar bar accelerated in 1 M NaOH (MB80NaOHU), showed significant variations (decreases) in basic parameters. ASR caused mortar bar expansion connected to cracking and a decrease of ultrasonic first onset amplitude and velocity. Mortar bar stiffening combined with ASR degradation resulted in fluctuations observed from day 2 to day 10 (even 15) of measurement. After the 15^{th} day of measurement, continuous ASR degradation can be observed in decreasing basic parameters.

The expansion values of mortar bars accelerated in a water solution is almost the same as for mortar bars heated at 20°C and those heated at 80°C (MB20WL and MB80WL) indicating the absence of ASR. Gradual stiffening (observed in mortar bars accelerated in water at 20°C) or fast stiffening (observed in mortar bars accelerated in water at 80°C) did not produce any length changes of mortar bars as measured by a length comparator. Length measurements are not sensitive enough to reflect processes occurring during the first days of measurement. Disadvantages of this method are that it takes a relatively long time, it is only sensitive to 0.5% of the measured length, and it is technically difficult with respect to work safety and handling the mortar bar. During the hardening process, deformation can also occur [27], but this is probably under the detection limit for this material.

6. Conclusions:

By using ultrasonic sounding and by analyzing the data obtained during laboratory testing of mortar bars exposed to three different temperature and storage conditions (temperature of 20 or 80°C, distilled water or 1M NaOH), the following conclusions can be drawn:

1. Adoption of a new measurement approach during laboratory testing of ASR potential of aggregates was possible by constructing a special experimental chamber enabling quasi-continuous (repetition of readings each 10 minutes) ultrasonic sounding of submerged mortar bars even at 80°C and 1M NaOH accelerating solution.
2. Evaluation of measured ultrasonic signals showed that ongoing deterioration of microstructure of mortar bars can be successively detected by both time and frequency domain analysis of recorded signals
3. Based on the extension and ultrasound experiments, ASR impact was identified in ultrasound data. It was found that at 80° 1M NaOH, the impact of ASR continued after the hardening process was complete.
4. Microstructural changes due to the ASR are manifested by reduced P-wave velocity, prolonged first onset amplitude, and a shift of the frequency spectra of direct longitudinal waves to lower frequencies.
5. Based on the results of current study, the proposed methodical approach to the adoption of ultrasonic sounding in the evaluation of experimental mortar bars in the testing of ASR potential is to measure both P-wave velocity and to record whole signal to be able to evaluate its amplitude. The velocity of wave propagation parameter enables better comparison between laboratories.
6. An advantage of ultrasound tests is that they provide comprehensive information about the state of the tested sample. A disadvantage of ultrasonic sounding measurement is that it requires more advanced equipment.

7. The proposed methodology must be tested on aggregates with varying reactivity.
8. The Vallen AMSY5 ultrasonic/AE system was proven to be successful for the study of alkali-silica reactions in concrete material with reactive forms of aggregates.

Standard accelerated mortar bar testing requires manual measurement of expansion values using a length comparator operated by skillful operator. Individual readings are taken each 24 hours which is probably sufficient in terms of the sensitivity of this type of measurement. Adoption of ultrasonic sounding with quasi-continous readings represents a significant improvement the laboratory testing of mortar bar due to its automated signal detection which minimizes the role of the operator and eliminates possible errors. The most important input, however, of the proposed approach is the much higher sensitivity of recorded and analyzed ultrasonic characteristics compared to the measurements of dimensional changes of experimental mortar bars. In the case of ultrasound, the recorded velocity changes were about 50 % and more than 80 % in case of the first onset amplitude. The dimensional (length) changes did not exceed 0.51 % of the original length of the tested mortar bars.

Based on the test results and analysis, we can conclude that ultrasonic testing is an efficient method for evaluating the degree of the mortar bar deterioration caused by ASR. In addition to ultrasonic pulse velocity (UPV) measurements, first onset amplitude and signal frequency content should also be considered in the evaluation of deterioration due to alkali-silica reaction.

7. Acknowledgement:

This study was financially supported through research project P104/12/0915 with funding provided by the Czech Science Foundation. The technical help of Mr. Filler, Mrs. Erdingerová, and Mr. Nemejovský was very much appreciated.

[1] P. Rivard, G. Ballivy, Clermont Gravel, Francois Saint-Pierre, Monitoring of an hydraulic structure affected by ASR: A case study, Cement and Concrete Research 40 (2010) 676 – 680.

[2] T. S. Hansen and J. M. Frederiksen, Micro structural analysis – An essential tool for diagnosis of concrete deterioration and choice of repair strategy, Materials and Corrosion 63 (2012).

[3] C. L. Page, Degradation of reinforced concrete: Some lessons from research and practice, Materials and Corrosion. 63 (2012).

[4] P. Rivard, F. Saint-Pierre, Assessing alkali-silica reaction damage to concrete with non-destructive methods: From the lab to the field, Construction and Building Materials. 23 (2009) 902–909

[5] J.W. Pan, Y.T. Feng, J.T. Wang, Q.C. Sun, C.H. Zhang, D.R.J. Owen, Modeling of alkali-silica reaction in concrete: a review, Front. Struct. Civ. Eng. 6 (2012) 1–18.

[6] M.D.A. Thomas, K.J. Folliard, B. Fournier, T. Drimalas, P. Rivard, Study of remedial actions on highway structures affected by ASR. Proceedings of the 14th ICAAR, May 20-25 2012, Austin, Texas, 051612-THOM.

[7] ASTM C1260-07 (2011) Test method for potential alkali reactivity of aggregates (Mortar-bar method). ASTM C1260, West Conshohocken, 04.02, 2011.

[8] J. Lindgård, Ö. Andiç-Çak, I. Fernandes, T.F. Rønning, M.D.A. Thomas, Alkali silica reactions (ASR): Literature review on parameters influencing laboratory performance testing, Cement and Concrete Research 42 (2012) 223 – 243.

[9] E. Proverbio, Evaluation of deterioration in reinforced concrete structures by AE technique. Materials and Corrosion (2011), 62, No. 2, DOI: 10.1002/maco.201005735, pp. 161-169.

[10] D. Breysse, Nondestructive evaluation of concrete strength: An historical review and a new perspective by combining NDT methods, Construction and Building Materials, 33 (2012) 139-163.

[11] O. Omikrine Metalssi, B. Godart, and F. Toutlemonde, Effectiveness of Nondestructive Methods for the Evaluation of Structures Affected by Internal Swelling Reactions: A Review of Electric, Seismic and Acoustic Methods Based on Laboratory and Site Experiences, Experimental Techniques (2013)

[12] M. Sargolzahi, S.A. Kodjo, P. Rivard, J. Rhazi, Effectiveness of nondestructive testing for the evaluation of alkali–silica reaction in concrete, Construction and Building Materials 24 (2010) 1398–1403.

[13] J.D. Stauffer, C.B. Woodward, K.R. White, Nonlinear ultrasonic testing with resonant and pulse velocity parameters for early damage in concrete. ACI Mater J 2005;102(2):118–21.

[14] T. Lokajíček, R.K. Goel, V.Rudajev & R.D. Dwivedi, Assessment of velocity anisotropy in rocks. International Journal of Rock Mechanics & Mining Sciences, 57 (2013) 142–152.

[15] M. Petružálek, J. Vilhelm, V. Rudajev, T. Lokajíček & T. Svitek, Determination of the anisotropy of elastic waves monitored by a sparse sensor network. International Journal of Rock Mechanics & Mining Sciences, 60 (2013) 208–216.

[16] M. Hoerbe, Final report of geological research: calculation of aggregate resources in Těchobuz quarry near Pacov, report No. FZ006900 (2005) (in Czech).

[17] Kamenolomy ČR s.r.o. http://www.mineral-cesko.com/cz/provozovny-lomy/morava-jih/contactid_24/kamenolom-techobuz.aspx (rev. 26.9.2013)

[18] P. Sedlák, Y. Hirose, S.A. Khan, M.Enoki, J. Sikula, New automatic localization technique of acoustic emission signals in thin metal plates. Ultrasonics 49 2009 254–62.

[19] Vallen, J. "Latest improvements on Freeware AGU-Vallen-Wavelet." Proceedings of the 29th European conference on acoustic emission testing. Vienna, Austria. (2010).

[20] H.W. Reinhardt and C.U. Grosse. Continuous monitoring of setting and hardening of mortar and concrete. *Construction and building materials* 18.3 (2004) 145-154.

[21] N. Robeyst, E. Gruyaert, Ch.U. Grosse, N. De Belie, Monitoring the setting of concrete containing blast-furnace slag by measuring the ultrasonic p-wave velocity. Cement and Concrete research 38.10 (2008): 1169-1176.

[22] R. Latif Al-Mufti and A.N. Fried, The early age non-destructive testing of concrete made with recycled concrete aggregate *Construction and Building Materials* 37 (2012): 379-386.

[23] G. Trtnik, and G. Matija, Recent advances of ultrasonic testing of cement based materials at early ages. *Ultrasonics* 54.1 (2014): 66-75.

[24] M. Krauß and H. Karim, Determination of initial degree of hydration for improvement of early-age properties of concrete using ultrasonic wave propagation. *Cement and Concrete Composites* 28.4 (2006): 299-306.

[25] L.M. del Río, A. Jiménez, F. López, F.J. Rosa, M.M. Rufo, J.M. Paniagua, Characterization and hardening of concrete with ultrasonic testing. Ultrasonics 42.1 (2004): 527-530.

[26] Y. Zhang, W. Zhang, W. She, L. Ma, and W. Zhu, Ultrasound monitoring of setting and hardening process of ultra-high performance cementitious materials. *NDT & E International* 47 (2012): 177-184.

[27] D.P. Bentz, A review of early-age properties of cement-based materials. *Cement and Concrete Research* 38.2 (2008) 196-204.

[28] RILEM TC 219-ACS 'Alkali–silica reactions in Concrete Structures': RILEM AAR-4.1 Detection of potential alkali-reactivity of aggregates: accelerated (60°C) concrete prism test, (unpublished draft), (2006).

[29] RILEM TC 106-AAR, 'Alkali aggregate reaction' A. TC 106-2—Detection of potential alkali-reactivity of aggregates—the ultra-accelerated mortar-bar test B. TC 106-3—Detection of potential alkali-reactivity of aggregates—method for aggregate combinations using concrete prisms, Mater. Struct. 33 (2000) 283–293.

Figure1

Click here to download high resolution image

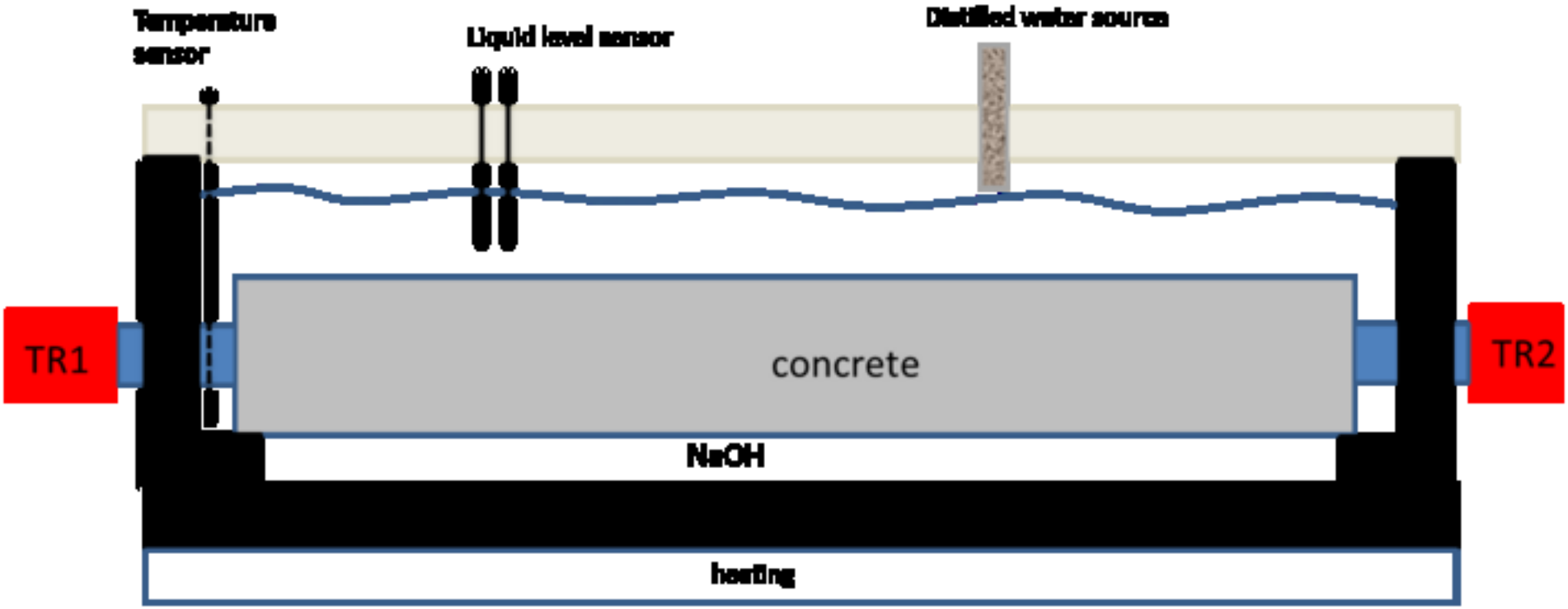

Figure2
Click here to download high resolution image

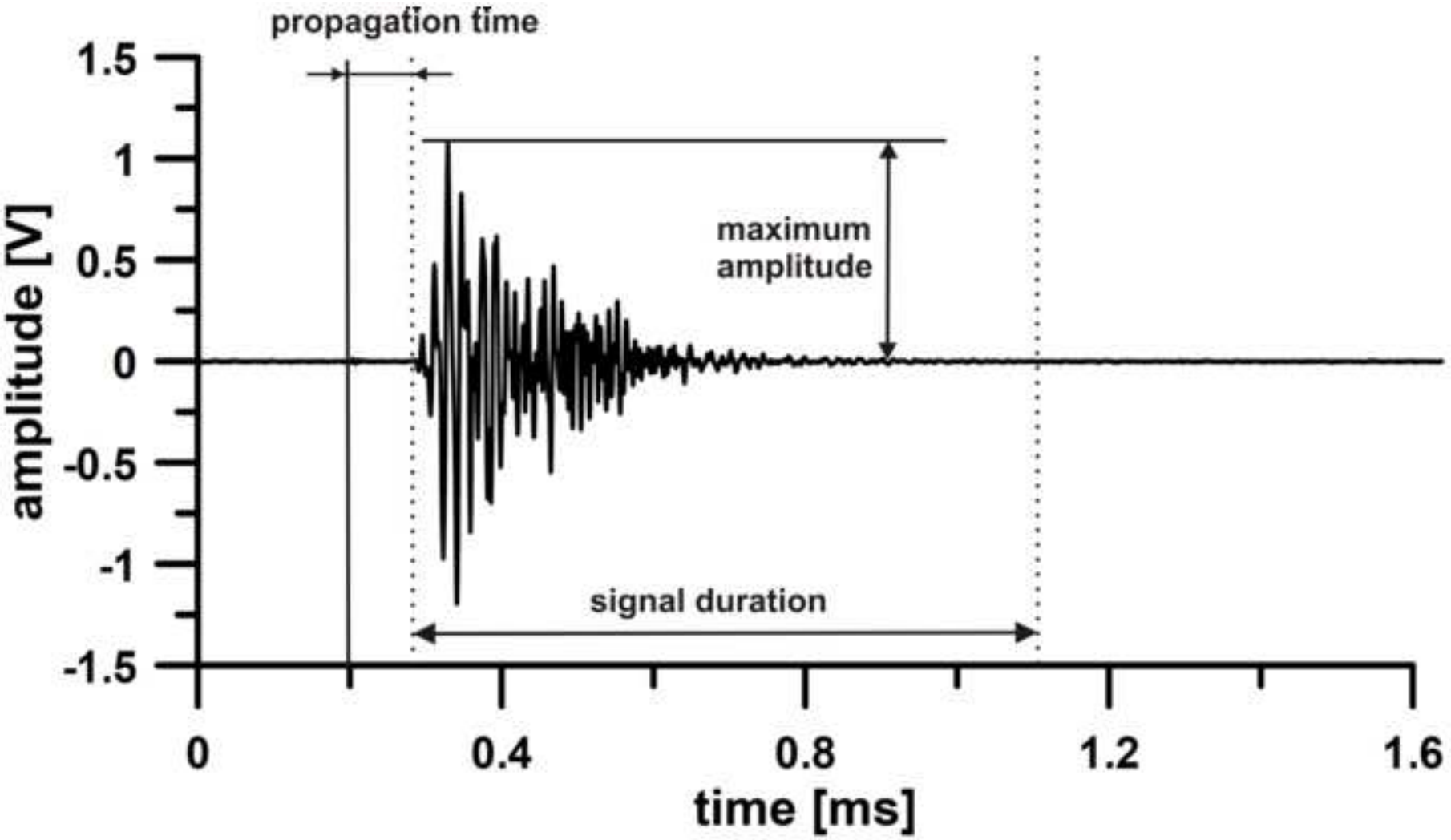

Figure3
Click here to download high resolution image

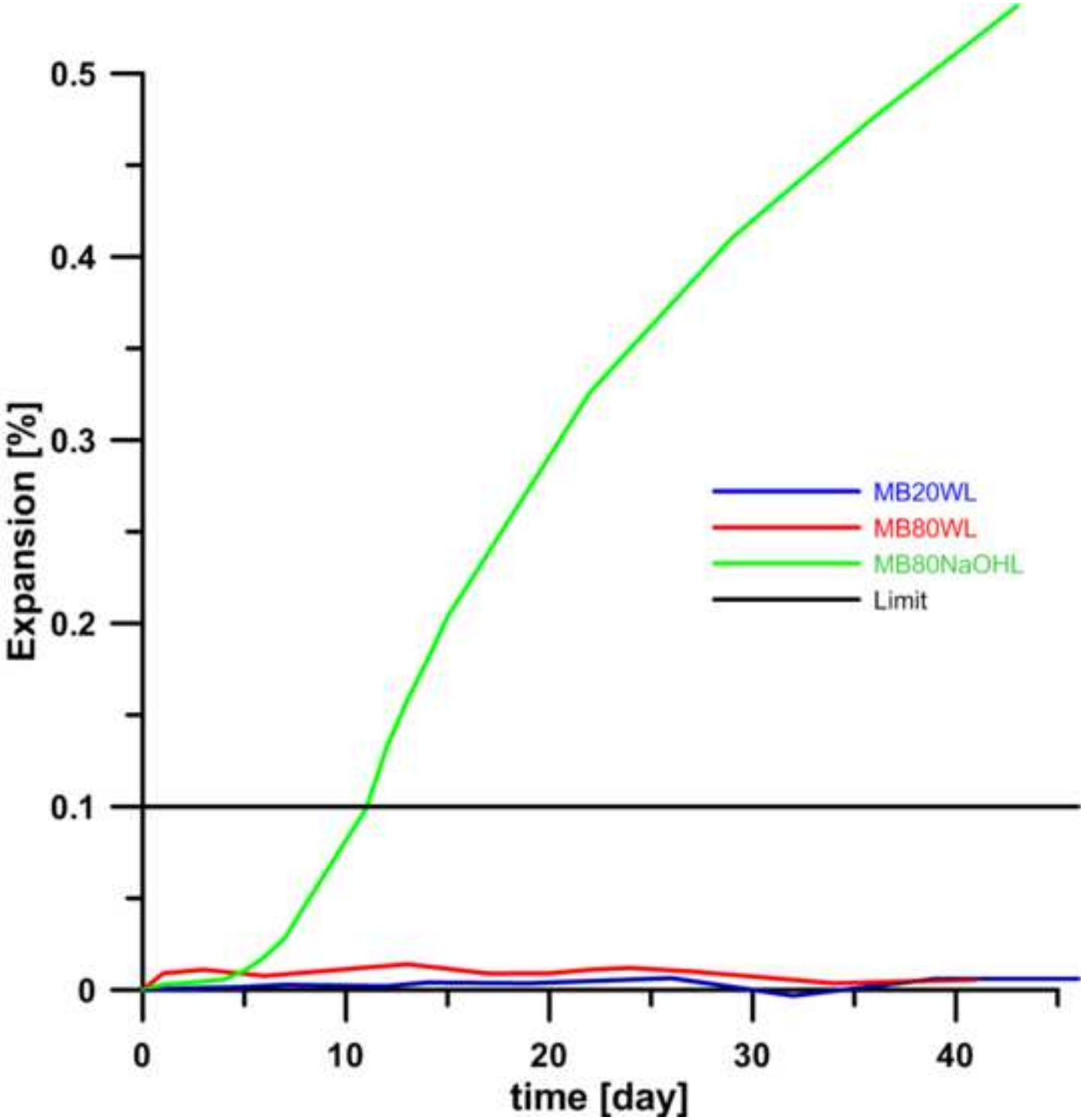

Figure4

Click here to download high resolution image

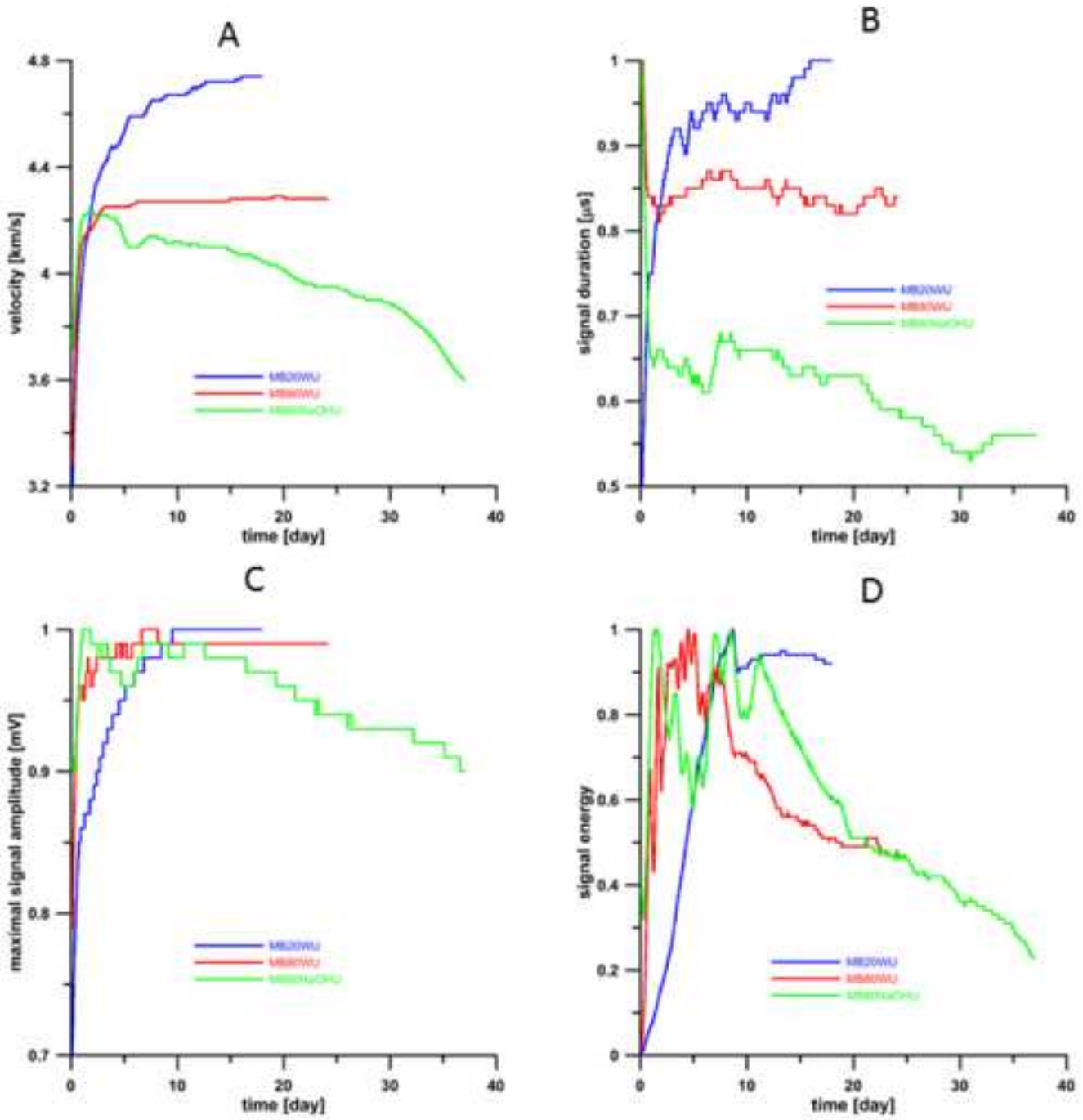

Figure5

Click here to download high resolution image

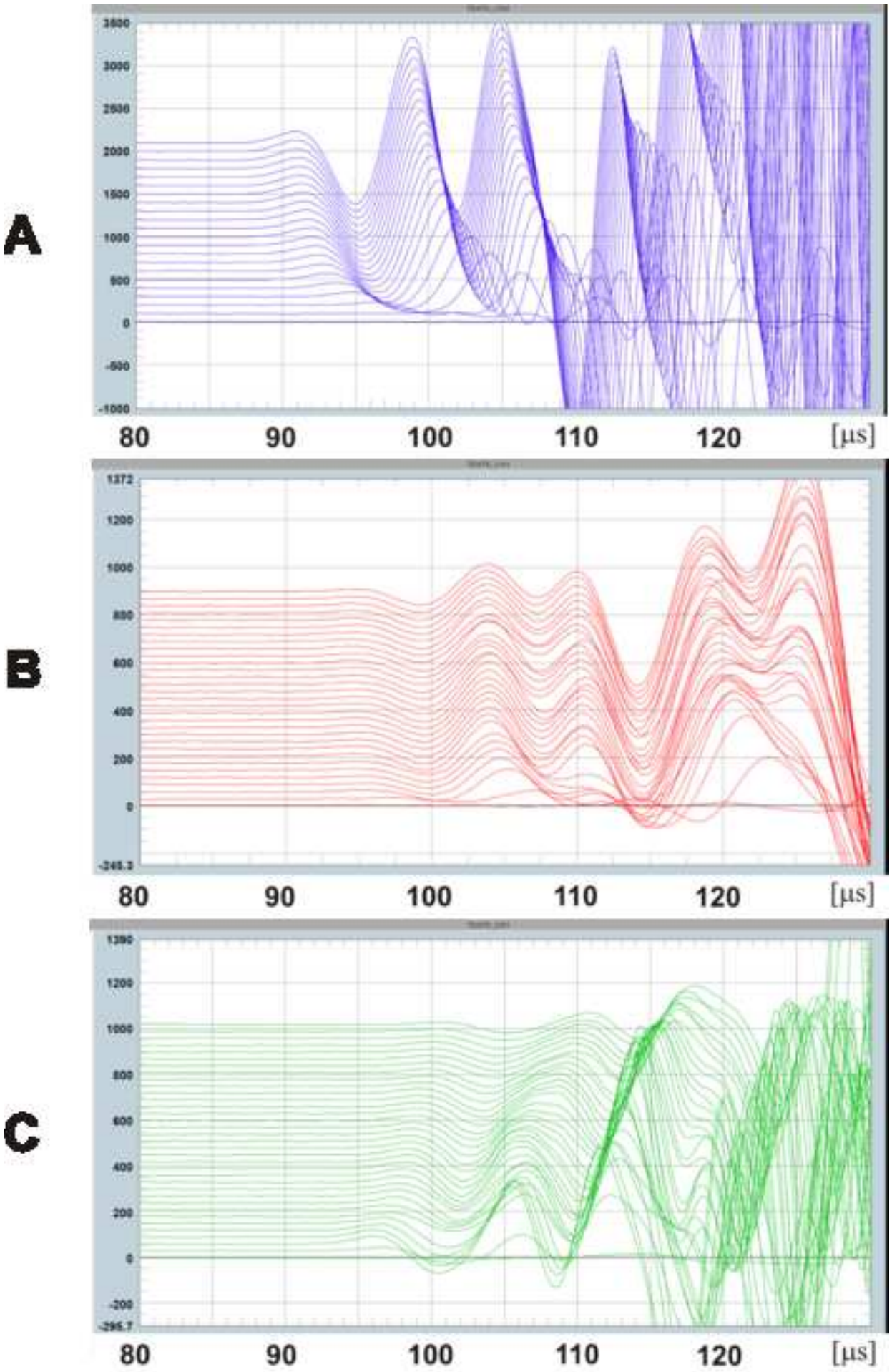

Figure6

Click here to download high resolution image

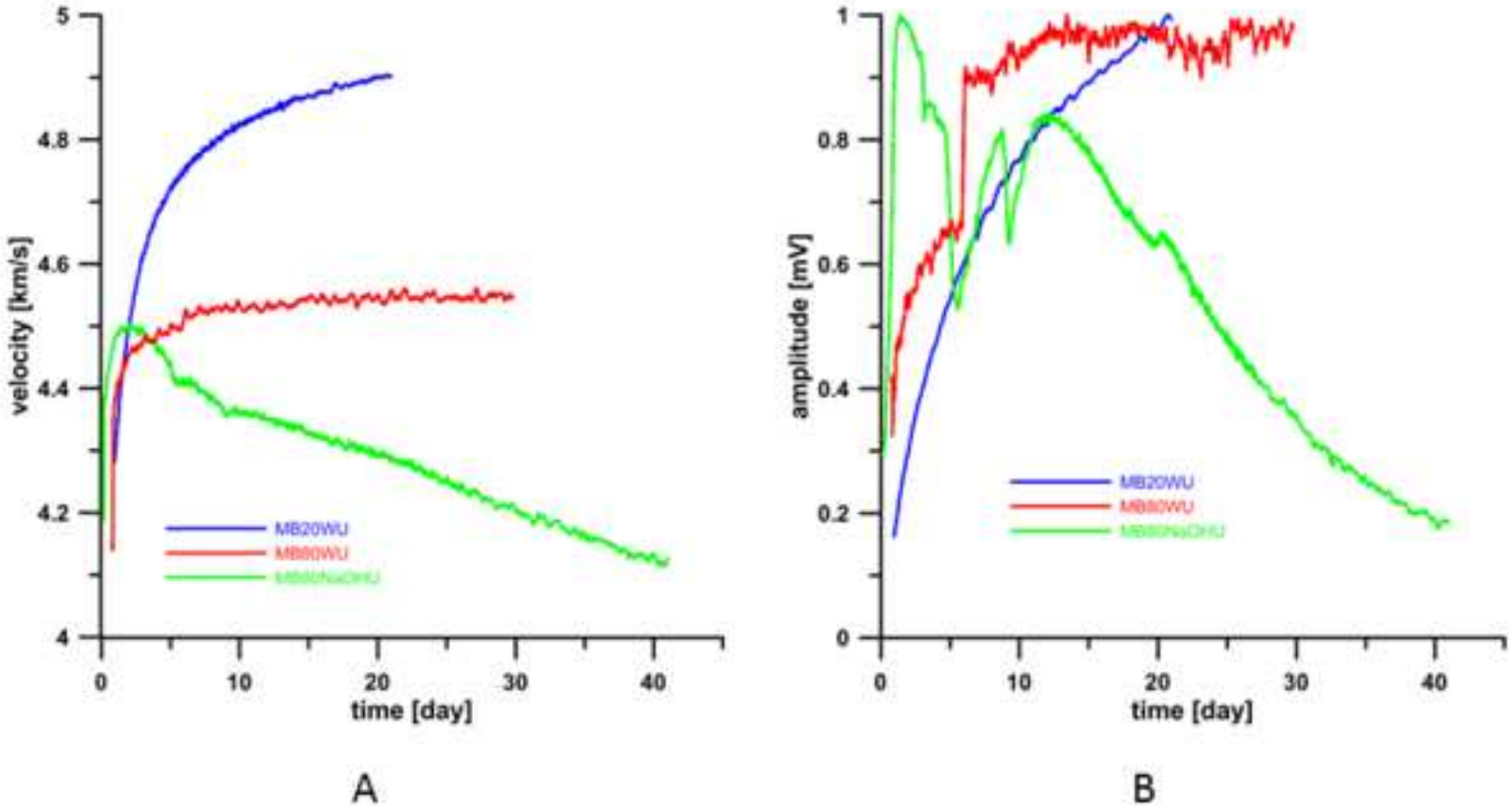

Figure7

Click here to download high resolution image

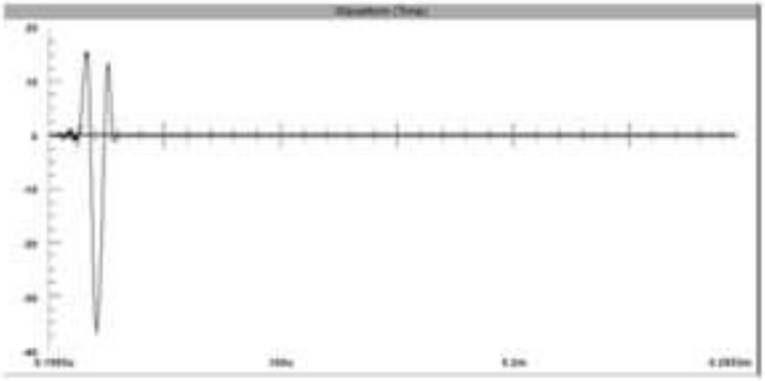

A

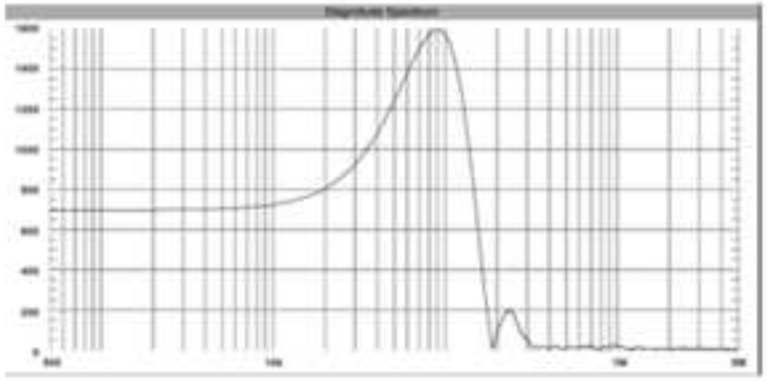

B

Figure8

Click here to download high resolution image

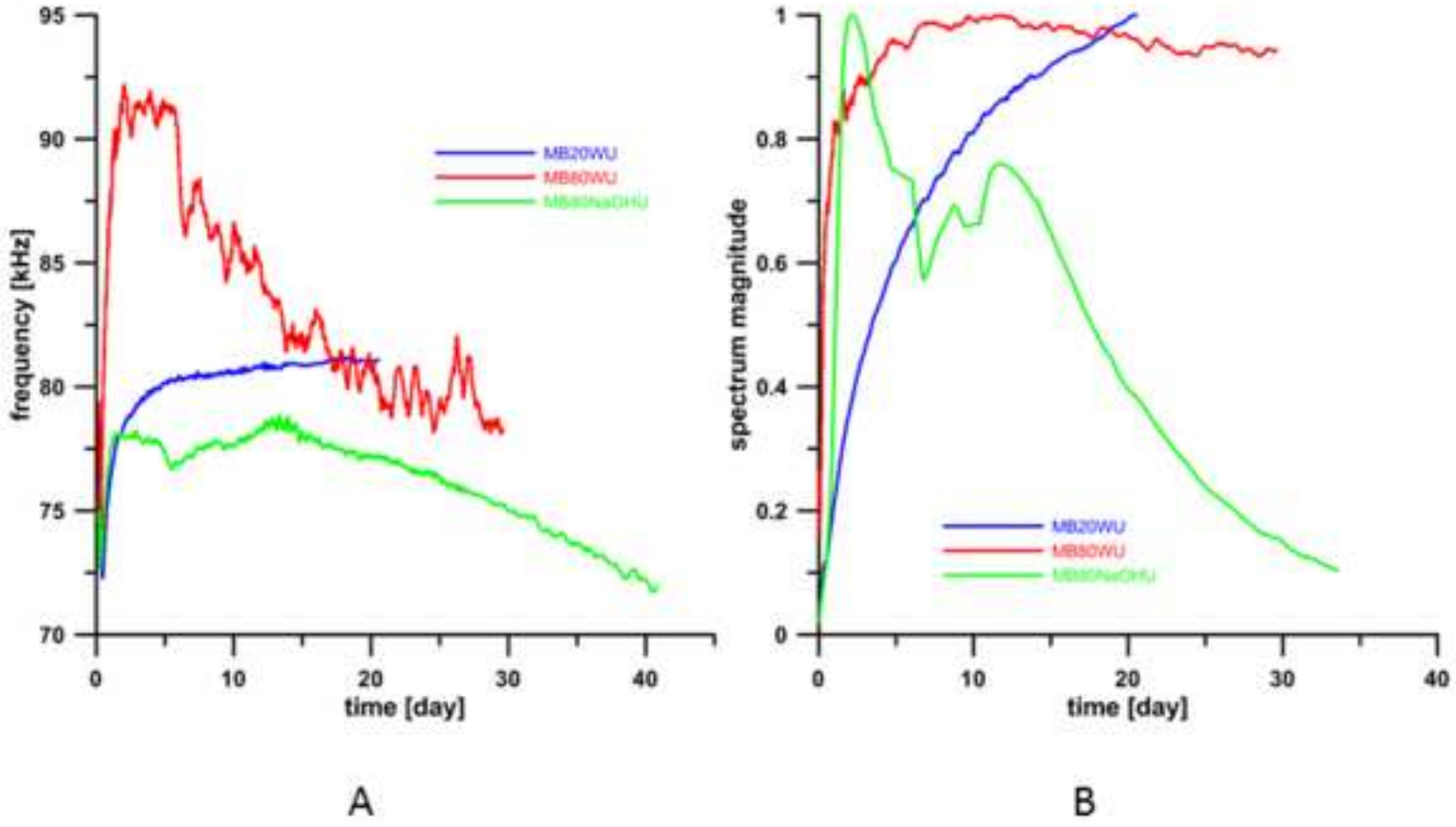

Figure9

Click here to download high resolution image

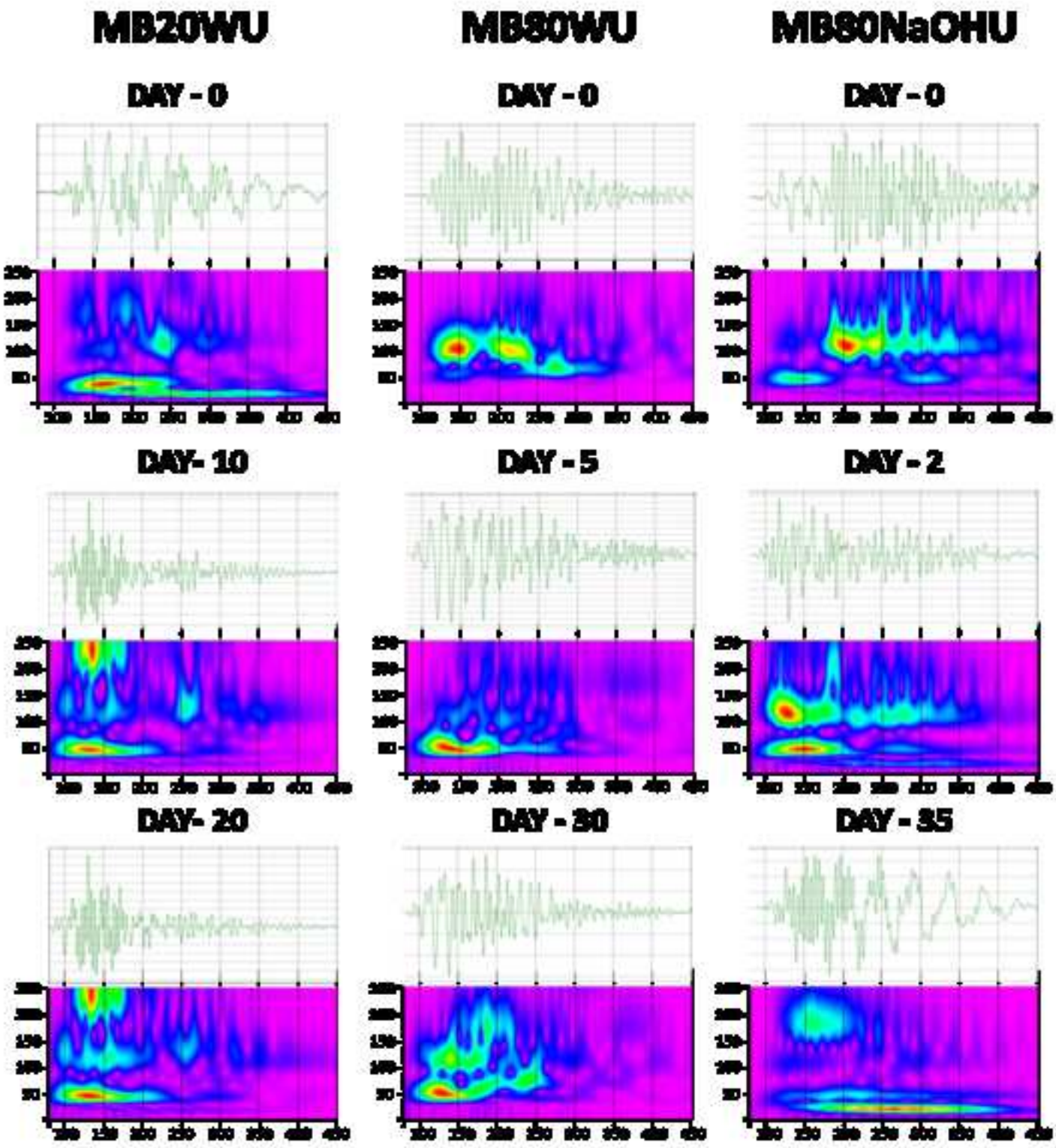

Figure caption:

Figure 1: Technical layout of heating chamber equipped with waveguides and ultrasonic sensors.

Figure 2: Example of transmitted ultrasonic signal with significant features used in our analysis

Figure 3: Expansion curves of mortar bars. MB20WL - mortar bars stored in water at 20°C, MB80WL - mortar bars stored in water at 80°C, MB80NaOHL - mortar bars stored in 1 M NaOH solution at 80°C.

Figure 4: Experimental data of mortar bars obtained by measurements in a temperature-controlled heating chamber. A – velocity/time dependence, B – signal duration/time dependence, C – maximal signal amplitude/time dependence, D – signal energy time/dependence of individual storage types.

Figure 5: Example of recorded waveforms in a temperature-controlled chamber. A – waveforms in the MB20WU sample, B - waveforms in the MB80WU sample, C - waveforms in the MB80NaOHU sample. Waveforms are plotted at 1 day time intervals. The bottom line of each frame is the first day of measurement. The time axis is the propagation time of ultrasonic waves in the sample.

Figure 6: A - P-wave velocity/time dependence; B – first arrival amplitude/time dependence

Figure 7: A –Part of signal waveform corrected by Hanning window; B – Frequency spectra of the signal extended to 16384 points.

Figure 8: Frequency domain analysis: A – frequency/time of the first onset dependence; B spectral amplitude/time dependence of first full wave of recorded signals.

Figure 9: AGU-Vallen wavelet analysis, A – sample MB20WU, B – sample MB80WU and C – sample MB80NaOHU. The time axis is 3700 samples (370 □s) for each image and the frequency range is 0 to 250 kHz, the frequency magnitude is denoted by color.